

STUDIES ON THE ROLE OF HVOF COATINGS TO COMBAT HOT CORROSION, OXIDATION AND EROSION OF MATERIALS USED IN TURBINE COMPONENTS

Thesis

Submitted in partial fulfillment of the requirements for the degree of

DOCTOR OF PHILOSOPHY

by

JEGADEESWARAN. N



**DEPARTMENT OF METALLURGICAL AND MATERIALS
ENGINEERING**

**NATIONAL INSTITUTE OF TECHNOLOGY KARNATAKA,
SURATHKAL, MANGALORE – 575025**

October, 2014

DECLARATION

by the

Ph. D. RESEARCH SCHOLAR

I hereby *declare* that the Research Thesis entitled “**Studies on the role of HVOF coatings to combat hot corrosion, oxidation and erosion of materials used in turbine components**” which is being submitted to the **National Institute of Technology Karnataka, Surathkal** in partial fulfillment of the requirements for the award of the Degree of **Doctor of Philosophy** in Metallurgical and Materials Engineering is a *bonafide report of the research work carried out by me*. The material contained in this Research Thesis has not been submitted to any University or Institution for the award of any degree.

JEGADEESWARAN. N

Register No. **MT09P01**

Department of Metallurgical and Materials Engineering

Place: NITK Surathkal, Srinivasnagar

Date:

C E R T I F I C A T E

This is to *certify* that the Research Thesis entitled “**Studies on the role of HVOF coatings to combat hot corrosion, oxidation and erosion of materials used in turbine components**” submitted by **Jegadeeswaran. N** (Register Number: **MT09P01**) as the record of the research work carried out by him, is *accepted as the Research Thesis submission* in partial fulfillment of the requirements for the award of degree of **Doctor of Philosophy**.

Research Guide(s)

Dr. Udaya Bhat K

Dr. Ramesh M R

Chairman – DRPC

ACKNOWLEDGEMENTS

*It is with great and profound sense of gratitude I thank my guide **Dr. Udaya Bhat K**, Associate Professor, Department of Metallurgical and Materials Engineering, and **Dr. Ramesh M R**, Assistant Professor, Department of Mechanical Engineering, NITK, Surathkal for their inspiring guidance, excellent research supervision and valuable discussions through out the course of this research work.*

*I am especially indebted to **Dr. Jagannath Nayak** Professor and Head, **Dr. K.Narayana Prabhu**, Former Head, Department of Metallurgical and Materials Engineering, NITK, Surathkal for their constant encouragement, help and suggestions from time to time.*

*I express my gratitude to **Prof. Vijay Desai**, RPAC member, Department of Mechanical Engineering and **Prof. Kasturi V Bangera**, RPAC member, Department of Physics, NITK, Surathkal, for their valuable suggestions during the research work.*

*I am immensely thankful to **Dr. R.P. Reddy**, Principal, REVA University, Bangalore, for permitting to carry out this investigation.*

*I wish to thank **Mr. Joshi**, Manager, Spraymet Industries Ltd, Bangalore, **Mr. Thandon**, Manager, ANOD Plasma Ltd, Kanpur, and **Prof. C.S. Ramesh**, PESIT, Bangalore for their help and encouragement.*

I would like to thank the non-teaching staff of the Metallurgical and Materials Engineering department for their direct and indirect help during the course work.

I also express my gratitude to my spouse and daughter for their support and help during the course of the research work. Finally, I acknowledge the encouragement and help received from all of my friends and well wishers.

JEGADEESWARAN. N

ABSTRACT

Degradation by high temperature oxidation, hot corrosion and erosion are the main failure modes of components in the hot sections of gas turbines, boilers, industrial waste incinerators, metallurgical furnaces, petrochemical installations, etc. The present research work explores the possibility of use of HVOF sprayed cermet coatings on the materials used in gas turbine systems. The coatings are investigated for their resistance to hot corrosion, oxidation and erosion, under laboratory conditions.

Three types of feed stock powders, namely, 10% $\text{Al}_2\text{O}_3+\text{CoCrAlTaY}$, 25% $(\text{Cr}_3\text{C}_2-25(\text{Ni}_20\text{Cr})) + 75\%\text{NiCrAlY}$ and Stellite-6 were sprayed on three alloys used in turbine related applications, namely Ti-6Al-4V (Ti-31), Cobalt based superalloy (Superco-605) and Fe-based special steel (MDN-121). The microstructure and mechanical properties of the coatings were characterized. It is followed by the investigation of their cyclic hot corrosion, cyclic oxidation and erosion of the coating behaviour is compared with the uncoated substrate alloys.

Hot corrosion resistance of the coatings and substrates were investigated in a molten salt environment of $\text{Na}_2\text{SO}_4-50\%\text{V}_2\text{O}_5$ at 800 °C for 50 cycles. Each cycle consisted of heating at 800 °C for 1 hour followed by 20 minutes of cooling in air. The analysis indicated that the carbide coated substrate alloys showed maximum resistance to hot corrossions, it was followed by alumina coating. The analysis also showed that the better resistance of carbide coating is due to the formation of oxides of alumina and chromium.

Similarly, the resistance cyclic oxidation is investigated at 800 °C for 50 cycles, Again each cycle consisted of heating at 800 °C for 1 hour which is followed by 20 minutes of air cooling. The investigation indicated that the carbide coating exhibits maximum resistance to cyclic oxidation which is followed by Stellite-6 coatings. All three coatings showed better resistance compared to uncoated alloys both under cyclic oxidation and cyclic hot corrosion conditions.

Solid particle erosion studies were conducted using silica sand as the erodent. Amongst three coatings, Stellite-6 coating performs better under sand erosion conditions. The 25% $(\text{Cr}_3\text{C}_2-25(\text{Ni}_20\text{Cr})) + 75\%\text{NiCrAlY}$ coating undergoes composite erosion mode, whereas the 10% $\text{Al}_2\text{O}_3+\text{CoCrAlTaY}$ and Stellite-6 coatings undergo damage by brittle mode. Erosion behaviour of the substrate materials is ductile and resistance is better than the coating material.

TABLE OF CONTENTS

<u>Topic</u>	<u>Page</u>	
Acknowledgements	<u>No.</u>	
Abstract		
Table of Contents	i	
List of Figures	vii	
List of Tables	xvi	
Nomenclature	xvii	
CHAPTER 1	INTRODUCTION	1
1.1	Objectives of the Present Investigation	2
1.2	Organization of the Thesis	3
CHAPTER 2	LITERATURE REVIEW	5
2.1	Alloy Developments for Gas Turbine Applications	5
2.2	Hot Corrosion	6
2.2.1	High temperature (Type I) hot corrosion (HTHC)	7
2.2.2	Low temperature (Type II) hot corrosion (LTHC)	7
2.2.3	Hot corrosion mechanisms	8
2.2.4	Hot corrosion degradation sequence	10
2.2.5	Hot corrosion in the molten salt environment (Na ₂ SO ₄ -V ₂ O ₅)	11
2.3	High Temperature Oxidation	16
2.4	Erosion	17
2.4.1	Erosion mechanisms	18

2.5	Surface Coatings	23
2.5.1	Thermal spray coatings	24
2.5.2	HVOF process	25
2.5.3	Coating formation and bonding mechanism	28
2.6	Coating Materials	29
2.6.1	Oxide coating	30
2.6.2	MCrAlY coating	33
2.6.3	Carbide coating	33
2.6.4	Stellite-6 coating	34
2.7	Summary	34
CHAPTER 3	EXPERIMENTAL SETUP	36
3.1	Substrate Materials	36
3.2	Composition of Powders Used for Coating	37
3.3	HVOF Process Parameters	37
3.4	Hot Corrosion Studies in Molten Salt Environment ($\text{Na}_2\text{SO}_4+50\% \text{V}_2\text{O}_5$)	39
3.5	Oxidation Studies in Static Air	40
3.6	Solid Particle Erosion Studies	40
3.7	Characterization of Coatings, Analysis of Corrosion and Erosion Products	42
3.7.1	Preparation of samples for cross sectional analysis	42
3.7.2	Measurement of thickness of as-sprayed coatings	43
3.7.3	Optical microscopy, porosity and density	43

	3.7.4	Microhardness measurements	43
	3.7.5	Surface roughness measurements	43
	3.7.6	X-Ray diffraction (XRD) analysis	43
	3.7.7	Scanning electron microscopy (SEM) and energy dispersive x-ray (EDX) analysis	43
CHAPTER 4		CHARACTERIZATION OF SUBSTRATES AND COATINGS	45
	4.1	Microstructure of Substrate Materials	45
	4.2	Morphology of Coating Powders	45
	4.3	Visual Examination and Roughness of Coatings	46
	4.4	Measurement of Coating Thickness, Porosity and Density	46
	4.5	Evaluation of Microhardness	47
	4.6	XRD Analysis	56
	4.7	SEM Analysis of As-Sprayed Coating	56
	4.8	Evaluation of Fracture Toughness	59
CHAPTER 5		HOT CORROSION STUDIES	65
	5.1	Uncoated Samples	65
	5.1.1	Visual observations	65
	5.1.2	Thermogravimetric studies	65
	5.1.3	X-ray diffraction analysis	66
	5.1.4	SEM/EDX analysis	67
	5.2	10% Al ₂ O ₃ +CoCrAlTaY Coating	67

5.2.1	Visual observations	67
5.2.2	Thermogravimetric studies	71
5.2.3	X-ray diffraction analysis	71
5.2.4	SEM/EDX analysis	71
5.3	25% (Cr ₃ C ₂ -25(Ni20Cr)) + 75%NiCrAlY Coating	74
5.3.1	Visual observations	74
5.3.2	Thermogravimetric studies	74
5.3.3	X-ray diffraction analysis	78
5.3.4	SEM/EDX analysis	78
5.4	Stellite-6 Coating	82
5.4.1	Visual observations	82
5.4.2	Thermogravimetric Studies	82
5.4.3	X-ray diffraction analysis	82
5.4.4	SEM/EDX analysis	82
5.5	Summary of Hot Corrosion Results	89
5.6	Discussion	91
5.6.1	Uncoated samples	91
5.6.2	10% Al ₂ O ₃ +CoCrAlTaY coating	92
5.6.3	25% (Cr ₃ C ₂ -25(Ni20Cr)) + 75%NiCrAlY coating	95
5.6.4	Stellite-6 coating	97
5.7	Comparative Discussion	99
CHAPTER 6	OXIDATION STUDIES	102
6.1	Uncoated Samples	102

6.1.1	Visual observations	102
6.1.2	Thermogravimetric studies	102
6.1.3	X-ray diffraction analysis	104
6.1.4	SEM/EDX analysis	104
6.2	10% Al ₂ O ₃ +CoCrAlTaY Coating	107
6.2.1	Visual observations	107
6.2.2	Thermogravimetric studies	107
6.2.3	X-ray diffraction analysis	107
6.2.4	SEM/EDX analysis	107
6.3	25% (Cr ₃ C ₂ -25(Ni20Cr)) + 75%NiCrAlY Coating	113
6.3.1	Visual observations	113
6.3.2	Thermogravimetric studies	113
6.3.3	X-ray diffraction analysis	113
6.3.4	SEM/EDX analysis	113
6.4	Stellite-6 Coating	119
6.4.1	Visual observations	119
6.4.2	Thermogravimetric studies	119
6.4.3	X-ray diffraction analysis	119
6.4.4	SEM/EDX analysis	119
6.5	Summary of Oxidation Results	125
6.6	Discussion	126
6.6.1	Uncoated samples	126
6.6.2	10% Al ₂ O ₃ +CoCrAlTaY coating	128

	6.6.3	25% (Cr ₃ C ₂ -25(Ni ₂₀ Cr)) + 75%NiCrAlY coating	129
	6.6.4	Stellite-6 coating	131
	6.7	Comparative Discussion	132
CHAPTER	7	SOLID PARTICLE EROSION STUDIES	135
	7.1	Solid Particle Erosion Studies on Uncoated Alloys	135
	7.1.1	Ti-31 alloy	135
	7.1.2	Superco-605 superalloy	140
	7.1.3	MDN-121 special steel	144
	7.1.4	Discussion	147
	7.2	Solid Particle Erosion Studies on Coated Samples	148
	7.2.1	10 % (Al ₂ O ₃) + CoCrAlTaY coating	148
	7.2.2	25% (Cr ₃ C ₂ -25(Ni ₂₀ Cr))+ NiCrAlY coating	152
	7.2.3	Stellite-6 coating	156
	7.2.4	Discussion	160
	7.3	Comparative Discussion	164
CHAPTER	8	COMPARISON OF CUMULATIVE DAMAGE DUE TO HOT CORROSION, OXIDATION AND SOLID PARTICLE EROSION.	167
CHAPTER	9	CONCLUSIONS	170
		REFERENCES	174
		SCOPE FOR FUTURE WORK	187
		LIST OF PUBLICATIONS	188
		BIO-DATA	190

LIST OF FIGURES

<u>Fig.No</u>	<u>Figure Caption</u>	<u>Page No.</u>
1.1	Electricity generations (Billion Kilowatt-hours) by fuel wise during 1970-2025.	1
2.1	Schematic diagram of hot corrosion mechanism.	13
2.2	Phase diagram for Na ₂ SO ₄ -V ₂ O ₅ system.	14
2.3	Erosive mass loss as a function of impact angle.	19
2.4	Characteristic mechanisms of ductile erosion based on the variation in erosion conditions.	20
2.5	Schematic cross-sectional view of impact by a blunt indenter on to a brittle material, resulting in the formation of a conical Hertzian crack.	20
2.6	Schematic representation of high velocity oxy fuel spray process.	26
2.7	Characteristics of HVOF and standard plasma process coatings.	28
2.8	Schematic of a typical structure of sprayed coating.	31
2.9	Coating formation.	31
2.10	Bonding interactions within a spray coating.	31
2.11	Corrosion and oxidation resistance of different types of coatings.	32
3.1	Photograph of HVOF gun. Model: METCO DJ2600.	38
3.2	Schematic view of an air jet erosion test rig.	41
3.3	SEM micrograph with EDX of erodent.	42
3.4	Schematic diagram of the erosion scar produced on the eroded surface at an impact angle of 30°, 60° and 90°.	42
4.1	Optical micrograph of substrate materials.	48
4.2	Scanning electron micrograph of different coating powders.	49
4.3	Optical macrograph of substrate materials, sample size is 25 mm X 25 mm.	50
4.4	Optical macrograph of 10% Al ₂ O ₃ +CoCrAlTaY coated materials.	51

4.5	Optical macrograph of 25% (Cr_3C_2 -25(Ni20Cr) + 75%NiCrAlY) coated materials.	52
4.6	Optical macrograph of Stellite-6 coated materials.	53
4.7	Microhardness profiles of HVOF sprayed coatings for different substrate materials.	54
4.8	SEM micrographs of cross section of coatings.	55
4.9	X-ray diffraction patterns for substrate materials.	57
4.10	X-ray diffraction patterns for powder and as-sprayed coatings.	58
4.11	SEM/EDX analysis on surface of as-sprayed coating showing coating morphology and elemental composition (wt. %) at selected points in the coating.	60
4.12	Back scattered electron image and EDX analysis (wt. %) across the cross- section of the as-sprayed coatings.	61
4.13	Comparison of geometries of Palmqvist and median cracks around Vickers indentation.	62
4.14	Back scattered electron image of indentation on the as-sprayed coatings	63
5.1	Macrograph of uncoated samples (25mm X 25mm X5 mm) after 50 cycles of hot corrosion under Na_2SO_4 -50 wt.% V_2O_5 salt environment at 800 °C.	66
5.2	Graph of weight gain/area versus number of cycles for uncoated samples subjected to hot corrosion.	68
5.3	X-ray diffraction patterns for uncoated substrate materials subjected to hot corrosion in Na_2SO_4 -50% V_2O_5 for 50 cycles at 800 °C.	68
5.4	SEM/EDX analysis for uncoated substrate materials subjected to hot corrosion for 50 cycles in Na_2SO_4 +50% V_2O_5 at 800 °C.	69
5.5	Macrographs of 10% Al_2O_3 +CoNiCrAlY coating subjected to hot corrosion in Na_2SO_4 -50% V_2O_5 environment at 800 °C for 50 cycles.	70
5.6	Plot of weight change versus number of cycles for 10% Al_2O_3 + CoCrAlTaY coated materials subjected to hot corrosion in Na_2SO_4 -50% V_2O_5 salt environment at 800 °C.	72

5.7	X-ray diffraction patterns for 10% Al ₂ O ₃ +CoCrAlTaY coated Ti -31, Superco-605 and MDN-121 subjected to hot corrosion in Na ₂ SO ₄ -50% V ₂ O ₅ at 800 °C.	72
5.8	SEM/EDX point analysis for 10% Al ₂ O ₃ +CoCrAlTaY coated materials subjected to hot corrosion in Na ₂ SO ₄ +50% V ₂ O ₅ at 800 °C.	73
5.9	Back scattered image and EDX point analysis (wt%) across the cross-section of the 10% Al ₂ O ₃ +CoCrAlTaY coated MDN-121 material subjected to hot corrosion for 50 cycles in Na ₂ SO ₄ +50% V ₂ O ₅ at 800 °C.	74
5.10	X-ray mapping along the cross-section of the 10% Al ₂ O ₃ +CoCrAlTaY coated MDN 121 material subjected to hot corrosion for 50 cycles in Na ₂ SO ₄ +50% V ₂ O ₅ environment at 800 °C.	75
5.11	Macrographs of 25% (Cr ₃ C ₂ -25(Ni20Cr) +75%NiCrAlY) coating subjected to hot corrosion in Na ₂ SO ₄ -50% V ₂ O ₅ environment at 800 °C for 50 cycles.	76
5.12	Plot of weight gain/area versus number of cycles for 25% (Cr ₃ C ₂ -25(Ni20Cr) + 75%NiCrAlY) coated samples subjected to hot corrosion	77
5.13	X-ray diffraction patterns for 25% (Cr ₃ C ₂ -25(Ni20Cr) + 75% NiCrAlY) coated Ti-31, Superco-605 and MDN-121 subjected to hot corrosion in Na ₂ SO ₄ -50% V ₂ O ₅ for 50 cycles at 800 °C.	77
5.14	SEM/EDX analysis for 25% (Cr ₃ C ₂ -25(Ni20Cr) + 75% NiCrAlY) coated materials subjected to hot corrosion for 50 cycles in Na ₂ SO ₄ +V ₂ O ₅ at 800 °C.	79
5.15	Back scattered image and EDX analysis (wt%) across the cross-section of the 25% (Cr ₃ C ₂ -25(Ni20Cr) + 75%NiCrAlY) coated MDN-121 material subjected to hot corrosion for 50 cycles in Na ₂ SO ₄ +50% V ₂ O ₅ at 800 °C.	80
5.16	X-ray mapping along the cross-section of the 25% (Cr ₃ C ₂ -25(Ni20Cr) +75% NiCrAlY) coated MDN-121 material subjected to hot corrosion for 50 cycles in Na ₂ SO ₄ +50% V ₂ O ₅ environment at 800 °C.	81
5.17	Macrographs of Stellite-6 coating subjected to hot corrosion in Na ₂ SO ₄ -50% V ₂ O ₅ environment at 800 °C for 50 cycles.	83

5.18	Plot of weight gain/area versus number of cycles for Stellite-6 coated samples subjected to hot corrosion.	84
5.19	X-ray diffraction patterns for Stellite-6 coated Ti-31, Superco-605 and MDN-121 subjected to hot corrosion in Na ₂ SO ₄ -50% V ₂ O ₅ for 50 cycles at 800 °C.	84
5.20	SEM/EDX analysis of Stellite-6 coated materials subjected to hot corrosion for 50 cycles in Na ₂ SO ₄ +50% V ₂ O ₅ at 800 °C.	86
5.21	Back scattered image and EDX analysis (wt%) across the cross-section of the Stellite-6 coated Ti-31 material subjected to hot corrosion for 50 cycles in Na ₂ SO ₄ +50% V ₂ O ₅ at 800 °C.	87
5.22	X-ray mapping along the cross-section of the Stellite-6 coated Ti-31 material subjected to hot corrosion for 50 cycles in Na ₂ SO ₄ +50% V ₂ O ₅ environment at 800 °C.	88
5.23	Graph of (weight gain/area) ² versus number of cycles for uncoated samples subjected to hot corrosion.	93
5.24	Plot of (weight change/area) ² versus number of cycles for 10% Al ₂ O ₃ + CoCrAlTaY coated materials subjected to hot corrosion in Na ₂ SO ₄ -50% V ₂ O ₅ salt environment at 800 °C.	94
5.25	Plot of (weight gain/area) ² versus number of cycles for 25% (Cr ₃ C ₂ -25(Ni20Cr)) + 75% NiCrAlY coated samples subjected to hot corrosion for 50 cycles.	97
5.26	Plot of (weight gain/area) ² versus number of cycles for Stellite-6 coated samples subjected to hot corrosion.	99
5.27	Bar chart showing cumulative weight gain (mg/cm ²) for uncoated and HVOF coated samples subjected to hot corrosion in Na ₂ SO ₄ -V ₂ O ₅ salt environment for 50 cycles at 800 °C.	101
6.1	Macrographs of substrate materials subjected to cyclic oxidation in air at 800 °C for 50 cycles.	103

6.2	Plot of weight gain/area versus number of cycles for uncoated samples subjected to oxidation in air at 800 °C.	104
6.3	X-ray diffraction patterns for uncoated materials subjected to cyclic oxidation for 50 cycles in air at 800 °C.	105
6.4	Surface scale morphology and EDX analysis for the uncoated substrate materials subjected to cyclic oxidation in air at 800 °C for 50 cycles.	106
6.5	Macrographs of the 10% Al ₂ O ₃ -CoCrAlTaY coating subjected to cyclic oxidation in air for 50 cycles at 800 °C.	108
6.6	Plot of weight gain/area versus number of cycles for 10% Al ₂ O ₃ -CoCrAlTaY coated materials subjected to oxidation in air at 800 °C.	109
6.7	X-ray diffraction patterns for 10% Al ₂ O ₃ -CoCrAlTaY coated Ti-31, Superco-605 and MDN-121 subjected to cyclic oxidation for 50 cycles in air at 800 °C.	109
6.8	Morphology and EDX analysis for the 10% Al ₂ O ₃ -CoCrAlTaY coated materials subjected to cyclic oxidation in air at 800 °C for 50 cycles.	110
6.9	Back scattered image and EDX analysis (wt%) across the cross-section of the 10% Al ₂ O ₃ +CoCrAlTaY coated MDN-121 material subjected to oxidation for 50 cycles at 800 °C.	111
6.10	X-ray mapping along the cross-section of the 10% Al ₂ O ₃ +CoCrAlTaY coated MDN-121 material subjected to oxidation for 50 cycles at 800 °C.	112
6.11	Macrographs of 25% (Cr ₃ C ₂ -25(Ni ₂₀ Cr) + 75%NiCrAlY) coating subjected to oxidation at 800 °C for 50 cycles.	114
6.12	Plot of weight gain/area versus number of cycles for 25% (Cr ₃ C ₂ -25(Ni ₂₀ Cr) + 75%NiCrAlY) coated samples subjected to oxidation at 800 °C.	115
6.13	X-ray diffraction patterns for 25% (Cr ₃ C ₂ -25(Ni ₂₀ Cr)+ 75% NiCrAlY) coated Ti-31, Superco-605 and MDN-121subjected to cyclic oxidation	115

6.14	Morphology of scales and EDX analysis for 25% (Cr ₃ C ₂ -25(Ni ₂₀ Cr)+75%NiCrAlY) coated materials subjected to oxidation for 50 cycles at 800°C.	116
6.15	Back scattered image and EDX analysis (wt%) across the cross-section of the 25% (Cr ₃ C ₂ -25(Ni ₂₀ Cr)+75%NiCrAlY) coated Ti-31 material subjected to oxidation for 50 cycles at 800 °C.	117
6.16	X-ray mapping along the cross-section of the 25% (Cr ₃ C ₂ -25(Ni ₂₀ Cr)+75%NiCrAlY) coated Ti-31 material subjected to oxidation for 50 cycles at 800 °C.	118
6.17	Macrographs of Stellite-6 coating subjected to oxidation at 800 °C for 50 cycles.	120
6.18	Plot of (weight gain/area) versus number of cycles for Stellite-6 coated samples subjected to oxidation at 800 °C.	121
6.19	X-ray diffraction patterns for Stellite-6 coated Ti-31, Superco-605 and MDN-121 subjected to cyclic oxidation for 50 cycles in air at 800 °C.	121
6.20	Morphology and EDX analysis for Stellite-6 coated samples after oxidation for 50 cycles at 800 °C.	122
6.21	Back scattered image and EDX analysis (wt.%) across the cross-section of the Stellite-6 coated Ti-31 material subjected to oxidation for 50 cycles at 800 °C.	123
6.22	X-ray mapping along the cross-section of the Stellite-6 coated Ti-31 material subjected to oxidation for 50 cycles at 800 °C.	124
6.23	Plot of (weight gain/area) ² versus number of cycles for uncoated samples subjected to oxidation in air at 800 °C.	128
6.24	Plot of (weight gain/area) ² versus number of cycles for 10% Al ₂ O ₃ -CoCrAlTaY coated materials subjected to oxidation in air at 800 °C.	129
6.25	Plot of (weight gain/area) ² versus number of cycles for 25% (Cr ₃ C ₂ -25(Ni ₂₀ Cr)+75%NiCrAlY) coated samples subjected to oxidation.	131

6.26	Plot of $(\text{weight gain/area})^2$ versus number of cycles for Stellite-6 coated samples subjected to oxidation at 800 °C.	132
6.27	Bar chart showing cumulative weight gain (mg/cm^2) for uncoated and HVOF coated samples subjected to oxidation in air environment for 50 cycles at 800 °C.	134
7.1	Macrographs of uncoated Ti-31 alloy impacted by silica erodent at different angles (a) Impact angle of 30° (b) Impact angle of 60° (c) Impact angle of 90°.	136
7.2	Plot of erosion rate versus cumulative mass of erodent of uncoated Ti-31 alloy subjected to erosion at 30°, 60° and 90° impact angle (a) Variation in erosion rate (b) Histogram illustrating the steady state volume erosion rate.	137
7.3	SEM micrographs showing the morphology of eroded surface on uncoated Ti-31, with an impact angle of 30°.	137
7.4	SEM micrographs showing the morphology of eroded surface on uncoated Ti-31, with an impact angle of 60°.	138
7.5	SEM micrographs showing the morphology of the eroded surface on Ti-31 at impact angle 90°.	139
7.6	Macrographs of uncoated Superco-605 superalloy impacted by silica erodent at different angles (a) Impact angle of 30° (b) Impact angle of 60° c) Impact angle of 90°.	140
7.7	Plot of erosion rate of uncoated Superco-605 superalloy impacted at 30°, 60° and 90° impact angle (a) Variation of the erosion rate (b) Histogram illustrating the steady state volume erosion rate.	141
7.8	SEM micrographs showing the morphology of eroded surface on uncoated Superco-605, with an impact angle of 30°.	141
7.9	SEM micrographs showing the morphology of eroded surface on uncoated Superco-605, with an impact angle of 60°.	142
7.10	SEM micrographs showing the morphology of eroded surface on uncoated Superco-605, with an impact angle of 90°.	143

7.11	Macrographs of uncoated MDN-121 impacted by silica erodent at different angles (a) Impact angle of 30° (b) Impact angle of 60° c) Impact angle of 90°.	144
7.12	Plot of erosion rate versus cumulative mass of erodent of uncoated MDN-121 steel subjected to erosion at 30°, 60° and 90° impact angle (a) Variation in erosion rate (b) Histogram illustrating the steady state volume erosion rate.	145
7.13	SEM micrographs showing the morphology of eroded surface on uncoated MDN-121, with an impact angle of 30°.	145
7.14	SEM micrographs showing the morphology of eroded surface on uncoated MDN-121, with an impact angle of 60°.	146
7.15	SEM micrographs showing the morphology of eroded surface on uncoated MDN-121, with an impact angle of 90°.	146
7.16	Macrographs of 10% Al ₂ O ₃ -CoCrAlTaY coated alloy impacted by silica erodent at different angles (a) Impact angle of 30° (b) Impact angle of 60° (c) Impact angle of 90°.	149
7.17	Plot of erosion rate versus cumulative mass of erodent of 10% Al ₂ O ₃ -CoCrAlTaY coated Ti-31 subjected to erosion at 30°, 60° and 90° impact angle (a) Variation in erosion rate (b) Histogram illustrating the steady state volume erosion rate.	150
7.18	SEM micrographs showing the morphology of eroded surface on 10% Al ₂ O ₃ -CoCrAlTaY coated Ti-31, with an impact angle of 30°.	150
7.19	SEM micrographs showing the morphology of eroded surface on 10% Al ₂ O ₃ -CoCrAlTaY coated Ti-31, with an impact angle of 60°.	151
7.20	SEM micrographs showing the morphology of eroded surface on 10% Al ₂ O ₃ -CoCrAlTaY coated Ti-31, with an impact angle of 90°.	152
7.21	Macrographs of 25% (Cr ₃ C ₂ -25(Ni20Cr)) + 75% NiCrAlY coated alloys impacted by silica erodent at different angles (a) Impact angle of 30° (b) Impact angle of 60° (c) Impact angle of 90°.	153
7.22	Plot of erosion rate versus cumulative mass of erodent of 25% (Cr ₃ C ₂ -25(Ni20Cr)) + 75% NiCrAlY coated Ti-31 subjected to erosion at 30°,	154

	60° and 90° impact angle (a) Variation in erosion rate (b) Histogram illustrating the steady state volume erosion rate.	
7.23	SEM micrographs showing the eroded surface morphology of 25% (Cr ₃ C ₂ -25(Ni ₂₀ Cr) + 75%NiCrAlY) at impact angle 30°.	154
7.24	SEM micrographs showing the eroded surface morphology of 25% (Cr ₃ C ₂ -25(Ni ₂₀ Cr) + 75%NiCrAlY) at impact angle 60°.	155
7.25	SEM micrographs showing the eroded surface morphology of 25% (Cr ₃ C ₂ -25(Ni ₂₀ Cr) + 75%NiCrAlY) at impact angle 90°.	156
7.26	Macrographs of Stellite-6 coated alloy impacted by silica (a) Impact angle of 30° (b) Impact angle of 60° (c) Impact angle of 90°.	157
7.27	Stellite-6 coated alloys at 30°, 60° and 90° impact angle (a) Variation in erosion rate (b) Histogram illustrating the steady state volume erosion rate.	158
7.28	SEM micrographs showing the morphology of eroded surface of Stellite-6 impacted with silica at 30°.	158
7.29	SEM micrographs showing the morphology of eroded surface of Stellite-6 impacted with silica at 60°.	159
7.30	SEM micrographs showing the morphology of eroded surface of Stellite-6 impacted with silica at 90°.	159
7.31	Bar chart indicating volumetric steady state erosion rate for uncoated and HVOF coated alloys at 30°, 60° and 90° impact angle.	166
8.1	Plot of comparison of cumulative damage due to hot corrosion, oxidation and solid particle erosion.	169

LIST OF TABLES

Table .No	Table Caption	Page No.
2.1	Alloy developed for gas turbine applications.	8
2.2	Comparison of the characteristics for various thermal spraying	26
3.1	Substrate material composition	36
3.2	Compositions of the powders used for coating	37
3.3	HVOF process parameters	38
3.4	Erosion test conditions	41
4.1	Etchant used for various substrate materials	45
4.2	Microhardness value for substrate materials	47
4.3	Microhardness value for coatings	47
4.4	Thickness, surface roughness and density of sprayed coatings	47
4.5	Vickers micro hardness, Young's modulus and fracture toughness of sprayed coatings,	64
5.1	Summary of the results for uncoated and coated alloys subjected to hot corrosion	89
6.1	Summary of results for uncoated and coated alloys subjected to oxidation in air	125
8.1	Cumulative damage values for HVOF sprayed coatings on Ti-31.	169

NOMENCLATURE

Symbols	
C: Carbon	B: Boron
Y: Yttrium	W: Tungsten
V: Vanadium	Cu: Copper
S: Sulphur	CO: Carbon Monoxide
O: Oxygen	N ₂ : Nitrogen
Cr: Chromium	μm: Micrometer
Co: Cobalt	Mo: Molybdenum
Ni: Nickel	NiO: Nickel Oxide
Al: Aluminium	H ₂ S: Hydrogen Sulphide
Ti: Titanium	MPa: Mega Pascals
Fe: Iron	H ₂ O: water
Si: Silicon	CO ₂ : Carbon dioxide
Mn: Manganese	NaCl: Salt (Sodium Chloride)
Zr: Zirconium	KCl: Potassium Chloride
Ta: Tantalum	Al ₂ O ₃ : Aluminium Oxide
XRD: X-ray Diffraction	V ₂ O ₅ : Vanadium Pentaoxide
SEM: Scanning Electron Microscope	K ₂ SO ₄ : Potassium Sulphate
EDX: Energy Dispersive X-ray Analysis	Na ₂ SO ₄ : Sodium Sulphate
HVOF: High Velocity Oxy Fuels	

CHAPTER 1

INTRODUCTION

Increasing global demand for energy is an immense challenge for power producers around the world. The global consumption of energy is expected to double by 2020 (Fig. 1.1). The main driver for the increased energy consumption is growing population and increasing urbanization taking place in the developing countries. Increasing energy requirements coupled with national and international regulations to reduce emissions have driven activities towards an increase in plant efficiency, modernization of plants using newer and better materials, use of different type of fuels, etc. (Oskarsson 2007).

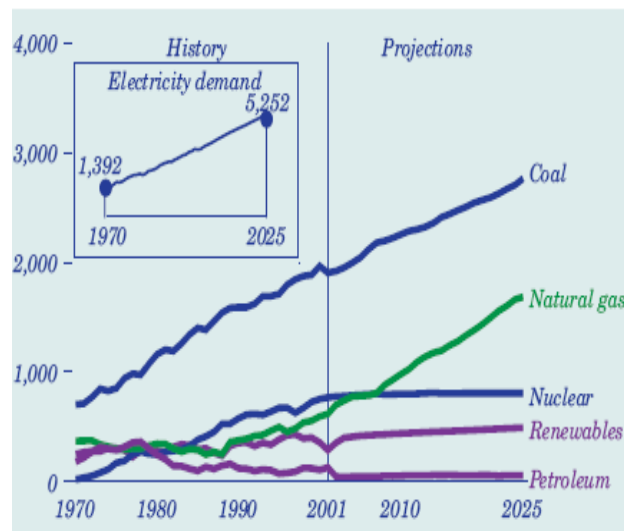


Fig. 1.1 Electricity generations (Billion Kilowatt-hours) by fuel wise during 1970-2025 (Annual energy outlook 2003).

Today, gas turbines are used extensively to produce power for satisfying the demands of electricity, chemical, pharmaceuticals, fertilizer sectors, etc. An important developing area in the gas turbines is the use of modern materials to improve efficiencies and to reduce emissions (Wright and Gibbons 2007). There are additional demands from the customer on to the power sector. Some of them are requirements to

operate the power on part load, run with frequent starts and flexibility to run on different fuels.

Though various alternatives exist for the fuel material, coal is still a predominant fuel material for the power suppliers. This means that turbine components will be exposed to an environment consisting of abrasion, erosion, corrosion and oxidation phenomenon under hostile chemical conditions (Sidhu et al. 2005, Sidhu et al. 2007, Oskarsson 2007, Wright and Gibbons 2007 and Kosel 1992). Surface engineering of these components helps in protecting the components against above said environments. Thermal spray coatings are especially interesting for their cost/performance ratio. Unique alloys and microstructures can be obtained by thermal spraying which are not possible with a wrought material. This includes continuously graded composites and corrosion resistant amorphous phases on the component surface. Thermal spray coatings, additionally offer the possibility of on-site applications and repair of components, if sufficient accessibility for the sprayer and his equipment is available. Thermal spray coatings are being increasingly and successfully used for a broad variety of high temperature corrosion applications (Heath et al. 1997). High-Velocity Oxy-Fuel (HVOF) spraying is a new type of thermal spray coating and rapidly developing technology in combating high-temperature corrosion and is now challenging the vacuum plasma spraying technique (VPS), which is very expensive. HVOF coatings have very low porosity, high hardness, high abrasion resistance, and good wear resistance with a strong ability to resist high-temperature corrosion, oxidation and erosion (Sidhu et al. 2006).

1.1 OBJECTIVES OF THE PRESENT INVESTIGATION

The specific objectives of the present investigation are as follows

1. Achieving successfully a spray coating of cermets/hard metals on special alloys which are explicitly used for gas turbine application to improve the corrosion, oxidation and erosion degradation resistance at elevated temperature. Three kinds of coatings selected are as given below
 - i. 10% Al_2O_3 + CoCrAlTaY
 - ii. 25% $(\text{Cr}_3\text{C}_2\text{-}25(\text{Ni}20\text{Cr}))\text{+}75\%$ NiCrAlY

iii. Stellite-6

2. Deposition of above said coating materials using High-Velocity Oxy-Fuel (HVOF) process on Titanium alloy (Ti-31), Cobalt based super alloy (Superco-605) and special steel (MDN-121) which are materials used in elevated temperature turbine components.
3. To carry out physical, mechanical and structural characterization of as-received substrate alloys and HVOF coated products to assess its suitability for use in gas turbine application.
4. To evaluate the thermocyclic oxidation resistance of the coated and uncoated alloys in static air at 800 °C.
5. To evaluate the hot corrosion resistance of the coated and uncoated alloys in molten salt environment of $\text{Na}_2\text{SO}_4 + 50\% \text{V}_2\text{O}_5$ at 800 °C.
6. To assess the erosion behaviour of coated and uncoated alloys under various impact angles (30°, 60° and 90°) of testing.
7. Identification and structural investigation of the reaction products of the corroded samples and morphology of the surfaces subjected to erosion.
8. To explain mechanisms of degradation of the coated and uncoated alloys subjected to oxidation, hot corrosion and erosion in laboratory simulated conditions, which would help in engineering the surface of high temperature materials.

1.2 ORGANIZATION OF THE THESIS

Chapter 1 deals with the importance of materials and coating related to industrial turbines and objectives of the investigation.

Chapter 2 contains a comprehensive review of the literature with a special reference to oxidation, hot corrosion and erosion studies. Also HVOF process has been described in detail.

Chapter 3 contains description of the experimental tools used and the procedures employed for deposition of the coatings, oxidation, hot corrosion and erosion studies and analyses of the corrosion products.

Chapter 4 describes substrate materials used in the present study and the characterization of various coatings applied on them.

Chapter 5 describes the results and discussion of hot corrosion behavior of the HVOF coated as well as the uncoated materials in an environment of molten salt (Na_2SO_4 -50% V_2O_5) at 800 °C under cyclic conditions.

Chapter 6 describes the results and discussion of the cyclic oxidation behavior of HVOF coated and uncoated materials.

Chapter 7 describes the results and discussion of the HVOF coated and uncoated Ti-31 subjected to solid particle erosion at room temperature, as per ASTM-G76 standard.

Chapter 8 gives a summary of coating performance under hot corrosion, oxidation and erosion conditions.

Chapter 9 summarizes the salient conclusions resulting from the present investigation.

It is followed by a list of references and scope for further work.

CHAPTER 2

LITERATURE REVIEW

This chapter contains a comprehensive review of the literature with a special reference to hot corrosion, oxidation and erosion studies. HVOF spray process has been described in detail. The problem has been formulated after critical analysis of the literature towards the end of this chapter.

2.1 ALLOY DEVELOPMENTS FOR GAS TURBINE APPLICATIONS

The inlet temperature of modern industrial gas turbines exceeds 900 °C. The life requirements for the highly loaded, high-temperature components are 25,000-50,000 h. Also, efficiency requirements limit the amount of compressor air available for cooling of turbine parts. The blades are exposed to high temperatures, together with stresses due to centrifugal load and gas load, resulting in creep damage. Start and stop cycles cause thermal fatigue. Due to high temperature and environmental conditions, oxidation occurs. Burnt gases from coal contain the impurities of sodium, sulfur and vanadium. These gaseous species condense and form the deposits of molten alkali sulfates and accelerate hot corrosion on turbine blades (Wright and Gibbons 2007). The materials have to operate under severe conditions such as erosion, corrosion and oxidation at higher temperatures in hostile chemical environments. The highly alloyed materials are able to meet such a demanding spectrum of requirements. Table 2.1 shows some of the alloys developed for gas turbine applications.

A **superalloy**, or **high-performance alloy**, is an alloy that exhibits excellent mechanical strength, creep resistance, good surface stability, corrosion and oxidation resistance at elevated temperatures. A superalloy's base element is usually nickel, cobalt or iron. Superalloy development has relied heavily on both chemical and process innovations and has been driven primarily by the aerospace and power industries.

In **Nickel base superalloys**, high temperature strength is achieved by solid solution strengthening by the addition of selected metals (Si, Mn, Zr, Co, Mo, W and Fe), carbide strengthening by the addition of carbide former (Ta, Ti, Cb) elements and intermetallic strengthening. For oxidation resistance, 20 to 25% Cr is required for developing self healing Cr₂O₃ layer (Nicholls and Rickerbery 2002).

In **Cobalt base superalloys**, high temperature strength is attained by addition of solid solution strengtheners like Mo, W, Cb, Ta & C. Strengthening is by carbide formation and/or precipitation hardening. The carbides are effective up to 900 °C and above 900 °C they are unstable. The oxidation resistance of Co-30% Cr is improved by the addition of zirconium, cerium, aluminium, boron and tantalum (Nicholls and Rickerbery 2002).

Iron base superalloys are used at lower operating temperatures, since strength rapidly reduces above 650 °C. These alloys contain (0.75-0.8% Ni), 13.5 to 16 wt% Cr with addition of Mo, Si, Ti & Al (Nicholls and Rickerbery 2002).

Titanium alloys have been increasingly used in aerospace, biomedical, and chemical industries due to their very high strength to weight ratio, good fatigue, biocompatibility and high corrosion resistance. Although titanium based alloys exhibit good corrosion resistance due to the formation of titania on its surface, the nature, composition and thickness of the protective oxide scales depend on environmental conditions (Anuwar et al. 2007).

It may be noted that titanium alloys, cobalt based superalloys and steel based superalloys are candidate materials for turbine nozzles, combustors, turbine wheels and compressor blades. The above mentioned materials are prone to damage by high temperature oxidation, hot corrosion and erosion. To protect the materials coating is essential.

2.2 HOT CORROSION

Metals and alloys experience accelerated corrosion when their surfaces are covered with a thin film of fused salt (generally sulphates) in an oxidizing gas

atmosphere, at elevated temperatures. This is known as hot corrosion. Here a porous non-protective oxide scale is formed at the surface and metal sulphates in the substrate. If concentration of the sulphate exceeds the saturation vapour pressure at the operating temperature for turbine blades, vanes and other energy generation components (700-1100 °C), then Na_2SO_4 will deposit on the surface of these components. At higher temperatures, the deposits of Na_2SO_4 will get molten (Melting point: 884 °C) and can cause an accelerated attack of Ni- and Co- based superalloys. Furthermore, the accelerated corrosion can also be caused by other salts, such as vanadates or mixtures of sulphate-vanadate in the presence of solid or gaseous salts such as chlorides (Singh et al. 2007). Generally, two types of hot corrosion exists, namely, high temperature hot corrosion (HTHC) and low temperature hot corrosion (LTHC).

2.2.1 High temperature (Type I) hot corrosion (HTHC)

High temperature (Type I) hot corrosion (HTHC) is normally observed in the temperature range of about 800-950 °C, when the condensed salt forms a liquid film on the component surface. The typical microstructure of HTHC shows the formation of sulphates and a corresponding depletion of the reactive component in the alloy substrate. The external corrosion products frequently comprises of oxide precipitates dispersed in the salt film (Rapp and Zhang 1994). The dominant salt in HTHC is Na_2SO_4 , due to its high thermodynamic stability. The macroscopic appearance of HTHC is characterized by severe peeling of the corrosion products and by significant colour changes (greenish tone resulting from the formation of NiO) in the area of the accelerated attack (Nicholls and Rickerby 2002).

2.2.2 Low temperature (Type II) hot corrosion (LTHC)

Low temperature (type II) hot corrosion (LTHC) occurs well below the melting point of pure Na_2SO_4 . The reaction product morphology for this type of corrosion is characterized by a non-uniform attack in the form of pits, with only little sulphate formation close to the alloy/scale interface and little depletion of Cr or Al in the alloy substrate (Elaiz et al. 2002). This form of corrosion is observed mainly within the temperature range of 650-800 °C (Pettit and Meier 1984). The formation of

low melting point eutectics causes typical LTHC pitting, for instance, the formation of Na_2SO_4 - NiSO_4 eutectics in the case of nickel based superalloys.

Table 2.1 Alloy developed for gas turbine applications.

Name of the material	ASTM Grade	Composition	Applications
Nickel base alloys			
Superni-75	Nimonic-75	Ni-3Fe-19.5Cr-0.3Ti-0.1C	Gas turbines, boiler tubes
Superni-76	Hastelloy X	Ni-18.5Fe-21Cr-2.5Co-9Mo-1Mn-0.1C-0.5W	Gas turbine parts
Superni-80A	Nimonic-80A	Ni-1Fe-19Cr-2Co-1.5Al-2.5Ti-0.07C	Turbines discs, automobile valves, sealing rings
Superni-718	Inconel-718	Ni-18.5Fe-19Cr-0.15Cu-0.5Al-3.5Mo-0.18Mn-0.9Ti-0.18Si-0.04C-5.13(C _b +T _a)	Jet engines, pump bodies and parts
Cobalt base alloy			
Superco-605	KC 20WN/L605	Co-3Fe-10Ni-20Cr-1.5Mn-0.3Si-0.08C-15W	Gas turbines, furnace muffles in oxidizing atmosphere
Iron base alloys			
MDN-121	X22 CrMoV121	Fe-0.8Ni-12Cr-1Mo-0.6Mn-0.25Si-0.2C-0.3V	Turbine blades
MDN-123	ASTMA 565 Gr616	Fe-0.75Ni-11.5Cr-0.015Cu-0.2Al-1Mo-0.75Mn-0.025Ti-0.3Si-0.25C	Turbine components and fasteners.
Titanium alloys			
Titanium-31	ASTM B338 Grade 5	Ti-6Al-4V	Rocket motor, structural forgings and fasteners, pressure vessel, gas turbine blades, gas and chemical pumps, marine components

2.2.3 Hot corrosion mechanisms

The initiation of HTHC is often attributed to failure of the protective oxide layer, which allows the molten salt to attack directly the substrate metal. This failure

may result from erosion, thermal stresses, erosion-corrosion, chemical reactions, etc. The mechanisms proposed for the HTHC propagation stage are the sulfidation-oxidation mechanism and salt fluxing mechanisms (Stringer 1987). The salt fluxing mechanism was originally proposed by Geobel and Pettit (1970). According to this model, the protection efficiency of the surface oxide layer might be lost as a result of fluxing of this layer in the molten salt. The fluxing can be caused either by the combination of oxides with O^{2-} to form anions (basic fluxing), or by the decomposition of oxides onto the corresponding cations and O^{2-} (acidic fluxing). Acidic fluxing takes place when the O^{2-} activity in the molten salt is markedly lowered; it leads to a much more severe oxidation compared to basic fluxing. As opposed to basic fluxing, acidic fluxing can be self-sustaining, since the displacement of the salt from stoichiometry does not become progressively more difficult as the reaction precedes (Stringer 1987). In general the hot corrosion of superalloys with high contents of aluminium and chromium is often reported to occur according to the basic fluxing mechanism, whereas the hot corrosion of alloys with high contents of tungsten, molybdenum and vanadium has been reported to follow the acidic fluxing mechanism.

Rapp and Goto (1981) measured the oxide solubilities in molten Na_2SO_4 as a function of the acidity of the salt. On the basis of these measurements, they suggested that a negative gradient of the solubility of the protective oxide in the salt film at the oxide/salt interface should lead to oxide dissolution at this interface and to precipitate a non-protective oxide away from the interface, where the solubility is lower. Fluxing arises in this case only because of the local variation of sodium oxide activity and/or oxygen partial pressure across the salt film, without any necessity of sulphate-forming reaction. This mechanism can explain a self-sustaining process of dissolution of the protective oxide to maintain an accelerated corrosion attack (Stringer 1987).

The effect of vanadium on HTHC has been explained by different researchers. Bornstein et al. (1975) and Geobel et al. (1973) suggested that a self-sustained acidic dissolution of the protective Cr_2O_3 or Al_2O_3 scales could occur when the salt film contains vanadium, because, V_2O_5 is a strongly acidic oxide. Zhang and Rapp (1987)

suggested that every oxide should contribute to the more rapid attack of oxides by mixed sulfate-vanadate melts than by a pure sulfate melt.

2.2.4 Hot corrosion degradation sequence

All corrosion resistant alloys degrade in two stages, namely, initiation and propagation stage. The initiation of hot corrosion is often attributed to failure of the protective oxide layer and repair of oxide layer by itself. Once the repair of the oxide layer is no longer possible, the propagation phase results in rapid consumption of the alloy (Nicholls and Rickerby 2002). Simens et al. (1955) first suggested the two-stage materials degradation; triggering stage and autocatalytic destruction stage. According to Pettit and Meier (1984), it is a fact that all corrosion resistant alloys degrade via these two stages and, it is the result of using selective oxidation to develop oxidation or corrosion resistance. They further elaborated that the conditions causing hot corrosion, therefore do nothing more than shortening the time for which the alloys can form protective oxides via selective oxidation.

During the initiation stage of hot corrosion, alloys are being degraded at rates similar to those that would have prevailed in the absence of the deposits. Elements in the alloy are oxidised and electrons are transferred from metallic atoms to the reducible substances in the deposit. Consequently, the reaction product barrier that forms beneath the deposit on the alloy surface usually exhibits primarily those features resulting from the gas–alloy reaction (Pettit and Giggins 1987).

In some cases of hot corrosion, an increasing amount of sulphide particles becomes evident in the alloy beneath the protective reaction product barrier. In others, small holes become evident in the protective reaction product barrier where the molten deposit begins to penetrate it. Eventually, the protective barrier formed via selective oxidation is rendered ineffective, and the hot corrosion process enters into the propagation stage. Obviously, in attempting to develop resistance to hot corrosion, one should strive to retain the superalloys in the initiation stage as long as possible. Initiation stage is important to the life of the alloy. Numerous factors affect the time at which the hot corrosion process moves from the initiation stage into the propagation

stage, as shown in Fig. 2.1. These factors also play a dominant role in determining the type of reaction product that is formed in the propagation stage (Pettit and Meier 1984).

The propagation stage of the hot corrosion sequence is the stage at which the alloy must be removed from service since this stage always has much higher corrosion rate than that in the initiation stage. The non-protective corrosion products are formed during the propagation stage and often results in catastrophic corrosion failures.

2.2.5 Hot corrosion in the molten salt ($\text{Na}_2\text{SO}_4\text{-V}_2\text{O}_5$) environment

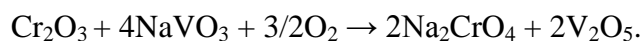
Molten sulphates-vanadates deposits, resulting from the condensation of combustion products of residual fuels are extremely corrosive to high-temperature materials (Natesan 1976). Luthra and Spacil (1982) carried out a thermo-chemical analysis of deposits in gas turbines for liquid fuels containing Na, S and V. They observed that the predominant species in the salt deposits formed on the gas turbine surfaces are Na_2SO_4 , V_2O_5 and $\text{Na}_2\text{V}_2\text{O}_6$. Barbooti et al. (1988) revealed that sodium vanadyl vanadate ($\text{Na}_2\text{O.V}_2\text{O}_4.5\text{V}_2\text{O}_5$), which melts at a relatively low temperature (550 °C), is found to be the most common salt deposit on boiler superheaters. Tiwari and Satya Prakash (1997) reported that the mixture of Na_2SO_4 and V_2O_5 in the ratio of 40:60 constitutes a eutectic with a low melting point of 550 °C and provides a very aggressive environment for hot corrosion to occur.

The kinetics of the reaction between Na_2SO_4 (X) and V_2O_5 (Y) is studied. Kolta et al. (1972) revealed that the rate of reaction depend, both on the temperature (600-1300 °C) and the molar ratio of X and Y. They further found that with increase in the reaction period (>30 min.), there was a decrease in the reaction rate which finally reached to zero order. This decrease in the reaction rate has been attributed to the formation of vanadosulphate complexes such as $(\text{NaV}_3\text{O}_8)_2$. Na_2SO_4 and $(\text{NaVO}_3)_2$. Na_2SO_4 which get decomposed at higher temperature, facilitates formation of the meta- and pyro-vanadates.

Kofstad (1988) proposed that during combustion, the vanadium contaminants are oxidized to the higher valence vanadium oxides (V_2O_4 and V_2O_5) which react with sodium salts to form low melting point sodium vanadates (lowest M.P. $535\text{ }^\circ\text{C}$) such as $(Na_2O)_xV_2O_4(V_2O_5)_{12-x}$, $(Na_2O)_5(V_2O_4)_x(V_2O_5)_{12-x}$, $NaVO_3$, $Na_4V_2O_7$ and Na_3VO_4 .

Metal oxides dissolved in the vanadates may suppress the melting points and eutectic temperatures even further (Kofstad 1988). It is also reported that the slags developed on valves of diesel engines consist predominantly of sodium sulphate and sodium vanadates and can have melting point as low as $400\text{ }^\circ\text{C}$. Singh (2003) reported that a strong ability of vanadium to reduce its oxidation state by consuming electrons released by oxidation of sulphate ion is mainly responsible for the enhancement of the corrosion of the metals and alloys in the sulphate melts. Presence of V_2O_5 seems to act as an electron sink in the sulphate melts that consume electrons released by oxidizing components of the system. Electrons, released during oxidation of sulphate ion, are consumed by vanadium which get reduced to its lower oxidation states. This process appears to enhance the hot corrosion of metals in sulphate melts.

Sidhu et al. (2006B) reported that iron-base superalloy, Superfer-800H underwent intense spalling, sputtering (disintegration of the scale accompanied by cracking sound during cooling) and peeling of the scale in an aggressive environment of Na_2SO_4 -60% V_2O_5 at $900\text{ }^\circ\text{C}$. During the cyclic study for 50 hours, the mass gained by the superalloy was enormous. It is found that the mass increased continuously, although the rate of increase was high during the initial period of exposure. This rapid increase in mass gain is attributed to the formation of $NaVO_3$ compound. The $NaVO_3$ acts as a catalyst and also serves as an oxygen carrier to the base alloy that leads to the rapid oxidation of the base elements of the superalloy to form the protective oxide scale. Slower increase in mass gain after initial mass gain was due to the simultaneous growth and dissolution of oxide scale in the molten salt due to the reaction



This Na_2CrO_4 gets evaporated as a gas.

Hot Corrosion Chronology

Initiation Stage

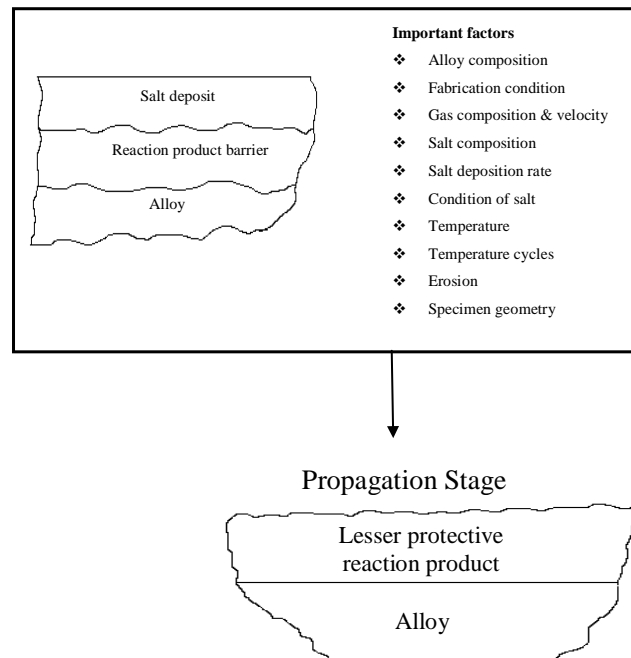


Fig. 2.1 Schematic diagram of hot corrosion mechanisms (Pettit and Meier 1984).

Otero et al. (1990) studied the hot corrosion behaviour of the same alloy (IN657) in a molten salt environment of 60% V_2O_5 -40% Na_2SO_4 . They observed that for duration less than 100 hours, the corrosion kinetics increased with temperature when the temperature was less than 727 °C. For temperatures greater than 727 °C, corrosion rate decreased. An increase in corrosion rate with temperature observed during the initial stages of exposure was related to the higher fluidity of the molten salt mixture. At temperatures greater than 727 °C, once the appropriate fluidity was achieved, the corrosion rate decreased due to the decrease in the oxygen solubility in the molten salt.

Lambert et al. (1991) studied the oxidation and hot corrosion behaviour of Ni-17Cr-6Al-0.5Y and Ni-16Cr-5.7Al-0.47Y-5Si alloys at 700 °C in Na_2SO_4 -60% V_2O_5

environment. They observed a layer of NiO on the surface of the Ni-17Cr-6Al-0.5Y alloy whereas a thin Al₂O₃ scale on the surface of Si-enriched alloy. They further opined that the condensed vanadates of sodium are highly corrosive and can markedly increase the rate of oxidation of nickel base superalloys.

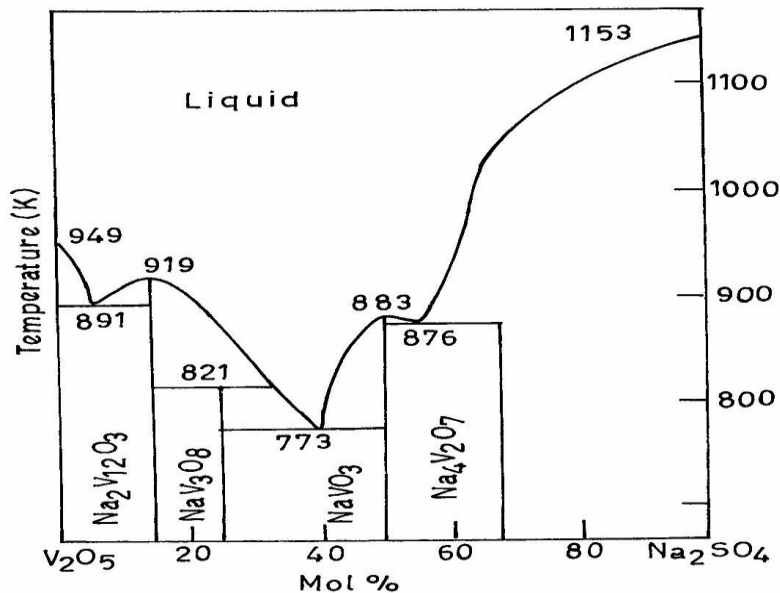


Fig. 2.2 Phase diagram for Na₂SO₄-V₂O₅ system (Otero et al. 1990).

Gurrappa (2003) investigated hot corrosion behaviour of air plasma spray coatings on CM 247 LC superalloy at 900 °C in the corrosive environments of 95% Na₂SO₄+5% NaCl and 90% Na₂SO₄+5%NaCl+5%V₂O₅ by using the crucible immersion technique. Different coatings used are NiCoCrAlY, NiCoCrAlY+1% Hf, NiCoCrAlY+1% Si, NiCrAlY, and CoCrAlY alloys. The coating of composition 22Co-18Cr-12Al-0.5Y is found to exhibit maximum life among the investigated coatings in both sodium chloride and vanadium containing environments. The improvement in the durability of the coating is attributed to the formation of a thick, protective, thermodynamically and chemically stable alumina scale on the surface of the coating after exposure to the given environment.

Uusitalo et al. (2004) investigated the high temperature behaviour of the NiCoCrAlY, NiCoCrAlY+1% Hf, NiCoCrAlY+1% Si, NiCrAlY, and CoCrAlY alloy coatings in the presence of a salt mixture of 40% Na₂SO₄-40% K₂SO₄-10NaCl-10KCl

in two environments, i.e., oxidising environment of N_2 -20 H_2O -14 CO_2 -3 O_2 -500 ppm HCl and reducing environment of N_2 -20 H_2O -5 CO -0.06 H_2S -500 ppm HCl. They found that the corrosion was more severe in oxidising environment as compared to the corrosion in reducing environment. Active oxidation was responsible for the accelerated corrosion in oxidising environments. The coatings were prone to chlorine attack in both atmospheres through the interconnected oxide network present at splat boundaries. The Ni-57CrMoSiB coating was the only material forming a protective oxide layer. Whereas, in reducing conditions, materials with high chromium content were found to form a protective layer containing chromium, sulphur, and sodium. The corrosion resistance of this layer increased with increasing chromium content. Further it is concluded that the corrosion resistance of nickel-based, high chromium coating materials was satisfactory in the test conditions.

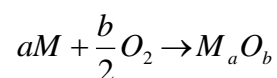
The Cr_3C_2 -NiCr coating provides good hot corrosion resistance to Superni-718 and has been found successful in reducing the weight gain by around 50% of that gained without a coating (Kamal et al. 2009). Coatings on Superni-75 and Superfer-800H superalloys reduce the weight gain by 30% and 20% of that gained by the uncoated superalloys, respectively. The superior corrosion resistance shown by the Cr_3C_2 -NiCr coated Superni-718 is attributed to the formation of Cr_2O_3 , NiO and $NiCr_2O_4$ spinel at the top of surface scale. Further, it has been observed that the scales formed on the coated Superni-718 superalloy were dense, compact and without any spallation, sputtering or peeling. This also contributes to the lower weight gain observed with the coated materials.

Mobarra et al. (2006) carried out studies on the low pressure plasma sprayed (LPPS) CoNiCrAlY coatings on Ni-based superalloy (IN 738LC) and studied hot corrosion behaviour at 850 °C temperature for 24 hours in Na_2SO_4 +10% NaCl salt environment. The microstructure of the coating following a 24 h cycle, in addition to the β -NiAl and γ -phases, displayed clearly identifiable interdiffusion zone at the interface of the coating and the substrate, and a β -NiAl depleted region in the boundary of coating and oxide layer. The specimens exposed to hot corrosion conditions exhibit a divergent change in the thickness of CoNiCrAlY coating and the oxide layer. It is well known that MCrAlY (M=Co or Ni) coatings protect the

substrate superalloy against oxidation and hot corrosion by forming a protective oxide layer.

2.3 HIGH TEMPERATURE OXIDATION

It has been established that most metals and alloys would react with oxygen to some extent in a gaseous atmosphere. Oxides are generally thermodynamically more stable than reaction products from other species (like N and S) which may be present in the environment. It is therefore common for oxides to form at the gas-metal interface (Pettit and Giggins 1987). Oxidation can be considered as a chemical reaction between a metal and oxygen gas to form the metal oxide. In general following equation can be written to represent oxidation.



Oxidation of metals may seem to be among the simplest chemical reactions. However, according to Kofstad (1988), the reaction path and oxidation behaviour of a metal may depend on a variety of factors, and reaction mechanisms and as a result may prove to be complex. The initial step in the metal-oxygen reaction involves the adsorption of gas on the metal surface. As the reaction proceeds, oxygen may dissolve in the metal, resulting in the formation of oxide on the surface either as a film or as separate oxide nuclei. Both the adsorption and the initial oxide formation are functions of surface orientation, crystal defects at the surface, surface preparation and impurities in both the metal and the gas. Thermodynamically, an oxide is likely to form on a metal surface when the oxygen potential in the environment is greater than the oxygen partial pressure in the equilibrium with the oxide.

When the oxidation process involves an alloy instead of a pure metal, many factors described for the oxidation of pure metals may be applied to the oxidation of the alloy. However, for alloys oxidation is generally much more complex as a result of some, or all, of the following (Kofstad 1988).

1. The elements of the alloy will have different affinities for oxygen reflected by the different free energies for formation of the oxides.
2. Ternary and higher oxides may be formed.
3. A degree of solid solubility between the oxides may exist.
4. Various metal ions will have different mobility in the oxide phases.
5. Various metals will have different diffusivities in the alloy.
6. Dissolution of oxygen into the alloy may result in sub-surface precipitation of oxides of one or more alloying elements (internal oxidation).

As the equilibrium partial pressure of oxygen for oxides is generally very small, initially all the elements on the surface of the alloy will form their respective oxides. However, as time goes on, the formation of the oxides on the surface of an alloy depends upon the individual activities of the elements and their relative affinities for oxygen (Li et al. 1996).

Further, the requirement of a protective oxide scale is to have a slow growth rate. Oxidation reactions of protective oxide generally follow a parabolic rate equation given by:

$$x^2 = K_p t$$

Where x is the scale thickness in dimensions of length, t is the time and K_p the parabolic growth rate constant in dimensions of length²/time. However, minor deviations from the parabolic behaviour are often observed (Doychak 1995).

2.4 EROSION

Erosive wear is caused in the solid bodies by the action of sliding or impact of solids, liquids, gases or a combination of these (Ramesh et al. 1991). Erosion can be divided into three basic types: Solid particle erosion, liquid impact erosion and cavitation erosion. Cavitation erosion is the loss of material due to the repeated formation and collapse of bubbles in a liquid. Liquid impact erosion is the damage by

liquid droplets. Solid particle erosion involves the impact of solid particles on a solid surface.

Solid particle erosion is an important material degradation mechanism encountered in a number of engineering systems such as thermal power plants, aircraft gas turbine engines, pneumatic bulk transport systems, coal liquefaction/gasification plants and ore or coal slurry pipelines. At the same time, the erosion process has been used as beneficial one in a number of situations like sand blasting of castings, shot peening of rotating components, cutting of hard and brittle materials by abrasive jets and rock drilling (Sundararajan and Manish 1997).

2.4.1 Erosion mechanisms

Several mechanisms have been proposed for the material removal by solid particle impact, for different alloys. Finnie (1958, 1960) suggested a process involving cutting or micromachining, as in metal cutting or grinding. According to him, the impacting particle penetrates the target by a small amount, translates along the surface, removing material ahead of it in a machining mode and finally leaves the surface. This analysis of the cutting action by a single particles launched against a ductile target was the first model of solid particle erosion capable of predicting material removal rate. He could solve for the trajectory of the particles in closed form as it cuts the surface, and thus predict material removal rates. This theory formed the foundation for later rigid-plastic models, which removed the restriction of particle rotation during impact. The model predicts well for angle dependency in the range less than 45° .

Sundararajan (1991) developed a model valid for all impact angles based on the assumption that the localization of plastic flow underneath the impacting particle is responsible for lip formation and hence erosion. He reported that it is capable of rationalizing the important experimental observations related to erosion, namely, the effects of material properties, impact velocity, and impact angle and particle shape.

The erosion mechanisms are generally classified into two categories, namely, ductile and brittle mechanisms. Such classifications were initially based on the

response of classical “ductile” and “brittle” materials, which, by virtue of their mechanisms, showed mass loss as a function of impact angle. This response is similar to those in Fig. 2.3. Subsequent work has shown that the material response as a function of impact angle depends on an extensive number of variables, well beyond those related to the material properties.

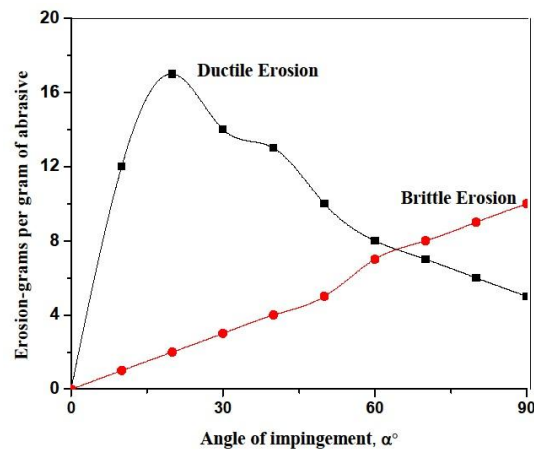


Fig. 2.3 Erosive mass loss as a function of impact angle (Finnie 1972).

The classical “ductile” erosion response, exhibit the greatest magnitude of mass loss at low impact angles of 15° - 30° . At higher angles, the erosion rate drops, although the rate does not tent to 0 at 90° . The severity of low angle impact damage has been related to the efficiency of the generalised “machining” mechanism postulated to account for erosive mass loss in ductile materials. This generalised mechanism has been sub divided into 3 modes of response, as shown in Fig. 2.4.

The glancing angle impact of rounded erodent results in furrow indentations, with material physically displaced outwards, to the sides and terminal end of the crater. While, mass loss typically does not occur by direct impact in this manner, the plastically deformed “lips” (Hutchings 1992) or “platelets” (Levy et al. 1984) of highly strained material are prone to fracture or fatigue during subsequent impacts (Hutchings 1992 and Levy et al. 1984). Angular particles impart more of a “cutting”

action during impact, the resulting damage dependent on one of two possible mechanisms. Type I cutting (Hutchings 1992) involves impact by an angular particle in a similar manner to the “ploughing” mechanism of rounded particles.

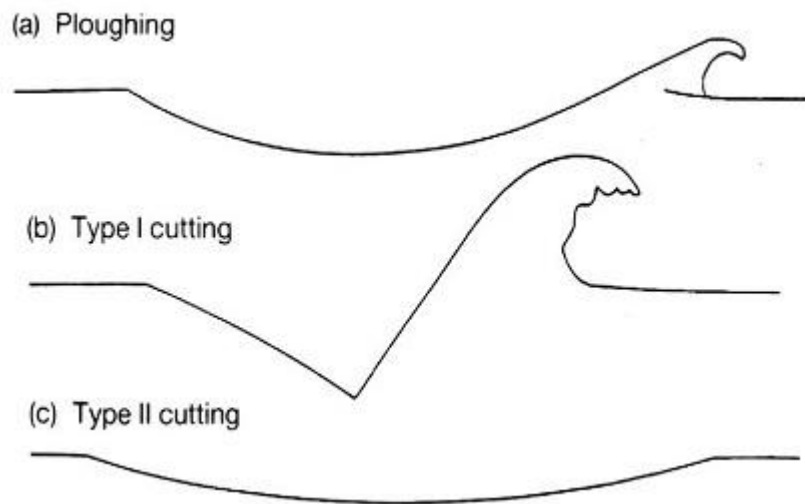


Fig. 2.4 Characteristic mechanisms of ductile erosion based on the variation in erosion conditions (Hutchings 1992).

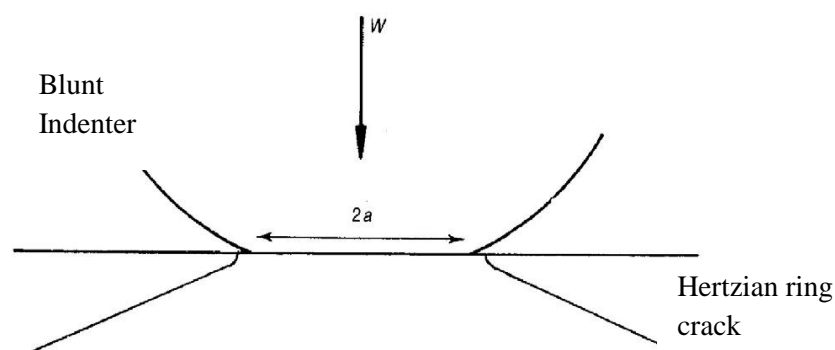


Fig. 2.5 Cross-sectional, schematic view of impact by a blunt indenter on to a brittle material, resulting in the formation of a conical Hertzian crack, (Hutchings 1992).

The erodent penetrates the surface and caves out an angular furrow of material, plastically deforming the material to the side of the crater and typically generating a chip or lip of the material at the terminal end of the crater.

As with the “ploughing” mechanism, no direct material loss occurs in this process, with degradation occurring through fracture of the displaced material upon subsequent impact. Type II cutting (Hutchings 1992) occurs in a similar manner to the Type I mechanism, however, rotation of the erodent particle during impact results in a machining type action that directly “cuts” chips of the material from the surface.

The classical “brittle” erosion response shows the greatest rate of mass loss at high impact angles (90°), with the rate continually decreasing to negligible degrees of mass loss at low impact angles (less than 60°). The response reflects the mechanism of fracture induced mass loss, whereby the extent of substrate damage is dictated by the magnitude of the vertical component of the impact load applied by the erodent particle. For a given particle impact velocity, the component of the load applied perpendicular to the surface, continually decreases with decreasing impact angle, resulting in reduced erosion damage. Mechanistically, particle impact generates brittle fracture within the near surface zone of the material, with cracks radiating outwards and downwards from the point of impact. Mass loss occurs by chipping, whereby segments of material formed by the intersection of crack networks are ejected from the surface (Hutchings 1992). The mechanism says erosive mass loss is very negligible initially, whereby successive particle impacts generate the extensive crack network required for steady state erosive mass loss to proceed. Generally crack generation takes place by two mechanisms, namely, blunt or sharp indentation (Hutchings 1992, and Ruff et al. 1975).

Impact by a blunt indenter, under light loads, generates a ring crack, termed Hertzian crack. Crack propagates into the material as a cone around the point of impact, as shown in Fig. 2.5. This is completely an elastic deformation and there is no plastic deformation. The extent of crack propagation depends upon pre-existing substrate flaws, the particle diameter and fracture resistance of the substrate

(Hutchings 1992, and Ruff et al. 1975). Under more aggressive conditions, particularly with sharp indenters, cracking becomes more extensive.

Solid particle erosion damage of brittle materials has been investigated by Sheldon and Finnie (1966), who studied the erosive regime, usually referred to as Hertzian fracture, where the contact between the particle and the body is exclusively elastic. In their analysis they considered dynamic forces between the surface and the particle and this resulted in the prediction of the material volume removed from a material with specific properties. They also concluded that the fracture at the surface is a function of the volume of the material constrained in the primary erosion zone in relation to the surface and volume flows.

The principal erosion mechanism in the brittle materials is mainly due to brittle fracture often accompanied by a small amount of plastic flow (Zambelli and Levy 1991, and Levy 1983). During the initial stage, network of fine cracks are created, which make it possible for the impacting erodent particles to remove small chips of the brittle materials.

Wensink and Elwenspoek (2002) reported that the brittle erosion is related to material removal due to crack formation. When a brittle material is impacted by a hard and sharp particle, the contact area is plastically deformed due to the high compressive and shear stresses and a radial crack is formed. After the impact, the plastic deformation leads to larger tensile stresses that result in lateral cracks causing the material removal.

Bellman and Levy (1981) and Levy (1984 and 1986) reported that the erosion of ductile materials can be described in terms of three distinct phases, which occur sequentially in the steady state condition. In the initial phase, an impacting particle forms a crater, and material is extruded or displaced from the crater to form a raised lip or mound. In the second phase, the displaced metal is deformed by subsequent impacts. This may lead to lateral displacement of the material which is part of the surface, and can be accompanied by some ductile fracture in heavily strained regions. Finally, after a few impacts, the displaced material becomes so severely strained that

it detaches from the surface by ductile fracture. In the steady state erosion, all three phases occur simultaneously at different locations over the surface. This erosion mechanism is identified as "platelet mechanism". Soderberg et al. (1981) tested about 50 metals and alloys and further classified them with respect to erosion mechanism. Their result indicates that almost all the metals and alloys loose material by formation of the lip or platelet and their subsequent fracture. Sidhu et al. (2007) reported the platelet mechanism during the erosion of HVOF coated Stellite-6. The material subjected to erosion undergoes, initially, plastic deformation and later damaged material is removed by subsequent impacts of the erodent on the surface. The cutting occurs by the impact (at 30° & 90°) of the erodent particles, and lips or ridges are formed at the bank of the grooves. These lips are fractured or removed from the grooves with further erosion.

Wheeler and Wood (2005) have examined the tungsten carbide coatings (86WC-10Co-4Cr) deposited on carbon steel (AISI 1020) to reduce the fluid erosion, wear and corrosion. These conditions were encountered by valves, drill bits and down hole assemblies used in mining as well as oil and gas drilling sectors. He reported that the erosion mechanism on the ductile and brittle material depends on the impact angle of the particles. For a ductile material, the effect of impact angle on the erosion rate is maximum at 20-30°. For brittle material the erosion rate is maximum at 90°.

Ramesh et al. (2010) investigated the erosion behaviour of GrA1 boiler tube steel (ASTM-SA210) and found that it exhibits lower steady state volume erosion rate in comparison to HVOF sprayed WC-Co/NiCrFeSiB coatings under room temperature. They attributed large differences in hardness between silica erodent particle and substrate steel as responsible for the penetration of silica particles into the surface which bestow some shielding effect against further impacting particles and indentation induced severe plastic deformation leads to lower erosion loss.

2.5 SURFACE COATINGS

Strong corrosion and erosion resistance is required for high temperature materials used in gas turbine applications, in addition to excellent mechanical

properties such as high temperature strength, good creep resistance and microstructure stability. However, these requirements, sometimes, cannot be achieved simultaneously by alloy development alone. An alternate approach, where mechanical strength is accomplished by alloy development and corrosion or erosion resistance by surface coating is now generally accepted practice in power generating industries. Coatings will be used, when resistance to environmental degradation cannot be combined with the necessary properties for the component to perform its function, or where the resulting alloy or its fabrication become so expensive that a coated system is economically preferable. Coatings can add value to products up to 10 times the cost of the coating (Matthews et al. 1998, and Stringer 1987).

Generally speaking, coatings can be regarded as materials with greater resistance to the significant surface degradation process. The role of the coating is to provide a metal surface composition that will react with the environment to produce the most protective scale possible, combining corrosion resistance with long term stability and resistance to cracking or spallation under mechanical and thermal stresses induced during operation of the component (Gurrappa 2003).

Among various coating techniques, the thermal spray coatings are especially interesting for their cost/performance ratio. It is a process with almost no limitation of materials and with the ability to deposit coatings with thickness ranging from several micrometers to tenths of millimeters. Additionally, it is suitable for a great variety of shapes and sizes and has the advantage of maintaining the substrate temperature relatively low (Rodriguez et al. 2003).

2.5.1 Thermal spray coating

In this process, the coating powders are heated to near or above its melting point and made to impact on the substrate materials by various methods. The coating layer is made up of thin lamellar particles or splats overlapping one over the other. The substrate is not heated above 150 °C, so its metallurgical properties remain unchanged. Advanced thermal spray coating methods like plasma spraying,

detonation gun spraying and high velocity oxy-fuel process (HVOF) are attractive in the recent past. Table 2.2 shows the characteristics of various thermal spray processes.

Generally, thermal barrier coatings (TBCs) are applied in order to reduce the heat flux between the surface and the substrate component (Nicholls 2002). Thermal barrier coatings are built up by an outer ceramic topcoat with low thermal conductivity and an intermediate oxidation and corrosion resistant bond coat. At high temperature exposure, oxygen easily penetrates the low-density topcoats and reacts with the bond coat, which oxidizes and produces a protective, thermally grown oxide layer (TGO) at the interface between the topcoat and the bond coat.

In general, the failure of TBCs is related to fracture and spallation in or close to the interface between the top and the bond coat (Evans et al. 2001). This zone is mostly considered to be a weak zone and without possessing sufficient adherence and strain tolerance to accommodate the strains imposed during high temperature operation. The relevant failure mechanism is the mismatch of the physical and thermal properties between the different zones in the coating system. Also, due to rapid heating and cooling conditions, additional transient stresses are built up due to the temperature gradient in the coating. The topcoat layer is experiencing thermal shock conditions. After several cycles, propagating cracks may have reached a stage where the topcoat spalls off. To overcome these problems, the cermets coating, deposited by HVOF spray method is the best solution (Evans et al. 2001)..

2.5.2 HVOF process

In HVOF process, the kinetic energy and the output of a supersonic flow of burnt gases is used to soften and propel the spray powder, producing a dense, very low porosity, good inter-particle cohesion and well-bonded coatings.

This process has been shown to produce coatings with better density, cohesive strength and bond strength than other thermal spray processes. Schematic representation of the HVOF spray process is as shown in Fig. 2.6. The HVOF deposition process involves the combustion fuels such as propylene, hydrogen or kerosene with oxygen.

Table 2.2 Comparison of the characteristics of various thermal spraying (Sobolev et al. 2004).

Deposition Technique	Heat Source	Propellant	Typical Temperature (°C)	Typical Particle Velocity (m s ⁻¹)	Average Spray Rate (kg h ⁻¹)	Coating Porosity (% by Volume)	Relative Bond Strength
Flame Spraying	Oxyacetylene/Oxyhydrogen	Air	3000	30-120	2-6	10-20	Fair
Plasma Spraying	Plasma Arc	Inert Gas	16000	120-600	4-9	2-5	Very Good to Excellent
Low Pressure Plasma Spraying	Plasma Arc	Inert Gas	16000	Up to 900	--	<5	Excellent
Detonation Gun Spraying	Oxygen/ Acetylene/ Nitrogen Gas Detonation	Detonation Shock Waves	4500	800	0.5	0.1-1	Excellent
High Velocity Oxyfuel (HVOF)	Fuel Gases	Combustion Jet	3000	800	2-4	0.1-2	Excellent

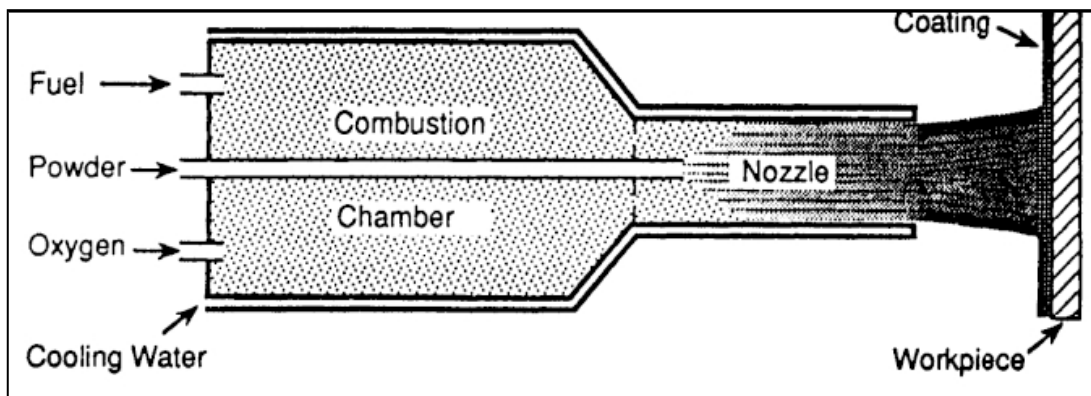


Fig. 2.6 Schematic representation of high velocity oxy fuel spray process (Bunshah 1994).

Combustion products come out under high pressure from a confined combustion chamber. The products of combustion are then discharged through a cooled nozzle at high velocity. Powders to be deposited are fed into the combustion area by a carrier gas, where they are heated and carried by the gases. Molten or partially molten powder particles arrive at the substrate, on impact flatten and solidify

rapidly. Coating thickness is normally in the range of 100 to 325 μm . Depending upon the injection pressures of the fuel gases, jet velocities exiting the nozzle can be in the order of 700 m/s (Mohanty et al. 1996).

HVOF spraying method is mostly used to apply cermets coating to impart wear resistance against abrasion and erosion in corrosive environment at high temperatures, typically up to 900 °C. They are used on superalloy components that are subjected to high temperature oxidation and hot corrosion during service conditions in the gas turbines used for various applications, such as aircrafts, thermal power plants, energy conversion systems, etc (Kamal et al. 2008).

Fig. 2.7 indicates the characteristics of HVOF coatings compared with those produced using the standard plasma spraying process (Helali and Hashmi 1996). Major advantages of the HVOF process include

1. Due to higher kinetic energy of the impacting particles, HVOF coating are homogeneous and dense, compared to other thermal sprayed coatings. The gas velocities of 700 m/s are typical with this process.
2. Due to shorter retention time of the particles in the flame, degradation of the powder during spraying is less (lower powder temperature).
3. Bond strength as high as 90 MPa and inert-particle cohesion are greater than any of the other processes.
4. Low porosity (<1%) and low oxide content (<1-2%) ensures increased corrosion and wear resistance of the coating.
5. Since particles are heated to moderate temperatures, it is preferably used for coating materials that tends to decompose at higher temperatures.
6. Large size components can be easily coated with this method.
7. It offers the possibility of on-site application and repair of industrial components.

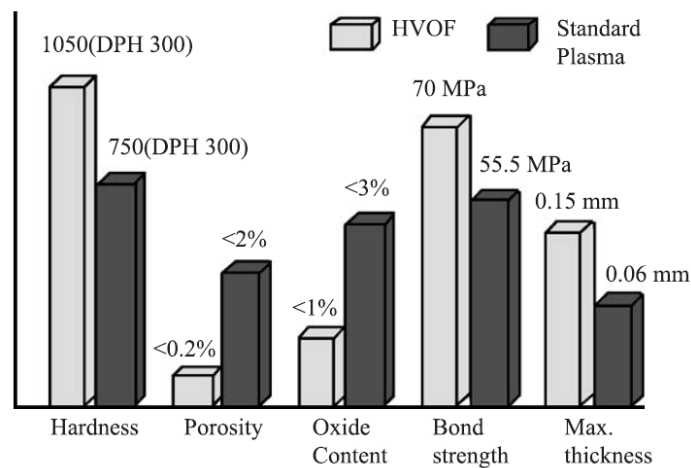


Fig. 2.7 Characteristics of HVOF and standard plasma process coatings (Helali and Hashmi 1996).

2.5.3 Coating formation and bonding mechanism

Fig. 2.8 shows the state of the particle as it exits the combustion zone and this has an effect on the final microstructure of the coating. The kinetics of droplet flattening depends upon the droplet size and the impact velocity. Initially, just after the impact, inertial effects dominate, the viscous flow effect becomes more important as the droplet spreads, and the influence of the surface energy could become a significant factor towards the end of the spreading process. During the rapid solidification of the spray particles there is a close contact between the particles and the substrate surface as shown in Fig. 2.9. This leads to improved bonding due to mechanical interlocking, adhesion, diffusion, chemical reactions, and sometimes partial fusion of the contact surfaces. These bonding effects permit the formation of a continuous coating layer. Mechanical interlocking is the main mechanism of thermal spray coating. The bond between the impacting particles and the substrate surface is established to a high degree through the arriving droplets, liquid flowing and solidifying around the substrate asperities/ roughness. Usually these asperities are formed by mechanical means such as abrasive blasting, grit blasting, or rough turning, which also activate and clean the surfaces prior to coating.

The quenching stresses within the spray particles increase the interlocking effects. Fig. 2.10 shows the possible bonding interactions. The adhesive bonding mechanisms are effective at micro contact areas between particles and/or substrate. These forces correspond to the atomic attractive forces within crystalline solid matter, since the particles approach one another as close as atomic scales. Depending on the type of atomic bonding, on the one hand, van der Waals forces and on the other hand an exchange of valence electrons may take place.

2.6 COATING MATERIALS

To protect the degradation of gas turbine substrate materials against a corrosive, oxidation and erosion environment, a coating that forms a thermally grown oxide should be applied. If the requirement is to protect against a high temperature, a coating type that acts as a cermets can be applied. Fig. 2.11 demonstrates how the applied coating can be selected on basis of corrosion and oxidation performance.

The effects of alloying elements in coatings are as follows (Nicholls and Rickerbery 2002)

Chromium: Chromia forming element; used in Ni and Co base coatings against hot corrosion and oxidation resistance upto, 900 °C; Carbide (Cr_{23}C_6 & Cr_7C_3) former.

Cobalt: Base element for overlay coatings on Co base substrates. It minimizes the interdiffusion; raises solvus temperature of Ni_3AlTi .

Nickel: Base element for overlay coatings on Ni base substrates. It minimizes the interdiffusion; depresses chemical activity of Al.

Aluminium: Alumina forming element in coatings and Ni and Co base alloys; protects against oxidation upto 1200 °C.

Yttrium: Improves adherence of alumina and chromia scales on Ni and Co base alloys; changes the oxide growth from cation diffusion to anion diffusion controlled mode; reduce the oxidation rate of chromia.

Tantalum: Solid solution strengthener, carbide former, improves oxidation and corrosion resistance, reduces thermal expansion coefficient.

Titanium: Accelerates formation of chromia at metal/oxide interface, reduces thermal expansion coefficient.

2.6.1 Oxide coating

Alumina based ceramic coatings exhibit extremely high hot corrosion, oxidation and wear resistance compared to coatings fabricated using conventional anodizing processes (Yerokhin et al. 1999 and Shigang Xin et al. 2006).

One of the most common method used to combat hot corrosion problems in gas turbines, involves utilization of surface coatings. Coatings for super alloys are usually designed in such a way that on exposure to reactive environments, the selective oxidation of an element occurs to form a protective oxide film such as Cr_2O_3 , Al_2O_3 or SiO_2 (Rhys Jones and Swindells 1985). Aluminum oxide (Al_2O_3) or alumina is preferred as insulating layer due to its high stability at elevated temperatures, with a bulk melting temperature of 2054 °C and a resistivity of approximately $5 \times 10^7 \Omega \text{ cm}$ at 1100 °C (Luer et al. 2000).

In general, high-temperature materials based on iron, nickel, and cobalt-based alloys have been designed to form protective scales of either chromium oxide (Cr_2O_3), aluminum oxide (Al_2O_3), or silicon dioxide (SiO_2), when exposed to oxidizing conditions. At temperatures above 900 °C, however, Cr_2O_3 has the tendency to react further with oxygen to form volatile Cr_2O_3 , severely limiting the lifetime of Cr_2O_3 forming alloys. While, both Al_2O_3 and SiO_2 are able to withstand higher temperatures up to around 1200–1300 °C, SiO_2 formers are limited to environments with adequate oxygen activity due to the propensity of forming volatile SiO_2 at low oxygen activities (Stott et al. 1995).

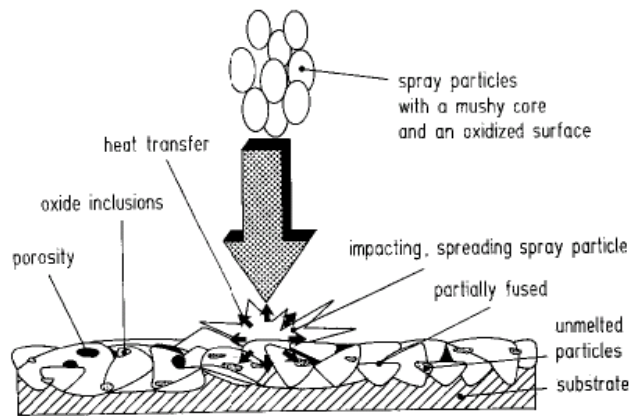


Fig. 2.8 Schematic of a typical structure of sprayed coating (Bunshah 2001)

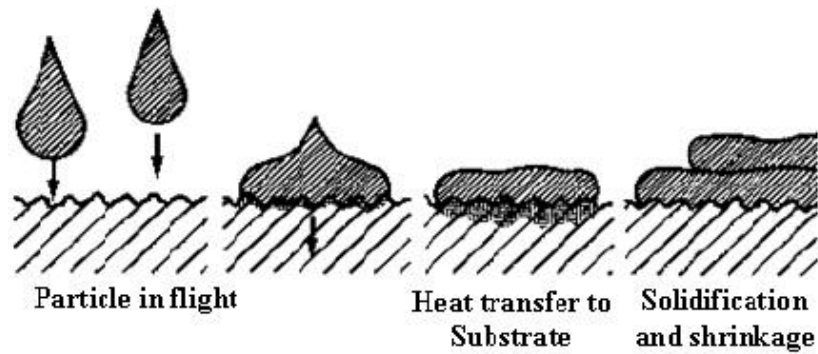


Fig. 2.9 Coating formation (Bunshah 2001)

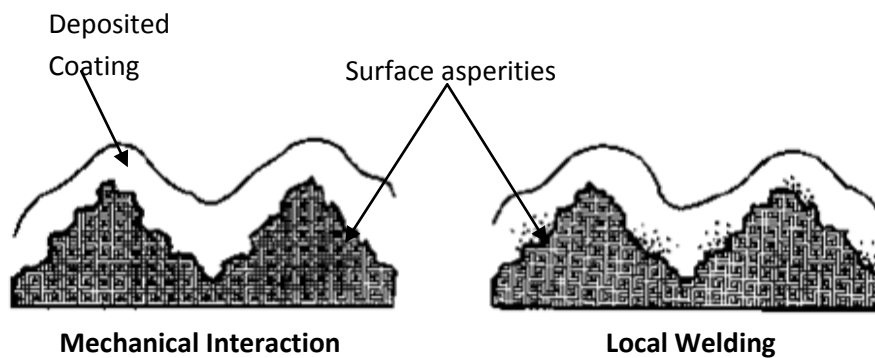


Fig. 2.10 Bonding interactions within a spray coating (Bunshah 2001)

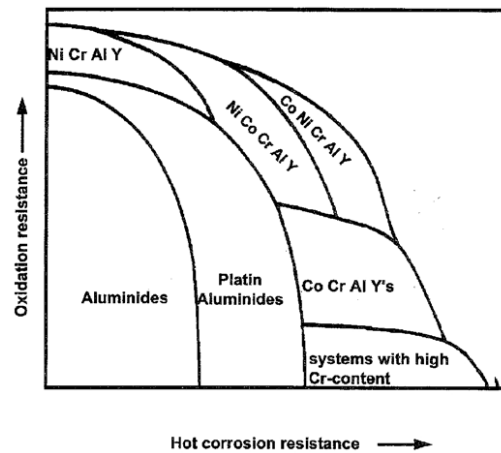


Fig. 2.11 Corrosion and oxidation resistance of different types of coatings. (Nicholls and Rickerbery 2002)

The nanometer Al_2O_3 dispersion strengthened NiCoCrAlY high-temperature protective coatings on Ni based superalloy, GH4033, are produced using crosscurrent CO_2 laser. Microscopic morphologies, phase constitutions of cladding coatings and distribution of nano- Al_2O_3 particles were examined using SEM and XRD. The results show that the grains, after adding proper nano- Al_2O_3 , grow from epitaxial to non-epitaxial shape, gradually and the columnar dendrites become thinner and denser with cellular shape. Cracks in the substrate close to the interface are eliminated (Wang et al. 2003).

Coatings protecting the blades of the first turbine stage from high-temperature oxidation have been used for over 40 years since the time when the maximum temperature on the blades attained $850 - 950^\circ\text{C}$. At first the blades were primarily protected by simple aluminizing performed by a powder or a slip method. Upon the creation of more powerful gas turbine engines (GTE), the gas temperature at the inlet to the turbine increased, this inevitably increased the maximum temperature on the blades. For some modern engines, it exceeds 1100°C . This reduces considerably, the rate of deterioration of the protective properties of the coatings on turbine blades and shortens their service life. The high-temperature oxidation of the coating is accompanied by the partial removal of the oxides from the most heated places due to high speeds of the gas flow. With growth in the temperature of the blades, the strength

of the base material and of the coating material decreases. This increases the probability of appearance of cracks in the coating and of propagation of the cracks into the material of the blade. In addition, growth at this temperature increases the rate of diffusion of alloying elements, primarily of nickel, from the alloy into the coating. As a result, the content of aluminum in the coating decreases at a rate comparable with the decrease due to oxidation and the formation of an Al_2O_3 film and its spalling (Frankel and Dapkunas 1977).

2.6.2 MCrAlY coating

Lambert et al. (1991) studied the oxidation and hot corrosion of Ni-17Cr-6Al-0.5Y and Ni-16Cr-5.7Al-0.47Y-5Si alloys at 700°C in Na_2SO_4 -60% V_2O_5 , to ascertain the effect of addition of Si. They observed an outer layer of NiO developed on the surface of the Ni-17Cr-6Al-0.5Y alloy whereas a thin Al_2O_3 oxide scale formed on the Si-enriched alloy. They further opined that the condensed vanadates of sodium are highly corrosive and can markedly increase the rate of oxidation of nickel base superalloys.

Coatings on the basis of a CoNiCrAlY system are widely used to protect gas-turbine blades against sulfide-oxide corrosion. However, no systematic investigations into the resistance of these coatings to this kind of corrosion have so far been carried out. CoNiCrAlY based coatings possess certain advantages over the CoCrAlY system based coatings, which are widely used in the industry. They have higher thermal stability, thermal fatigue strength, and adhesion to the base (the nickel alloy of which the blades are made). In addition, they have a lower temperature of viscous transition and a lower content of cobalt, a very poorly available material (Nikitin 1987). It is known that deposition of condensed coatings of the Ni (Co)-Cr-Al-Y system is an effective means to increase the service life of turbine blades under temperatures, not exceeding $1050 - 1100^\circ\text{C}$ (Kolomytsev et al. 2001).

2.6.3 Carbide coating

It has been shown that Cr_3C_2 -NiCr material, amongst other cermets, is one of the best coatings at counteracting wear due to its oxidation resistance up to

temperatures of 850 °C. Hussainova et al. (1999) indicated that although satisfactory results have been obtained with cermets coating systems, much debate still exists over the best hard phase/matrix ratio for optimum erosion resistance.

HVOF sprayed Cr₃C₂-NiCr and WC-Co coatings are widely studied with regards to their wear resistance behaviour, but now there is an increasing interest being shown in their application for protection against high temperature corrosion (Sidhu et al. 2006A).

2.6.4 Stellite-6 coating

Sidhu et al. (2006B) reported the effectiveness of CrC-NiCr, NiCrSiB, Ni-Cr and Stellite-6 coating on nickel based superalloy substrate. The Ni-Cr coating has high corrosion resistance compared to other coatings. The Stellite-6 coating shows the lowest corrosion resistance amongst the investigated systems.

Sidhu et al. (2005) reported that Stellite-6 coated boiler steel to possess higher resistance to erosion and corrosion compared to uncoated steels at 755 °C.

Singh et al. (2005) conducted thermogravimetric hot corrosion test on NiCrAlY, Ni-Cr, and Stellite-6 plasma coated, Fe based superalloy at 900 °C. All overlay coatings showed better resistance to hot corrosion as compared to that of uncoated superalloy. Stellite-6 was least effective, but still decreased the weight gain to around 60% of that of the bare superalloy. The formation of oxides and spinals of nickel, aluminium, chromium or cobalt are possibly contributing to the development of hot corrosion resistance in the coating.

2.7 SUMMARY

Degradation by high temperature oxidation, hot corrosion and erosion are the main failure modes of components in the hot sections of gas turbines, boilers, industrial waste incinerators, metallurgical furnaces, petrochemical installations, etc. Advances in materials development and cooling schemes have led to increase in operation temperatures of new generation gas turbine engines. The higher gas and metal temperatures in hot paths of turbines, working in the environment that contain

contaminants such as sodium, sulfur, vanadium and various halides require special attention with respect to the phenomenon of hot corrosion, oxidation and erosion. Under these conditions the material will be degraded at an unpredictable rapid rate, consequently the load carrying ability of the component is reduced, leading to the catastrophic failure.

Special alloys (Superalloys) have been developed for high temperature applications but they are not able to meet the requirements of the high temperature strength and the high temperature corrosion, oxidation and erosion resistance, simultaneously. One possible way to overcome this problem is use of coatings on the superalloy component. Coatings take care of the problems related to erosion and corrosion whereas the superalloys take care of the requirement of high temperature strength. Use of coatings has been often justified because of difficulties associated with mechanical properties, workability and high material price of highly alloyed superalloy material. Hence various types of coatings have become highly attractive. HVOF process can produce coatings satisfying some of the requirements of gas turbine applications. The high-velocity-oxy-fuel (HVOF) process belongs to the family of thermal spray techniques producing a coating having a unique microstructure. The performance of the HVOF coating under the conditions of hot corrosion, cyclic oxidation and erosion will be investigated. Three coating materials, namely, 10% Al_2O_3 +CoCrAlTaY, 25% $(\text{Cr}_3\text{C}_2$ -25(Ni20Cr)) + 75% NiCrAlY and Stellite-6 will be deposited on three materials (Ti-31, Superco-605 and MDN-121) which are candidate materials for high temperature components used in land based power production applications.

CHAPTER 3

EXPERIMENTAL SETUP

This chapter contains description of the experimental equipments used and the procedures employed for deposition and characterizations of the coatings, hot corrosion, oxidation and erosion studies and analyses of the corrosion, oxidation and erosive products.

3.1 SUBSTRATE MATERIALS

Titanium alloy (Ti-31), Cobalt based superalloy (Superco-605) and Special steel (MDN-121) are the substrate materials used in this study are candidate materials for turbine blades and are procured from Mishra Dhatu Nigam Limited, Hyderabad, India. The stated composition of the substrate materials is given in the Table 3.1. Materials were brought in sheet form and coupons of size 25 mm X 25 mm X 5 mm were cut and used for HVOF spraying.

Table 3.1 Substrate materials composition

Sl. No.	Name of the Material	ASTM Grade	Composition	Applications
1	Titanium alloy (Ti-31)	ASTM B338 Grade 5	Ti-6Al-4V	Pressure vessels, gas turbine blades, gas and chemical pumps, marine components
2	Cobalt base superalloy (Superco-605)	(ASTM F90-09)	Co-3Fe-10Ni-20Cr-1.5Mn-0.3Si-0.08C-15W	Gas turbines, furnace muffles in oxidizing atmospheres
3	Special steel (MDN-121)	(ASTM A565 Gr616)	Fe-0.8Ni-12Cr-1Mo-0.6Mn-0.25Si-0.2C-0.3V	Turbine blades

3.2 COMPOSITION OF POWDERS USED FOR COATING

Powders were chosen based on their resistance against hot corrosion and erosion. Three types of powders were chosen for deposition and the nominal compositions of the powder are given in the Table 3.2.

Table 3.2 Composition of the powders used for coating

Sl.No.	Coating powder	Chemical composition	Shape	Particle size
1	Oxide alloy powder	10% Al ₂ O ₃ +90% (Bal Co-23Cr-7Al-9Ta-0.68Y) (Fused powder) Powder Alloy Corporation, Cincinnati, Ohio, U.S.A.	Spherical	-45 to +15 μm
2	Carbide alloy powder	25% (Cr ₃ C ₂ -25(Ni20Cr))+ 75% (Bal Ni-21Cr-8Al-0.5Y) (Mechanical blend) Sulzer Metco (Japan) Ltd; Japan	Irregular	-45 to +15 μm
3	Stellite-6	58.6Co-28.8Cr-2.64Ni-4.51W-2.48Fe-1.15C-1.31Si-0.3Mn-0.02P-0.009S-0.04Mo Shanghai Zhong Zhou Special Alloy Materials Co Ltd, China.	Spherical	-45 to +15 μm

3.3 HVOF PROCESS PARAMETERS

HVOF spraying was carried out using METCO DJ2600 equipment (Fig. 3.1), which utilizes a supersonic jet generated by the combustion of liquid petroleum gas and oxygen mixture. The spraying parameters employed during HVOF deposition is listed in Table 3.3. Before HVOF spraying, substrate materials were grit-blasted with alumina, to develop better adhesion between the substrate and the coating. The HVOF

coating process was carried out in Spraymet Coating Industries, Bangalore, India and Anod Plasma Industries, Kanpur, India.

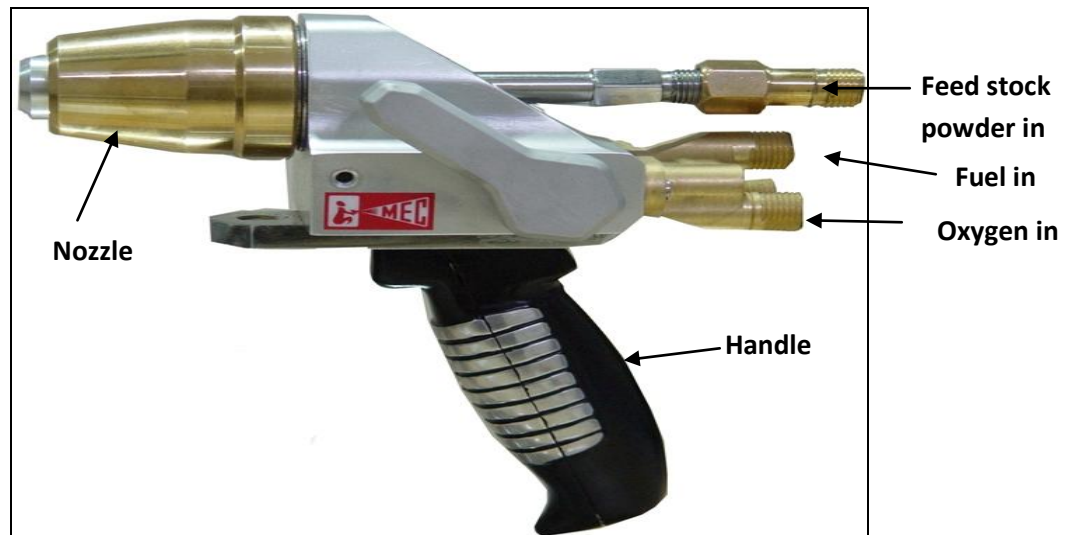


Fig. 3.1 Photograph of HVOF gun. Model: METCO DJ2600

Table 3.3 HVOF process parameters

Oxygen flow rate	250 LPM
Fuel (LPG) flow rate	60-70 LPM
Air flow rate	700 LPM
Spray distance	0.20-0.25 m
Powder feed rate	4-5 g/min
Fuel pressure	$68 \times 10^4 \text{ N/m}^2$
Oxygen pressure	$98 \times 10^4 \text{ N/m}^2$
Air pressure	$54 \times 10^4 \text{ N/m}^2$
Nitrogen gas (powder carrying gas) pressure	$49 \times 10^4 \text{ N/m}^2$

3.4 HOT CORROSION STUDIES IN MOLTEN SALT ($\text{Na}_2\text{SO}_4+50\%\text{V}_2\text{O}_5$)

Hot corrosion studies were conducted at 800°C in a laboratory silicon carbide tube furnace with an accuracy of ± 5 °C. The uncoated specimens were polished with 600-1000 grade emery paper and coated samples were not polished to retain original coated surface before being subjected to hot corrosion run. The physical dimension of the specimen was then recorded carefully with a vernier caliper, to evaluate their surface area. Subsequently specimen were washed properly with acetone and dried in hot air by heating both boat and specimen in an oven at 150 °C for about 30 minutes to remove the moisture. During experimentation the prepared specimen was kept in an alumina boat and the weight of boat and the specimen was measured. The hot corrosion studies, under cyclic conditions, were conducted in a molten salt environment of $\text{Na}_2\text{SO}_4-50\%\text{V}_2\text{O}_5$. The tests were conducted for 50 cycles, of which each cycle consisted of 1 hour heating at 800 °C in silicon carbide tube furnace followed by 20 minutes cooling in air. Salt coating of uniform thickness with coverage of 3-5 mg/cm² of $\text{Na}_2\text{SO}_4-50\%\text{V}_2\text{O}_5$ was applied using camel hairbrush on the preheated samples (250 °C). The melting temperature of the salt mixture is 800 °C. The coated samples were dried by heating in an oven at 250 °C for 1 hour. The boat containing the specimen was inserted into hot zone of tubular furnace set at a temperature of 800 °C. Holding time in the furnace was one hour (in molten salt) after which the boat with specimen was taken out and cooled to room temperature for 20 minutes. Following this, weight of the boat along with the specimen was measured and this constituted one cycle of the hot corrosion study. Any spilled scale in the boat was also taken into consideration for the weight change measurements. Electronic balance (model AY120, make Shimadzu Analytical (India) Pvt. Ltd, India) with a sensitivity of 10^{-4} g was used to conduct the thermogravimetric studies. Weight change values were measured at the end of each cycle with the aim to understand the kinetics of hot corrosion. Visual observation was made after the end of each cycle with respect to colour, luster or any other physical aspect of the oxide scales being formed. During this investigation, the hot corrosion studies were cyclic and were carried out for 50 cycles. The corrosion products of the uncoated and HVOF coated materials are analyzed by using XRD, SEM and EDX to reveal their microstructural and compositional features for elucidating the corrosion mechanisms.

3.5 OXIDATION STUDIES IN STATIC AIR

The uncoated as well as coated samples were subjected to oxidation in air at 800 °C for 50 cycles. Thermogravimetric studies were conducted as discussed in section 3.4. The oxidation products of the uncoated and HVOF coated samples were analyzed by using XRD, SEM and EDX to reveal their microstructural and compositional features for elucidating the oxidation mechanisms.

3.6 SOLID PARTICLE EROSION STUDIES

Room temperature, solid particle erosion studies were carried out using air jet erosion test rig (Fig. 3.2) as per ASTM G76-02 standard. Tests were conducted at the Surface Engineering Laboratory, PESIT, Bangalore, India. The erosion studies were performed on uncoated as well as coated samples for the purpose of comparison. The erosion test conditions utilized in the present study are listed in Table. 3.4. The velocity of the erodent particles was determined according to rotating double-disc method as described by Ruff and Ives (Ruff and Ives 1975). The samples were first cleaned with acetone using an ultrasonic cleaner, dried and then weighed using an electronic balance with a least count of 0.01 mg. The samples were then fixed to the sample holder of the erosion test rig and eroded with silica sand at the predetermined particle feed rate, impact velocity and impact angle for a period of about 5 minutes. Then samples were removed, cleaned with acetone, dried and weighed to determine the weight loss. The measured values were computed as the dimensionless incremental erosion rate (Ramesh et al. 2010). The above procedure was repeated till the attained incremental erosion rate value became independent of the mass of the erodent particles or, equivalently, of testing time. This constant value of the incremental erosion rate was defined as the steady state erosion rate. The incremental erosion rate was converted into volume wear rate to take into account the different densities of the coating material and the substrate. Figure 3.3 shows the SEM/EDX analysis of the erodent (silica sand), which was used for the present erosion studies. Figure 3.4 shows the schematic diagram of the erosion scar produced on the eroded surface at an impact angle of 30°, 60° and 90°.

Table 3.4 Erosion test conditions.

Erodent material	Silica sand (angular)
Erodent size (μm)	125-180
Erodent average hardness	880 Hv
Particle velocity (m/s)	40
Erodent feed rate (g/min)	5
Impact angle ($^\circ$)	30, 60 and 90
Test temperature (30°C)	Room Temperature
Test time (min)	Cycles of 5 min
Sample size (mm)	25x25x5
Nozzle diameter (mm)	4.5
Stand-off distance (mm)	10

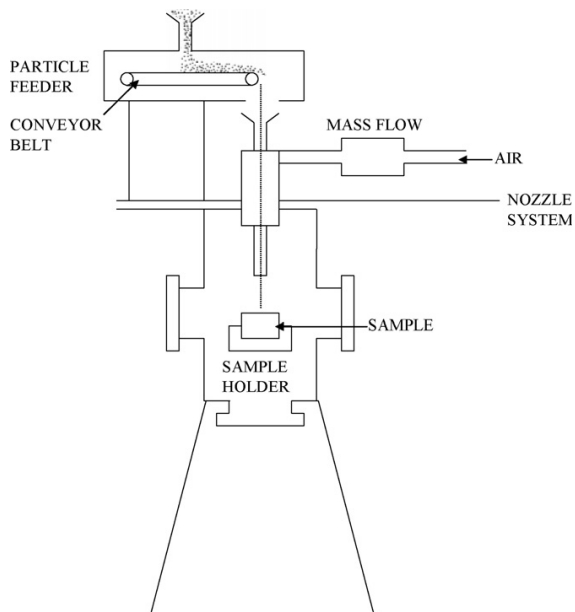


Fig. 3.2 Schematic view of an air jet erosion test rig.

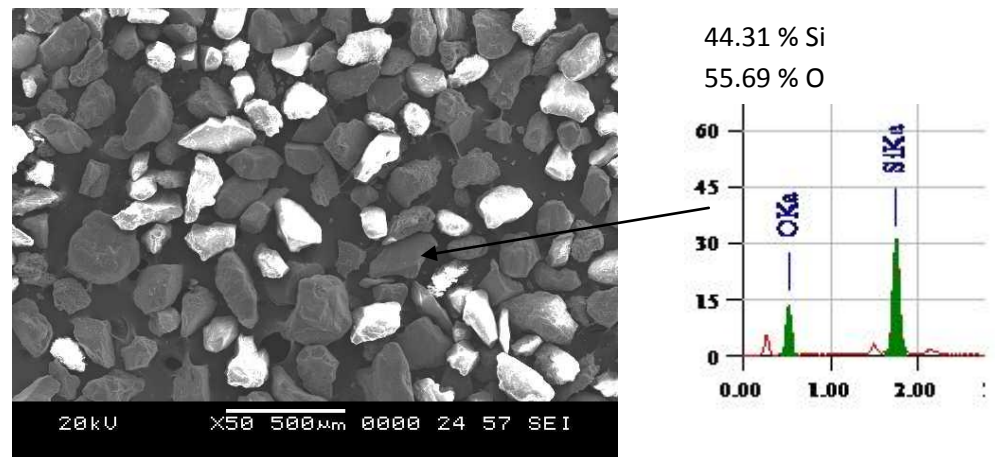


Fig. 3.3 SEM micrograph with EDX of erodent.

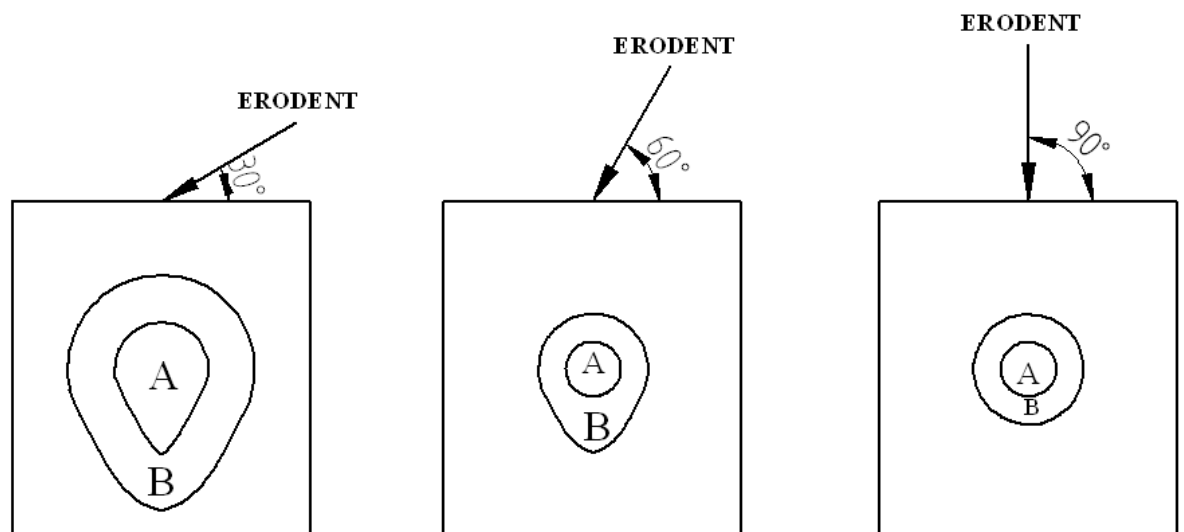


Fig. 3.4 Schematic diagram of the erosion scar produced on the eroded surface at an impact angle of 30°, 60° and 90°.

3.7 CHARACTERIZATION OF COATINGS, ANALYSIS OF CORROSION AND EROSION PRODUCTS

3.7.1 Preparation of samples for cross-sectional analysis

Samples were cut along their cross-section with diamond cutter (Model MS 10, make Ducom, India). Thereafter, the cut sections were cold mounted using resin (Transoptic powder 20-3400-080, make Buehler) and polished down to 1000 grit using SiC emery papers. Fine polishing was carried out using diamond paste.

3.7.2 Measurement of thickness of as-sprayed coating

The thickness of the as-sprayed coatings was checked with the help of scanning electron microscope (Model: JSM-6380 LA, make JEOL, Japan). Cross sectional samples were used for this purpose.

3.7.3 Optical microscopy, porosity and density measurements

The porosity were measured by using Biovismaterials plus V4.56, make serial 7482 inverted optical microscope to obtain an optical images along with the cross-section of as-sprayed coatings and to determine the porosity content according to ASTM B276. Twenty fields of view were taken per sample at 250X magnification. The densities of the coatings were measured by the method of water immersion according to the ASTM standard C135-96 (2003).

3.7.4 Microhardness measurements

Vickers microhardness measurement (Model: MMT X7, make Matsuzawa, Japan) was done using 100 gram load over as-sprayed coatings and substrate materials. Hardness values were calculated from the relation

$$H_v = 189030 \times F/d^2$$

Where, F is load in Newton and d is length of the indentation diagonal in micrometer. The microhardness profile of the coatings as a function of distance from the coating-substrate interface is generated.

3.7.5 Surface roughness measurements

Surface roughness of the as-sprayed coatings was measured using stylus based surface roughness tester (Model: SJ-201P, Taly Surf Plus, make Mitutoya, Japan).

3.7.6 X-ray diffraction (XRD) analysis

X-ray diffraction patterns were obtained for feed stock powders, as-sprayed coatings and corrosion products. Diffraction patterns were obtained using x-ray diffractometer (Model: JDX 8P, make JEOL, Japan). CuK α radiation and nickel filter were used at 20 mA tube current and 35 kV accelerating voltage. The scanning range is between 10 to 110°. The peaks were identified using JCPDF (International centre for Diffraction Data Files).

3.7.7 Scanning electron microscopy (SEM) and energy dispersive x-ray (EDX) analysis

The surface morphology of the coating powder, as-sprayed coatings, eroded surface and corrosion products were studied using scanning electron microscopy.

Back scattered images were taken along the cross-section of the polished samples. The elemental compositions of different phases observed on the surface as well as along the cross-section have been obtained using energy dispersive X-ray analysis. (SEM-model: JSM-6380LA, make JEOL, Japan. EDX: oxford. U.K).

CHAPTER 4

CHARACTERIZATION OF SUBSTRATES AND COATINGS

This chapter describes the characterization of the microstructures and physical properties of the substrates and HVOF coatings applied on them.

4.1 MICROSTRUCTURE OF SUBSTRATE MATERIALS

Standard metallographic polishing technique is used to obtain the microstructure of the substrate materials. The etchant used for various substrate materials are given in Table 4.1. The optical microstructures of the substrate materials are shown in Fig. 4.1. The microstructure of Ti-31 (Fig. 4.1 a) shows fine beta phase distributed in a matrix of alpha phase. The microstructure of Superco-605 superalloy shows fine carbides distributed in Co-rich phase (Fig 4.1 b). The microstructure of MDN-121 consists of fine carbide particles in martensitic matrix and the stringers of delta ferrite (Fig. 4.1 c).

Table 4.1 Etchant used for various substrate materials (ASTM E407)

Substrate Materials	Etchant used
Ti-31	1.5 ml HF-4 ml HNO ₃ -94.5 ml water
Superco-605	50 ml distilled water, 50 ml HCl and 10 g of CuSO ₄
MDN-121	Picral (100 ml Ethanol + 2-4 g of Picric Acid)

4.2 MORPHOLOGY OF COATING POWDERS

The morphology of the coating powders was investigated using the scanning electron microscopy (SEM). Fig. 4.2a shows the morphology of oxide alloy (10%

$\text{Al}_2\text{O}_3+\text{CoCrAlTaY}$) powders. They are spherical in shape. Particle size is in the range of -45 to +15 μm . Fig. 4.2b shows morphology of carbide alloy (25% Cr_3C_2 -25(Ni20Cr) +75% NiCrAlY) powder particles. It is a mixture of spherical and irregular shapes with particle size in the range of -45 to +15 μm . Fig. 4.2c shows morphology of Stellite-6 powders. They are spherical in shape with particle size in the range of -45 to +15 μm . The particle size distribution of the powder as determined by the image analyzer is found to be consistent with the nominal size distribution, provided by the manufacturer.

4.3 VISUAL EXAMINATION AND ROUGHNESS OF COATINGS

The optical macrograph of substrate materials, over a size of 25 mm X 25 mm are shown in Fig. 4.3, for the purpose of comparison. The optical macrographs of the as-sprayed samples are shown in Figs. 4.4, 4.5 and 4.6. In each case a, b, c corresponds to substrate materials Ti-31, Superco-605 and MDN-121 respectively. The coatings are free from surface cracks. The colour of the as-sprayed oxide alloy (10% $\text{Al}_2\text{O}_3+\text{CoCrAlTaY}$) coating (Fig. 4.4), carbide alloy (25% Cr_3C_2 -25(Ni20Cr) +NiCrAlY) coating (Fig. 4.5) and Stellite-6 coating (Fig. 4.6) is dark grey. The measured surface roughness value for the oxide alloy (10% $\text{Al}_2\text{O}_3+\text{CoCrAlTaY}$), carbide alloy (25% Cr_3C_2 -25(Ni20Cr) +75%NiCrAlY) and Stellite-6 coatings are found to be 4.13 μm 7.67 μm and 10.1 μm , respectively. Average value of 10 readings is reported as the roughness value (Ra) and reported in Table 4.2.

4.4 MEASUREMENT OF COATING THICKNESS, DENSITY & POROSITY

Coating thickness was measured using the Back Scattered Image (BSE) obtained along the cross-section of the coated specimens (Fig. 4.8 a, b, c). The measured values of the coating thickness are tabulated in Table 4.4. The thickness of as-sprayed coatings is in the range of 250 to 325 μm . The density values of the coatings are calculated based on ASTM C135-96 (2003) standard water immersion testing method. The measured density of the coatings is reported in Table 4.3. The coatings surface porosity was measured according to ASTM B276, using porosity

measurement device (Biovismaterials Plus V4.56, make serial 7482). The porosity values are reported in Table 4.2.

4.5 EVALUATION OF MICROHARDNESS

The microhardness values were measured across the coating cross section. The microhardness profile of all the coatings as a function of distance from the coating-substrate interface is shown in Fig. 4.7 a, b, c. The micro hardness values of uncoated and coated samples are measured and tabulated in Table 4.3 and 4.4 respectively. The micro hardness of the coatings is found to vary along the cross section and, further, considerable increase in micro hardness values are measured on the substrate region closer to the coating-substrate interface.

Table 4.2 Thickness, porosity, surface roughness and density of sprayed coatings

Coating type	Average thickness (μm)	Porosity %	Surface roughness (Ra)	Density (g/cm ³)
10%Al ₂ O ₃ + CoCrAlTaY	259	0.84	4.1	3.702
25%(Cr ₃ C ₂ -25(Ni20Cr)) + 75% NiCrAlY	306	0.7	7.6	2.678
Stellite-6	325	1.08	10.1	8.33

Table 4.3 Microhardness value of substrate materials

Sl. No.	Substrate Material	Microhardness (Hv)
1	Titanium alloy (Ti-31)	388-392
2	Cobalt based superalloy (Superco-605)	403-406
3	Special steel (MDN-121)	301-306

Table 4.4 Microhardness value of coatings

Sl. No.	Coating	Microhardness (Hv)
1	10%Al ₂ O ₃ + CoCrAlTaY	563-580
2	25%(Cr ₃ C ₂ -25(Ni20Cr))+75%NiCrAlY	550-580
3	Stellite-6	960-980

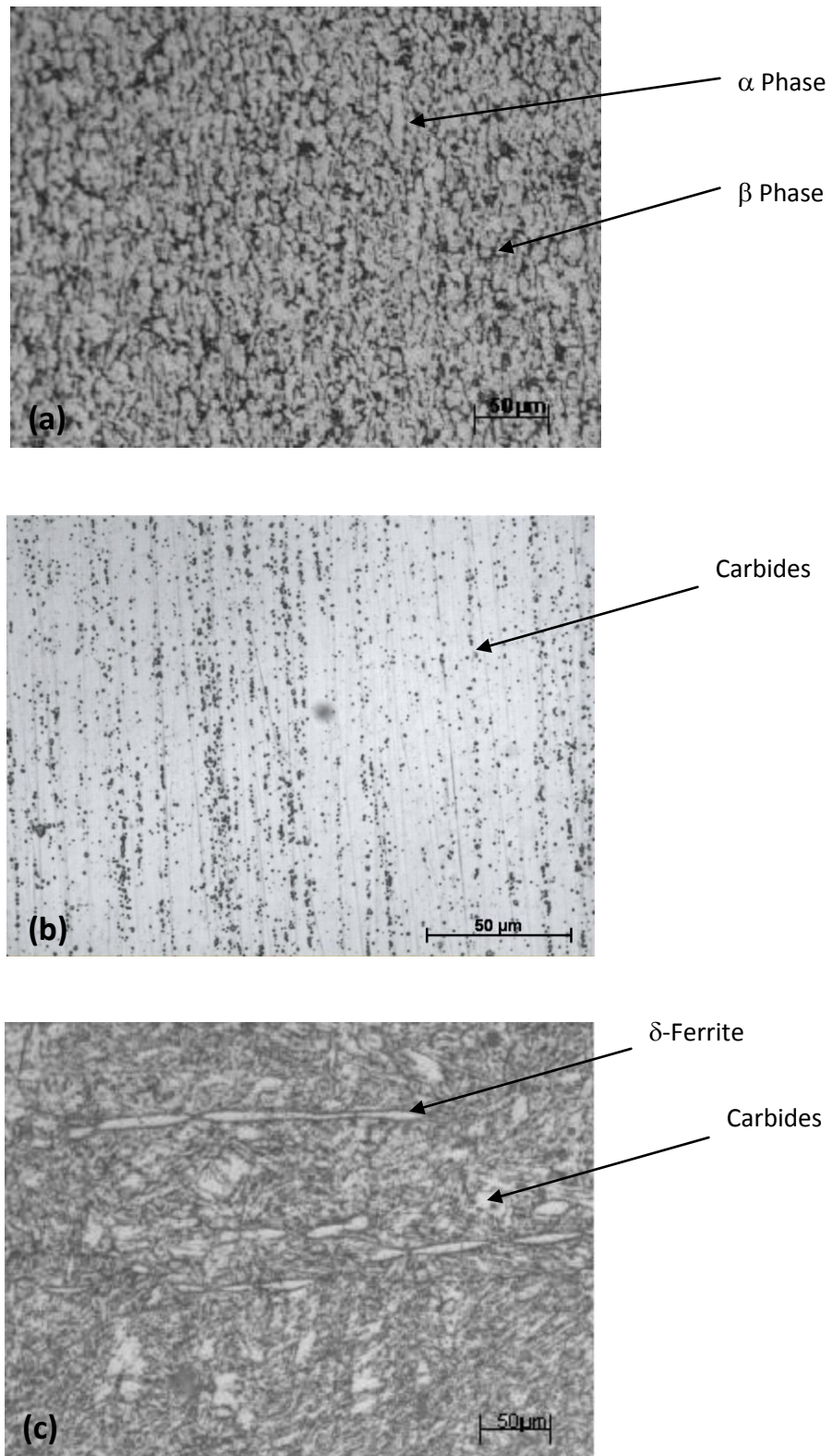


Fig. 4.1 Optical photo micrograph of substrate materials (a) Ti-31 (b) Superco-605 (c) MDN-121

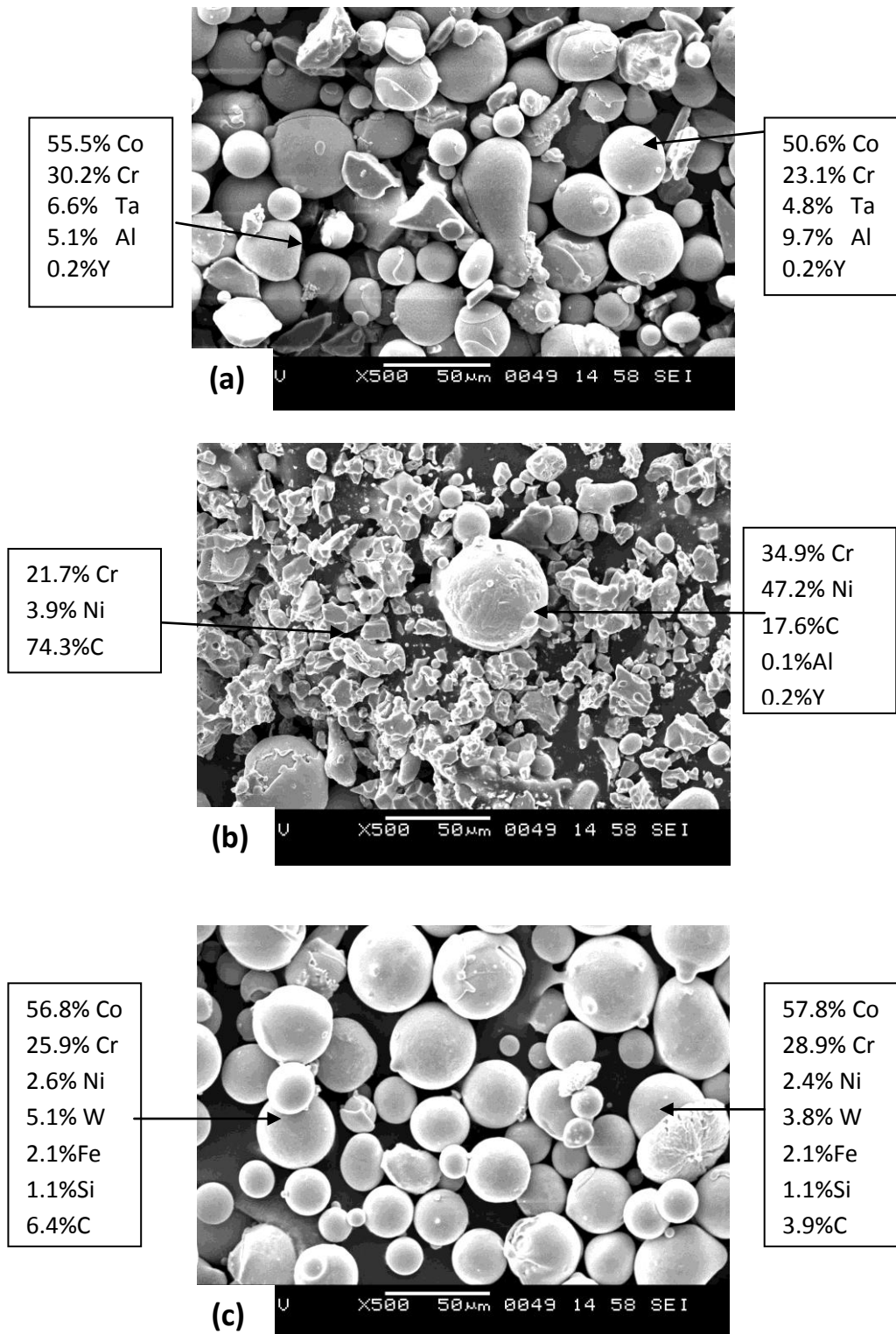


Fig. 4.2 Scanning electron micrograph of different coating powders, composition given in weight percentage (a) 10%Al₂O₃+CoCrAlTaY (b) 25%(Cr₃C₂-25(Ni₂₀Cr))+75%NiCrAlY (c) Stellite-6

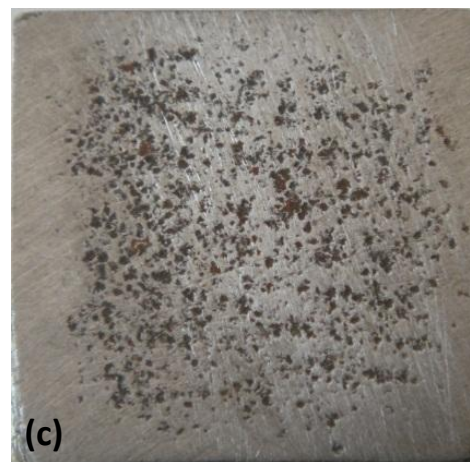
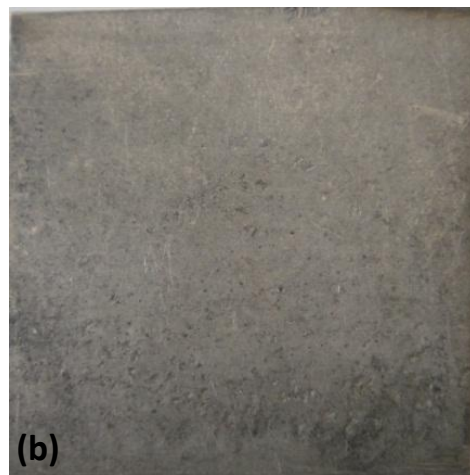
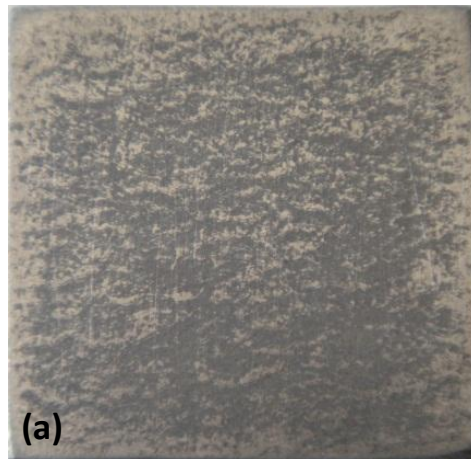


Fig. 4.3 Optical macrograph of substrate materials. Sample size is 25 mm X 25 mm (a) Ti-31 (b) Superco-605 (c) MDN-121

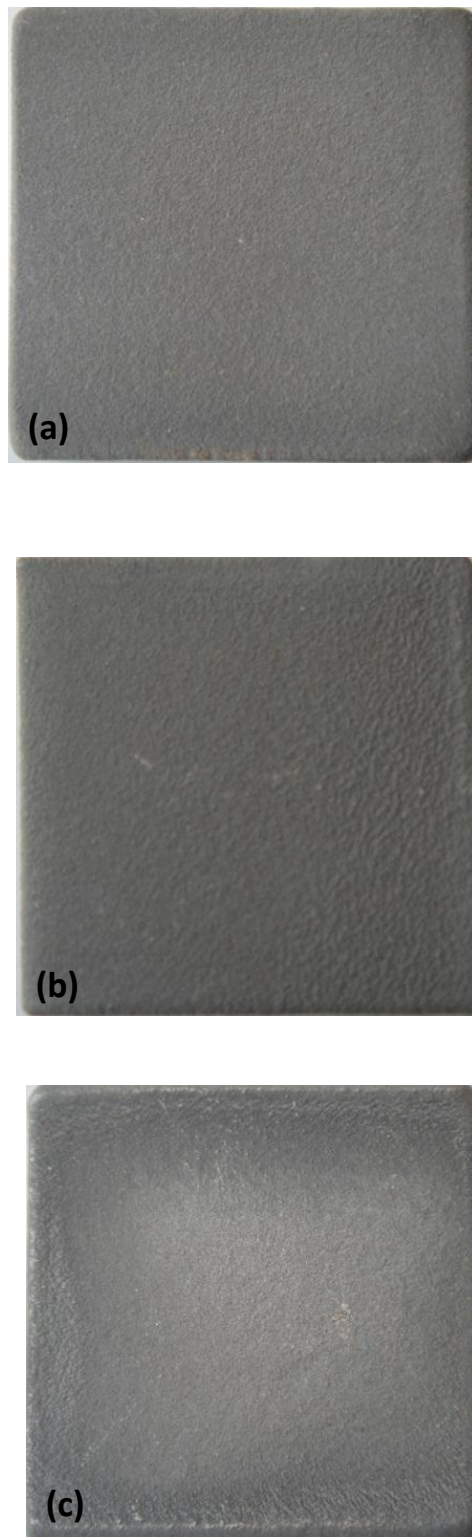


Fig. 4.4 Optical macrograph of 10% $\text{Al}_2\text{O}_3+\text{CoCrAlTaY}$ coated materials. Sample size is 25 mm X 25 mm (a) Ti-31 (b) Superco-605 (c) MDN-121

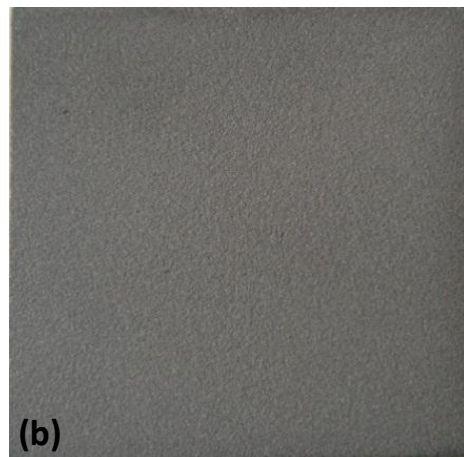
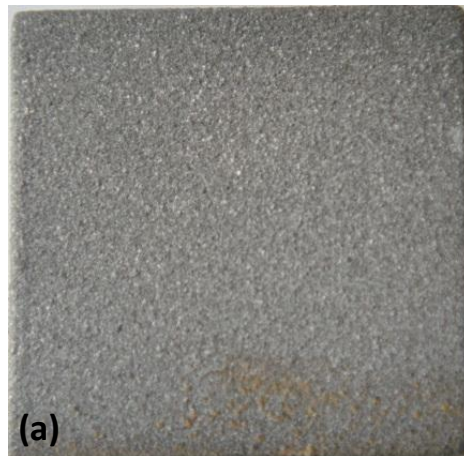


Fig. 4.5 Optical macrograph of 25%(Cr₃C₂-25(Ni₂₀Cr)) + 75%NiCrAlY coated materials. Sample size is 25 mm X 25 mm (a) Ti-31 (b) Superco-605 (c) MDN-121

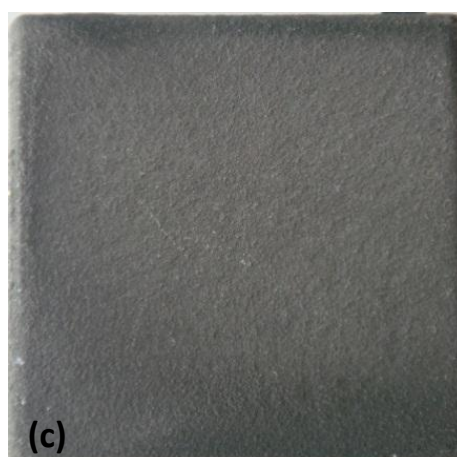
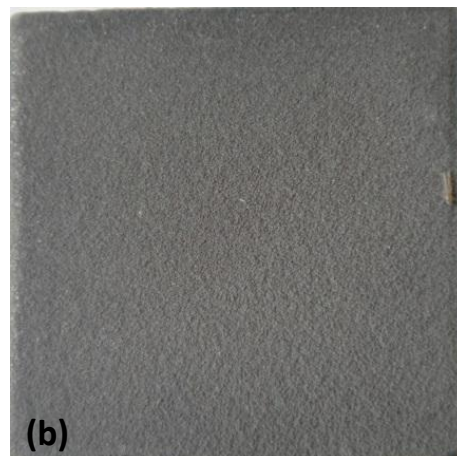
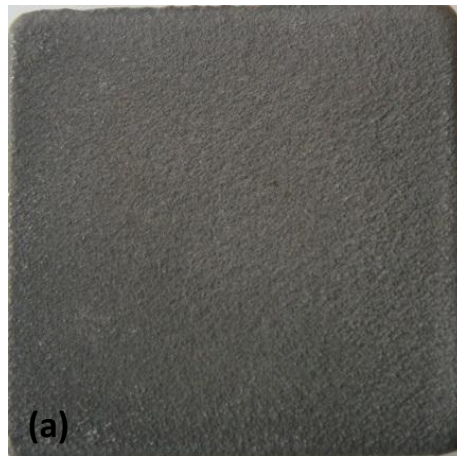


Fig. 4.6 Optical macrograph of Stellite-6 coated materials. Sample size is 25 X 25 mm (a) Ti-31 (b) Superco-605 (c) MDN-121

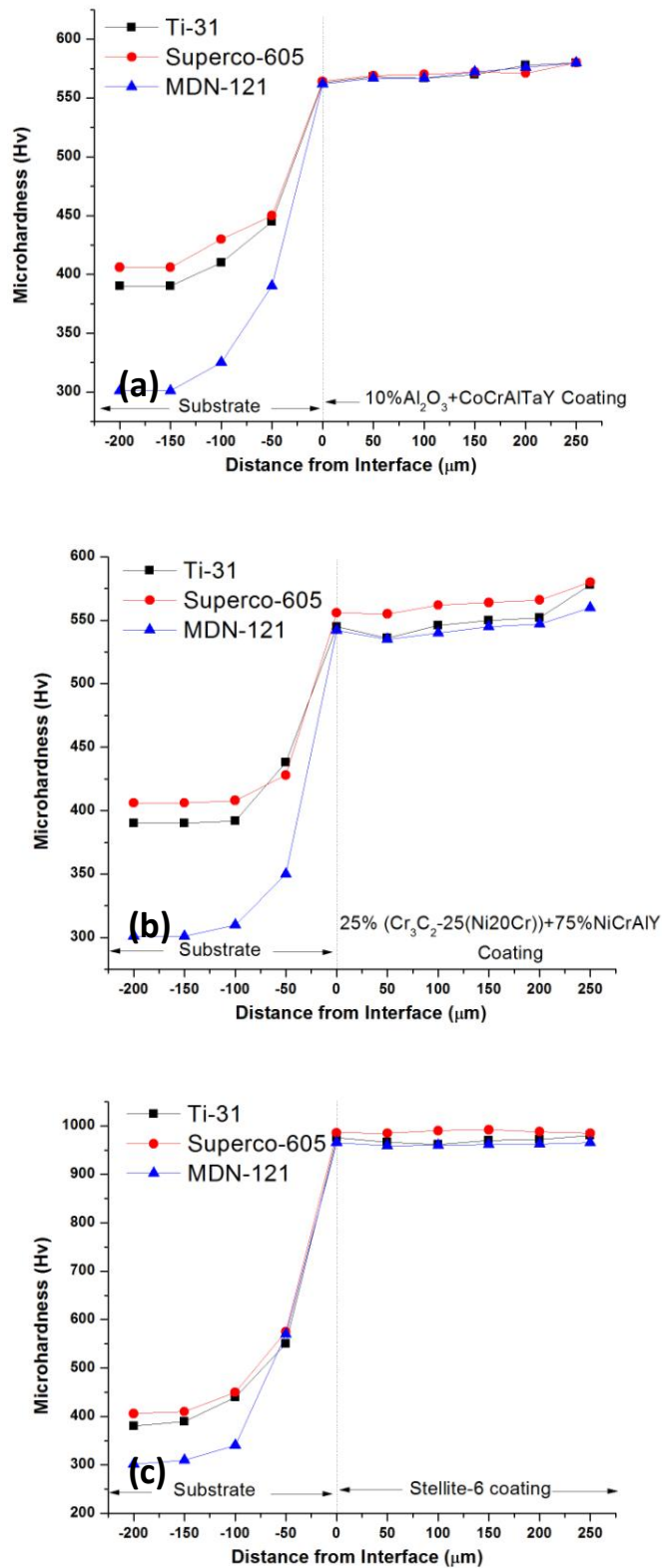


Fig. 4.7 Microhardness profiles of HVOF sprayed coatings for different substrate materials (a) 10% $\text{Al}_2\text{O}_3 + \text{CoCrAlTaY}$ (b) 25% $(\text{Cr}_3\text{C}_2 - 25(\text{Ni}20\text{Cr})) + 75\% \text{NiCrAlY}$ (c) Stellite-6

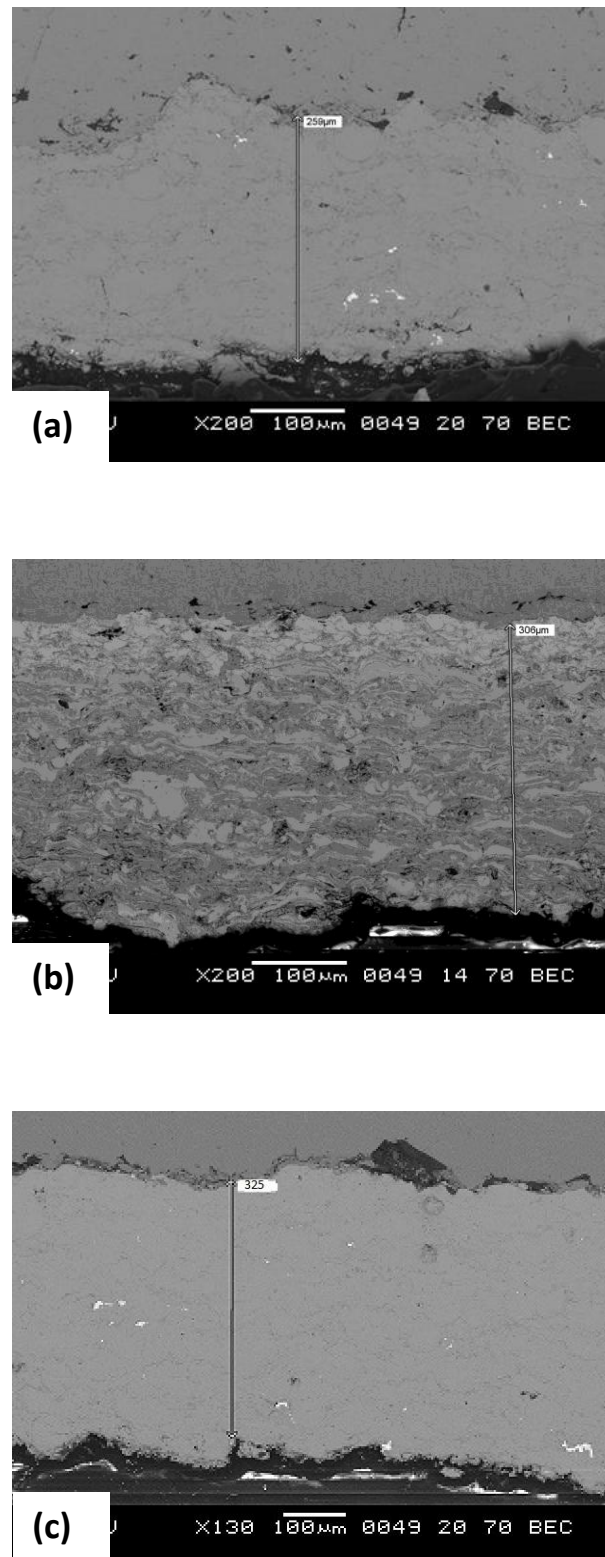


Fig. 4.8 SEM micrograph of coating cross sections indicating coating thickness (a) 10%Al₂O₃+CoCrAlTaY coating (b) 25% (Cr₃C₂-25(Ni₂₀Cr)) +75%NiCrAlY coating (c) Stellite-6 coating

4.6 XRD ANALYSIS

The X-ray diffraction patterns for the substrate materials, surfaces of the HVOF sprayed 10% Al₂O₃+CoCrAlTaY, 25% (Cr₃C₂-25(Ni20Cr)) +75% NiCrAlY and Stellite-6 coatings and powders are shown in Fig. 4.9 and 4.10 respectively. The alloy Ti-31 consists of β-Ti, Al and TiO₂ phases and Superco-605 contains Co as a major phase and MDN-121 consist of α'-Fe (martensite) as major phase. The XRD patterns for the as-sprayed coatings are presented in Fig. 4.10. For comparison, XRD patterns of as-received powders are incorporated in Fig. 4.10. All the coatings exhibit almost similar peaks as compared to that of powder indicating no change in their phase composition during spraying. The XRD patterns for 25% (Cr₃C₂-25(Ni20Cr)) +75% NiCrAlY powder and HVOF sprayed coating have nickel rich FCC phase as principal phase. The XRD patterns for 10% Al₂O₃+CoCrAlTaY and Stellite-6 shows cobalt rich phase as principal phase. In all the coatings, the presence of weak intensity peaks, indexed to Cr₂O₃, indicate that a small amount of oxidation has occurred during spraying. The surface of the 25% (Cr₃C₂-25(Ni20Cr)) + 75% NiCrAlY coating consists of Cr and Ni as major phase and Al, CrC are minor phases taken place during the HVOF spraying.

4.7 SEM ANALYSIS OF AS-SPRAYED COATING

The scanning electron micrographs showing surface morphologies along with the EDX composition analysis, at the selected points, on the surface of the as-sprayed HVOF coatings are shown in Fig. 4.11. The surface of the 10% Al₂O₃+CoCrAlTaY (Fig. 4.11 a) consists of globules of melted cobalt rich alloy. The surface of 25% (Cr₃C₂-25(Ni20Cr)) +75% NiCrAlY coating (Fig. 4.11 b) shows the distribution of chromium carbide splats in the matrix rich with melted nickel rich alloy. The surface morphology of as-sprayed Stellite-6 (Fig. 4.11 c) coating seems to be made of overlapping of the individual splats rich with cobalt and chromium.

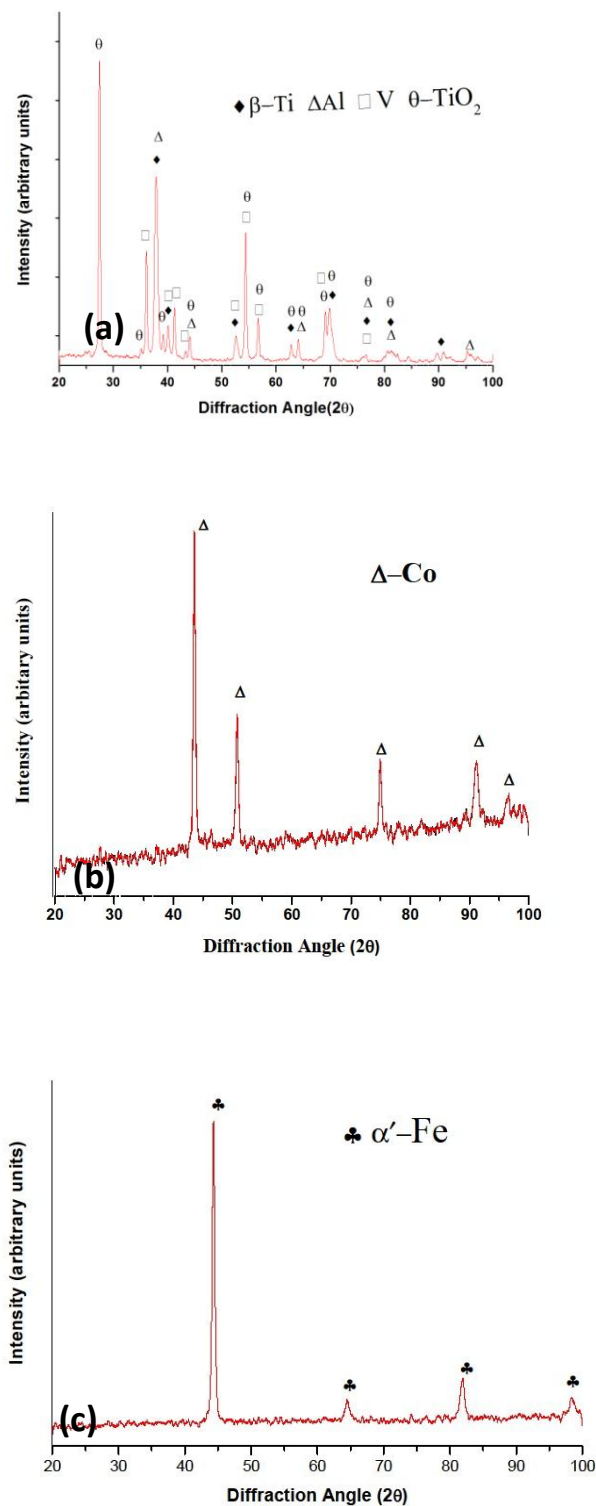


Fig. 4.9 X-ray diffraction patterns for substrate materials

(a) Ti-31 (b) Superco-605 (c) MDN-121

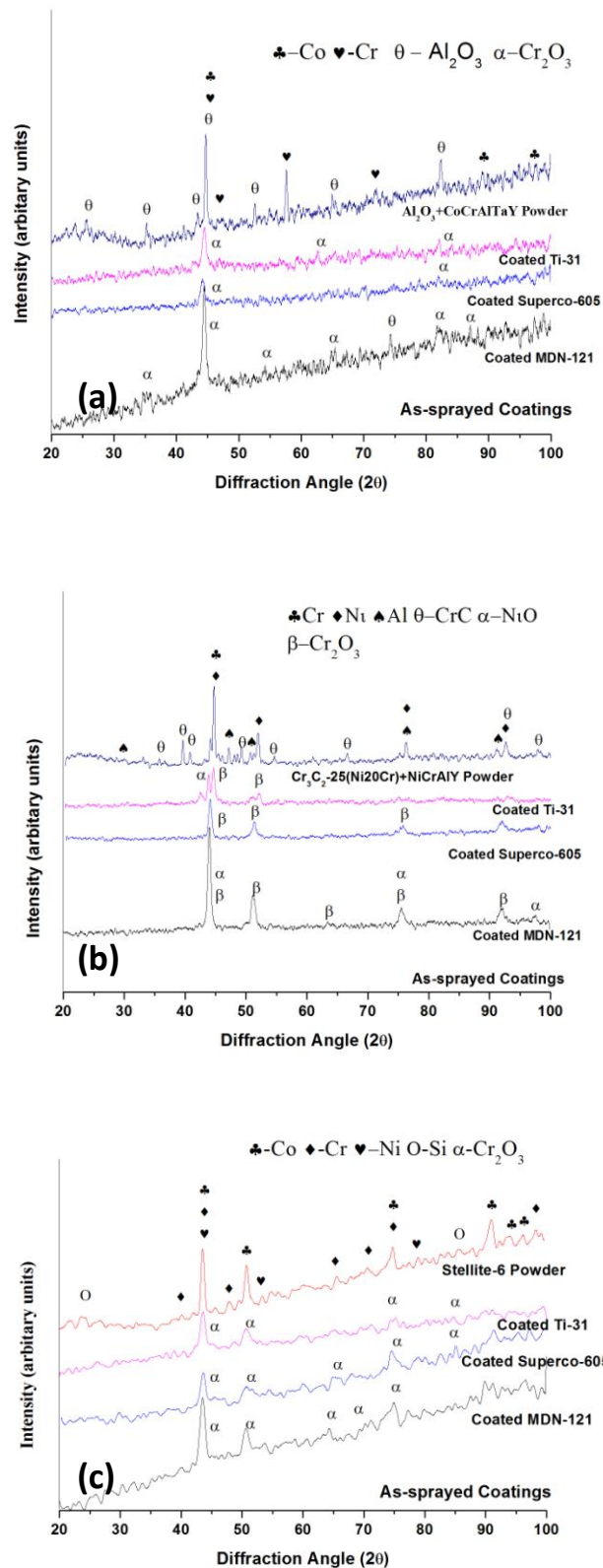


Fig. 4.10 X-ray diffraction patterns for powder and as-sprayed coatings
(a) 10% $\text{Al}_2\text{O}_3 + \text{CoCrAlTaY}$ (b) 25% $(\text{Cr}_3\text{C}_2\text{-}25(\text{Ni}_{20}\text{Cr})) + 75\% \text{NiCrAlY}$
(c) Stellite-6

The BSE image showing the cross-section microstructure of the coatings along with EDX compositional analyses at different locations is reported in Fig. 4.12. The coatings have a typical laminar structure. The coatings are deposited on a stationary substrate by moving the HVOF gun and the required thickness of the coating is achieved by varying number of passes. Hence, each layer of the coating is supposed to represent one pass of the HVOF deposition over the previous one. In the images, the dark areas correspond to porosity and voids. Very thin streaks of oxides appear to be oriented parallel to the substrate. Some dark areas appearing at the coating-substrate interface are the inclusions induced during grit blasting of alumina while preparing the surface for HVOF spraying.

The cross sectional microstructure of the 10%Al₂O₃+CoCrAlTaY coating (Fig. 4.12 a) shows the presence of partially melted splats, rich in cobalt and chromium content as assessed by EDX analysis. The microstructure of 25% (Cr₃C₂-25(Ni20Cr)) + 75% NiCrAlY coating (Fig. 4.12 b) show the layered structure, which is rich in nickel and enveloping the chromium carbide splats. The EDX analysis of Stellite-6 coating (Fig. 4.12 c) shows the homogeneous distribution of cobalt and chromium in splats. Coating seems to be laminar structure, built as a result of overlapping of individual splats.

4.8 EVALUATION OF FRACTURE TOUGHNESS

The fracture toughness or critical stress intensity factor (K_{IC}) is an important mechanical property required for the improved mechanical performance of structural materials (Thomas Wasik 2005 and George Dieter 1988). In this investigation indentation hardness method is used for estimating K_{IC} (Niihara 1983). The method uses Vickers microhardness test facility. A normal load of 2 kgf is used. The length of the crack generated during indentation is measured using SEM micrographs. A schematic diagram of crack generated during indentation is shown Fig.4.13. In Fig. 4.13, “a” is called as radial crack length, d is half diagonal length and c is crack radius measured from the center of the indentation. Based on the relative values of c/d, two types of cracks are observed during the indentation.

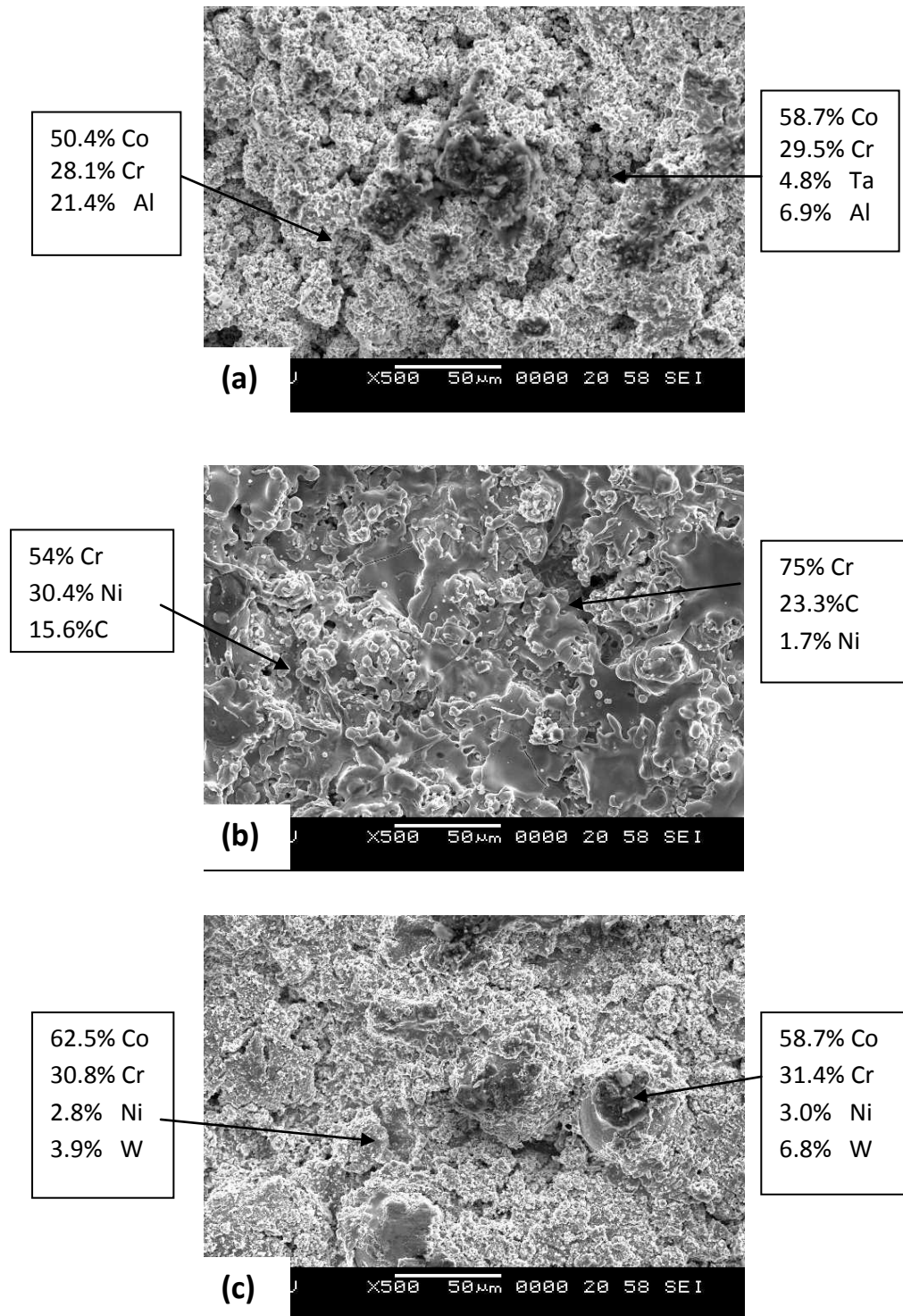


Fig. 4.11 SEM/EDX analysis on surface of as-sprayed coating showing coating morphology and elemental composition (wt. %) at selected points in the coating (a) 10% Al_2O_3 +CoCrAlTaY (b) 25% $(\text{Cr}_3\text{C}_2$ -25(Ni20Cr))+75% NiCrAlY (c) Stellite-6

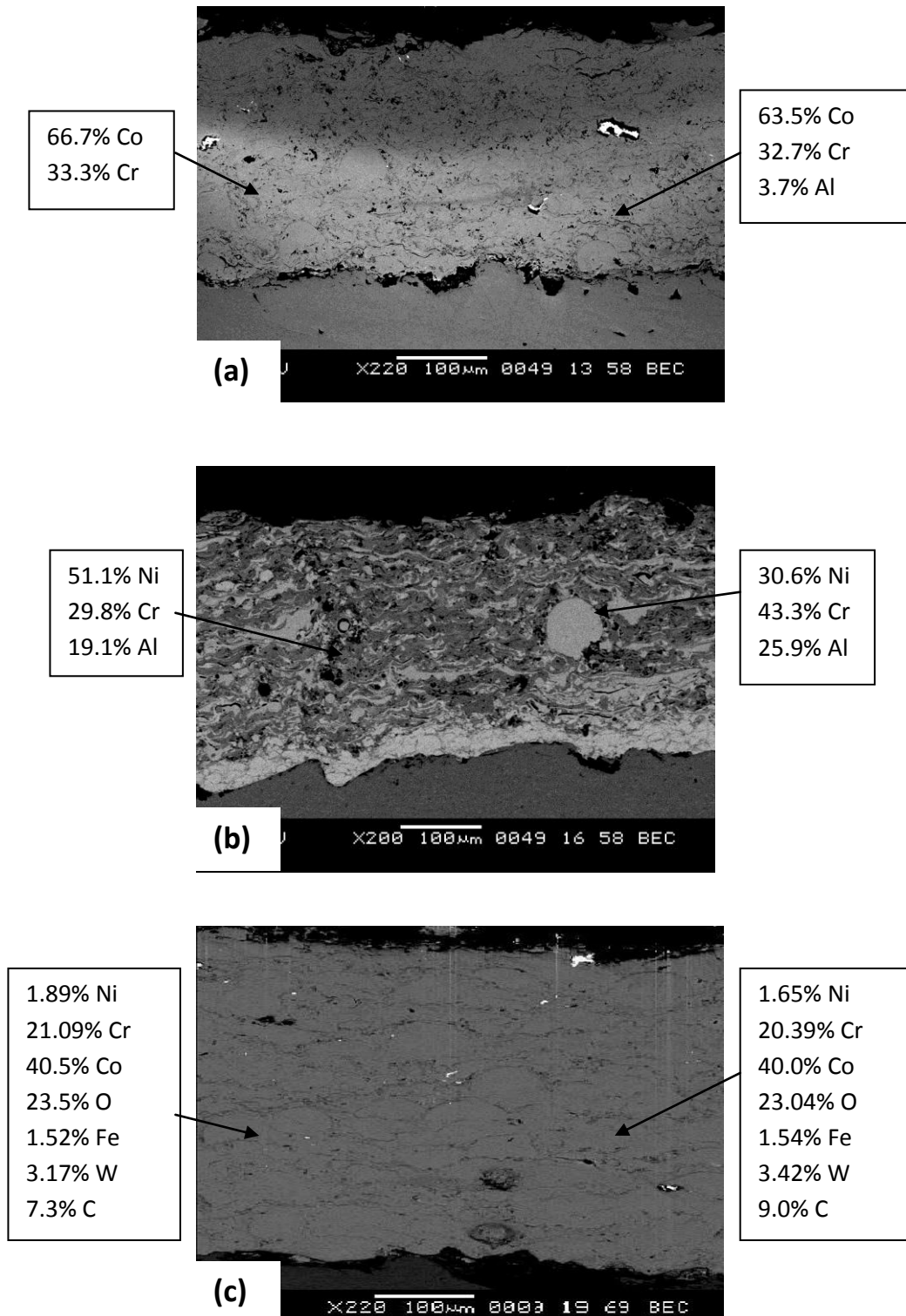


Fig. 4.12 Back scattered electron micrograph and EDX analysis (wt%) across the cross-section of the as-sprayed coatings: (a) 10%Al₂O₃+CoCrAlTaY (b) 25% (Cr₃C₂-25(Ni20Cr))+75%NiCrAlY (c) Stellite-6

When $c/d \leq 2.5$ the crack is called as Palmqvist crack and $c/d \geq 2.5$ the crack is called as Half penny crack. The fracture toughness is calculated using the following equations (Mingxiang et al. 2013).

$$K_{IC} = 0.0193(Hvd) (E/Hv)^{2/5} (a)^{-1/2} \quad (c/d \leq 2.5) \text{ Palmqvist cracks}$$

$$K_{IC} = 0.0711(Hvd^{1/2}) (E/Hv)^{2/5} (c/d)^{-3/2} \quad (c/d \geq 2.5) \text{ Half penny cracks}$$

Where Hv is the Vickers hardness, E is the Young's modulus, Fig. 4. 14 show the typical indentations on transverse section with in-plane cracks for three coatings, 10%Al₂O₃ + CoCrAlTaY, 25% Cr₃C₂-25(Ni20Cr)+ 75% NiCrAlY and Stellite-6 in sequence from top to bottom. Table 4.5 shows the estimated fracture toughness values for above three coatings on Ti-31substrate.

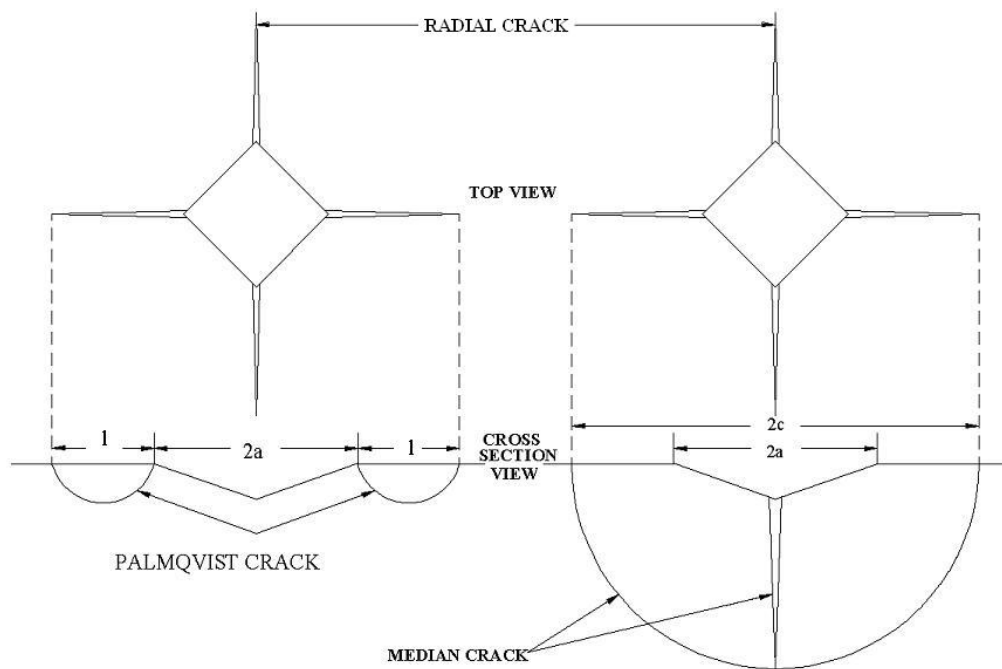


Fig. 4.13 Comparison of geometries of Palmqvist and median cracks around Vickers indentation (Niihara 1983).

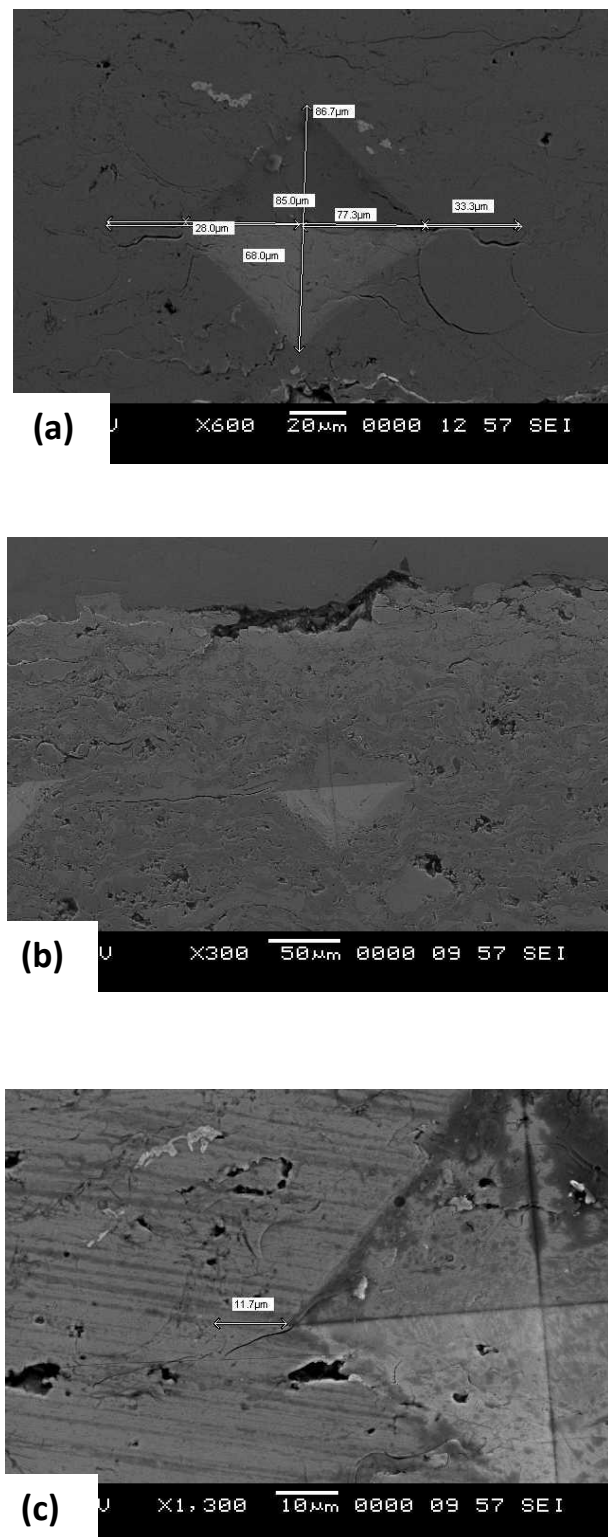


Fig. 4.14 Back scattered electron image of indentation on the as-sprayed coatings: (a) 10%Al₂O₃+CoCrAlTaY (b) 25% (Cr₃C₂-25(Ni₂₀Cr)) +75% NiCrAlY (c) Stellite-6.

Table 4.5 Vickers microhardness, Young's modulus and fracture toughness of sprayed coatings. (Young's modulus is taken from www.matweb.com).

Coating type	Vickers Micro hardness (Hv)	Young's Modulus (GPa)	Fracture Toughness K_{IC} (MPa m ^{1/2})
10% Al ₂ O ₃ + CoCrAlTaY	580	325	5.6
25% (Cr ₃ C ₂ -25(Ni20Cr)) +75% NiCrAlY	580	323	6.18
Stellite-6	980	207	10.54

CHAPTER 5

HOT CORROSION STUDIES

This chapter describes the hot corrosion behaviour of the HVOF coated as well as the uncoated substrate materials in an aggressive environment of molten salt (Na_2SO_4 -50% V_2O_5) at 800 °C under cyclic conditions. The reaction rate and kinetics have been studied by means of thermogravimetric. The identification and structural investigation of reaction products of the corroded specimens are made of the XRD and SEM/EDX.

5.1 UNCOATED SAMPLES

5.1.1 Visual observations

The macrographs of samples of Ti-31, Superco-605, and MDN-121 which were subjected to hot corrosion in Na_2SO_4 - 50% V_2O_5 molten salt for 50 cycles at 800 °C are shown in Fig. 5.1. It is to be noted that there was formation of oxide scales on the surface of Ti-31 from the first cycle itself; on the 23rd cycle the surface appeared to be brownish. Severe spalling of oxide scales was observed from 31st cycle onwards. The surface of Superco-605 appeared to be grey in color. The surface of the MDN-121 was shiny grey in color.

5.1.2 Thermogravimetric studies

The plots of cumulative weight gain (mg/cm^2) as a function of time expressed in number of cycles are shown in Fig. 5.2. The weight gain for Ti-31 and MDN-121 at end of 50 cycles are found to be 75.79 and 2.69 mg/cm^2 respectively. Evidently the Ti-31 showed a maximum weight gain during the hot corrosion studies in a molten salt environment as compared to MDN-121. Superco-605 exhibited weight loss during the complete cycles of hot corrosion studies as a result of intense spalling and sputtering of the oxide scale formed on the surface which made it difficult to measure the overall weight gain.

5.1.3 X-ray diffraction analysis

The X-ray diffraction patterns of the top scale, after its exposure to the salt environment at 800 °C for 50 cycles are shown in Fig. 5.3. The scale on Ti-31 surface under study consisted of TiO_2 , Al_2O_3 , $\text{V}_3\text{Ti}_6\text{O}_{17}$, TiVO_4 , and AlVO_4 as major phases and TiVO_4 , AlV_2O_4 as minor phases.

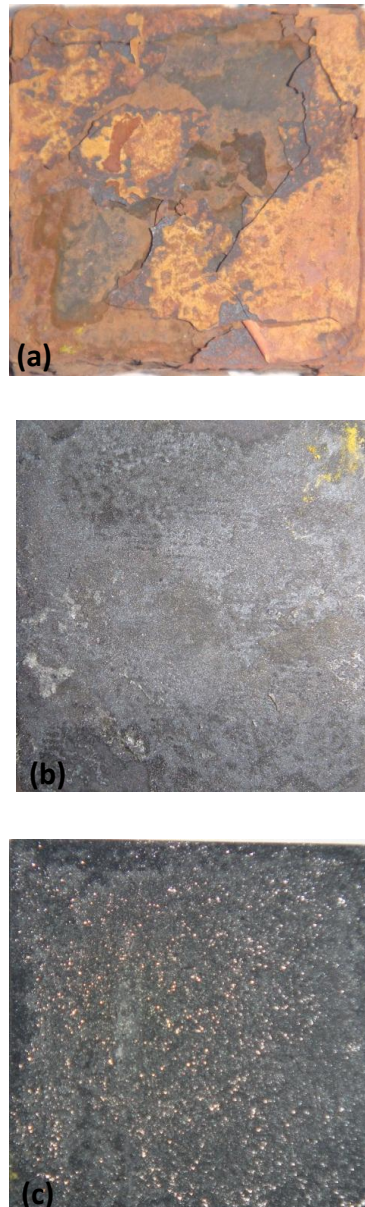


Fig. 5.1 Macrograph of uncoated samples (25mm X 25mm X 5 mm) after 50 cycles of hot corrosion under Na_2SO_4 -50wt% V_2O_5 salt environment at 800 °C (a) Ti-31 (b) Superco-605 (c) MDN- 121.

The Superco-605 consisted of CoO, Cr₂O₃, NiO, Na₂O as major phases and WO₃, SO₂, SiO₂ as minor phases and Ni₃V₂O₈, CrVO₄, FeVO₄ and Na₄FeO₃ spinals. Whereas MDN-121 showed phases such as FeO, Cr₂O₃, SO₃, V₂O₅ as major phases and CrVO₄, FeVO₄, and FeS₂ as minor phases.

5.1.4 SEM/EDX analysis

The SEM micrograph showing the morphology of scales along with the EDX analysis is illustrated in Fig. 5.4. Figure 5.4a shows TiO₂ (varying from 54 to 93 wt%) as the main constituent of the surface layer of the corroded Ti-31 and small amount of Al₂O₃ (2.7%). In isolated places alumina content is high (40%). Figure 5.4b shows the CoO (33.7%) and Cr₂O₃ (22.7%) as the main constituent of the surface layer of the corroded Superco-605. About 17% each of sodium oxides and sulfur containing oxides are observed at isolated places. Figure 5.4c shows FeO (69.4%) and Cr₂O₃ (20.2%) as the main constituent of the surface layer of the corroded MDN-121.

5.2 10% Al₂O₃+CoCrAlTaY COATING

5.2.1 Visual observations

The macrographs of the HVOF sprayed 10% Al₂O₃+CoCrAlTaY coatings on the Ti-31, MDN-121 and Superco-605 materials subjected to hot corrosion in Na₂SO₄-50% V₂O₅ molten salt for 50 cycles at 800 °C are shown in Fig. 5.5. Shining surface over black background is observed on the corroded surface of coated Ti-31 during the 9th cycle which has changed to web kind of appearance in the very next cycle i.e. the 10th cycle and from 39th cycle onwards greenish color is observed with expansion of the colored area over the coating surface. Slight cracks are observed during the 47th cycle of the hot corrosion test. In coated Superco-605 material, the green colored shining surface is observed from the 14th cycle which then converted to grey color during its 34th cycle.

In the case of coated MDN-121 steel, during the 16th cycle of the hot corrosion test, greenish color is observed which remained as green throughout the hot corrosion cycles.

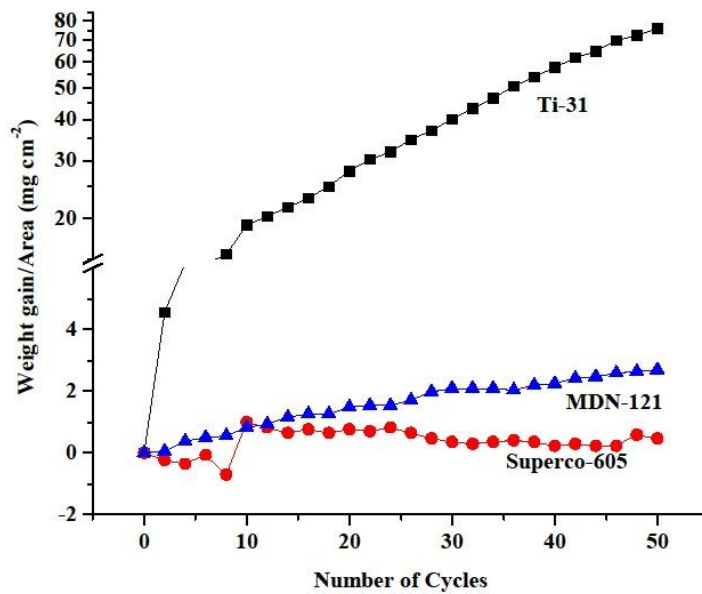


Fig. 5.2 Plot of weight gain/area versus number of cycles for uncoated samples subjected to hot corrosion.

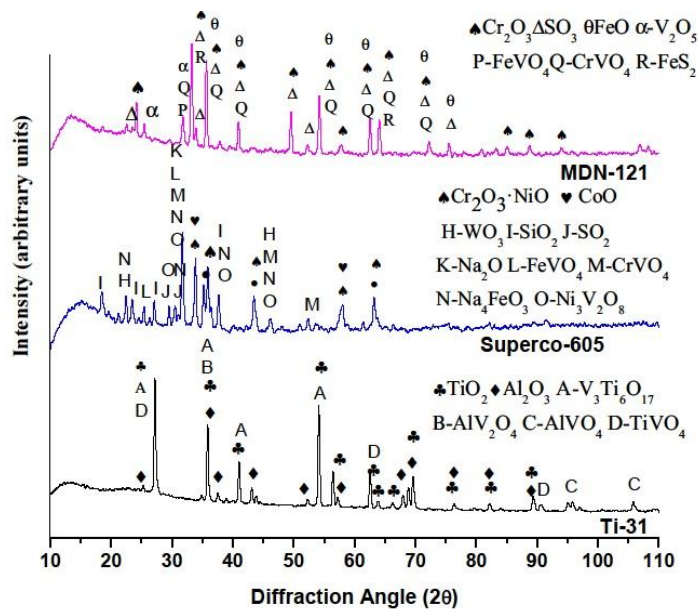


Fig. 5.3 X-ray diffraction patterns for uncoated substrate materials subjected to hot corrosion in Na₂SO₄-50% V₂O₅ for 50 cycles at 800 °C.

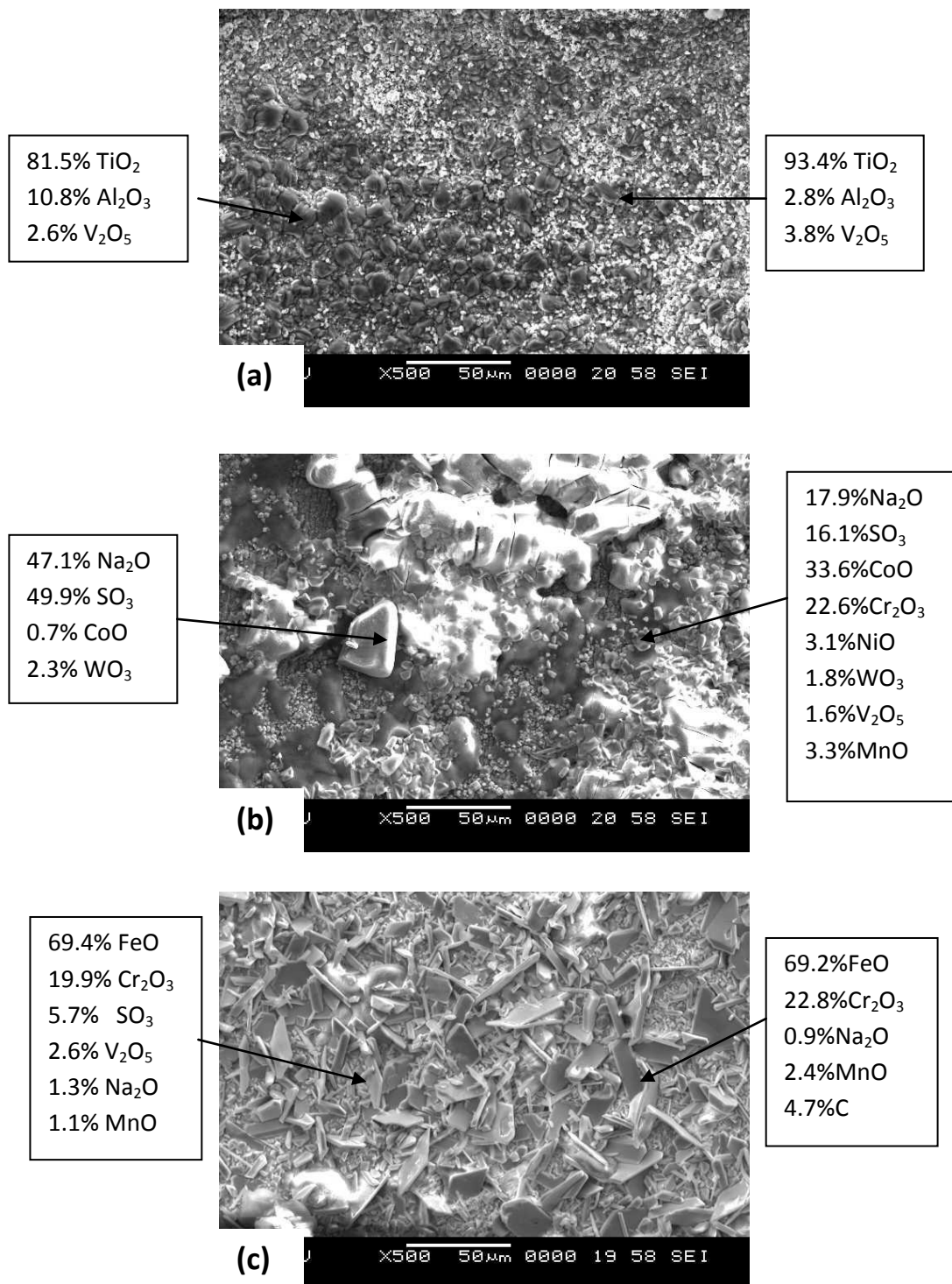


Fig. 5.4 SEM/EDX analysis for uncoated substrate materials subjected to hot corrosion for 50 cycles in $\text{Na}_2\text{SO}_4+50\%\text{V}_2\text{O}_5$ at 800 °C (a) Ti-31 (b) Supercor-605 (c) MDN-121.

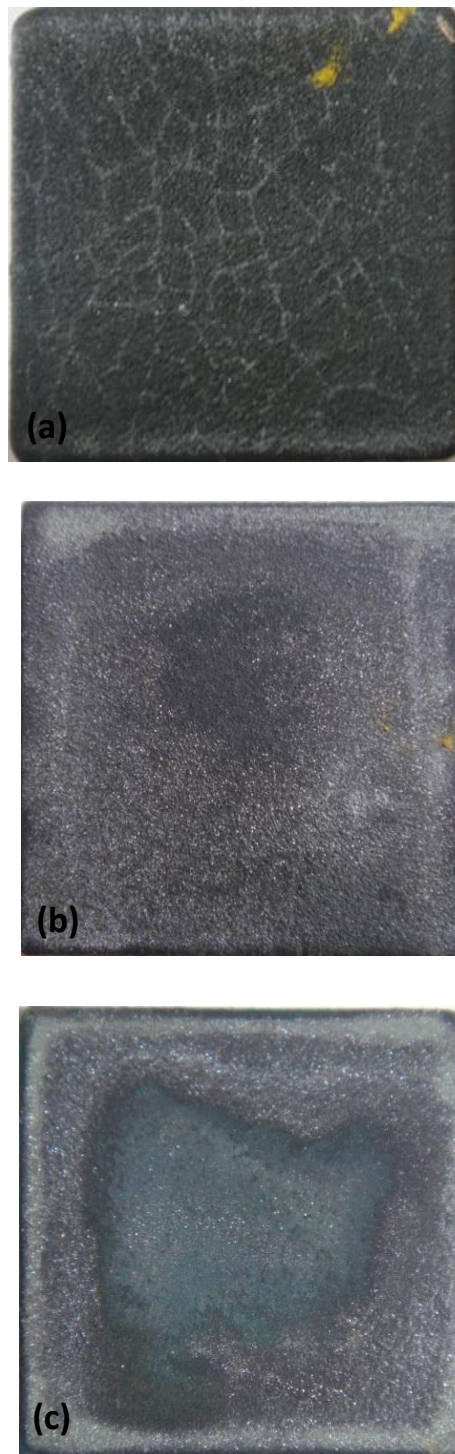


Fig. 5.5 Macrographs of 10% $\text{Al}_2\text{O}_3+\text{CoCrAlTaY}$ coating (25mm X 25mm X 5 mm) subjected to hot corrosion in $\text{Na}_2\text{SO}_4-50\%\text{V}_2\text{O}_5$ environment at 800 °C for 50 cycles (a) Ti-31 (b) Superco-605 (c) MDN-121.

5.2.2 Thermogravimetric studies

The plots of cumulative weight gain (mg/cm^2) as a function of time expressed in number of cycles are shown in Fig. 5.6. The values of overall weight gain after 50 cycles of hot corrosion, for the 10% $\text{Al}_2\text{O}_3+\text{CoCrAlTaY}$ coated Ti-31, Superco-605 and MDN-121 are found to be $10.3 \text{ mg}/\text{cm}^2$, $2.2 \text{ mg}/\text{cm}^2$ and $1.11 \text{ mg}/\text{cm}^2$ respectively.

5.2.3 X-ray diffraction analysis

The X-ray diffraction patterns of the top scale, after its exposure to salt environment at 800°C for 10% $\text{Al}_2\text{O}_3+\text{CoCrAlTaY}$ coated substrates for 50 cycles are shown in Fig 5.7. The scale on oxide coated on Ti-31, Superco-605 and MDN-121 surfaces under study consisted of CoO , Cr_2O_3 , $\alpha\text{-Al}_2\text{O}_3$, and V_2O_5 as major phases. The coated surfaces also consisted of AlVO_4 , CoCr_2O_4 , CoAl_2O_4 , and CrVO_3 spinals, as minor phases.

5.2.4 SEM/EDX analysis

The morphologies of the corroded 10% $\text{Al}_2\text{O}_3+\text{CoCrAlTaY}$ coated samples along with EDX analysis are shown in Fig. 5.8. The matrix has relatively higher concentration of oxides of Co, Cr and Al.

A typical cross-sectional micrograph for the 10% $\text{Al}_2\text{O}_3+\text{CoCrAlTaY}$ coated and hot corroded sample is presented for the case of MDN-121 steel substrate (Fig.5.9). The back scattered electron image presented in Fig. 5.9 shows a discontinuous and fragmented oxide scale formed on the uppermost surface and EDX analysis on this scale (Point 1) revealed oxides of Co, Cr and Al as the main constituent. A high value of O at point 3 is possibly due to EDX signal from Al_2O_3 particle present in the splat. Fig. 5.10 shows X-ray mapping of the cross section for major elements in the coating after hot corrosion studies. The mapping shows that a thin layer of coating is oxidized and consists high fraction of Al_2O_3 .

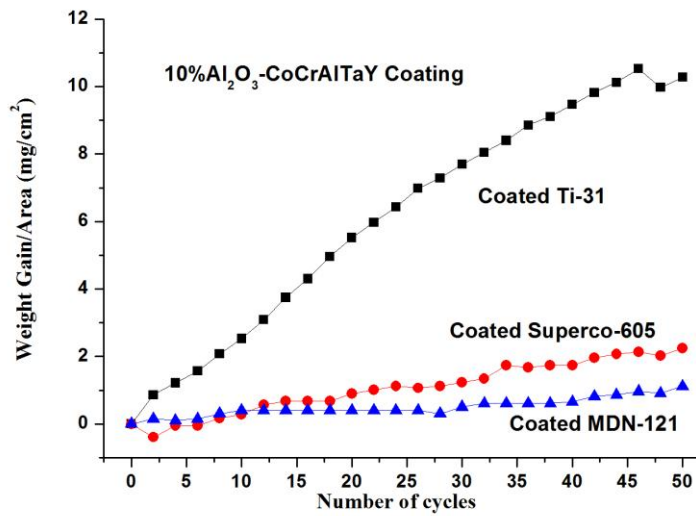


Fig. 5.6 Plot of weight change versus number of cycles for 10% Al₂O₃ + CoCrAlTaY coated materials subjected to hot corrosion in Na₂SO₄-50%V₂O₅ salt environment at 800 °C.

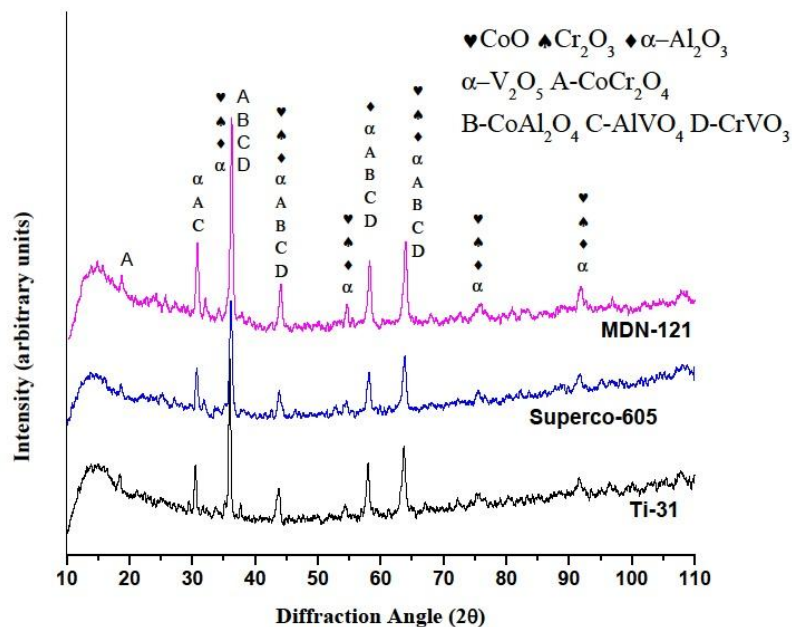


Fig. 5.7 X-ray diffraction patterns for 10% Al₂O₃+CoCrAlTaY coated Ti-31, Superco-605 and MDN-121 subjected to hot corrosion in Na₂SO₄-50%V₂O₅ at 800 °C

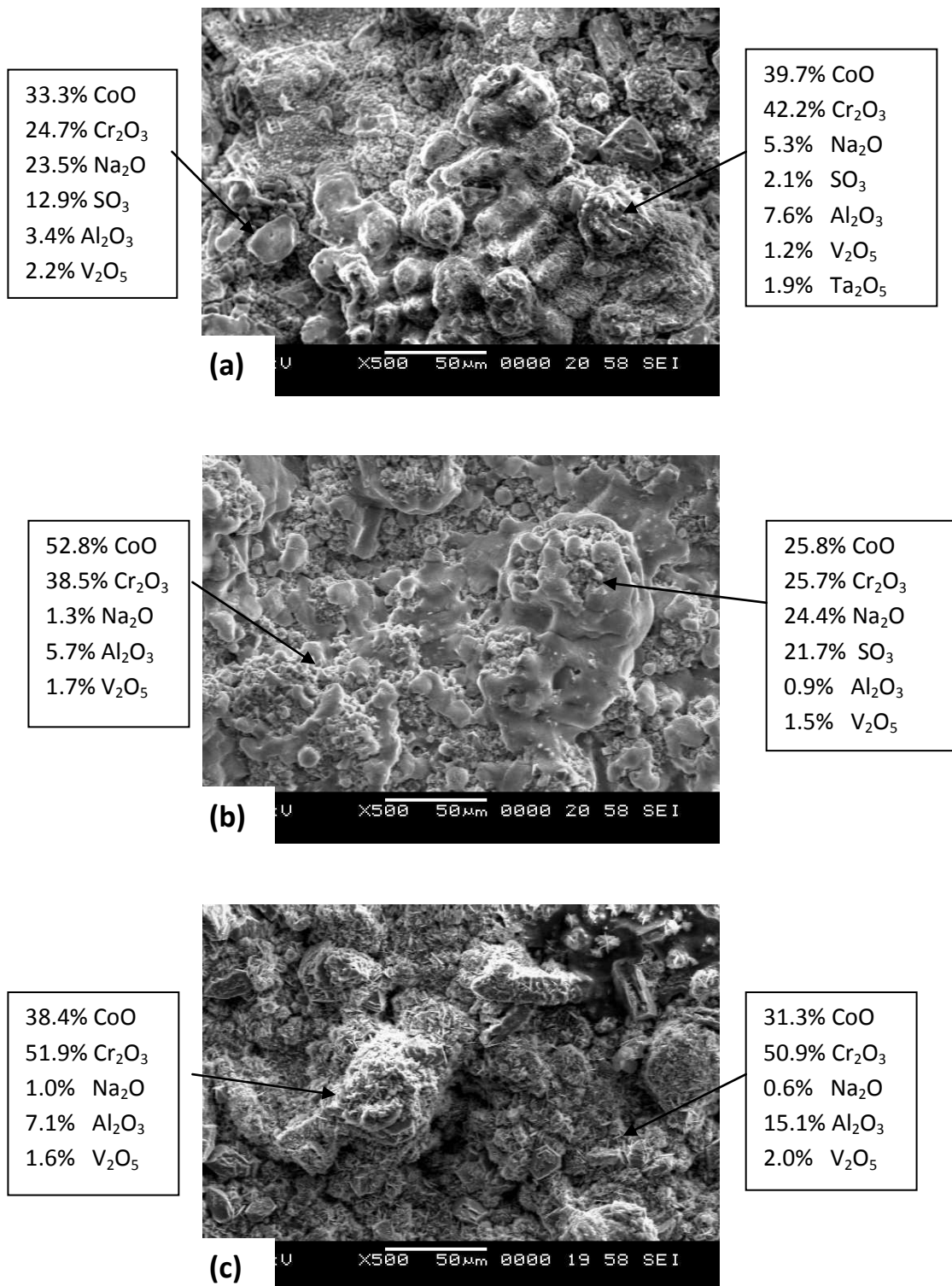


Fig. 5.8 SEM/EDX point analysis for 10% Al₂O₃+CoCrAlTaY coated samples subjected to hot corrosion in Na₂SO₄+50%V₂O₅ at 800 °C (a)Ti-31 (b) Superco-605 (c) MDN- 121.

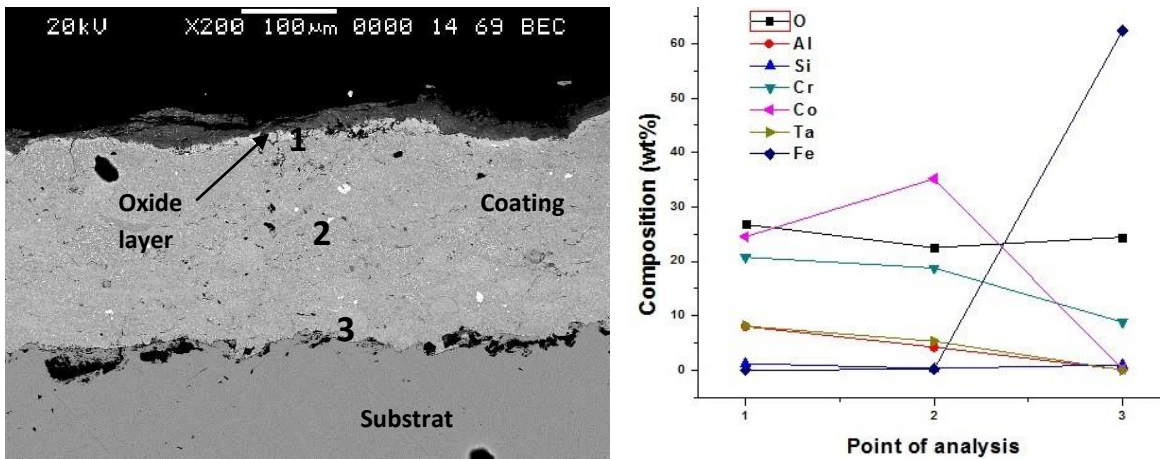


Fig. 5.9 Back scattered image and EDX analysis of across the cross-section of the 10% Al_2O_3 +CoCrAlTaY coated MDN-121 material subjected to hot corrosion for 50 cycles in Na_2SO_4 +50% V_2O_5 at 800 °C.

5.3 25% (Cr_3C_2 -25(Ni20Cr)) + 75%NiCrAlY COATING

5.3.1 Visual observations

The macrographs of the HVOF sprayed 25% (Cr_3C_2 -25(Ni20Cr)) + 75% NiCrAlY coatings on the Ti-31, Superco-605 and MDN-121 which are subjected to hot corrosion in Na_2SO_4 -50% V_2O_5 environment for 50 cycles at 800 °C are illustrated in Fig. 5.11. In all three cases, the colour of the as-sprayed coating was light grey which turned into brownish colour during the first cycle of exposure to salt environment.

5.3.2 Thermogravimetric studies

The plots of cumulative weight gain (mg/cm^2) as a function of time expressed in number of cycles for 25% (Cr_3C_2 -25(Ni20Cr)) + 75% NiCrAlY coating are shown in Fig. 5.12. The values of overall weight gain after 50 cycles of hot corrosion for 25% (Cr_3C_2 -25(Ni20Cr)) + 75% NiCrAlY coated Ti-31, Superco-605 and MDN-121 are found to be 1.37, 1.25 and 1.20 mg/cm^2 respectively. Evidently, the coated MDN-121 showed a lower weight gain during the initial stages of hot corrosion studies in molten salt environment as compared to the Ti-31 and Superco-605.

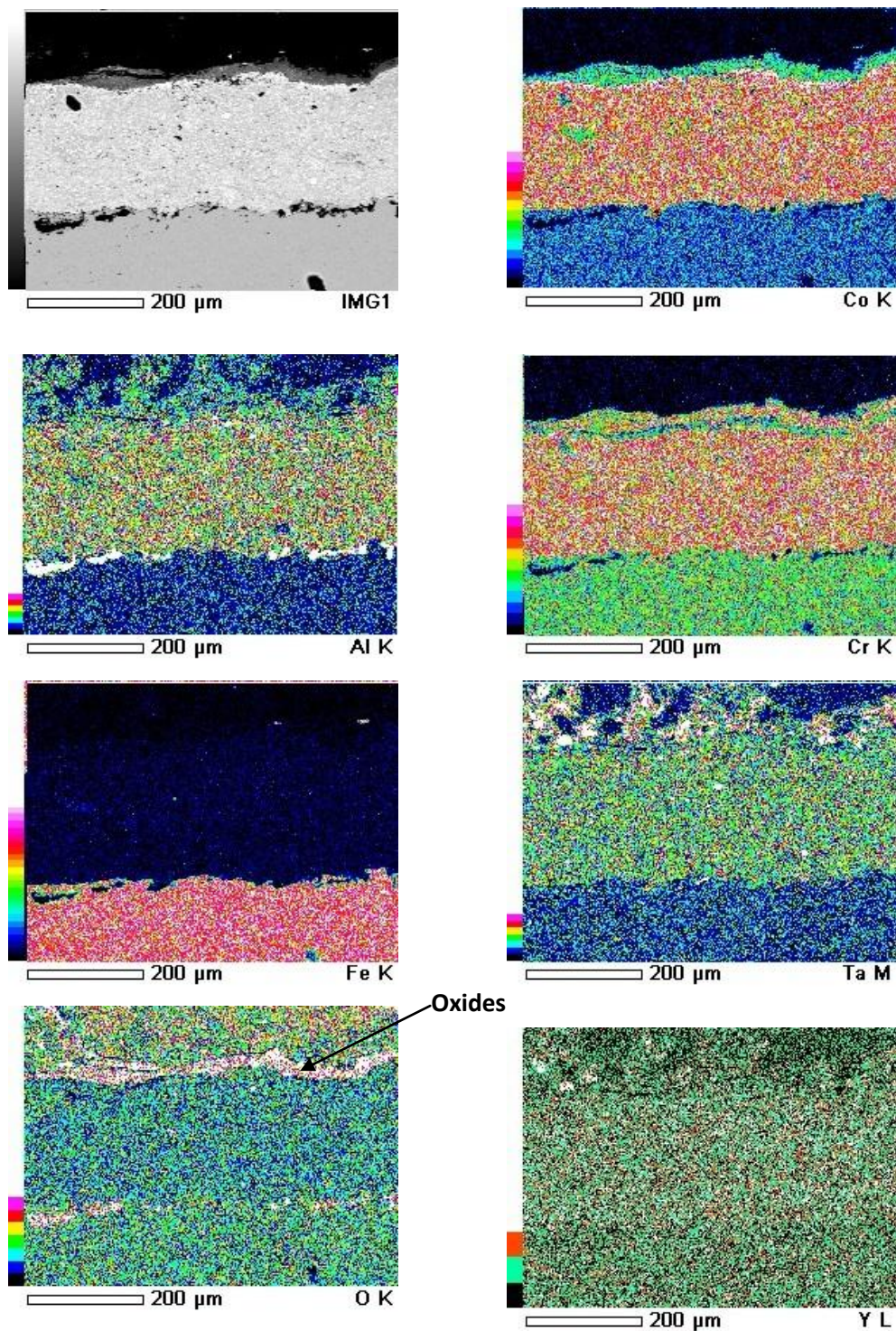


Fig. 5.10 X-ray mapping along the cross-section of the 10% Al_2O_3 +CoCrAlTaY coated MDN-121 material subjected to hot corrosion for 50 cycles in Na_2SO_4 + 50% V_2O_5 environment at 800 °C.

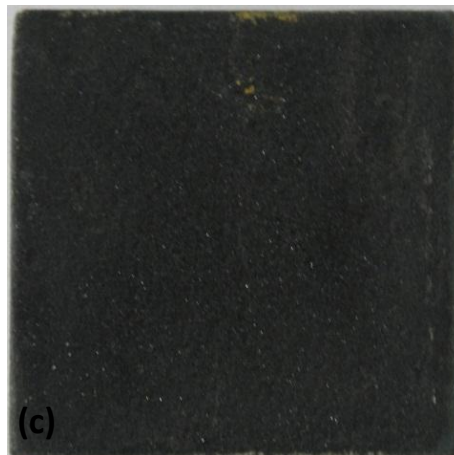
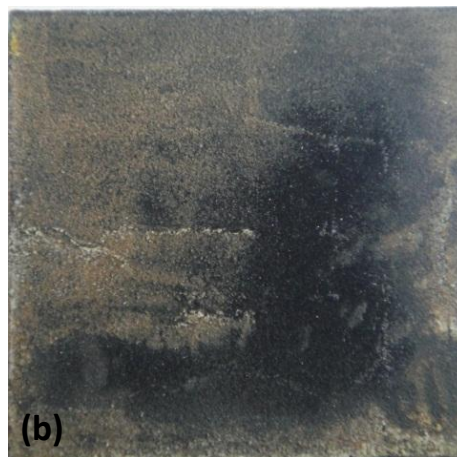
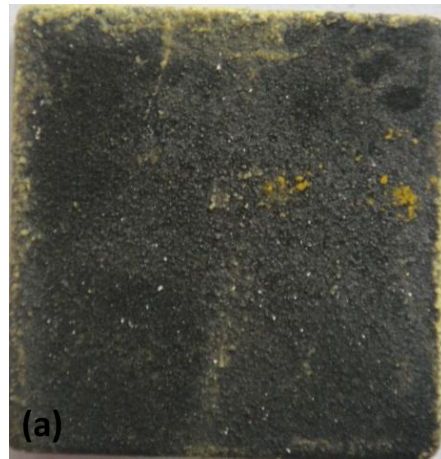


Fig. 5.11 Macrographs of 25% (Cr_3C_2 -25(Ni20Cr)) + 75% NiCrAlY coating (25mm X 25mm X 5mm) subjected to hot corrosion in Na_2SO_4 -50% V_2O_5 environment at 800 °C for 50 cycles (a) Ti-31 (b) Superco-605 (c) MDN-121.

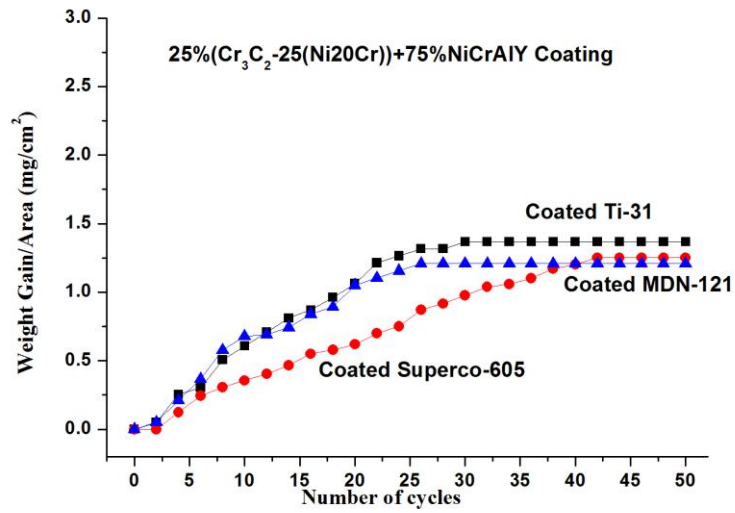


Fig. 5.12 Plot of weight gain/area versus number of cycles for 25% (Cr_3C_2 -25(Ni20Cr)) + 75% NiCrAlY coated samples subjected to hot corrosion.

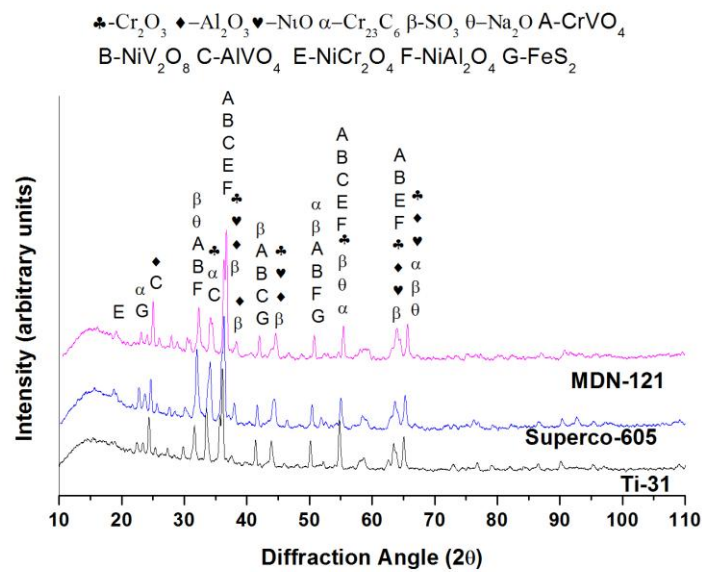


Fig. 5.13 X-ray diffraction patterns for 25% (Cr_3C_2 -25(Ni20Cr)) + 75%NiCrAlY coated Ti-31, Superco-605 and MDN-121 subjected to hot corrosion in Na_2SO_4 -50% V_2O_5 for 50 cycles at 800 °C.

5.3.3 X-ray diffraction analysis

The X-ray diffraction patterns of the top scale, after its exposure to the salt environment at 800 °C for 50 cycles for 25% (Cr_3C_2 -25(Ni20Cr)) + 75% NiCrAlY coated samples are shown in Fig. 5.13. The scale on all the coated samples under study consisted of Cr_2O_3 , and NiO are major phases and Al_2O_3 as minor phase. The samples also showed the presence of NiCr_2O_4 , Cr_{23}C_6 , AlVO_4 , AlV_2O_4 , NiCr_2O_4 , CrVO_4 and FeS_2 as minor phases.

5.3.4 SEM/EDX analysis

The morphologies of the corroded, 25% (Cr_3C_2 -25(Ni20Cr)) + 75% NiCrAlY coated materials along with EDX analysis are shown in Fig. 5.14. Cr_2O_3 and NiO are observed on all three coated surfaces as major phases. Coating on Ti-31 (Fig. 5.14a) shows Cr_2O_3 in the range of 54 to 82 wt%, and NiO about 5%. Sulphur contamination is also observed. Coating on Superco-605 (Fig. 5.14b) shows a thin oxide layer rich in Cr_2O_3 and NiO. Cr_2O_3 is in the range of 13 to 50% and NiO is in the range of 24 to 48%. Along with them small quantities of V_2O_5 are also observed. Similarly, corroded surface of coated MDN-121 (Fig. 5.14c) shows Cr_2O_3 in the range of 25 to 75% and NiO in the range of 17 to 46% as major phases. Small amounts of V_2O_5 , and FeO are also observed on the corroded surface. It may be noticed that the percentage of Cr_2O_3 has increased in the top region of the scale.

Cross-section microstructural analysis for the corroded, 25% (Cr_3C_2 -25(Ni20Cr)) + 75% NiCrAlY coated samples are done and a typical result is presented for the coated substrate Ti-31 in Fig. 5.15. A continuous and adherent oxide scale is formed on the top of the coating. It is continuous and dense even after 50 cycles of hot corrosion run. EDX analysis of corroded, 25% (Cr_3C_2 -25(Ni20Cr)) + 75% NiCrAlY coated Ti-31 (Fig. 5.15) shows the scale (point 1) is rich in oxides of Cr and Al. X-ray maps of the cross-section of hot corroded samples were done. X-ray maps of the scale formed on (25% (Cr_3C_2 -25(Ni20Cr)) + 75% NiCrAlY) HVOF coated Ti-31, after hot corrosion in Na_2SO_4 -50% V_2O_5 environment at 800 °C for 50 cycles are shown in Fig. 5.16. The maps show that a thin layer of coating is oxidized and consists of high fraction of Cr_2O_3 and Al_2O_3 . Further this analysis shows a higher

percentage of nickel at the interface between coating and substrate. This indicates that nickel is not oxidized.

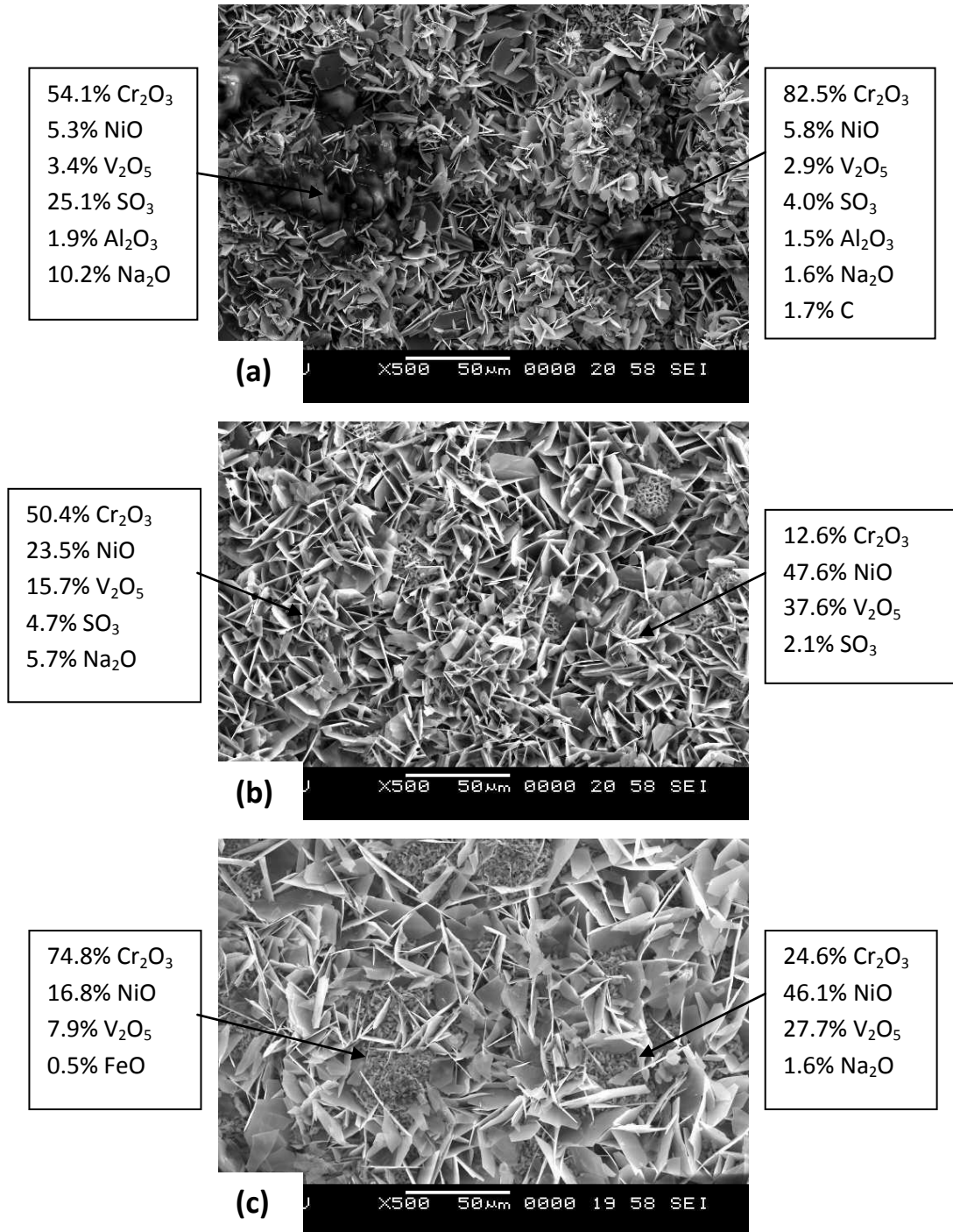


Fig. 5.14 SEM/EDX analysis for 25% (Cr₃C₂-25(Ni20Cr)) + 75%NiCrAlY coated samples subjected to hot corrosion for 50 cycles in Na₂SO₄+50% V₂O₅ at 800 ° C

(a) Ti-31 (b) Superco-605 (c) MDN-121.

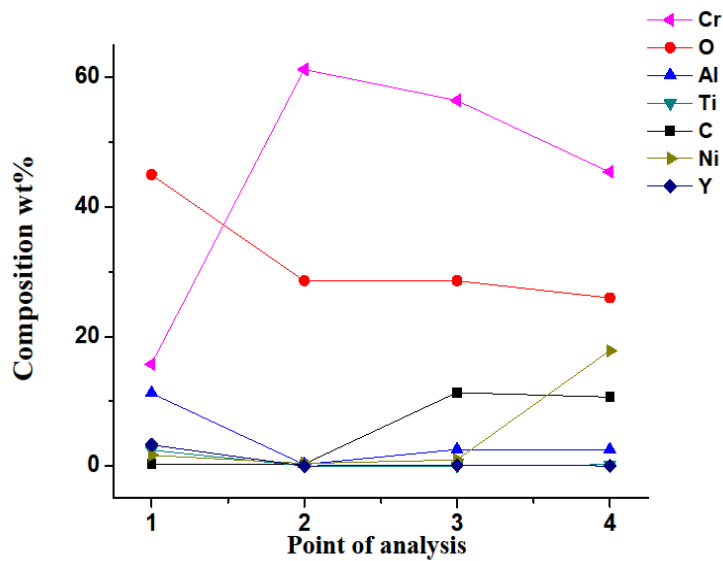
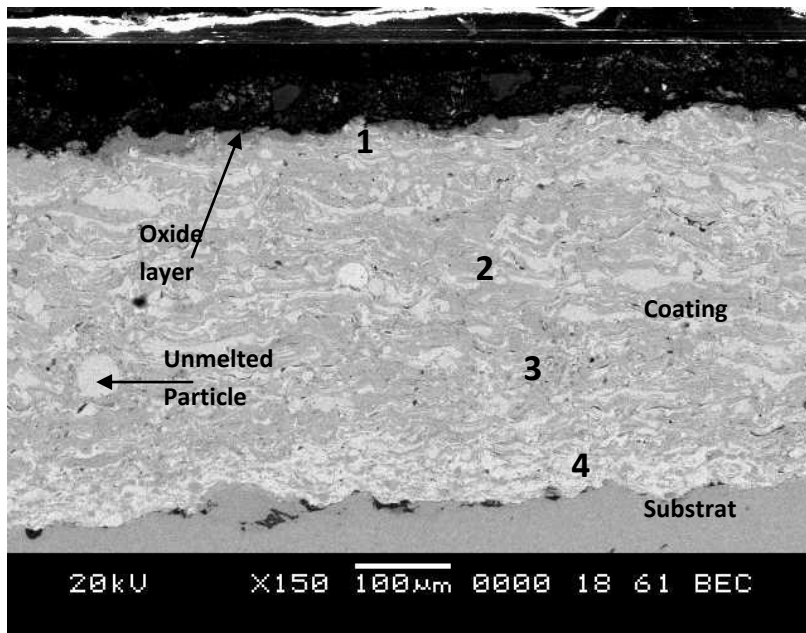


Fig. 5.15 Back scattered image and EDX analysis of the cross-section of the 25% (Cr_3C_2 -25(Ni20Cr)) + 75%NiCrAlY coated Ti-31 material subjected to hot corrosion for 50 cycles in Na_2SO_4 +50% V_2O_5 at 800 °C.

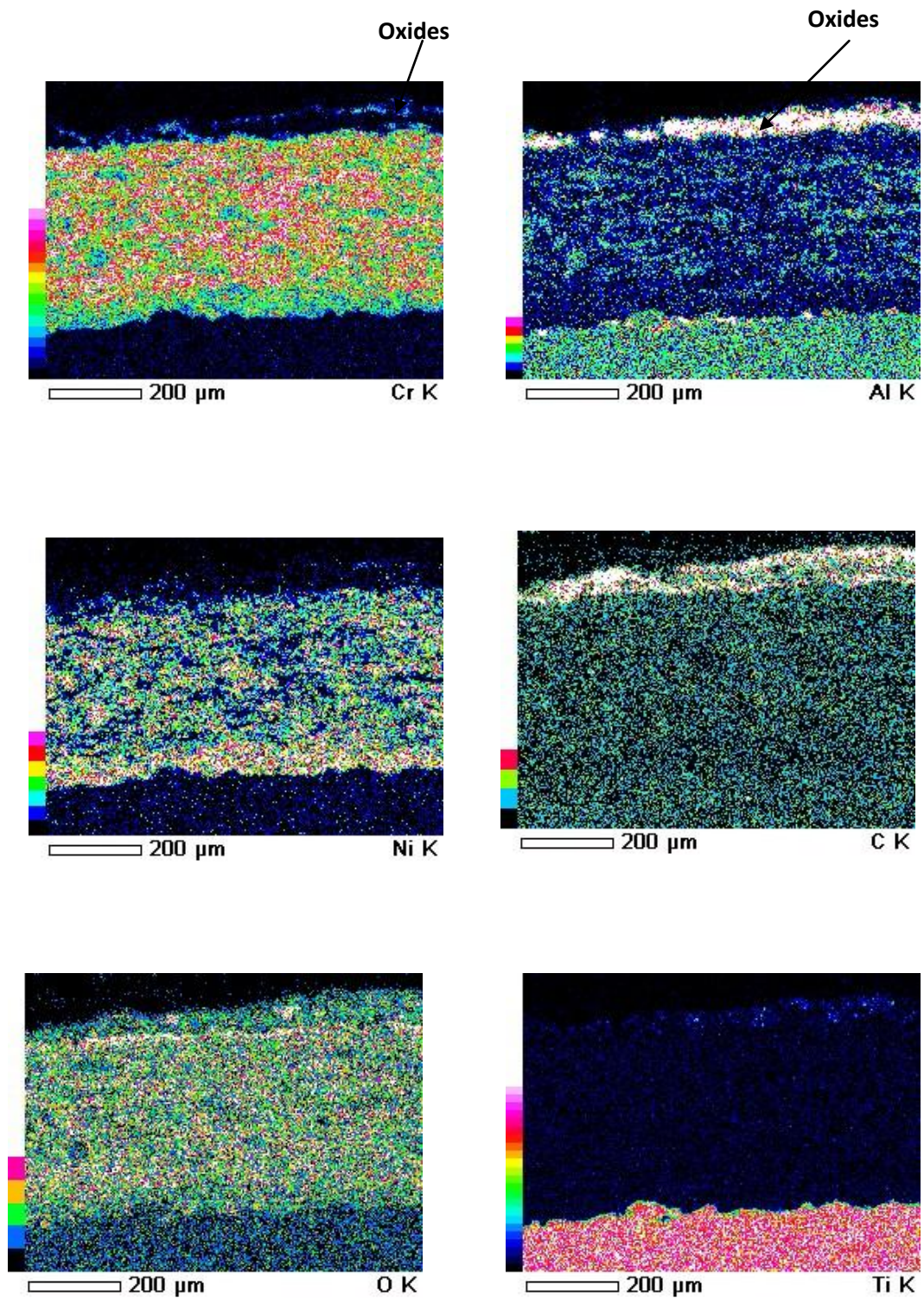


Fig. 5.16 X-ray mapping along the cross-section of the 25% (Cr_3C_2 -25(Ni20Cr)) + 75%NiCrAlY coated Ti-31 material subjected to hot corrosion for 50 cycles in Na_2SO_4 +50% V_2O_5 environment at 800 °C.

5.4 STELLITE-6 COATING

5.4.1 Visual observations

The macrographs of the HVOF sprayed Stellite-6 coatings on the Ti-31, Superco-605 and MDN-121 subjected to hot corrosion in Na_2SO_4 -50% V_2O_5 environment for 50 cycles at 800 °C are illustrated in Fig. 5.17. The colour of the as-sprayed coating was dark grey and it turned into black colour during the first cycle of exposure to salt environment.

5.4.2 Thermogravimetric studies

The plots of cumulative weight gain (mg/cm^2) as a function of time expressed in number of cycles are shown in Fig. 5.18. The values of overall weight gain after 50 cycles of hot corrosion for Stellite-6 coated Ti-31, Superco-605 and MDN-121 are found to be 8.11, 2.48 and 6.37 mg/cm^2 respectively. Evidently, the coated Ti-31 showed a maximum weight gain during the hot corrosion studies in molten salt environment and coated Superco-605 gained minimum weight gain.

5.4.3 X-ray diffraction analysis

The X-ray diffraction patterns of the top scale, after its exposure to the salt environment at 800 °C for Stellite-6 coated samples for 50 cycles are shown in Fig. 5.19. The scale on all the coated substrates under study consisted of CoO , Cr_2O_3 , NiO , V_2O_5 and FeO as major phases on the surface. The samples also showed the presence of CoCr_2O_4 , NiCr_2O_4 , CoAl_2O_4 , NiAl_2O_4 , AlV_2O_4 , AlVO_4 and FeVO_4 as minor phases.

5.4.4 SEM/EDX analysis

The morphologies of the corroded, Stellite-6 coated materials along with EDX analysis are shown in Fig. 5.20. The EDX analysis of hot corroded Stellite-6 coated scale shows the formation of CoO and Cr_2O_3 as major phases on all coated substrate materials. Coating on Ti-31 (Fig. 5.20a) shows Cr_2O_3 in the range of 20 to 39% and CoO range is 25 to 41.4%. Coating on Superco-605 (Fig. 5.20 b) shows Cr_2O_3 in the range of 1.6 to 28.8% and CoO in the range of 19 to 62% along with small quantities of SO_3 , V_2O_5 and Na_2O .

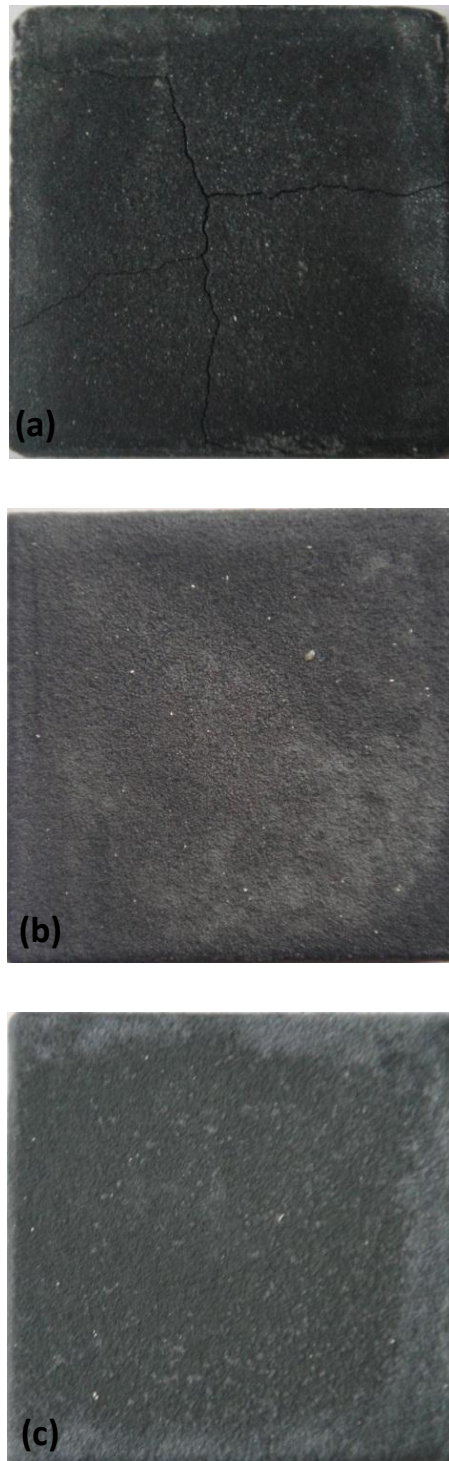


Fig. 5.17 Macrographs of Stellite-6 coated substrates subjected to hot corrosion in Na_2SO_4 -50% V_2O_5 environment at 800 °C for 50 cycles (a) Ti-31 substrate (b) Superco-605 substrate (c) MDN-121 substrate.

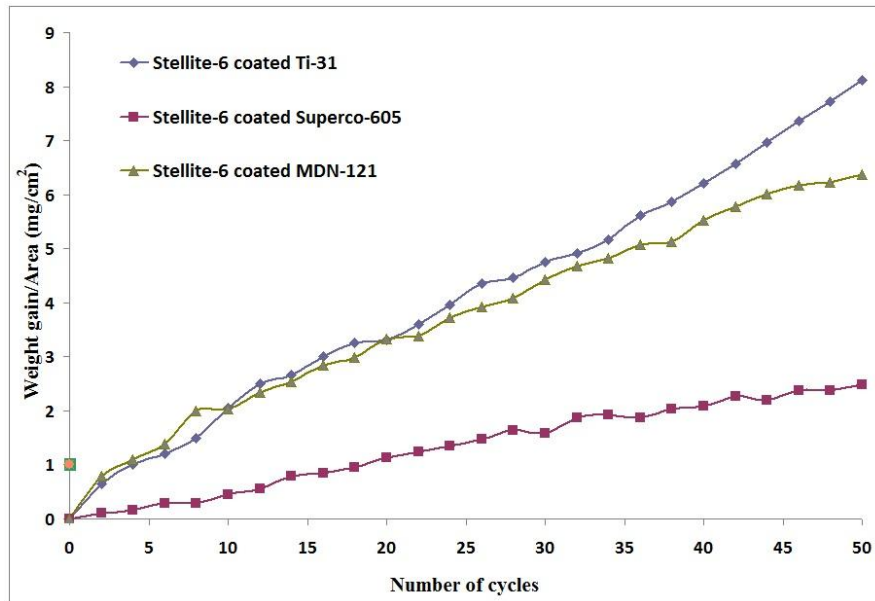


Fig. 5.18 Plot of weight gain/area versus number of cycles for Stellite-6 coated samples subjected to hot corrosion.

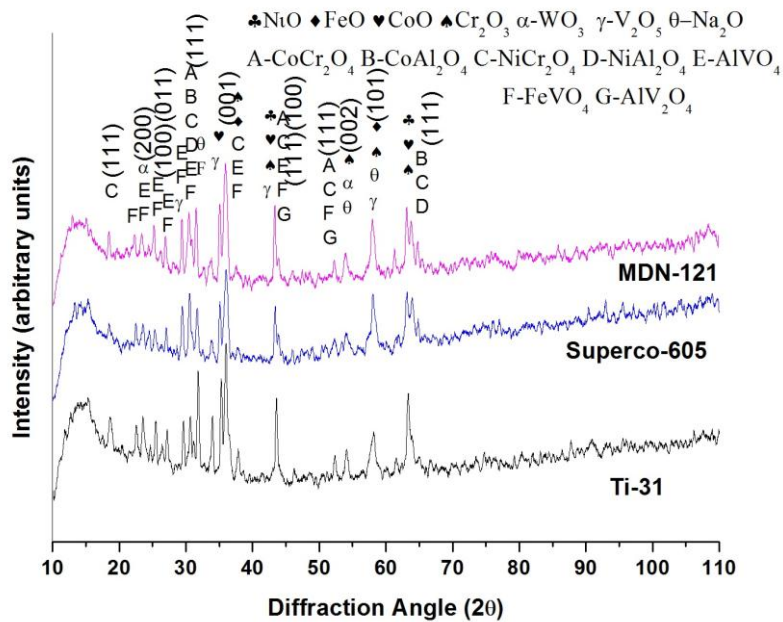


Fig. 5.19 X-ray diffraction patterns for Stellite-6 coated Ti-31, Superco-605 and MDN-121 subjected to hot corrosion in Na₂SO₄-50%V₂O₅ for 50 cycles at 800 °C.

Similarly, coating on MDN-121 (Fig. 5.20c) shows Cr_2O_3 in the range of 31 to 48% and CoO in the range of 48 to 60% as major phases with small amounts of V_2O_5 , FeO , SiO_2 , NiO and WO_3 . It may be noticed that the percentage of Cr_2O_3 is maximum in this scale.

Cross-section microstructural analysis for the corroded, Stellite-6 coated MDN-121 is shown in Fig. 5.21. A continuous and adherent oxide scale is formed on the coated substrate materials, which has retained the dense structure of the as sprayed coatings even after the hot corrosion run for 50 cycles. EDX analysis of corroded Stellite-6 coated MDN-121 (Fig. 5.21) shows that the top surface of the scale contains mainly oxides of Cr and Co.

X-ray maps of the cross-section of the hot corroded samples were done. X-ray maps of the scale formed on HVOF sprayed Stellite-6 on MDN-121, after hot corrosion in Na_2SO_4 -50% V_2O_5 environment at 800 °C for 50 cycles are shown in Fig. 5.22.

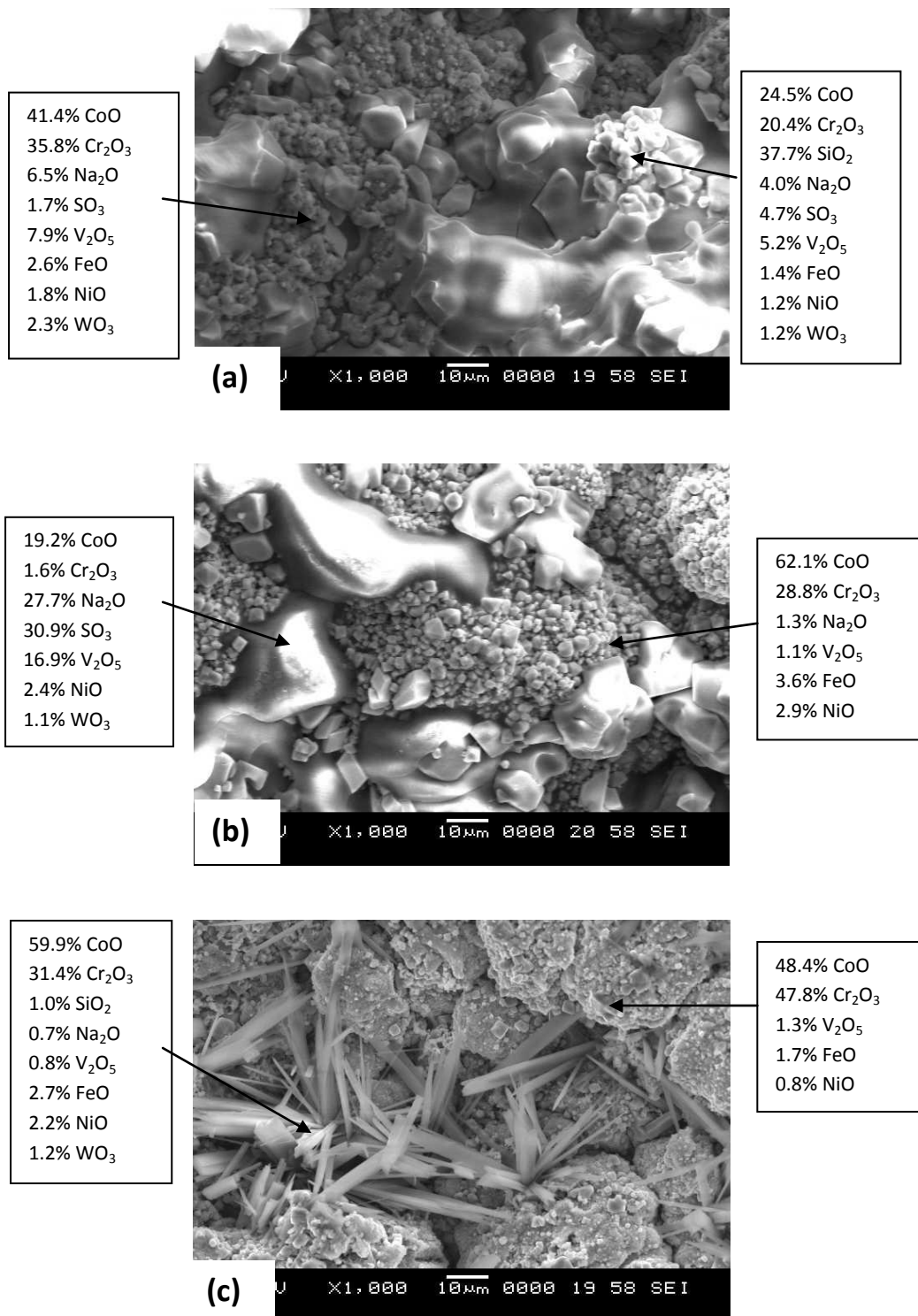


Fig. 5.20 SEM/EDX analysis of Stellite-6 coated samples subjected to hot corrosion for 50 cycles in Na₂SO₄+50%V₂O₅ at 800 °C (a) Ti-31 (b) Superco-605 (c) MDN- 121.

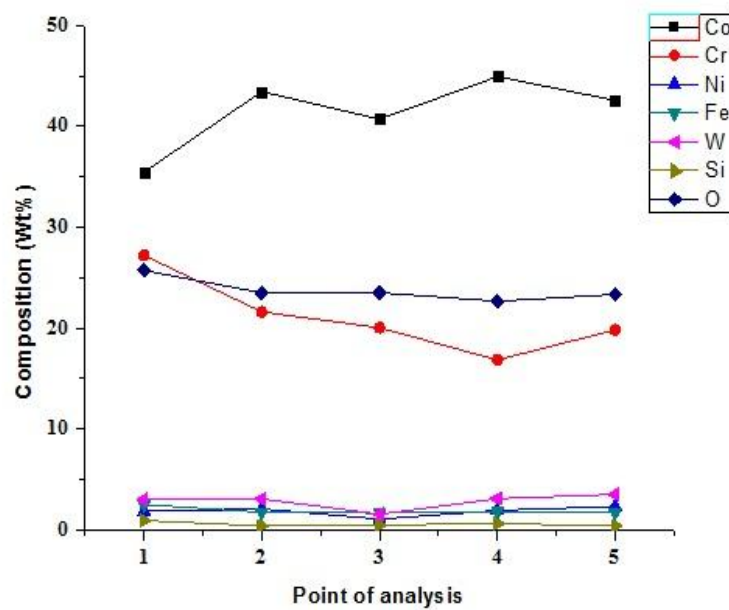
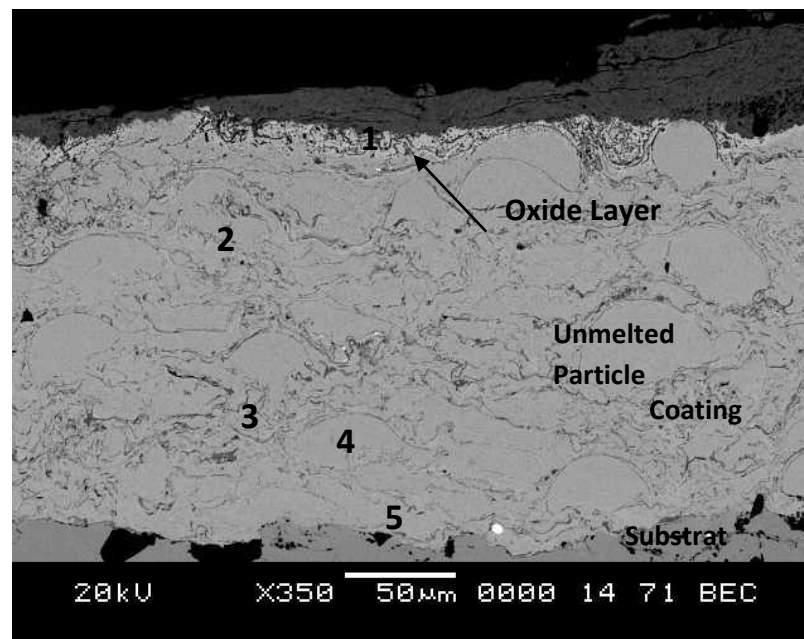


Fig. 5.21 Back scattered image and EDX analysis across the cross-section of the Stellite-6 coated MDN-121 material subjected to hot corrosion for 50 cycles in $\text{Na}_2\text{SO}_4+50\% \text{V}_2\text{O}_5$ at 800 °C.

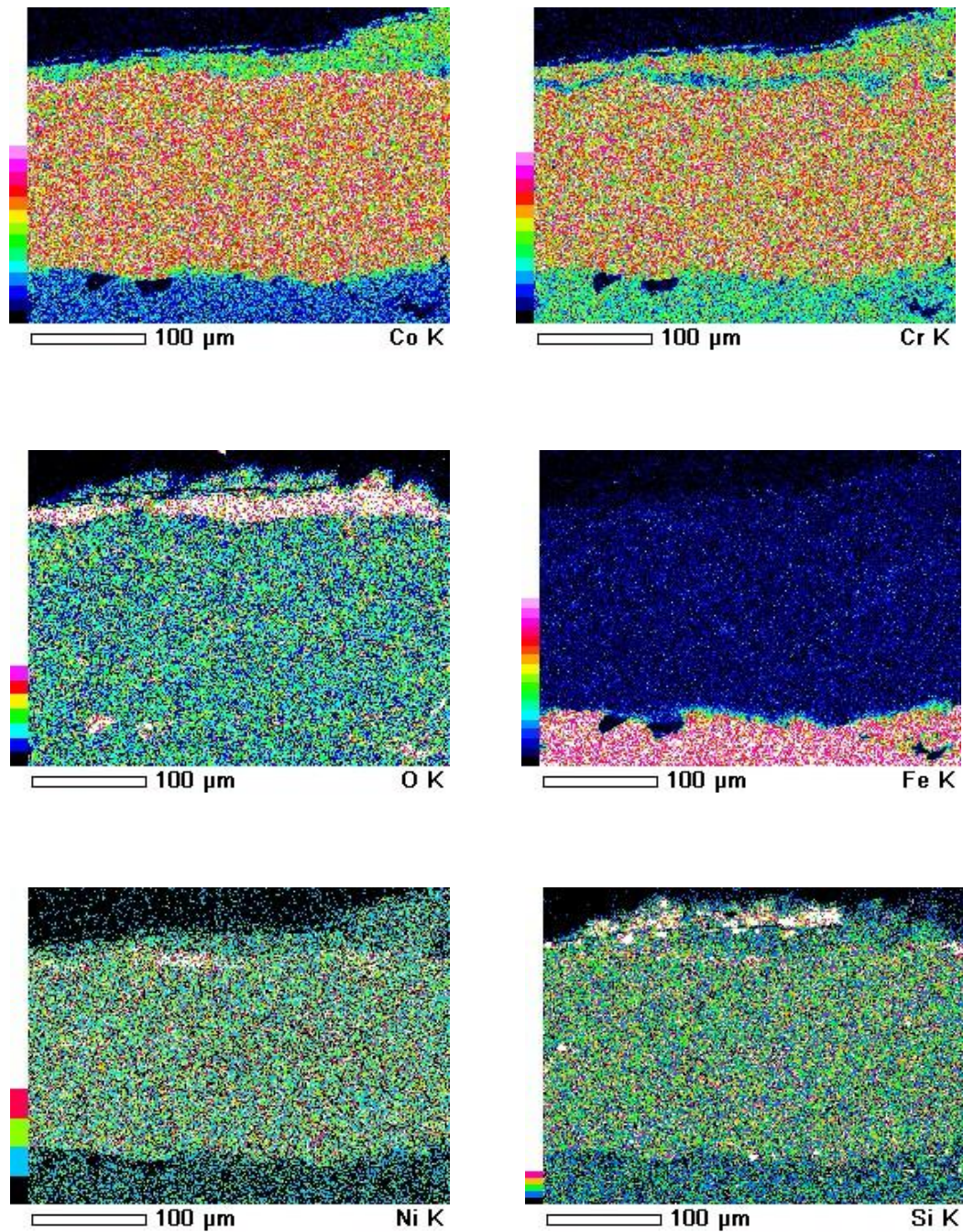


Fig. 5.22 X-ray maps along the cross-section of the Stellite-6 coated MDN-121 material subjected to hot corrosion for 50 cycles in $\text{Na}_2\text{SO}_4+50\%\text{V}_2\text{O}_5$ environment at 800 °C.

5.5 SUMMARY OF HOT CORROSION RESULTS

Results of hot corrosion studies in molten Na_2SO_4 -50% V_2O_5 salt mixture, for coated and uncoated alloys are summarized in Table 5.1, to elicit comparisons among the various coatings and substrate.

Table 5.1 Summary of the results for uncoated and coated alloys subjected to hot corrosion

Coatings	Substrate	Weight gain mg/cm^2	Parabolic constant $\text{kp} \times 10^{-8}$ $\text{g}^2\text{cm}^{-4}\text{s}^{-1}$	XRD phases	Remarks
Uncoated samples	Ti-31	75.79	2.99	TiO_2 , TiVO_4 , $\text{V}_3\text{Ti}_6\text{O}_{17}$, Al_2O_3 and AlVO_4	<ul style="list-style-type: none"> Excessive peeling of Ti-31
	Superco-605	Weight loss	---	Cr_2O_3 , CoO , NiO , WO_3 , SiO_2 , SO_2 , Na_2O , FeVO_4 , CrVO_4 and $\text{Ni}_3\text{V}_2\text{O}_8$	<ul style="list-style-type: none"> Colour changes: Ti-31-brownish: Superco-605-grey: MDN-121-shiny grey. Net weight gain Superco-605 < MDN-121 < Ti-31
	MDN-121	2.69	0.00423	FeO , Cr_2O_3 , SO_3 , FeVO_4 , CrVO_4 and FeS_2	

10% Al ₂ O ₃ + CoCrAlTaY	Ti-31	10.3	0.069	α-Al ₂ O ₃ , CoO, Cr ₂ O ₃ , AlVO ₄ , CrVO ₃	<ul style="list-style-type: none"> • Greenish colour has been observed for all the three substrates. • Preferential oxidation of Al has been revealed. Formation of α-Al₂O₃ was also revealed by XRD.
	Superco-605	2.24	0.0027	α-Al ₂ O ₃ , CoO, Cr ₂ O ₃ , CoCr ₂ O ₄ , CoAl ₂ O ₄ and AlVO ₄ ,	
	MDN-121	1.11	0.00047	α-Al ₂ O ₃ , CoO, Cr ₂ O ₃	
25% (Cr ₃ C ₂ - 25(Ni ₂₀ Cr))+ 75% NiCrAlY	Ti-31	1.37	0.00125	Cr ₂ O ₃ , NiO, Al ₂ O ₃ , NiCr ₂ O ₄ , SO ₃ , Na ₂ O, Cr ₂₃ C ₆ and AlVO ₄	<ul style="list-style-type: none"> • Net weight gain MDN-121 < Superco-605 < Ti-31 • Colour formation: Coated Ti-31, Superco-605 and MDN-121 were light grey turned into brownish.
	Superco-605	1.25	0.00093	Cr ₂ O ₃ , NiO, Al ₂ O ₃ , NiCr ₂ O ₄ , NiAl ₂ O ₄ , CrVO ₄ and Cr ₂₃ C ₆	
	MDN - 121	1.20	0.00105	Cr ₂ O ₃ , NiO, NiCr ₂ O ₄ , AlVO ₄ , Cr ₂₃ C ₆ and FeS ₂	

Stellite-6	Ti-31	8.11	0.0341	CoCr ₂ O ₄ , NiCr ₂ O ₄ , CoO, Cr ₂ O ₃ , NiO and FeO	<ul style="list-style-type: none"> • Crack formation on Ti-31 surface • Rough surface • Net weight gain Superco-605 < MDN-121 < Ti-31 • Colour formation: All three coated are black.
	Superco-605	2.48	0.00366	CoAl ₂ O ₄ , NiAl ₂ O ₄ , CoO, Cr ₂ O ₃ , FeVO ₄ and AlV ₂ O ₄	
	MDN - 121	6.37	0.0236	CoCr ₂ O ₄ , NiCr ₂ O ₄ , CoO, Cr ₂ O ₃ and FeO	

5.6 DISCUSSION

5.6.1 Uncoated samples

The results of thermo gravimetric data demonstrate the accelerated kinetics induced due to Na₂SO₄-50% V₂O₅ salt mixture. Thick oxide layer formed on the Ti - 31 shows a higher corrosion rate and intense spalling of oxide scale in comparison to Superco-605 and MDN-121. Identical results have been reported by Anuwar et al. (2007). Further the weight gain for Ti-31 is more compared to Superco-605 and MDN-121 at the end of 50 cycles as the corrosion on Ti-31 has taken place continuously due to non-adherent nature of the scale. The weight gain indicates the formation of oxides on the surfaces but the oxides are incapable of resisting further corrosion due to the peeling of it from the surface. Peeling off is maximum in the case of Ti-31, which is also displayed by the higher weight gain: Piling-Bedworth Ratio. Comparison for superco-605 was difficult as the uncoated substrate was undergoing sputtering during corrosion study. Further the weight gain square (mg²/cm⁴) data is plotted as a function of time in Fig. 5.23. The plot shows an observable deviation

from the parabolic rate law for Ti-31 and MDN-121, which indicate that the oxide scale developed on the surface is not protective in molten salt environment. The deviation is more for Ti-31 compared to MDN-121. The Superco-605 was undergoing sputtering. This also necessitates that all three substrates need to be protected from the hot corrosion environment. The parabolic rate constants, K_p for the Ti-31 and MDN-121 are 2.99×10^{-8} and $0.00423 \times 10^{-8} \text{ g}^2 \text{ cm}^{-4} \text{ s}^{-1}$ respectively.

The K_p values indicate that the corrosion rate is higher for Ti-31 but comparatively less for MDN-121. The various phases found from XRD on the surface of the substrate material indicate the nature of corrosion products. The oxides of titanium and vanadate found on the surface of titanium confirm the reason for the weight gain during the process. Gurappa (2003) reports that the coating, which is rich in oxides of titanium spalls at high temperature due to adhesion problems. At test temperature of 800 °C, the salt mixture ($\text{Na}_2\text{SO}_4 + 50\% \text{V}_2\text{O}_5$) forms a sheet of liquid and spread over the component surface. The molten salt accelerates the attack of oxide scales. Also, at temperature exceeding 700 °C the Na_2O and SO_3 are formed (Gurappa 2001, Little 1998) reacts with TiO_2 and Al_2O_3 to produce sodium titanate and sodium aluminates, respectively. Sodium oxide reacts with liquid V_2O_5 (M.P 690 °C). It increases corrosivity of the salt mixture which further accelerates the corrosion rate (Singh et al 2007). All these mechanisms are responsible for accelerated corrosion of Ti-31. EDX analysis shows TiO_2 as major phase in corroded Ti-31 surface, Cr_2O_3 and CoO as major phases in corroded Superco-605 surface and FeO in corroded MDN-121 surface. It may be noted that the corresponding metallic elements are the major constituents in the selected three substrates.

It is reported that during the hot corrosion of Ti-31, TiO_2 reacts with $\text{Na}_2\text{SO}_4 - 50\% \text{V}_2\text{O}_5$ (Anuwar et al. 2007). The reaction is accelerated due to non-adherent nature of TiO_2 film. This leads to a higher weight gain of Ti-31 compared to other substrate.

5.6.2 10% $\text{Al}_2\text{O}_3 + \text{CoCrAlTaY}$ coating

The 10% $\text{Al}_2\text{O}_3 + \text{CoCrAlTaY}$ coated Ti-31, Superco-605 and MDN-121 materials showed a lower weight gain in comparison with the uncoated materials when exposed to $\text{Na}_2\text{SO}_4 + 50\% \text{V}_2\text{O}_5$ salt environment.

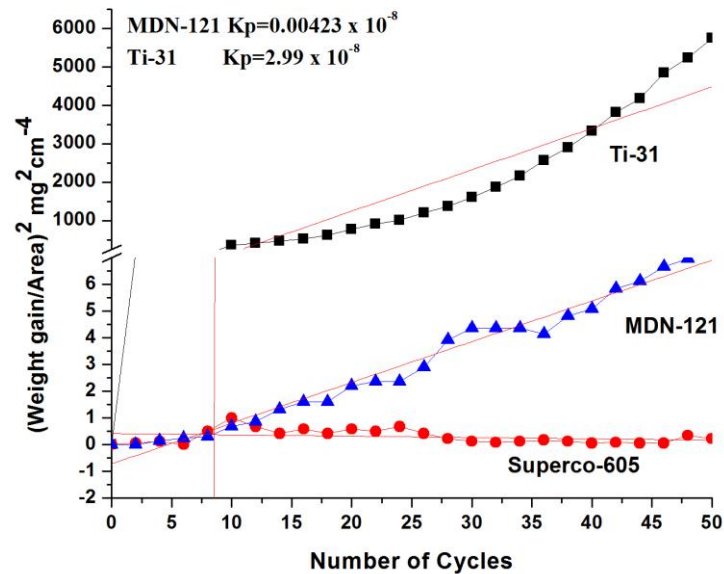


Fig. 5.23 Graph of $(\text{weight gain/area})^2$ versus number of cycles for uncoated samples subjected to hot corrosion.

The weight gain after 50 cycles of exposure of the 10% $\text{Al}_2\text{O}_3+\text{CoCrAlTaY}$ coated Ti-31, Superco-605 and MDN-121 materials are found to be 10.3, 2.2 and 1.11 mg/cm^2 , respectively. Further, to explore the possibility of a parabolic relationship between weight gain and time of exposure, square of weight gain (mg^2/cm^4) data are plotted as a function of cycles (Bolles 1995, Kamal et al. 2010, Toma et al. 2000, Sreedhar et al. 2009). They are given in Fig. 5.24. From this plot, the values of parabolic rate constants are estimated and they are (K_p in $10^{-8} \text{ g}^2 \text{ cm}^{-4} \text{ s}^{-1}$) 0.069×10^{-8} , 0.0027×10^{-8} and $0.00047 \times 10^{-8} \text{ g}^2 \text{ cm}^{-4} \text{ s}^{-1}$ for the 10% $\text{Al}_2\text{O}_3+\text{CoCrAlTaY}$ coated Ti-31, Superco-605 and MDN-121 materials, respectively.

Further, weight gain after 50 cycles of hot corrosion and the parabolic rate constant (K_p) decreases for coated Ti-31, Superco-605 and MDN-121 materials in comparison with the uncoated materials and therefore, it can be inferred that the necessary protection has been provided by the HVOF sprayed 10% $\text{Al}_2\text{O}_3+\text{CoCrAlTaY}$ coatings to the Ti-31, Superco-605 and MDN-121 substrate materials.

The weight gain in 10% $\text{Al}_2\text{O}_3+\text{CoCrAlTaY}$ coated Ti-31 material is higher than that of the Superco-605 and MDN-121 materials and this may be attributed to

the development of cracks after 9th cycle of hot corrosion studies in molten salt environment for 50 cycles. The thermal shocks generated due to the differences in thermal expansion coefficients of coatings, substrate, and oxides may be responsible for the development of cracks (Mishra et al. 2006).

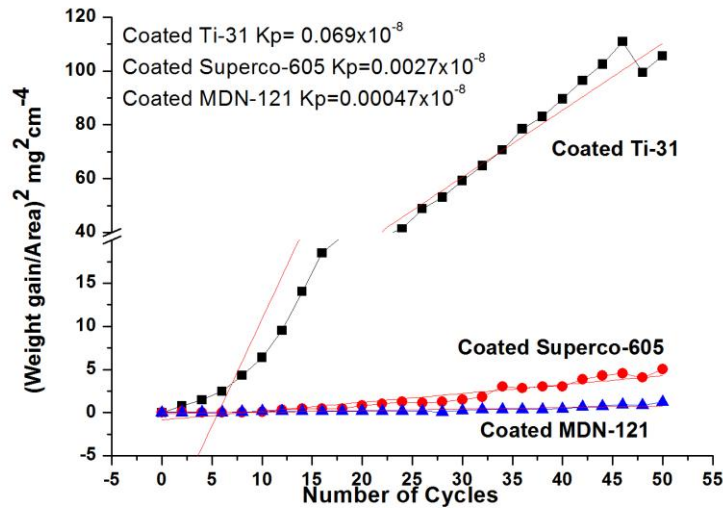
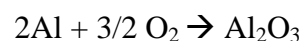


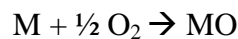
Fig. 5.24 Plot of (weight change/area) ² vs number of cycles for 10% Al₂O₃ + CoCrAlTaY coated materials subjected to hot corrosion in Na₂SO₄-50%V₂O₅ salt environment at 800 °C.

It is revealed from the x-ray diffraction analysis on the surface of the coatings (Fig. 5.7) that α -Al₂O₃ is a major phase. α -Al₂O₃ is the thermodynamically stable phase, having nearly a close-packed corundum structure which shows a low scale growth kinetics during the corrosion (Wang et al. 2007).

In order to form α -Al₂O₃ scale, the thermodynamic conditions must be such that the following reaction is favorable on the surface of the alloy (Ajdelstajn et al. 2002)

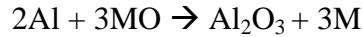


If oxygen supply is different other oxides in addition to Al₂O₃ are formed via reactions of the following type.

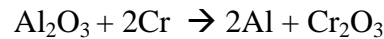


Where M indicates other metallic elements

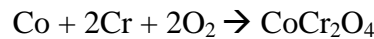
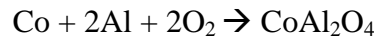
For the Al_2O_3 to develop as a continuous scale, the following additional reaction must be favorable



Usually, the Al_2O_3 develops as a continuous scale beneath some of the MO layer. With further oxidation, a condition of aluminum depletion occurs. Then, the formation of other oxides and spinals takes place according to the following reactions (Wang et al. 2003, Evans et al. 2001, Niranatlumpong et al. 2000)



Cobalt, in presence of Al and Cr can form spinals.



On the surface of the coated specimens, these reactions are more favorable, XRD and EDX analysis also confirms the formation of these spinals on the surface of the coating.

5.6.3 25% (Cr_3C_2 -25(Ni20Cr)) + 75% NiCrAlY coating

By comparing the graphs of (weight gain/area) versus number of cycles of both the uncoated (Fig. 5.2) and the 25% (Cr_3C_2 -25(Ni20Cr)) + 75% NiCrAlY coated substrates (Fig. 5.12), it is observed that the uncoated samples showed a higher weight gain in comparison to the coated samples. Since the weight gain is less in the coated samples, it conveys that the formation of oxide layers is less compared to the uncoated samples and the initially formed oxide layers itself resists further formation of oxide layers. This reduces the corrosion. The plot of square of weight gain (mg^2/cm^4) vs number of cycles is shown in Fig. 5.25. The estimated parabolic constants for the 25% (Cr_3C_2 -25(Ni20Cr)) + 75% NiCrAlY coated Ti-31, Superco-605 and MDN-121 are 0.00125×10^{-8} , 0.00093×10^{-8} and $0.00105 \times 10^{-8} \text{ g}^2\text{cm}^{-4}\text{s}^{-1}$ respectively.

On comparing the parabolic rate constants K_p of the uncoated (Fig. 5.23) and the coated substrates it is found that the parabolic rate constants of the uncoated substrates of Ti-31, Superco-605 and MDN-121 are greater than that of the coated substrate. The plots (Fig. 5.25) show the growth behaviour for all three coated

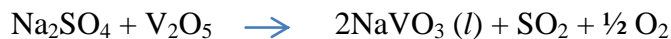
substrates and it indicates that the oxide scale on the coated surfaces is more protective than uncoated surfaces (Fig. 5.23). It is evident from the plot (Fig. 5.25) that the Ti-31, Superco-605 and MDN-121 nearly follow parabolic behavior.

The x-ray diffraction patterns of the upper oxide scale on all the coated substrates under study consisted of Cr₂O₃, NiO, NiCr₂O₄, and Cr₂₃C₆. The presence of unoxidized carbides in the top scale, as detected by the XRD, indicates that the amount of oxidation of the top scale is small.

Further, with the help of results we conclude that the coating provided the necessary protection against the oxidation by forming a Cr₂O₃ scale on the uppermost part of the coating and NiO in the subscale region. Presence of oxygen in the inside of coating may be due to the in-flight oxidation of the coating during HVOF spraying, which leads to the formation of Cr₂O₃ (Kamal et al. 2009).

In the present investigation, cross sectional analyses indicated the presence of reacting species upto the coating-substrate interface in the case of coated alloys but have not attacked the base material. This has been confirmed by the x-ray mapping analysis (Fig. 5.16, map).

The EDX analysis along the cross section shows the distribution of Na and V on the uppermost oxide scale. And, hence, the acidic fluxing by a Na₂SO₄-50% V₂O₅ mixture may be expected (Otero et al. 1987). Na₂SO₄ can react with V₂O₅ to increase the acidity of melt by the formation of vanadate, NaVO₃ (m.p. 610 °C), at 900 °C as per following reactions (Kolta et al. 1972).



This NaVO₃ act as a catalyst and the acidic dissolution of NiO, Al₂O₃ and Cr₂O₃ probably might have occurred according to the reactions (Hwang and Rapp 1989).



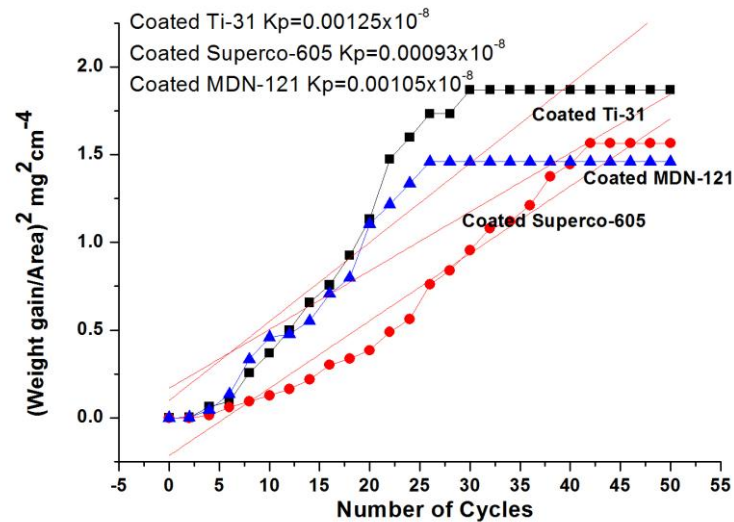


Fig. 5.25 Plot of $(\text{weight gain/area})^2$ versus number of cycles for 25% ($\text{Cr}_3\text{C}_2\text{-}25(\text{Ni}_{20}\text{Cr})$) + 75% NiCrAlY coated samples subjected to hot corrosion for 50 cycles.

These dissolution reactions could have caused breakdown of the initially formed oxide film on the coating surface. The XRD and EDX results also corroborated the formation of these metal vanadates which are concentrated mainly in the top scale (Fig. 5.13 and Fig. 5.14).

5.6.4 Stellite-6 coating

By comparing the plots of $(\text{weight gain/area})$ versus number of cycle's both the uncoated (Fig. 5.2) and the Stellite-6 coated substrates (Fig. 5.18) it is observed that the uncoated samples showed a higher weight gain in comparison to the Stellite-6 coated samples. Since the weight gain is less in the coated samples (for Ti-31 and Superco-605), it conveys that the formation of oxide layers is less compared to the uncoated samples. Also, Stellite-6 coated Ti-31 exhibited higher weight gain compared to Stellite-6 coated MDN-121 samples. In the case of coated Ti-31, the coating exhibited cracks during thermal cycling. The cracks accelerated the corrosion kinetics compared to Stellite-6 coated MDN-121. The weight gain of the coated substrate of MDN-121 was found to be greater than that of the uncoated substrate.

These may be due to the higher value of porosity in the coating, which enhances the penetration of the species and hence accelerating the corrosion. Also some amount of spalling of the oxide scale of Stellite-6 coated MDN-121, is observed during cooling periods of the thermal cycles. This is attributed to different values of thermal expansion coefficients of the coatings, substrates and oxides. Similar observations are reported by Sidhu et al. (2005) and Sidhu et al. (2006).

Further the weight gain square (mg^2/cm^4) data are plotted as a function of time in Fig. 5.26. The plot shows an observable deviation from the parabolic rate law for the Stellite-6 coated Ti-31 and MDN-121 which indicates that the oxide scale is not fully protective in molten salt environment. The parabolic rate constants, K_p for the stellite-6 coated Ti-31, Superco-605 and MDN-121 are 0.0341×10^{-8} , 0.00366×10^{-8} and $0.0236 \times 10^{-8} \text{ g}^2 \text{ cm}^{-4} \text{ s}^{-1}$, respectively.

From these observations it could be inferred that since the K_p value is decreased for the stellite-6 coated substrates of Ti-31 and Superco-605, the coating has provided good corrosion protection to the substrate materials whereas the higher K_p of the uncoated samples shows that they have less corrosion resistance. Also, the uncoated MDN-121 substrate has a lower K_p value compared to stellite-6 coated MDN-121. It indicates that the MDN-121 has better corrosion resistance when compared to coat other substrates.

The x-ray diffraction patterns of the upper oxide scale have shown that all the coated substrates under study consisted of CoCr_2O_4 , NiCr_2O_4 , CoO , and Cr_2O_3 as phases of oxide layers.

Since the formation of oxides is comparatively less compared to uncoated samples, it indicates that the coating has the capacity to resist the corrosion. Also, it confirms the reduced weight gain during the process compared to uncoated samples (Sidhu and Prakash 2005, Sidhu et al. 2006B, Singh et al. 2007).

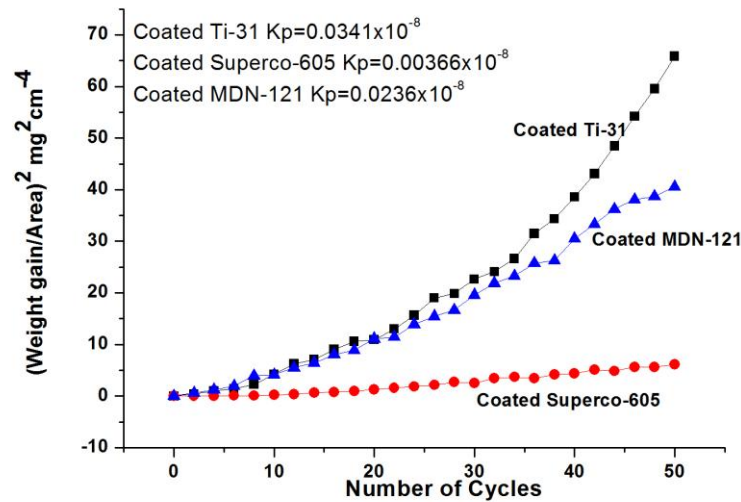


Fig. 5.26 Plot of $(\text{weight gain/area})^2$ versus number of cycles for Stellite-6 coated samples subjected to hot corrosion.

5.7 COMPARATIVE DISCUSSION

The cumulative weight gain (mg/cm^2) for uncoated and HVOF coated 10% $\text{Al}_2\text{O}_3+\text{CoCrAlTaY}$, 25% $(\text{Cr}_3\text{C}_2-25(\text{Ni}20\text{Cr})) + 75\% \text{NiCrAlY}$ and Stellite-6 subjected to hot corrosion in $\text{Na}_2\text{SO}_4-50\% \text{V}_2\text{O}_5$ molten salt environment for 50 cycles at 800°C is shown in Fig. 5.27. From the bar charts, it can be inferred that the weight gains for most of the HVOF coated samples are significantly lower than that of uncoated samples in the molten salt environment. Uncoated Ti-31 suffered a higher corrosion rate and intense spalling of oxide scales. The acidic fluxing of oxides by molten salt mixture has resulted in massive, porous oxide scale. The stress developed due to higher volume of oxide scale (Piling Bedworth ratio) leads to cracks, in turn resulted in spallation. Uncoated Ti-31 showed higher corrosion rate in comparison to uncoated MDN-121 and Superco-605.

Based on the thermo gravimetric data it can be inferred that the 25% $(\text{Cr}_3\text{C}_2-25(\text{Ni}20\text{Cr})) + 75\% \text{NiCrAlY}$ coating provides the highest hot corrosion resistance whereas 10% $\text{Al}_2\text{O}_3+\text{CoCrAlTaY}$ and Stellite-6 coatings indicates the comparatively less resistance to the molten salt environment. The relative hot corrosion resistance of the various coatings under study can be arranged in the following sequence:

25% (Cr_3C_2 -25(Ni20Cr)) + 75% NiCrAlY > 10% Al_2O_3 + CoCrAlTaY > Stellite-6 >

Uncoated

The superior hot corrosion resistance of 25% (Cr_3C_2 -25(Ni20Cr)) + 75% NiCrAlY is attributed to the protective oxide scale developed on the surface. The uppermost layer of the oxide scale mainly consisted of continuous film of Cr_2O_3 which have minimal solubility in highly acidic Na_2SO_4 -50% V_2O_5 melt. The slow corrosion kinetics (and parabolic behaviour) observed during the thermo gravimetric study shows that the reaction rate is diffusion limited.

From the graph given below it is observed that base material Ti-31 has corroded more whereas 25% (Cr_3C_2 -25(Ni20Cr))+ 75% NiCrAlY and 10% Al_2O_3 +CoCrAlTaY coatings have corroded the least, but in the case of Stellite-6 coated substrate, the corrosion rate is comparatively more than the other coatings. It is attributed to higher value of porosity. MDN-121 coated with 10% Al_2O_3 +CoCrAlTaY coating has resisted well than the base material. The Stellite-6 coated substrates have corroded more compared to uncoated Superco-605 and MDN-121. From the above conclusions we infer that (10% Al_2O_3 +CoCrAlTaY) and 25% (Cr_3C_2 -25(Ni20Cr))+ 75% NiCrAlY coated Ti-31, Superco-605 and MDN-121 materials are resisting hot corrosion reasonably well compared to uncoated substrates.

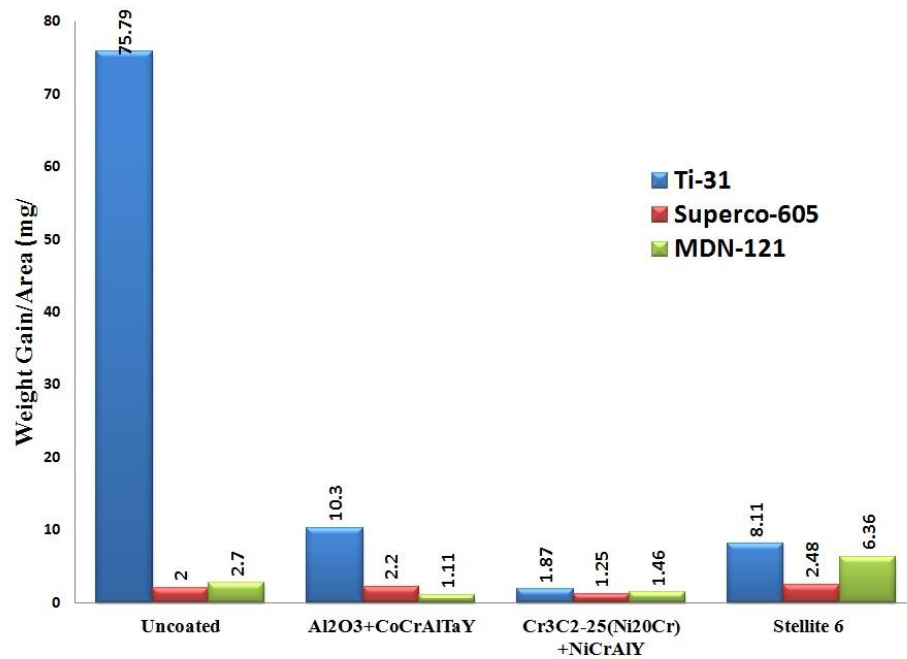


Fig. 5.27 Bar chart showing cumulative weight gain (mg/cm^2) for uncoated and HVOF coated samples subjected to hot corrosion in Na_2SO_4 -50% V_2O_5 salt environment for 50 cycles at 800 °C.

CHAPTER 6

OXIDATION STUDIES

This chapter describes the oxidation behaviour of HVOF coated and uncoated substrate materials. The cyclic oxidation was conducted in air for 50 cycles at an elevated temperature of 800 °C. Thermogravimetric is used to study the reaction rate and kinetics of the oxidation process. The XRD and SEM/EDX were used to investigate reaction products.

6.1 UNCOATED SAMPLES

6.1.1 Visual observations

The macrographs of Ti-31, Superco-605 and MDN-121 which are subjected to oxidation in an air environment for 50 cycles at 800 °C are shown in Fig. 6.1. From the first cycle itself oxidation was taking place. It is indicated by a colour change on the surface of the samples. The surface of Ti-31 became brown from the first cycle itself. Also, there was an intense spalling of oxide scales from the oxidized surface of Ti-31. The surface of Superco-605 turned to green colour initially and it turned to ash colour at 14th cycle and after 37th cycle green colour was observed at the edges. The surface of MDN-121 became light in colour with isolated red spots and after two cycles spots became brown in colour and after 37th cycle, a shining background surface was observed. The scale on the Superco-605 and MDN-121 was exhibiting sputtering during the cyclic oxidation study.

6.1.2 Thermogravimetric studies

The plots of cumulative weight gain (mg/cm^2) as a function of time expressed in number of cycles are shown in Fig. 6.2. The weight gain for Ti-31, Superco-605 and MDN-121 samples, at the end of 50 cycles is found to be 11.03, 0.13 and 0.032 mg/cm^2 , respectively. Evidently, the Ti-31 showed a higher weight gain during the oxidation studies in air environment as compared to the Superco-605 and MDN-121. The weight gain plot for Superco-605 and MDN-121 were fluctuating during the

course of study due to intense sputtering of the scale formed on the surface. Because of this measuring overall weight gain was difficult.

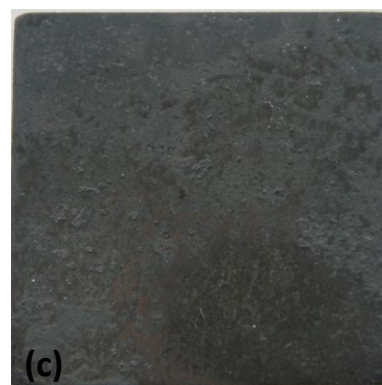
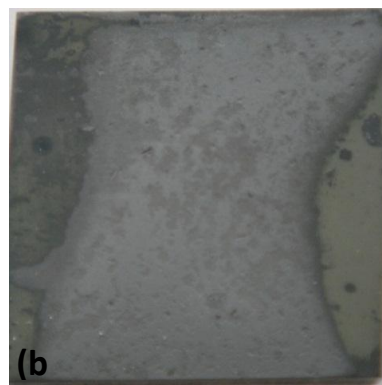
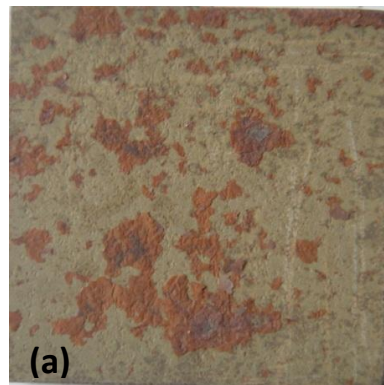


Fig. 6.1 Macrographs of substrate materials subjected to cyclic oxidation in air at 800 °C for 50 cycles: Size 25 X 25 X 5 mm (a) Ti-31 (b) Superco-605 (c) MDN-121.

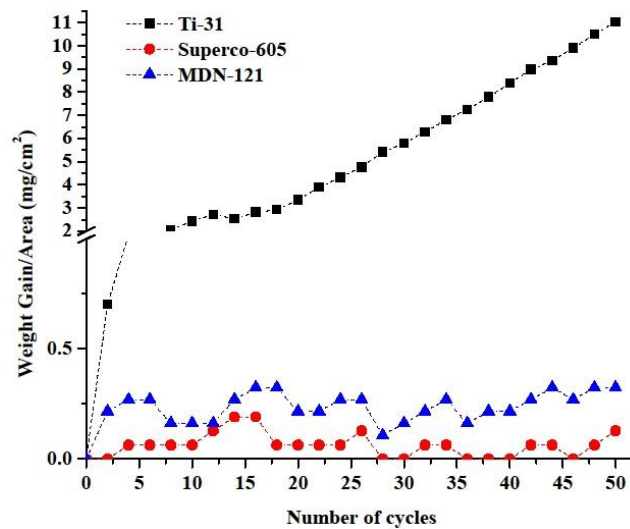


Fig. 6.2 Plot of weight gain/area versus number of cycles for uncoated samples subjected to oxidation in air at 800 °C.

6.1.3 X-ray diffraction analysis

The X-ray diffraction patterns of the upper oxide scale, after its exposure to air environment at 800 °C for 50 cycles are shown in Fig. 6.3a. The oxide scale on the Uncoated substrate Ti-31 consisted of TiO_2 (rutile) and $\alpha\text{-Al}_2\text{O}_3$ as major phases. The oxide scale also showed the presence of V_2O_3 , V_2O_5 , AlTi_3 , TiVO_4 and $\text{Al}_2\text{V}_2\text{O}_4$ as minor phases. Fig. 6.3b shows the oxide scale formed on the uncoated Superco-605 has CoO and Cr_2O_3 as major phases. Fig. 6.3c shows the MDN-121 surfaces formed an oxide layer of Cr_2O_3 and FeO as major phases.

6.1.4 SEM/EDX analysis

The SEM micrograph showing the morphology of oxidized surface (scales) along with the EDX analysis is illustrated in Fig. 6.4. Figure 6.4a shows oxidized surface on Ti-31. It has TiO_2 (varying from 79 to 86 wt %) and Al_2O_3 (varying from 11 to 17%) as the main constituents and small amount of V_2O_5 (2.5 to 4.6%) in the outer layer of the Ti-31 oxidized surface. Superco-605 (Fig. 6.4b) shows CoO (in the range of 89 to 92%) and NiO (in the range of 6 to 8%), along with small quantities of Cr_2O_3 and MnO . Similarly oxidized surface of MDN-121 (Fig. 6.4c) shows FeO (in the range of 83 to 89%) and Cr_2O_3 (in the range of 8 to 12%) as major phases, with small amounts of SiO_2 and MnO .

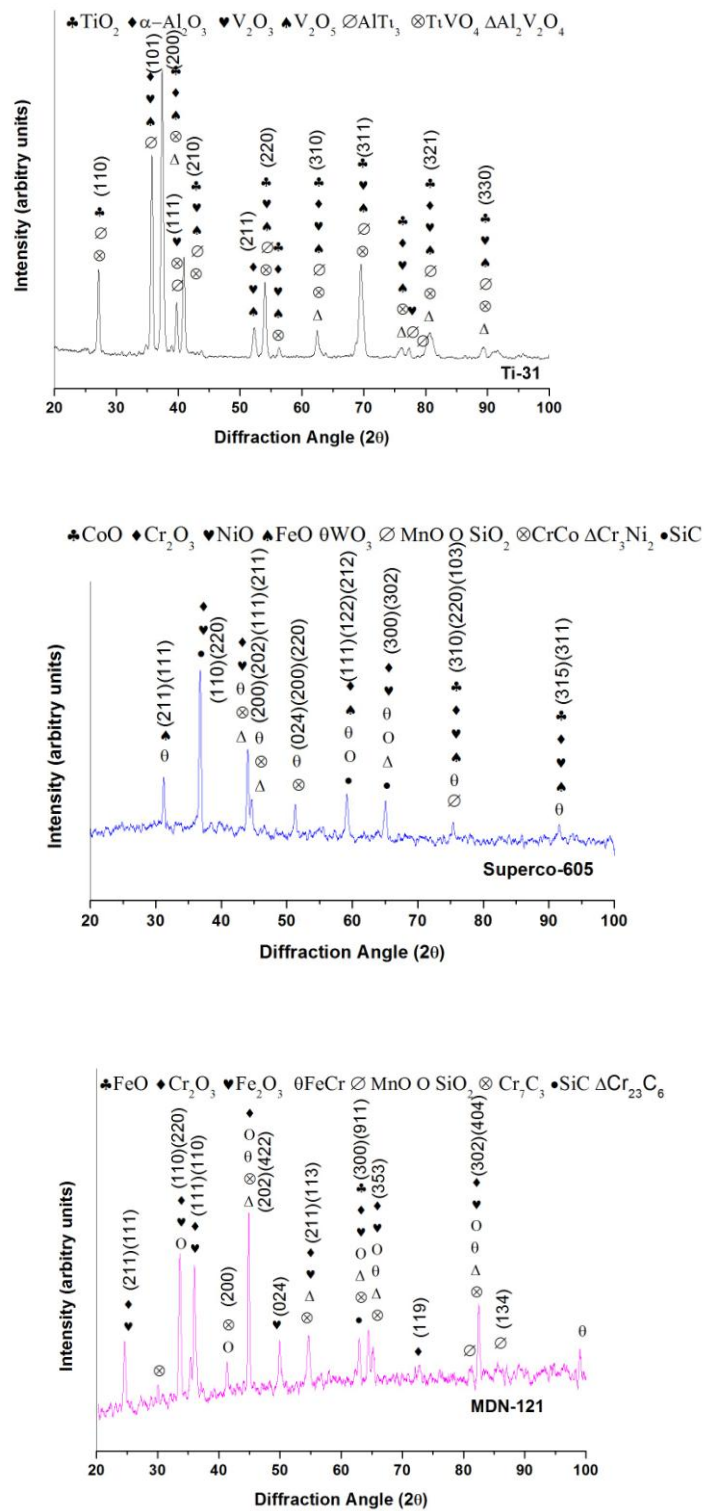


Fig. 6.3 X-ray diffraction patterns for uncoated materials subjected to cyclic oxidation for 50 cycles in air at 800 °C (a) Ti-31 (b) Superco-605 (c) MDN-121.

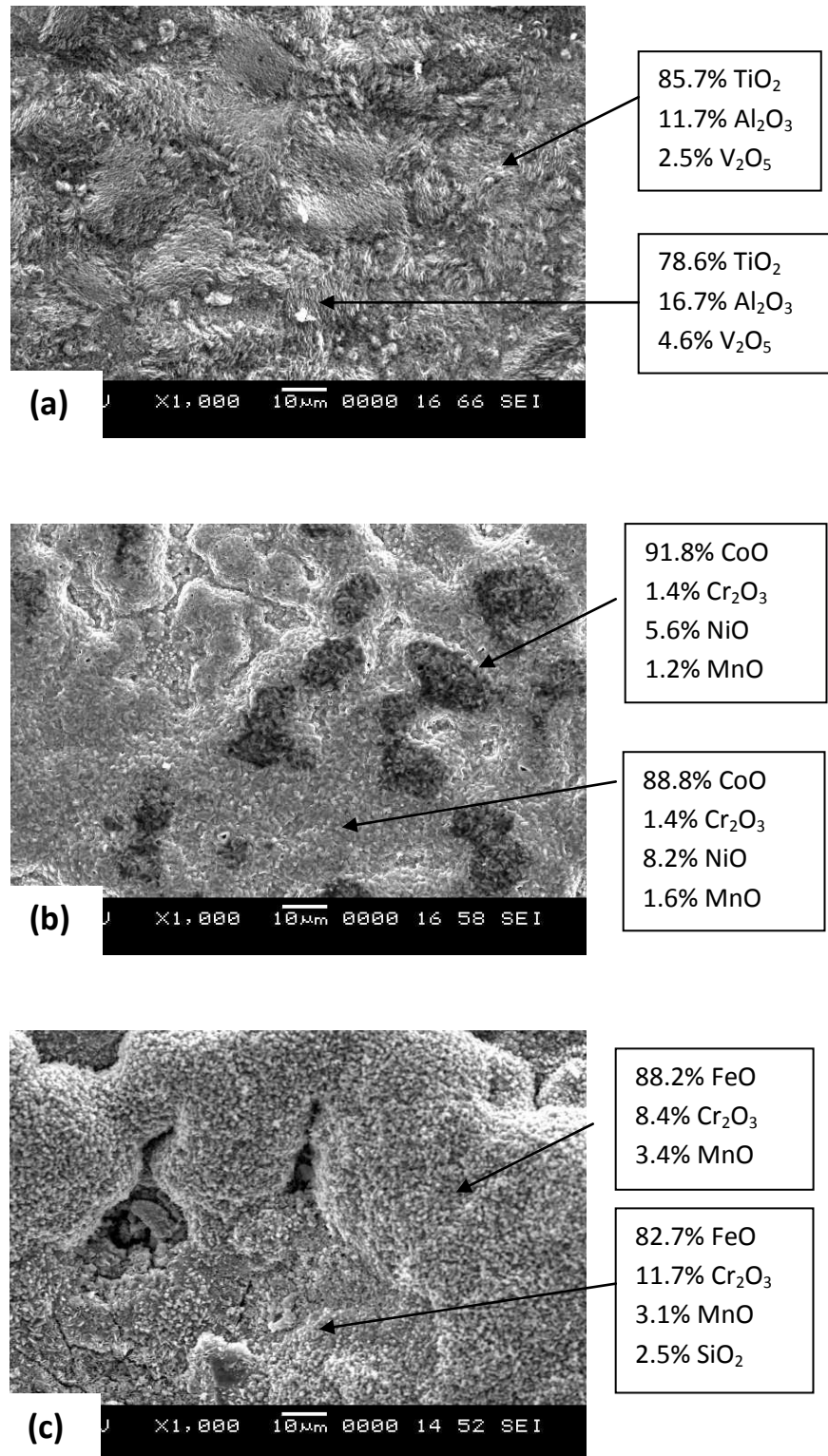


Fig. 6.4 Morphology of oxide scales and EDX analysis on the scale for the uncoated substrate materials subjected to cyclic oxidation in air at 800 °C for 50 cycles (a) Ti-31 (b) Superco-605 (c) MDN-121.

6.2 10% Al₂O₃-CoCrAlTaY COATING

6.2.1 Visual observations

The macrographs of the HVOF sprayed 10% Al₂O₃-CoCrAlTaY coatings on the Ti-31, Superco-605 and MDN-121 subjected to oxidation in an air environment for 50 cycles at 800 °C are illustrated in Fig. 6.5. The colour of the as-sprayed coating on all three substrates was light grey in colour. After the first cycle of oxidation, coated Ti-31 surface showed dark grey in colour, surfaces of coated Superco-605 and MDN-121 showed brown colour.

6.2.2 Thermogravimetric studies

The plots of cumulative weight gain (mg/cm²) as a function of time expressed in number of cycles are shown in Fig. 6.6. The values of overall weight gain after 50 cycles of oxidation for 10% Al₂O₃-CoCrAlTaY coated Ti-31, Superco-605 and MDN-121 are found to be 4.28, 1.03 and 1.28 mg/cm², respectively. Evidently, the coated Ti-31 showed a maximum weight gain during the oxidation studies in air environment as compared to the coated Superco-605 and MDN-121.

6.2.3 X-ray diffraction analysis

The X-ray diffraction patterns of the top scale, after its exposure to air environment at 800 °C for 50 cycles are shown in Fig. 6.7. The scales on the 10% Al₂O₃-CoCrAlTaY coating on substrates of Ti-31, Superco-605 and MDN-121 under study consisted of CoO, Cr₂O₃ and α-Al₂O₃ as major phases. The scales also showed the presence of Ta₂O₅, CrCo, AlCo and AlCrCo as minor phases.

6.2.4 SEM/EDX analysis

The morphologies of the scales on the 10% Al₂O₃+CoCrAlTaY coated samples along with EDX analysis are shown in Fig. 6.8. In all three cases, the scales on the coating are rich in oxides of Co, Cr, Al and Ta.

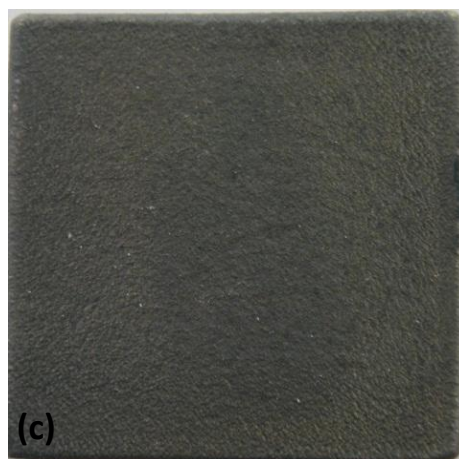
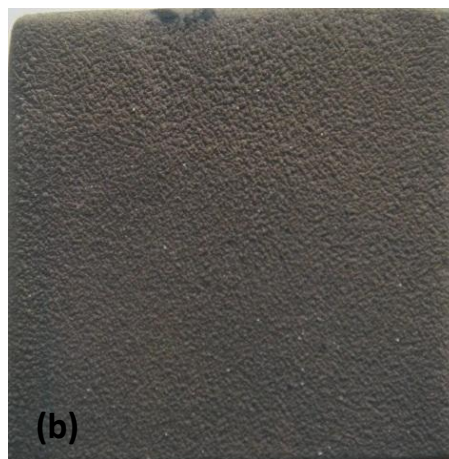
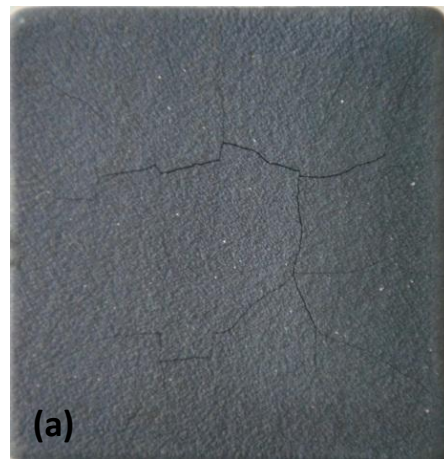


Fig. 6.5 Macrographs of the 10% Al_2O_3 -CoCrAlTaY coated samples subjected to cyclic oxidation in air for 50 cycles at 800 °C. Size 25 X 25 X 5 mm

(a) Ti-31 substrate (b) Superco-605 substrate (c) MDN-121 substrate

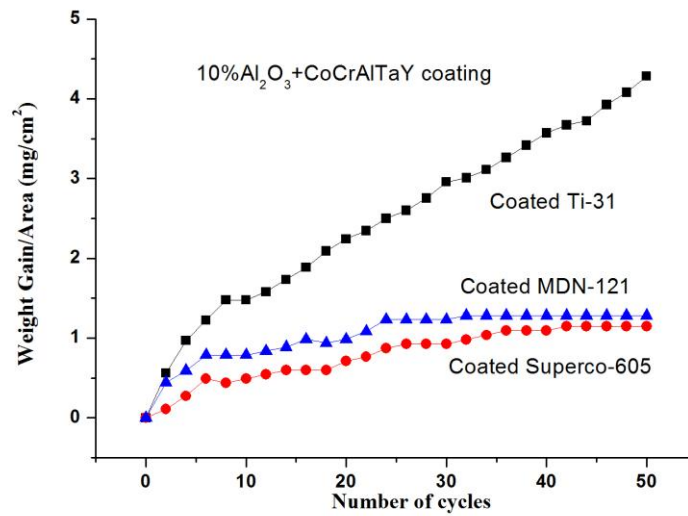


Fig. 6.6 Plot of weight gain/area versus number of cycles for 10% $\text{Al}_2\text{O}_3+\text{CoCrAlTaY}$ coated samples subjected to cyclic oxidation in air at 800 °C.

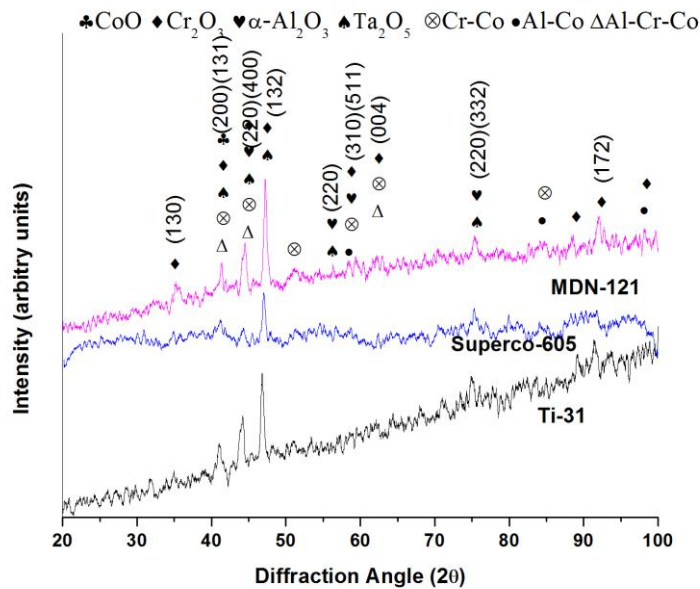


Fig. 6.7 X-ray diffraction patterns for 10% $\text{Al}_2\text{O}_3+\text{CoCrAlTaY}$ coated Ti-31, Superco-605 and MDN-121 subjected to cyclic oxidation for 50 cycles in air at 800 °C.

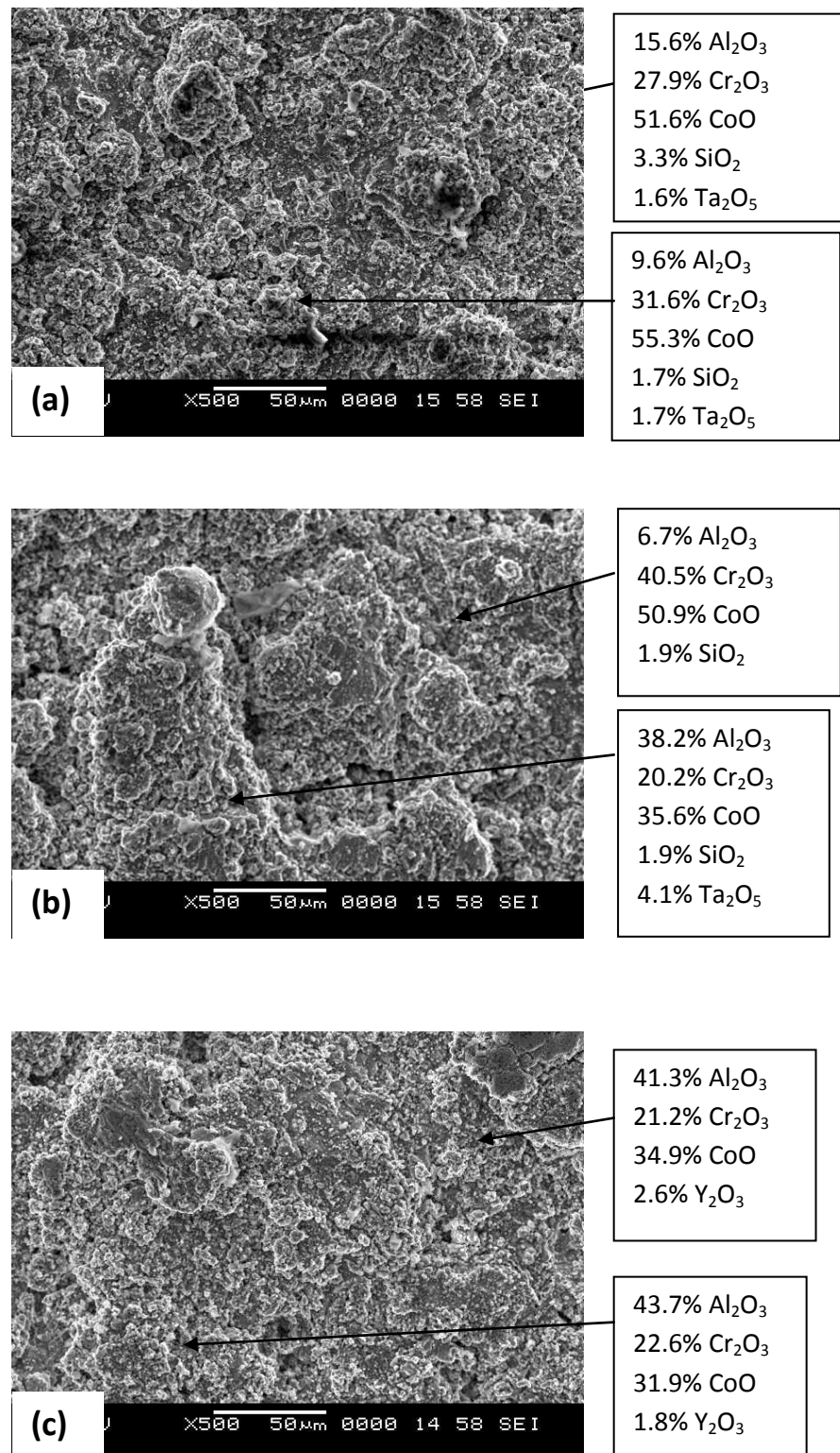


Fig. 6.8 Morphology of scales and EDX analysis for the 10% Al₂O₃+CoCrAlTaY coated samples subjected to cyclic oxidation in air at 800 °C for 50 cycles
(a) Ti-31 substrate (b) Superco-605 substrate (c) MDN-121 substrate.

Cross sectional analysis of 10% Al₂O₃+CoCrAlTaY coated Ti-31 subjected to cyclic oxidation in air is shown in Fig. 6.9. The microstructure shows a continuous oxide scale formed on the top surface. In few locations the splats were separated from each other. EDX analysis on this scale revealed oxides of Co, Cr and Al as the major constituents. The oxidation is predominant at the splat boundary. The oxides at the boundary are rich in Co, Cr and Al.

Fig 6.10 shows the X-ray maps of the cross-section of the scale formed on 10% Al₂O₃+CoCrAlTaY coated Ti-31 at 800 °C for 50 cycles of thermal oxidation. X-ray maps show that only top of the coating has been oxidized (few micrometers). The scale consists of mainly oxides of Co and Cr.

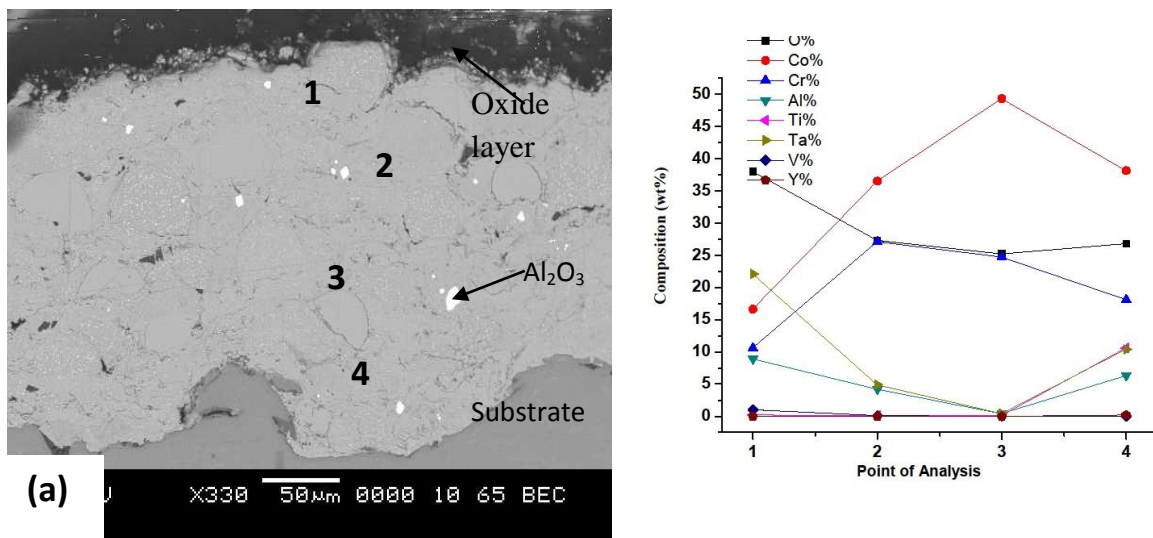


Fig. 6.9 Back scattered image and EDX analysis across the cross-section of the 10% Al₂O₃ + CoCrAlTaY coated Ti-31 material subjected to oxidation for 50 cycles at 800 °C

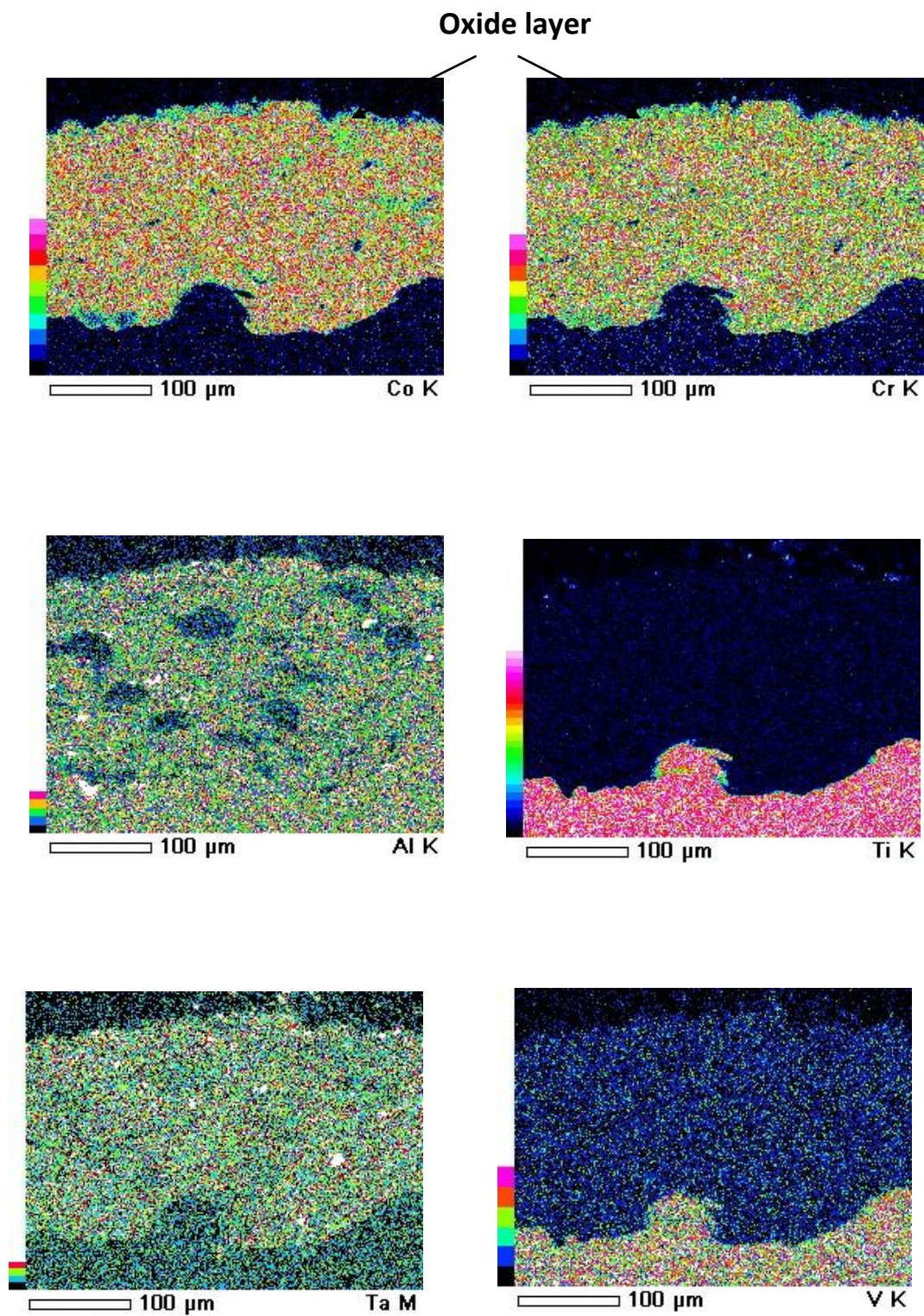


Fig. 6.10 X-ray mapping along the cross-section of the 10% Al_2O_3 +CoCrAlTaY coated Ti-31 material subjected to oxidation for 50 cycles at 800 °C.

6.3 25% (Cr₃C₂-25(Ni20Cr)) + 75%NiCrAlY COATING

6.3.1 Visual observations

The macrographs of the HVOF sprayed 25% (Cr₃C₂-25(Ni20Cr))+75% NiCrAlY coatings on the Ti-31, Superco-605 and MDN-121 subjected to oxidation in an air environment for 50 cycles at 800 °C are illustrated in Fig. 6.11. The colour of the as-sprayed coating was light grey and it turned into dark grey colour during the first cycle of exposure.

6.3.2 Thermogravimetric studies

The plots of cumulative weight gain (mg/cm²) as a function of time expressed in number of cycles are shown in Fig. 6.12. The values of overall weight gain after 50 cycles of oxidation for 25% (Cr₃C₂-25(Ni20Cr)) + 75% NiCrAlY coated Ti-31, Superco-605 and MDN-121 are found to be 0.81, 0.06 and 0.21 mg/cm², respectively. Evidently, the coated Ti-31 showed maximum weight gain during the oxidation studies in air as compared to the coated Superco-605 and MDN-121.

6.3.3 X-ray diffraction analysis

The X-ray diffraction patterns of the top scale, after cyclic oxidation studies in air at 800 °C for 50 cycles are shown in Fig. 6.13. The scales on all three coated samples consisted of α -Al₂O₃, Cr₂O₃ and NiO as major phases. The scales also showed the presence of CrC, Cr₃Ni₂, Al₃Ni₂ intermetallic phases and NiAl₂O₄, NiCr₂O₄ spinals in the form of minor phases.

6.3.4 SEM/EDX analysis

The morphologies of the oxidized, 25% (Cr₃C₂-25(Ni20Cr)) + 75% NiCrAlY coated samples along with EDX analysis are shown in Fig. 6.14. In all three cases the surface morphologies appear to be nodular, growing perpendicular to the coating surface. The EDX analysis of scales shows the formation of Cr₂O₃ and NiO as major phases on coatings on all three substrate materials. Coating on Ti-31 (Fig. 6.14a)

shows Cr_2O_3 in the range of 65 to 95% and NiO 5 to 36%. Coating on Superco-605 (Fig. 6.14b) shows Cr_2O_3 in the range of 52 to 56% and NiO is 43 to 46%, along with small quantities of Y_2O_3 . Similarly, coated MDN-121 (Fig. 6.14c) shows Cr_2O_3 in the range of 30 to 58% and NiO (in the range of 43 to 69%) as major phases.

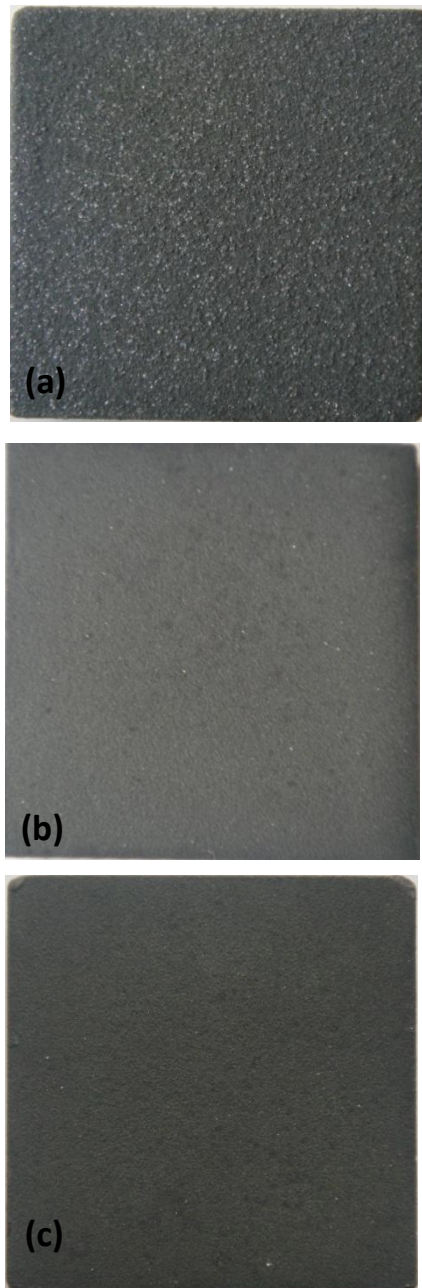


Fig. 6.11 Macrographs of 25% (Cr_3C_2 -25(Ni20Cr)) + 75% NiCrAlY coated samples subjected to thermal oxidation at 800 °C for 50 cycles. Size 25 X 25 X 5 mm (a) Ti-31 substrate (b) Superco-605 substrate (c) MDN-121 substrate.

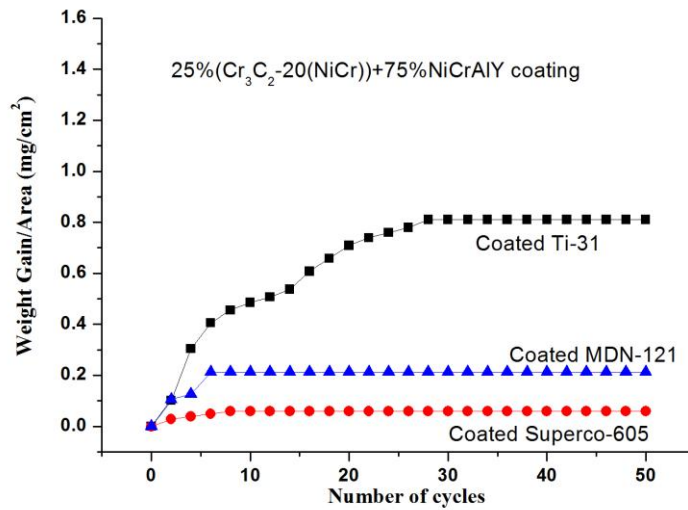


Fig. 6.12 Plot of weight gain/area versus number of cycles for 25% (Cr_3C_2 -25(Ni20Cr)) + 75% NiCrAlY coated samples subjected to cyclic oxidation at 800 °C for 50 cycles.

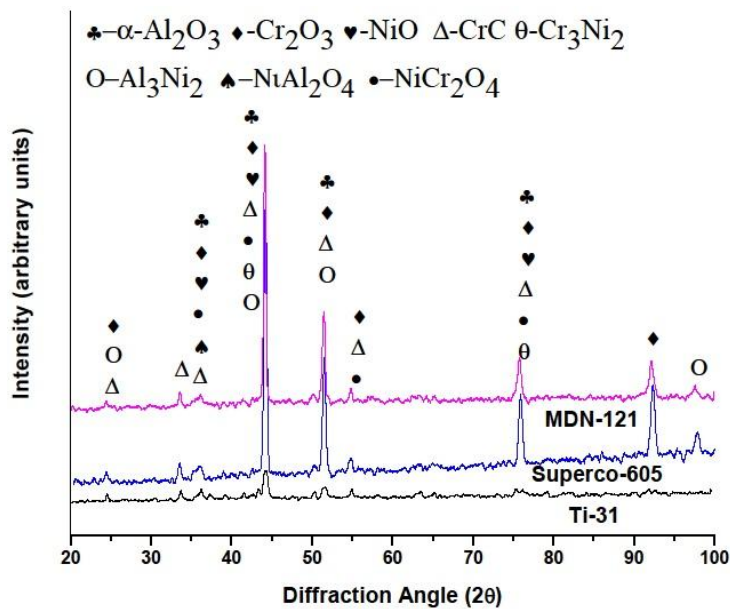
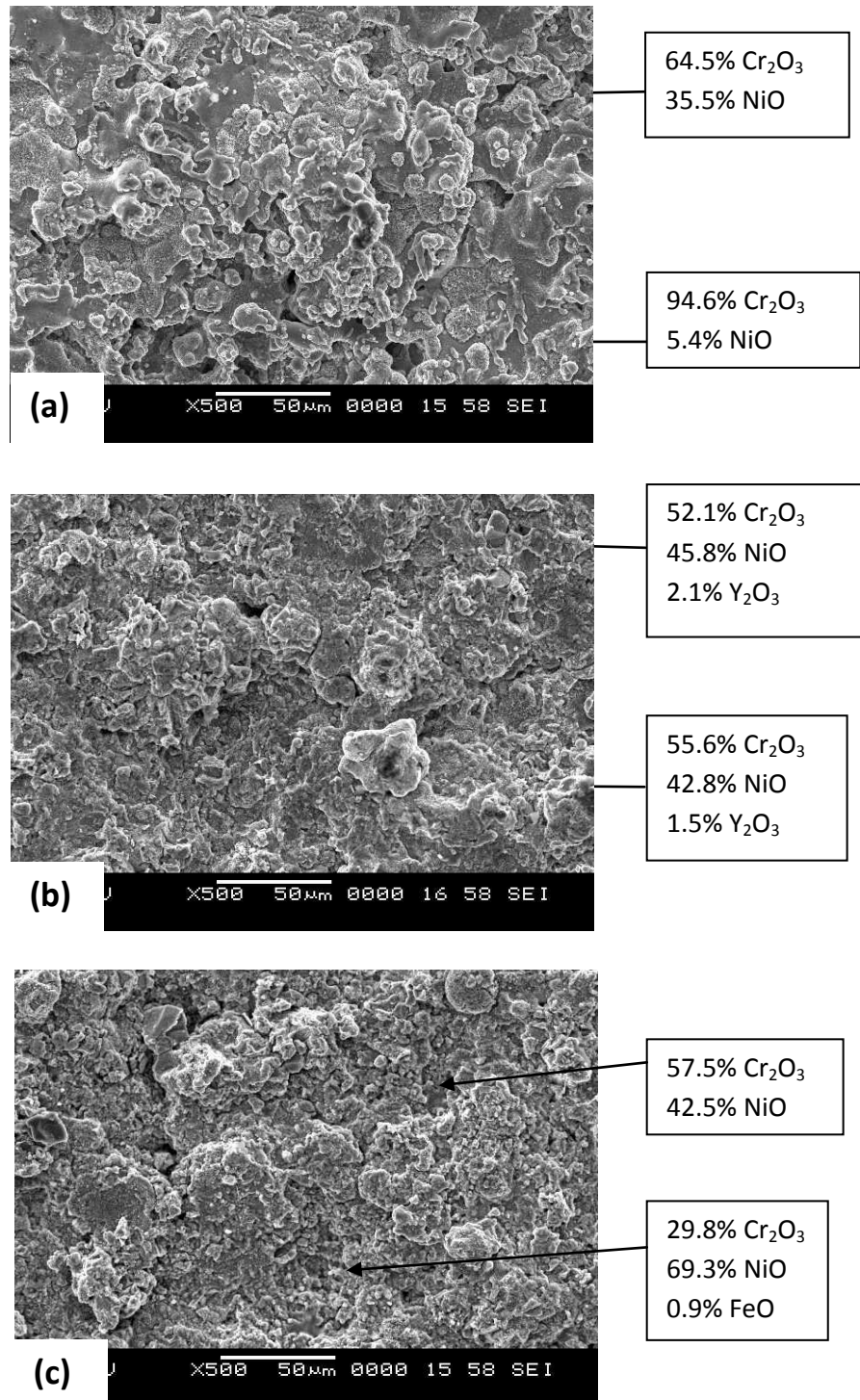


Fig. 6.13 X-ray diffraction patterns for 25% (Cr_3C_2 -25(Ni20Cr)) + 75% NiCrAlY coated samples subjected to cyclic oxidation for 50 cycles in air at 800 °C.



**Fig. 6.14 Morphology of scales and EDX analysis for 25% (Cr_3C_2 -25(Ni_{20}Cr)) + 75% NiCrAlY coated samples subjected to oxidation for 50 cycles at 800 °C
(a) Ti-31 substrate (b) Superco-605 substrate (c) MDN-121 substrate.**

Cross sectional analysis of the scale formed during cyclic oxidation at 800 °C of HVOF sprayed coating on Ti-31 is shown in Fig. 6.15. A continuous and adherent scale is formed on the coated samples, which has retained the dense structure of the as sprayed coatings even after the oxidation run for 50 cycles. There is no indication of any crack in the scale. Also, the oxygen concentration is maximum on the surface of the coating. It indicates that the top layer of the coating is oxidized. EDX analysis indirectly indicates that the top surface of the scale contains mainly oxides of Cr and Ni, with splat boundaries showing Cr₃C₂ rich layer. A thin oxide scale at the top of the coating (marked 1 in Fig 6.15) indicates that the coating gives necessary protection against the oxidation by forming a Cr₂O₃ scale.

Fig. 6.16 shows the X-ray mapping of the cross-section of oxidized, HVOF sprayed, 25% (Cr₃C₂-25(Ni20Cr)) + 75% NiCrAlY coating on Ti-31. X-ray mapping also indicates a thin scale, consisting of chromium oxide, predominantly. Ni peaks are found mostly at places where Cr is depleted.

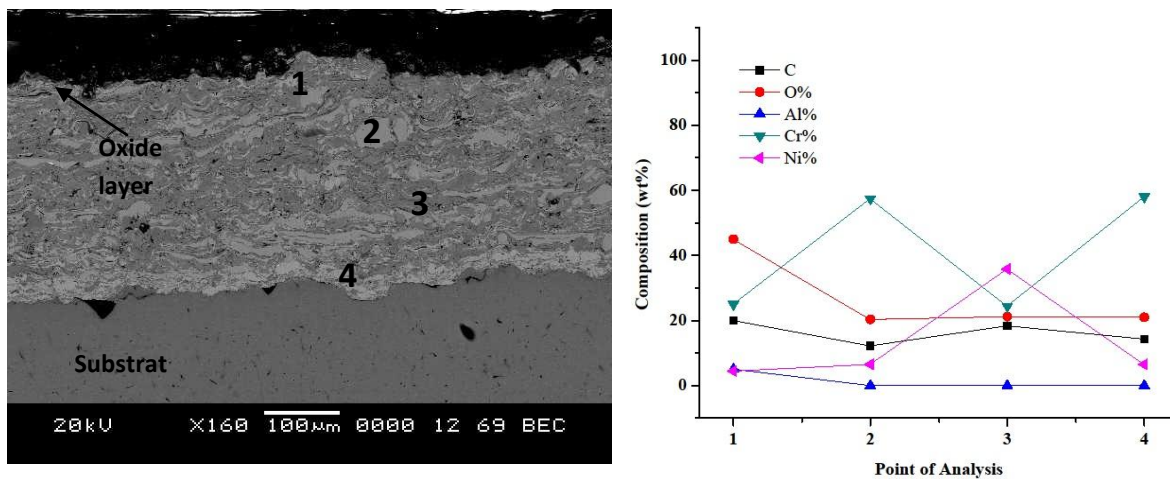


Fig. 6.15 Back scattered image and EDX analysis (wt %) across the cross-section of the 25% (Cr₃C₂-25(Ni20Cr)) + 75% NiCrAlY coated Ti-31 material subjected to oxidation for 50 cycles at 800 °C.

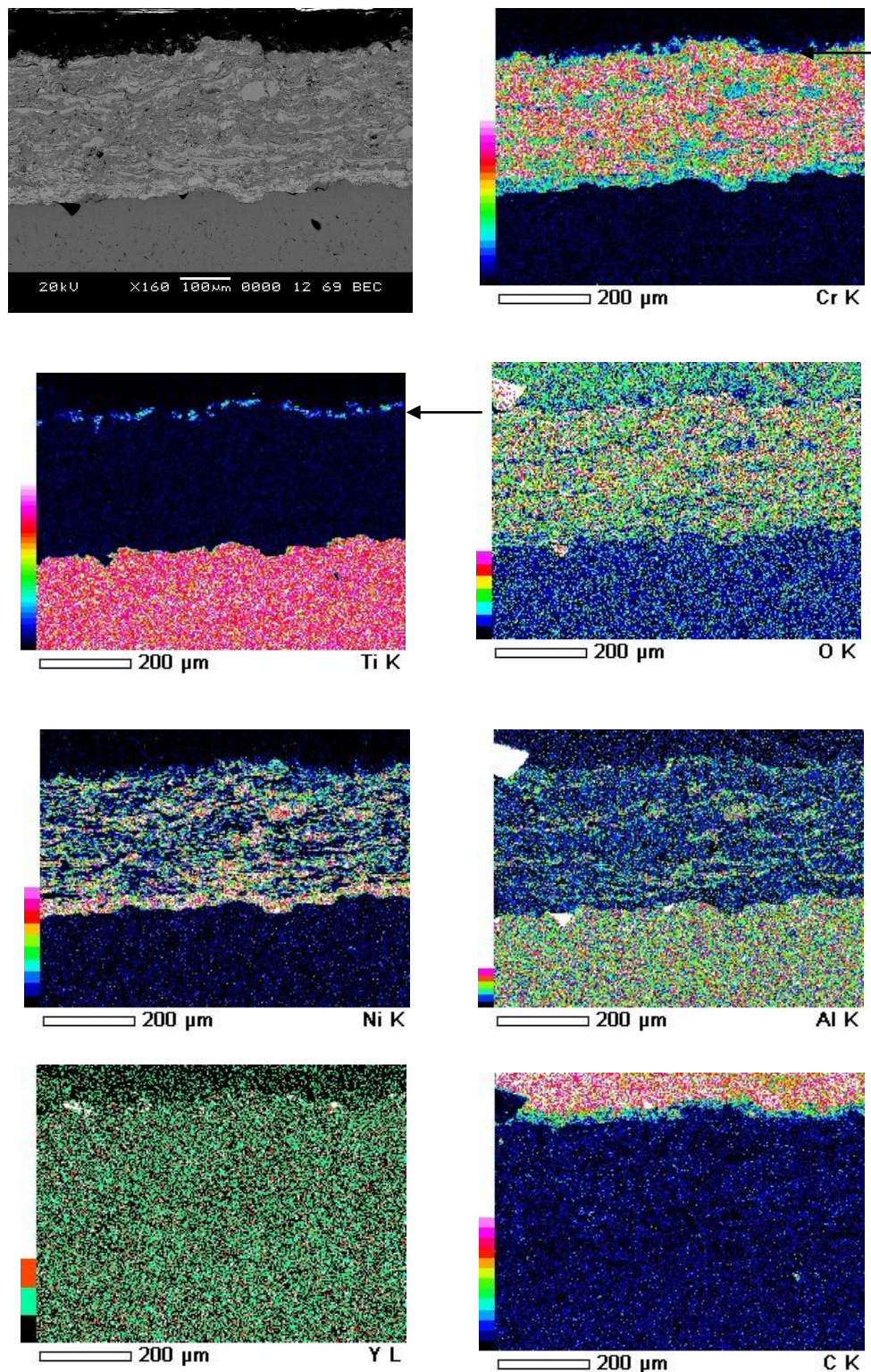


Fig. 6.16 X-ray mapping along the cross-section of the 25% (Cr_3C_2 -25(Ni20Cr) + 75% NiCrAlY coated Ti-31 material subjected to oxidation for 50 cycles at 800 °C.

6.4 STELLITE-6 COATING

6.4.1 Visual observations

The macrographs of the HVOF sprayed Stellite-6 coatings on the Ti-31, Superco-605 and MDN-121 subjected to oxidation in an air environment for 50 cycles at 800°C are illustrated in Fig. 6.17. The colour of the as-sprayed coating is dark grey which remained same during the course of thermal cycling. Stellite-6 coated Superco-605 and MDN-121 did not show any specific observations during the oxidation studies, whereas, Stellite-6 coated Ti-31 formed cracks on the top surface and at the sides after 15th cycle which propagated further, after 32nd cycle.

6.4.2 Thermogravimetric studies

The plot of cumulative weight gain (mg/cm^2) as a function of time expressed in number of cycles is shown in Fig. 6.18. The values of overall weight gain after 50 cycles of oxidation for Stellite-6 coated Ti-31, Superco-605 and MDN-121 are found to be 4.09, 0.92 and 0.92 mg/cm^2 , respectively. Evidently, the coated Ti-31 showed a maximum weight gain during the oxidation studies in an air environment as compared to coated Superco-605 and MDN-121.

6.4.3 X-ray diffraction analysis

The X-ray diffraction patterns of the top scale, after its exposure to air environment at 800 °C for 50 cycles are shown in Fig. 6.19. The scale on the Stellite-6 coated Ti-31, Superco-605 and MDN-121 consisted of CoO, Cr₂O₃ and NiO as major phases. The scales also showed the presence of FeO, MnO, WO₃, and SiO₂ as minor oxides, CrC, as an intermetallic compounds and NiAl₂O₄, NiCr₂O₄, CoAl₂O₄ and CoCr₂O₄ as spinals. They all are in small fractions.

6.4.4 SEM/EDX analysis

The morphological features of the oxidized Stellite-6 coated samples along with EDX analysis are shown in Fig. 6.20. The features indicate that the nodular morphology grows in a non-uniform fashion during the thermal cycling study. EDX analysis of the scale on the coating shows the formation of Cr₂O₃ and CoO as major

phases. The scale on coated Ti-31 (Fig. 6.20a) shows Cr_2O_3 in the range of 45 to 50% with CoO 44 to 48% (all are wt %). Small quantities of FeO and NiO are also observed.

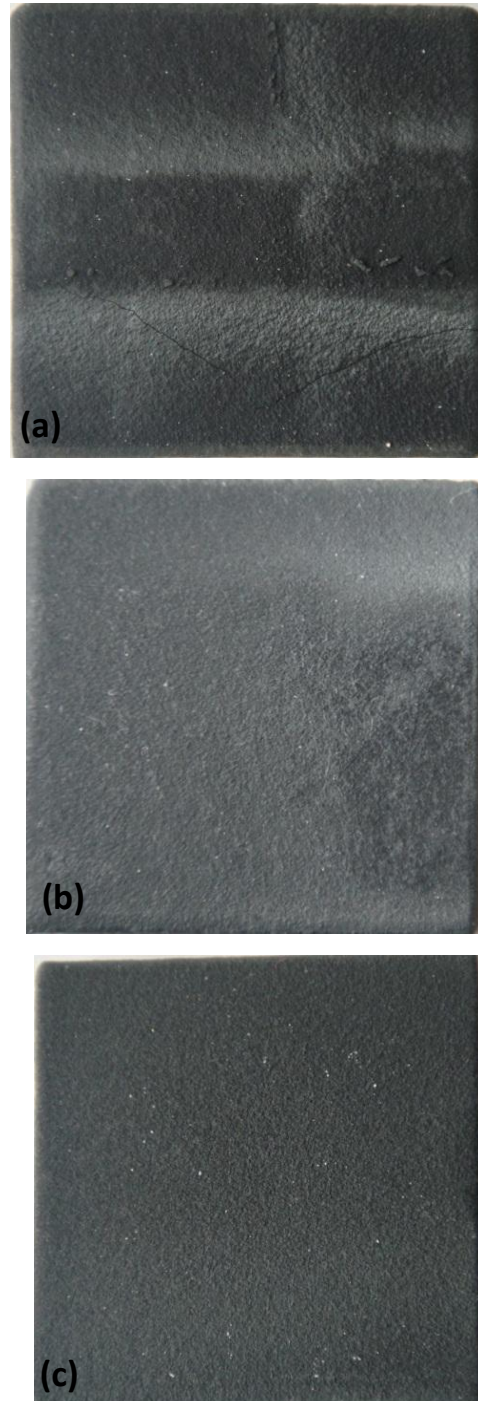


Fig. 6.17 Macrographs of Stellite-6 coating subjected to oxidation at 800 °C for 50 cycles. Size 25 X 25 X 5 mm (a) Ti-31 substrate (b) Superco-605 substrate (c) MDN-121 substrate.

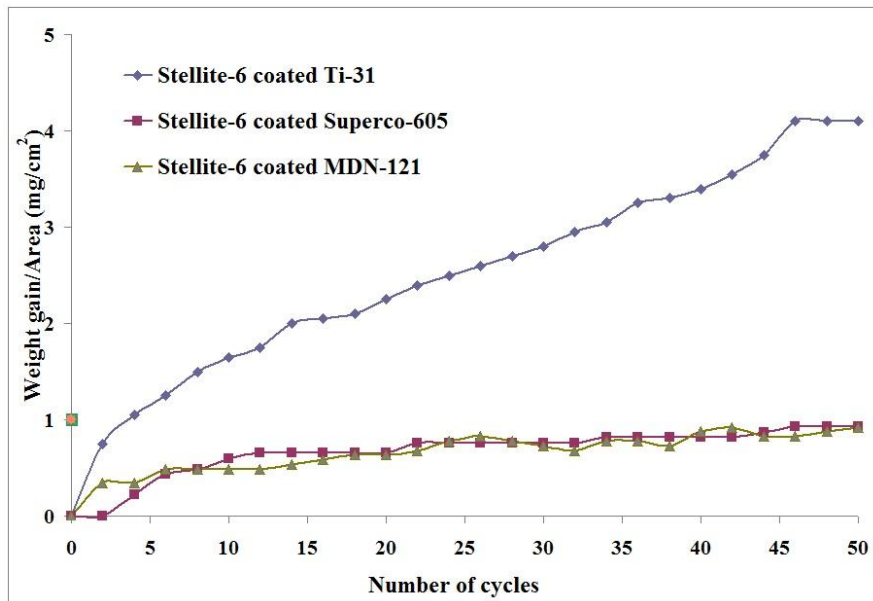


Fig. 6.18 Plot of (weight gain/area) versus number of cycles for Stellite-6 coated samples subjected to oxidation at 800 °C.

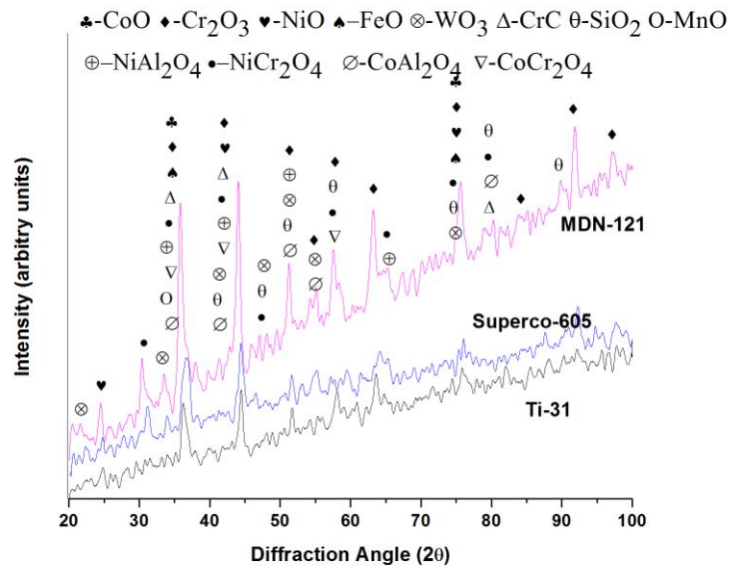


Fig. 6.19 X-ray diffraction patterns for Stellite-6 coated Ti-31, Superco-605 and MDN-121 subjected to cyclic oxidation for 50 cycles in air at 800 °C.

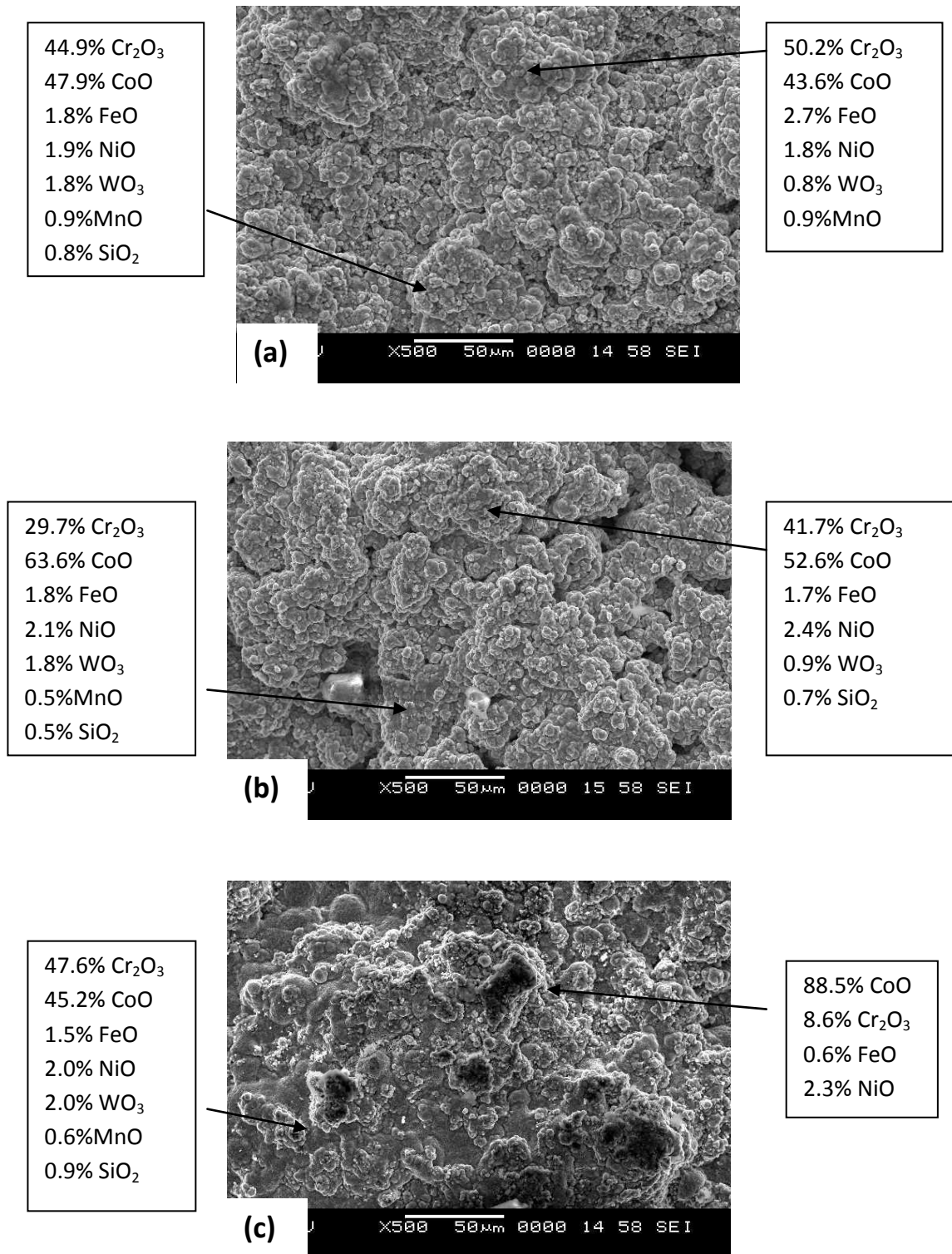


Fig. 6.20 Morphologies and EDX analysis of the Stellite-6 coated samples after oxidation for 50 cycles at 800 °C. (a) Ti-31 substrate (b) Superco-605 substrate (c) MDN-121 substrate.

The scale on coated Superco-605 (Fig. 6.20b) shows the oxide layer of Cr_2O_3 (in the range of 30 to 42%) and CoO (in the range 53 to 64%), along with small quantities of FeO and NiO . Similarly, the scale on stellite-6 coated MDN-121 steel shows Cr_2O_3 (in the range of 9 to 48%) and CoO (in the range of 45 to 89%) as major phases, with small amount of FeO and NiO .

The results of the cross sectional analysis of the oxidized, Stellite-6 coated Ti-31 is shown in Fig. 6.21. A continuous and adherent scale is formed on the coating, which has retained the dense structure of the as sprayed coating even after the oxidation run for 50 cycles. The scale formation is not uniform throughout the surface. EDX analysis of the top scale indicates that the main constituents are oxides of Al, Cr, Si and Co.

Fig. 6.22 shows the X-ray mapping of the cross-section of oxidized coating. The mapping shows a thin layer on the top of the scale enriched with Si, Al and O. Also, in this zone, the amount of Co and Ni is slightly less compared to that in the bulk.

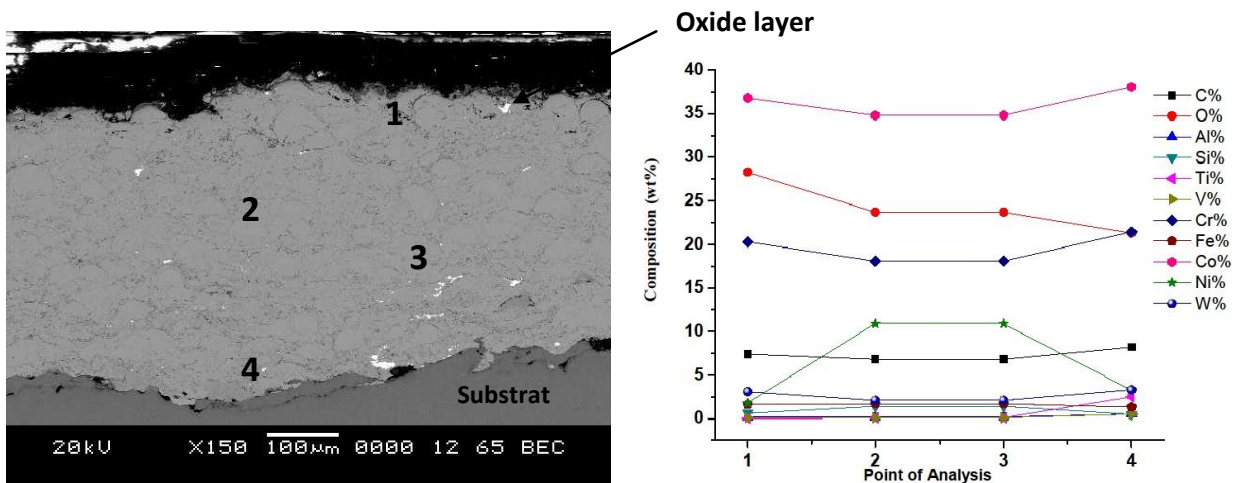


Fig. 6.21 Back scattered image and EDX analysis (wt %) across the cross-section of the Stellite-6 coated Ti-31 material subjected to oxidation for 50 cycles at 800 °C.

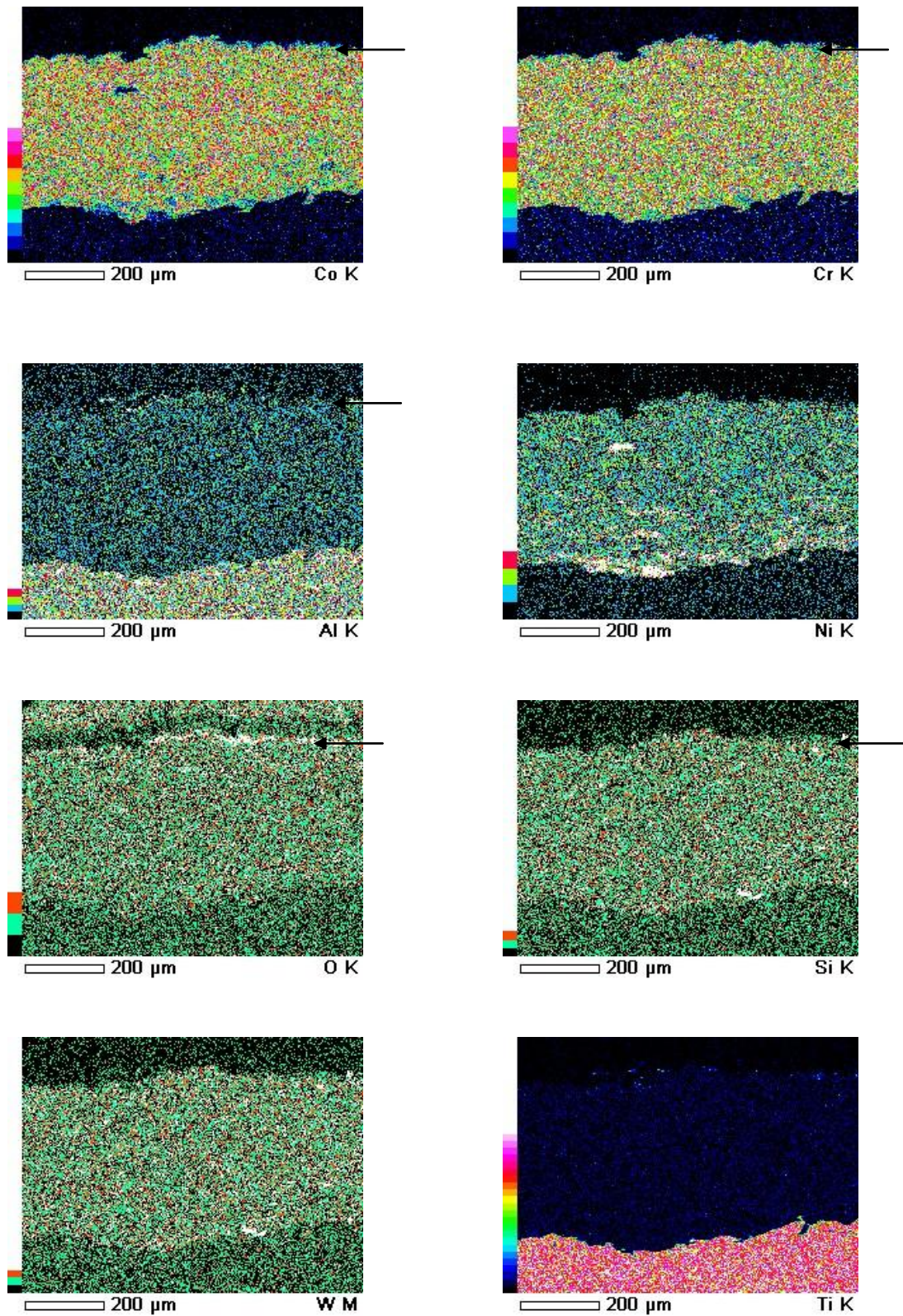


Fig. 6.22 X-ray mapping along the cross-section of the Stellite-6 coated Ti-31 material subjected to oxidation for 50 cycles at 800 °C.

6.5 SUMMARY OF OXIDATION RESULTS

Results of oxidation studies reported in section 6.1 through 6.4 for uncoated and coated alloys are summarized in Table 6.1, to highlight comparisons among the various coatings and substrate.

Table 6.1 Summary of results for uncoated and coated samples subjected to oxidation in air

Coatings	Substrate	Weight gain mg/cm ²	Parabolic constant Kp*10 ⁻⁸ g ² cm ⁻⁴ s ⁻¹	Remarks
Uncoated Samples	Ti-31	11.0389	0.0636	<ul style="list-style-type: none"> • Excessive peeling of Ti-31 • Colour changes: Ti-31- Brown, Superco-605- Green, MDN-121-Brown spots with red spots • Net weight gain: Superco-605 < MDN-121 < Ti-31
	Superco-605	0.127	----	
	MDN-121	0.324	-----	
10%Al ₂ O ₃ -CoCrAlTaY	Ti-31	4.28	0.00966	<ul style="list-style-type: none"> • Net weight gain: Superco-605 < MDN-121 < Ti-31 • Colour change: Ti-31- Grey, Superco-605-Brown, MDN-121- Brown
	Superco-605	1.03	0.00083	
	MDN-121	1.28	0.0009	

25%(Cr ₃ C ₂ - 25(Ni ₂₀ Cr)) +75% NiCrAlY	Ti-31	0.81	0.000386	<ul style="list-style-type: none"> • Net weight gain: Superco-605 < MDN-121 < Ti-31 • Colour change: Coated Ti-31, Superco-605, MDN-121 light grey turned into dark grey
	Superco-605	0.06	0.000011	
	MDN-121	0.21	0.000011	
Stellite-6	Ti-31	4.097	0.0919	<ul style="list-style-type: none"> • Crack formation on Ti-31 on top surface • Net weight gain: MDN-121 < Superco-605 < Ti-31 • Colour change: Ti-31, Superco-605, MDN-121-dark grey
	Superco-605	0.924	0.00043	
	MDN-121	0.922	0.00041	

6.6 DISCUSSION

6.6.1 Uncoated samples

From the (weight gain/area) vs. number of cycles graph (Fig. 6.2) of the uncoated samples it is observed that the Ti-31 sample showed a very high weight gain whereas the Superco-605 substrate has the least weight gain. The weight gain of the MDN-121 substrate is found to be comparatively higher than Superco-605. The weight gain after 50 cycles for the uncoated samples of Ti-31, Superco-605 and MDN-121 were found to be 11.04, 0.13 and 0.32 mg/cm², respectively. The weight gain plot for Superco-605 and MDN-121 were fluctuating during the course of study due to intense sputtering of the scale formed on the surface. Because of this measuring overall weight gain was difficult. Among Superco-605 and MDN-121, sputtering was more intense in the case of Superco-605 and due to that weight gain during some of the 50 cycles. When sputtering was taking place, there was net loss in weight and the sputtering promoted exposure of fresh material to oxidation environment. When fresh material is oxidized, weight is increased.

Further the weight gain square (mg^2/cm^4) data are plotted as a function of time in Fig. 6.23. The plot shows an observable deviation from the parabolic rate law for the Ti-31 which indicates that the oxide scale (TiO_2) is not very protective in air environment. Similar observations are reported by Anuwar et al. (2007) and Gurappa (2003). The macrograph of oxidized samples shows the spalling behaviour of the top scale. The XRD and EDX analysis shows that TiO_2 as the main phase with small amount of V_2O_5 and Al_2O_3 . The amount of Al is not sufficient to form a continuous and adherent alumina scale on the top surface. Along with discontinuous alumina, TiO_2 (rutile phase) formed on the oxidized surface. Rutile phase is not protective at high temperature in air environments. Perkins et al. (1987) and Meier et al. (1990) reported that the titanium alloys containing less than 50 at% aluminum do not form a continuous, dense and protective alumina scale upon exposure to elevated temperatures due to thermodynamic reasons. The scale (with a mixture of alumina and rutile) started to spall after reaching critical thickness because of adherence problems. Such behaviour is reported by Anuwar et al. (2007) and Gurappa (2003).

Fig. 6.23 shows plot of $(\text{weight gain/area})^2$ vs number of cycles, for three uncoated samples. This is drawn to investigate the possibility of parabolic growth behaviour, as reported by similar investigators (Sidhu et al. (2006), Kamal et al. (2008) and Sidhu et al. (2007)). Estimated parabolic rate constants (K_p) for uncoated Ti-31 is $0.0636 \times 10^{-8} \text{ g}^2\text{cm}^{-4}\text{s}^{-1}$. Also, a clear deviation from the parabolic growth behaviour is observed, indicating actual oxidation kinetics is much higher than parabolic growth kinetics. The uncoated Superco-605 and MDN-121 surfaces were undergoing intense sputtering during oxidation studies and hence K_p values are not estimated. From the earlier statements, it is imperative that, the coatings are very essential to prevent the degradation of the materials selected in this study. Similar observations are reported by Goyal et al. (2008).

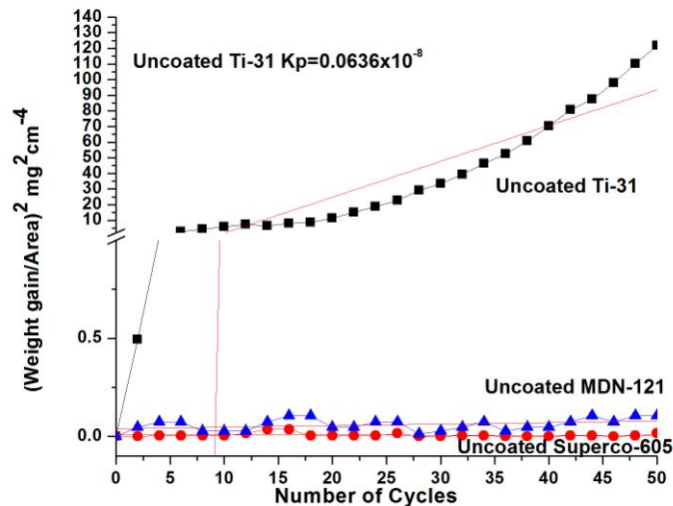


Fig. 6.23 Plot of $(\text{weight gain/area})^2$ versus number of cycles for uncoated samples subjected to oxidation for 50 cycles in air at 800 °C.

6.6.2 10% Al_2O_3 + CoCrAlTaY Coating

Using the results presented in section 6.2, the weight gain/area, after 50 oxidation cycles are 4.28, 1.03 and 1.28 mg/cm^2 for the 10% Al_2O_3 +CoCrAlTaY coated Ti-31, Superco-605 and MDN-121 samples, respectively. The weight gain/area value is comparatively higher for the 10% Al_2O_3 +CoCrAlTaY coated Ti-31 sample. The coated Superco-605 sample showed less weight gain. The difference in the values of the weight gain/area for the coated Superco-605 and coated MDN-121 is small. Thus it can be inferred that 10% Al_2O_3 +CoCrAlTaY coated Superco-605 shows the highest resistance to oxidation whereas the 10% Al_2O_3 +CoCrAlTaY coated Ti-31 has the least resistance to oxidation. Cracks appeared in the 10% Al_2O_3 +CoCrAlTaY coated Ti-31, during the course of oxidation studies and this is attributed to differences in the values of thermal expansion coefficients of the coatings and substrate. Similar observations are reported by Niranatlumpong et al. (2000), Singh (2003), Evans and Taylor (2001) and Wang et al. (2003).

Again, to investigate the possibility of parabolic growth relation, the plot of the weight gain square (mg^2/cm^4) versus number of cycles is drawn for 10% Al_2O_3 +CoCrAlTaY coated substrates and it is given in Fig. 6.24. The estimated parabolic rate constants, K_p , for the coated Ti-31, Superco-605 and MDN-121 are 0.0096×10^{-8} , 0.00083×10^{-8} and $0.0009 \times 10^{-8} \text{ g}^2\text{cm}^{-4}\text{s}^{-1}$, respectively. The parabolic rate constant K_p ,

for the coated Ti-31 is much higher compared to coated Superco-605 and coated MDN-121. It indicates that the rate of oxidation is much higher in coated Ti-31, compared to other two coated substrates. Also, the plot shows an observable deviation from the fitted parabolic rate law for the coated Ti-31. It indicates that the coating is not protective in air environment at 800 °C, under cyclic conditions. It is found that though Superco-605 has lesser K_p value the plot does not follow the parabolic behaviour to that extent (especially towards the end of 50 cycles) but it is evident that MDN-121 nearly follows parabolic behavior. Also, by comparing with K_p values for uncoated samples (section 6.1), it could be noted that the oxidation resistance value is improved by HVOF spraying of 10% $Al_2O_3 + CoCrAlTaY$ on to all three substrates.

In the case of 10% $Al_2O_3 + CoCrAlTaY$ coating on Ti-31, applied without a diffusion barrier on to the substrate, the interdiffusion between coating and the substrate is very serious and is a cause for faster degradation. A higher rate of degradation and serious oxidation is reported in similar cases by Li et al. (2010), Li-Young et al. (2011) and Hui Huang et al. (2011).

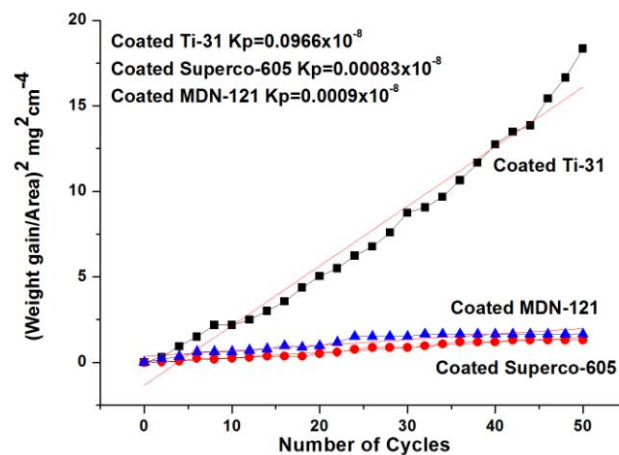


Fig. 6.24 Plot of $(weight\ gain/area)^2$ versus number of cycles for 10% $Al_2O_3 + CoCrAlTaY$ coated materials subjected to oxidation in air at 800 °C.

6.6.3 25% ($Cr_3C_2-25(Ni20Cr)$) + 75%NiCrAlY Coating

In Fig. 6.11, the plot of (weight gain/area) vs. number of cycles is presented for the case of HVOF sprayed 25% ($Cr_3C_2-25(Ni20Cr)$) + 75% NiCrAlY on Ti-31, Superco-605 and MDN-121. Coated Ti-31 showed a very high weight gain whereas

the Superco-605 substrate has the least weight gain. The weight gain of the MDN-121 substrate is found to be slightly higher than Superco-605. Thus it can be inferred that Coated Superco-605 shows the highest resistance to oxidation whereas the coated Ti-31 coated substrate has the least resistance to oxidation.

Further, the weight gain square (mg^2/cm^4) data are plotted as a function of time and it is given in Fig. 6.25. The parabolic rate constants, K_p , for the coated Ti-31, Superco-605 and MDN-121 are 0.00038×10^{-8} , 0.00001×10^{-8} and $0.00001 \times 10^{-8} \text{ g}^2 \text{ cm}^{-4} \text{ s}^{-1}$, respectively. This also indicates the coated Ti-31, undergoes rapid oxidation compared to other two coated substrates. Like in alumina coated substrates, the plot for coated Ti-31, also deviates from the parabolic growth behaviour. It also indicates that the coating is less effective as far as resistance to thermal oxidation in air environment. Literature also says that for a given coating process, the coated Ti-31 has poor resistance compared to other substrates with the Cr_3C_2 -NiCr coating (Anuwar et al. (2007), Yuan et al. (2008), Guo et al. (2006)).

The XRD and EDX analysis show that the scale formed in 25% (Cr_3C_2 -25(Ni20Cr)) + 75% NiCrAlY coated, followed by oxidation and have α - Al_2O_3 , Cr_2O_3 and NiO as major phases. Some amount of oxides are visible at the splat boundaries, as displayed in O map (Fig 6.16) This is attributed to oxidation of the surface of the splats, during HVOF spraying of the coating. Never the less, there is a clear indication of oxidation of the top of the coating (a few micrometers), as indicated by arrow in the oxidation map in Fig 6.16. The scales mainly consist of Cr_2O_3 . Similar observations are reported by Kamal et al. (2009). The oxide layer is continuous and adherent. This oxide layer acted as diffusion barriers to the inward diffusion of oxidizing species. As a consequence, the formation of oxides is limited mainly to the surface of the coatings. The steady state of oxidation might have reached with the experimental duration. This explains improved protection by the formation of a thin oxide scale on the coated surface. Similar features are reported by various investigators (Sidhu et al. (2006), Sidhu et al. (2007) and Kamal et al. (2008)).

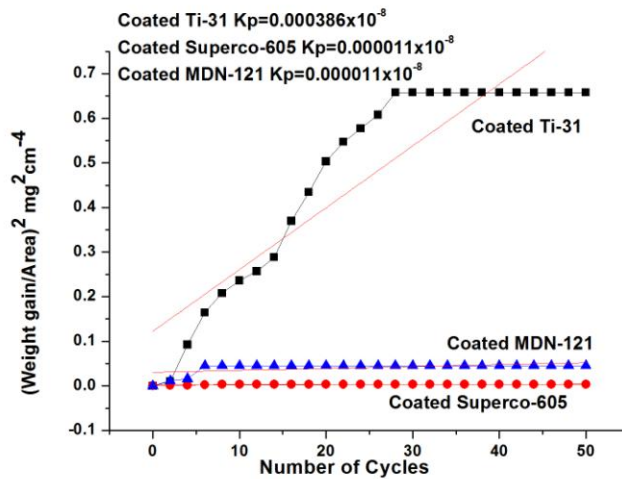


Fig. 6.25 Plot of $(\text{weight gain/area})^2$ versus number of cycles for 25% ($\text{Cr}_3\text{C}_2\text{-}25(\text{Ni}_{20}\text{Cr})$) + 75% NiCrAlY coated samples subjected to oxidation at 800 °C for 50 cycles.

6.6.4 Stellite-6 coating

In Fig. 6.18, plot of (weight gain/area) vs. number of cycles is presented for the case of HVOF sprayed Stellite-6 coated Ti-31, Superco-605 and MDN-121. From the plot, the Stellite-6 coated Ti-31 sample has maximum weight gain and coated Superco-605 sample has the least weight gain. The weight gain of the coated MDN-121 sample is same as than that for coated Superco-605. Thus it can be inferred that the Stellite-6 coated Superco-605 shows the highest resistance to cyclic oxidation whereas the coated Ti-31 sample has the least resistance to oxidation. Further, the weight gain square (mg^2/cm^4) data are plotted as a function of time in Fig. 6.26. The parabolic rate constants, K_p for the Stellite-6 coated Ti-31, Superco-605 and MDN-121 are 0.0919×10^{-8} , 0.00043×10^{-8} and $0.00041 \times 10^{-8} \text{ g}^2\text{cm}^{-4}\text{s}^{-1}$, respectively.

The plot shows an observable deviation from the parabolic rate law for the coated Ti-31, especially towards the end of the oxidation cycles. This indicates that accelerated oxidation takes place and the coating and the scale formed on the surface of the coating due to oxidation is not able to protect the sample to a major extent. Also, the plots and K_p values are of similar for coated MDN-121 and Superco-605. This indicates that the Stellite-6 coating performance is similar, for both the MDN-121 and Superco-605 samples. The appearance of cracks on the Stellite-6 coated Ti-31 sample, during oxidation studies may be attributed to different values of thermal

expansion coefficients, as reported by Niranatlumpong et al. (2000), Singh (2003), Evans and Taylor (2001) and Wang et al. (2003).

The XRD and EDX analysis shows that the scale on the Stellite-6 coated and oxidized surface is rich in Cr_2O_3 and CoO as major phases in all three coated samples. As far as protection is concerned, they are desired (Sidhu et al. (2007)) and they are responsible for improved oxidation resistance exhibited by the Stellite-6 coated samples compared to uncoated samples. Also, spinals of cobalt-chromium (CoCr_2O_4) and nickel-chromium (NiCr_2O_4) are observed in the scales. They add to the improved performance of the Stellite-6 coatings. Sidhu et al. (2006B) reported that the spinals, like, CoCr_2O_4 , blocks the diffusion of species (oxide ions) through the CoO and thus suppressing the further formation of this oxide (CoO).

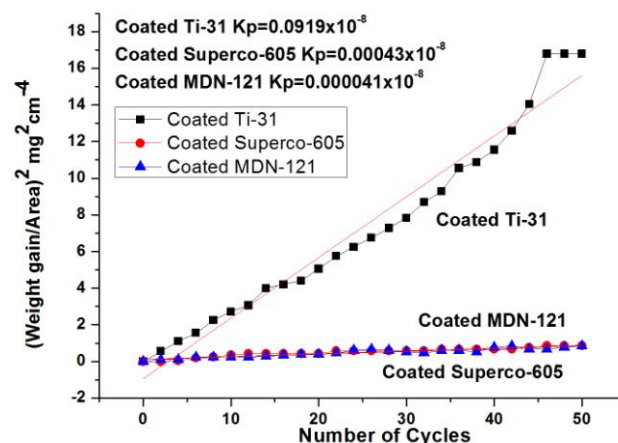


Fig. 6.26 Plot of $(\text{weight gain/area})^2$ versus number of cycles for Stellite-6 coated samples subjected to oxidation at 800°C .

6.7 COMPARATIVE DISCUSSION

The cumulative weight gain (mg/cm^2) for uncoated and HVOF coated 10% $\text{Al}_2\text{O}_3+\text{CoCrAlTaY}$, 25% $(\text{Cr}_3\text{C}_2-25(\text{Ni}20\text{Cr})) + 75\% \text{NiCrAlY}$ and Stellite-6 subjected to oxidation in air environment for 50 cycles at 800°C is shown in Fig. 6.27. From the bar charts, it can be inferred that the weight gains for all the HVOF coated samples are significantly lower than that of uncoated samples in air environment. It must be stressed that uncoated Superco-605 and MDN-121 were

undergoing sputtering during the course of the study. Uncoated Ti-31 suffered higher oxidation rate and spalling of oxide scale. The stress developed due to higher volume of oxide scale (Pilling-Bedworth ratio) leads to cracks, in turn resulted in spallation.

Among various coatings applied for three different substrates used in this investigation, it can be inferred that the 25% (Cr_3C_2 -25(Ni20Cr)) + 75%NiCrAlY coating provides the highest oxidation resistance, whereas 10% Al_2O_3 +CoCrAlTaY coating offered the least resistance. The oxidation resistance offered by the Stellite-6 coating is marginally better than that of 10% Al_2O_3 +CoCrAlTaY. The relative oxidation resistance of the various coatings under study can be arranged in the following sequence:

$$[25\% (\text{Cr}_3\text{C}_2\text{-}25(\text{Ni}20\text{Cr})) + 75\% \text{NiCrAlY}] > [\text{Stellite-6}] > [10\% \text{Al}_2\text{O}_3 + \text{CoCrAlTaY}] > \text{Uncoated}$$

The superior oxidation resistance of 25% (Cr_3C_2 -25(Ni20Cr)) + 75%NiCrAlY could be attributed to the thick protective oxide scale developed on the surface during cyclic oxidation. The uppermost layer of the oxide scale mainly consisted of continuous film of Cr_2O_3 which has minimum affinity towards atmospheric air. Added to that the coating was dense and impervious. The slow oxidation kinetics as well as good parabolic curve fitting as observed during the thermogravimetric studies shows that the oxidation is diffusion controlled and both Stellite-6 coating and 25% (Cr_3C_2 -25(Ni20Cr)) + 75%NiCrAlY coating are effective in reducing the diffusion of oxidizing species.

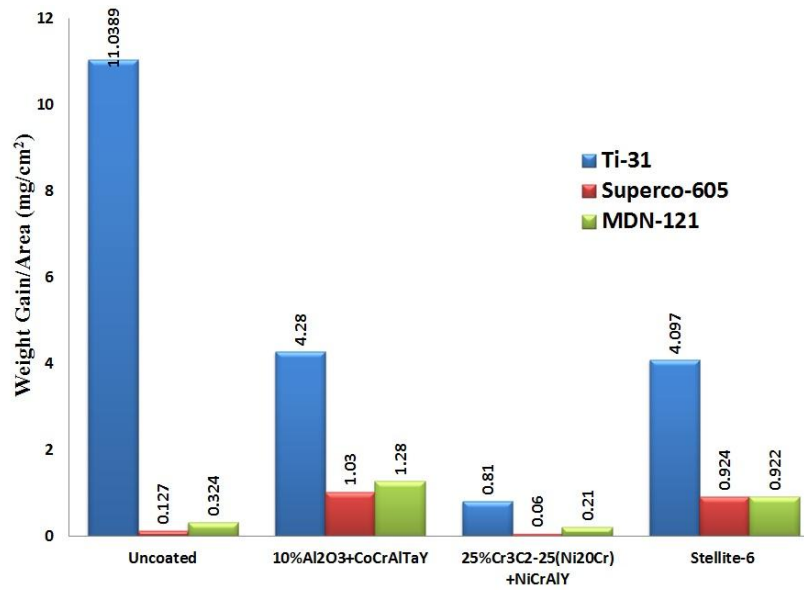


Fig. 6.27 Bar chart showing cumulative weight gain (mg/cm^2) for uncoated and HVOF coated samples subjected to oxidation in air environment for 50 cycles at $800\text{ }^\circ\text{C}$.

CHAPTER 7

SOLID PARTICLE EROSION STUDIES

This chapter deals with solid particle erosion studies on uncoated samples (Ti-31, Superco-605, MDN-121), and HVOF sprayed 10% Al₂O₃-CoCrAlTaY, 25% (Cr₃C₂-25(Ni₂₀Cr)) +75% NiCrAlY and Stellite-6 on Ti-31alloy. Erosion studies were done with impact angles of 30°, 60° and 90°.

7.1 SOLID PARTICLE EROSION STUDIES ON UNCOATED ALLOYS

7.1.1 Ti-31 alloy

The photographs of the erosion scar produced on the Ti-31 sample, with 30°, 60° and 90° of erodent impact angle are shown in Fig. 7.1. The centre portion of the eroded scar (A) represents a localized region of material removal and it is surrounded by a region of elastically loaded material (B). The loss in weight of the sample after each 5 minutes is measured and using weight loss and mass of the erodent, erosion rate is measured as follows.

Erosion rate (g/g) = Cumulative weight loss of sample/ Mass of erodent

An erosion rate curve is drawn as plot of erosion rate versus cumulative mass of the erodent, for each erodent impact angle.

Steady state volume erosion rate is estimated as follows.

Steady state volume erosion rate (cm³/g) = Average of erosion rate/ Density

The erosion rate curves along with the bar chart indicating the steady state volume erosion rate are shown in Fig. 7.2. From Fig. 7.2a, the sample shows highest erosion rate, when it is impacted at 30° and minimum erosion rate when it is impacted at 90°. A similar trend is observed in steady state volume erosion rate (Fig. 7.2b) also. This is characteristic behaviour of materials which exhibit ductile mode of erosion (Ramesh et al. (2010)). In general, erosion rate curves go up, reaching a peak after 50-65 g of erodent mass and subsequently, dropping a bit. Similar behaviour is observed in ductile steels eroded at 90° (Murthy et al. (2001), Hutchings (1992), Levy (1986)).

Fig. 7.3 shows the micrographs of erosion scar produced on uncoated Ti-31, at an impact angle of 30° . The micrographs show clear indications of material damage in the form of ploughing (Fig. 7.3a), groove (Fig. 7.3b) and loose debris (Fig. 7.3c). The loose debris is predominantly oxide of Ti. Along with plough marks indications of plastic deformation is also observed at an impact angle of 30° . Fig. 7.4 shows the micrographs of erosion scar on uncoated Ti-31. Fig. 7.4a shows material damage in the form of ploughing. In Fig. 7.4b, the entrapment of the erodent (SiO_2) within the substrate Ti-31 is observed and in Fig.7.4c, the crater created when the embedded erodent is fallen off during the erosion process is presented. In Fig. 7.5, microstructures on the scar produced due to normal impact (90°) of erodent on the uncoated Ti-31 are presented. Microstructures present evidences of ploughing (Fig. 7.5a), embedment of silica erodent (Fig. 7.5b) and groove (Fig. 7.5c).

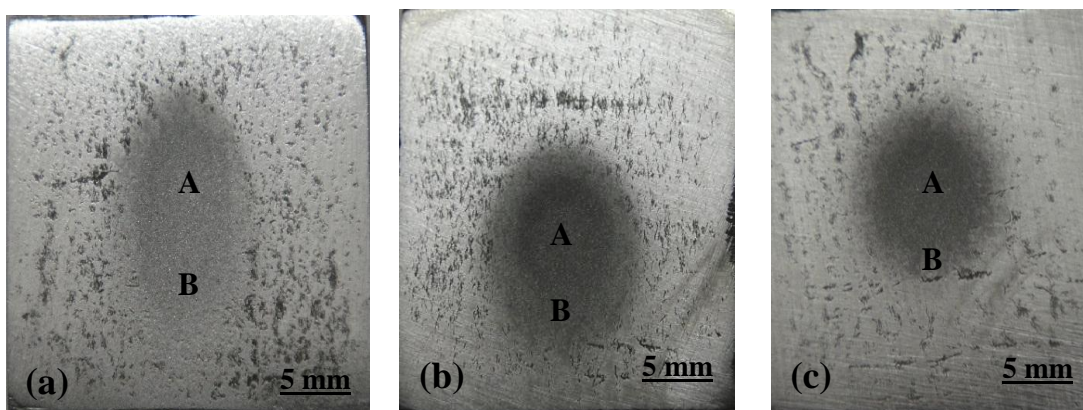


Fig. 7.1 Macrographs of uncoated Ti-31 alloy impacted by silica erodent at different angles. (a) Impact angle of 30° (b) Impact angle of 60° (c) Impact angle of 90° .

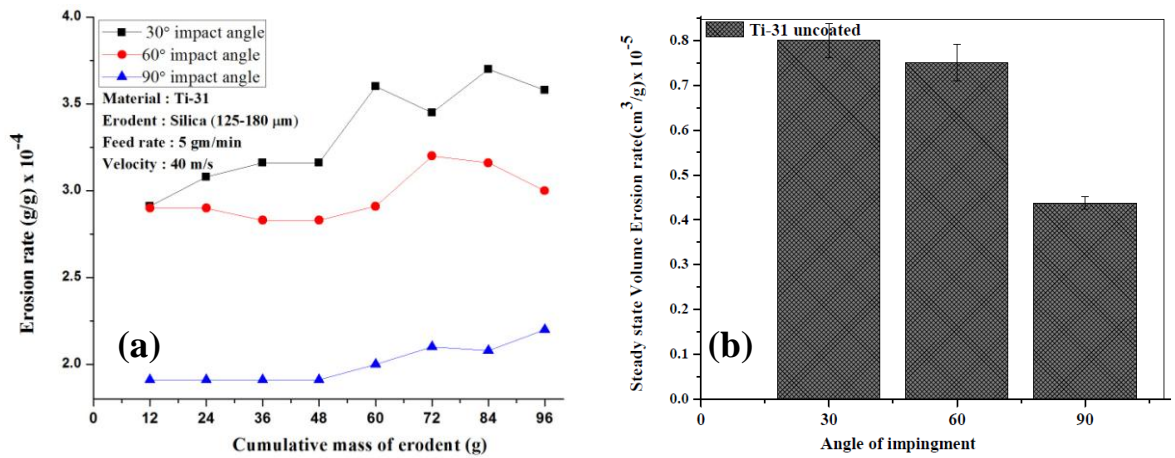


Fig. 7.2 Plot of erosion rate versus cumulative mass of erodent of uncoated Ti-31 alloy subjected to erosion at 30°, 60° and 90° impact angle. (a) Variation of the erosion rate (b) Histogram illustrating the steady state volume erosion rate.

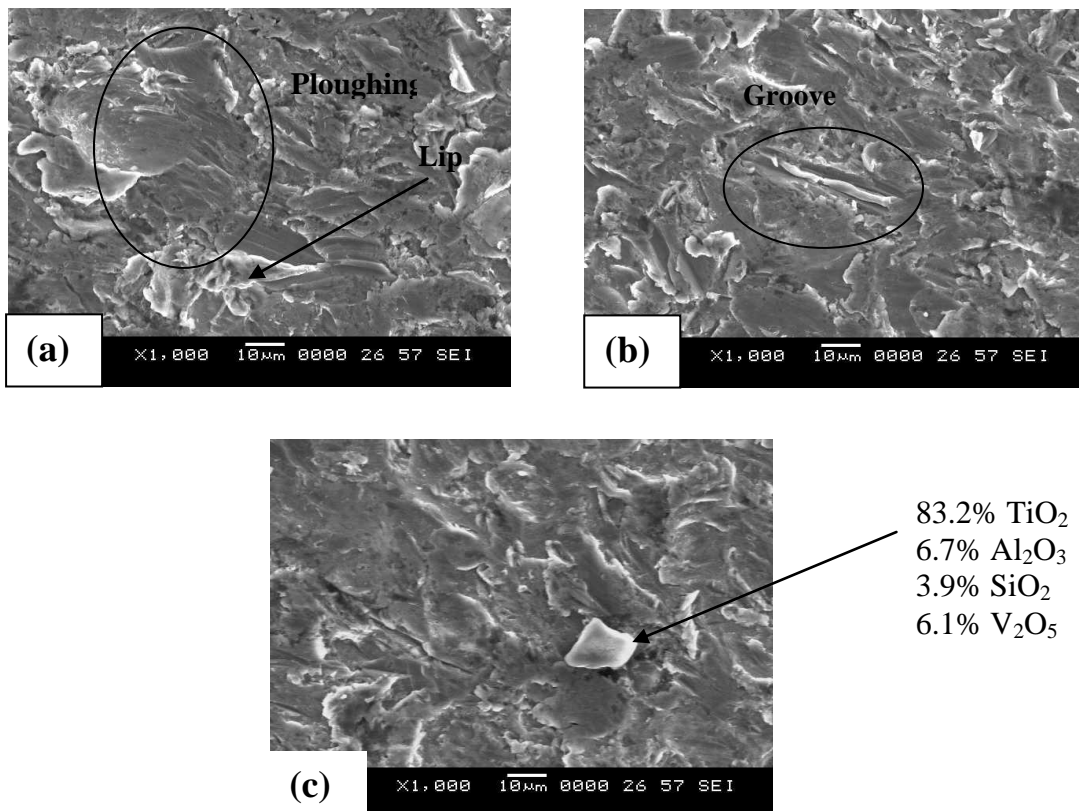


Fig. 7.3 SEM micrographs showing the morphology of eroded Ti-31 at an impact angle of 30°.

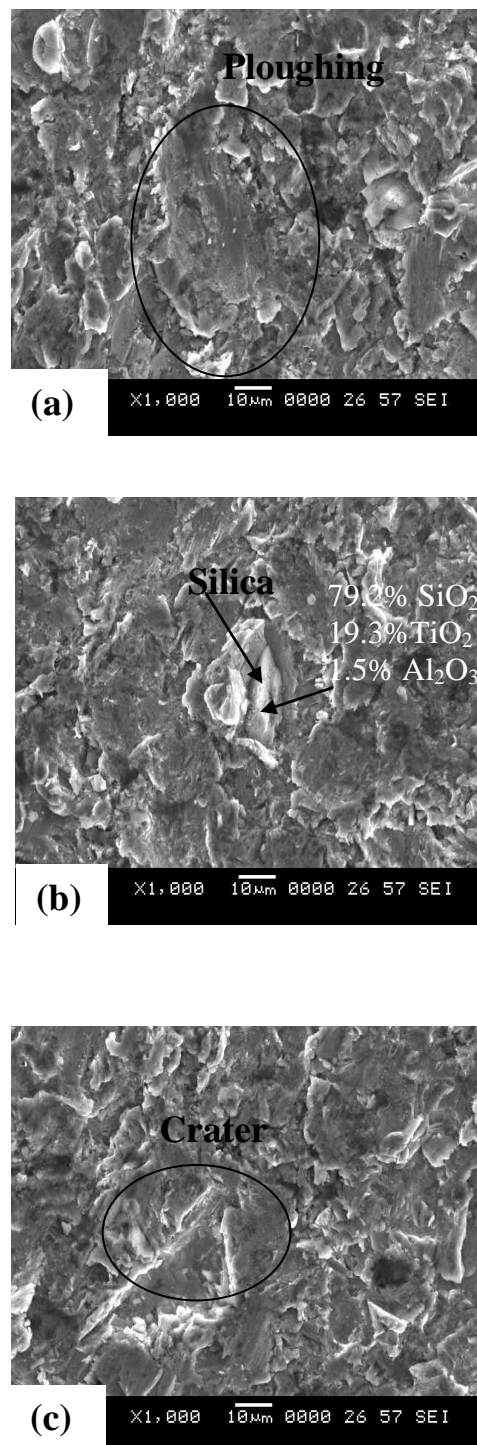


Fig. 7.4 SEM micrographs showing the morphology of eroded surfaces on uncoated Ti-31, with an impact angle of 60°.

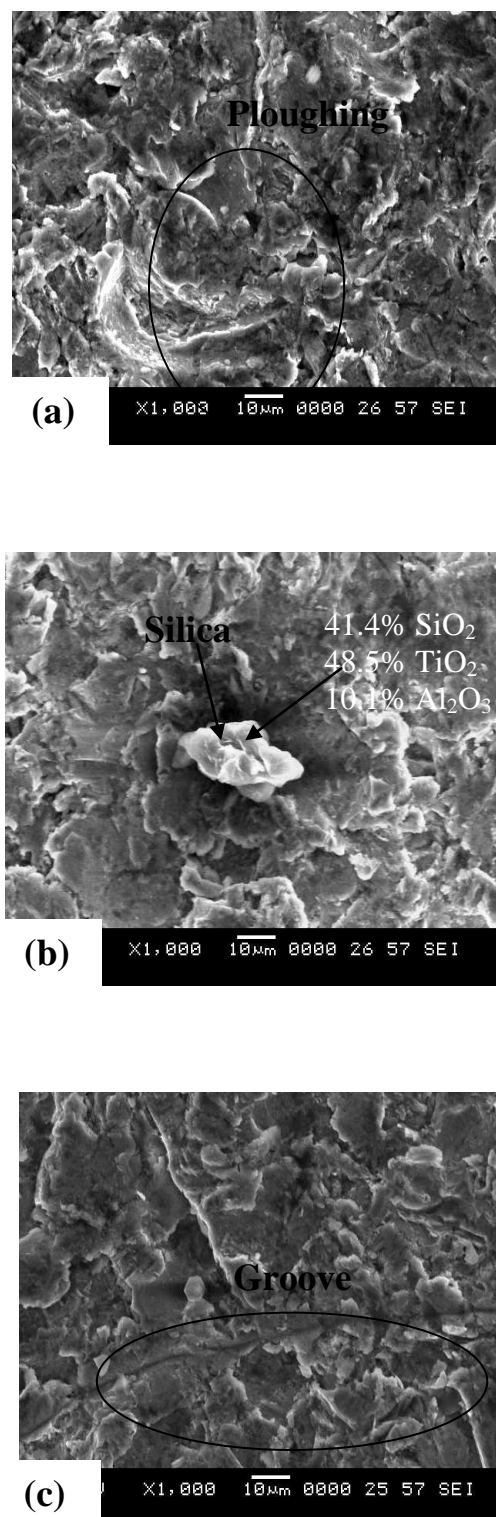


Fig. 7.5 SEM micrographs showing the morphology of Ti-31 eroded with silica erodent at an angle of impact of 90°.

7.1.2 Superco-605

The photographs of the erosion scar produced on the Superco-605 sample, with 30°, 60° and 90° of erodent impact angle are shown in Fig. 7.6 a, b, c, respectively. The centre portion of the eroded scar (A) represents a localized region of material removal and it is surrounded by a region of elastic loading (B). Erosion rate and steady state volume erosion rate are estimated as explained in section 7.1.1. The erosion rate curves along with the bar chart indicating the volumetric steady state wear loss are shown in Fig. 7.7. It is seen that, the steady state volume erosion rate is highest at 30° and least at 90° impact angle (Fig. 7.7b). This is the characteristic behaviour of materials which exhibit ductile mode of erosion. Fig. 7.8 shows microstructural details in the scar produced on uncoated Superco-605 using 30° impact angle. The microstructures show damage in the form of ploughing (Fig. 7.8a), entrapment of debris (Fig. 7.8b) and groove formation (Fig. 7.8c). Similarly, Fig. 7.9 shows microstructural details in the scar produced using impact angle of 60°. It also shows material damage in the form of ploughing (Fig. 7.9a), groove formation (Fig. 7.9b) and craters (Fig. 7.9c). Possibly, craters are formed due to falling off of entrapped erodent particles. Fig. 7.10 shows micrographs presenting the type of material damage during the 90° impact of erodent. Here also, the material damage by ploughing (Fig. 7.10a), crater formation (Fig. 7.10b) and entrapment of erodent particles is observed.

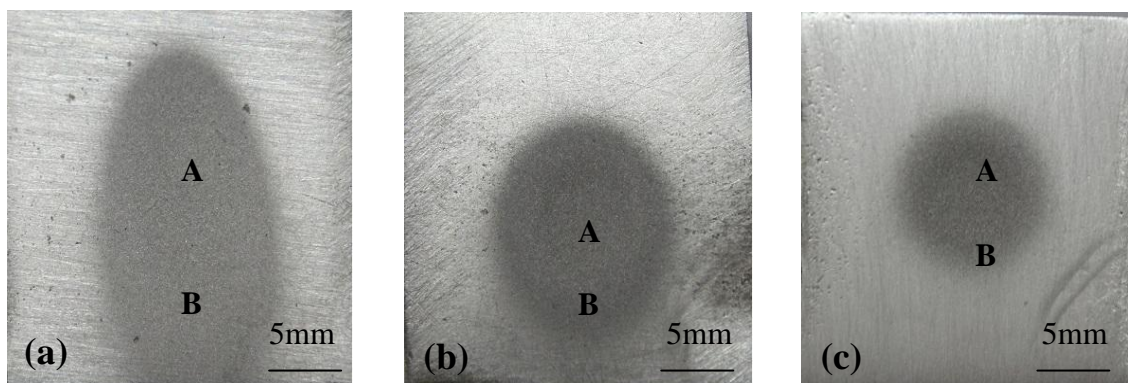


Fig. 7.6 Macrographs of uncoated Superco-605 superalloy impacted by silica erodent at different angles. (a) Impact angle of 30° (b) Impact angle of 60° c) Impact angle of 90°.

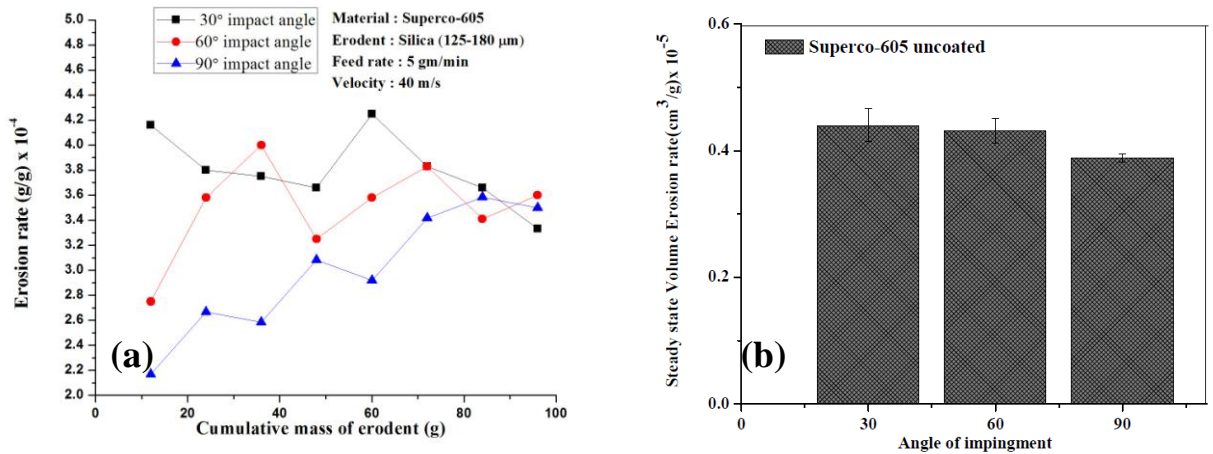


Fig. 7.7 Plot of erosion rate of uncoated Superco-605 superalloy impacted at 30°, 60° and 90° impact angle. (a) Variation of the erosion rate (b) Histogram illustrating the steady state volume erosion rate.

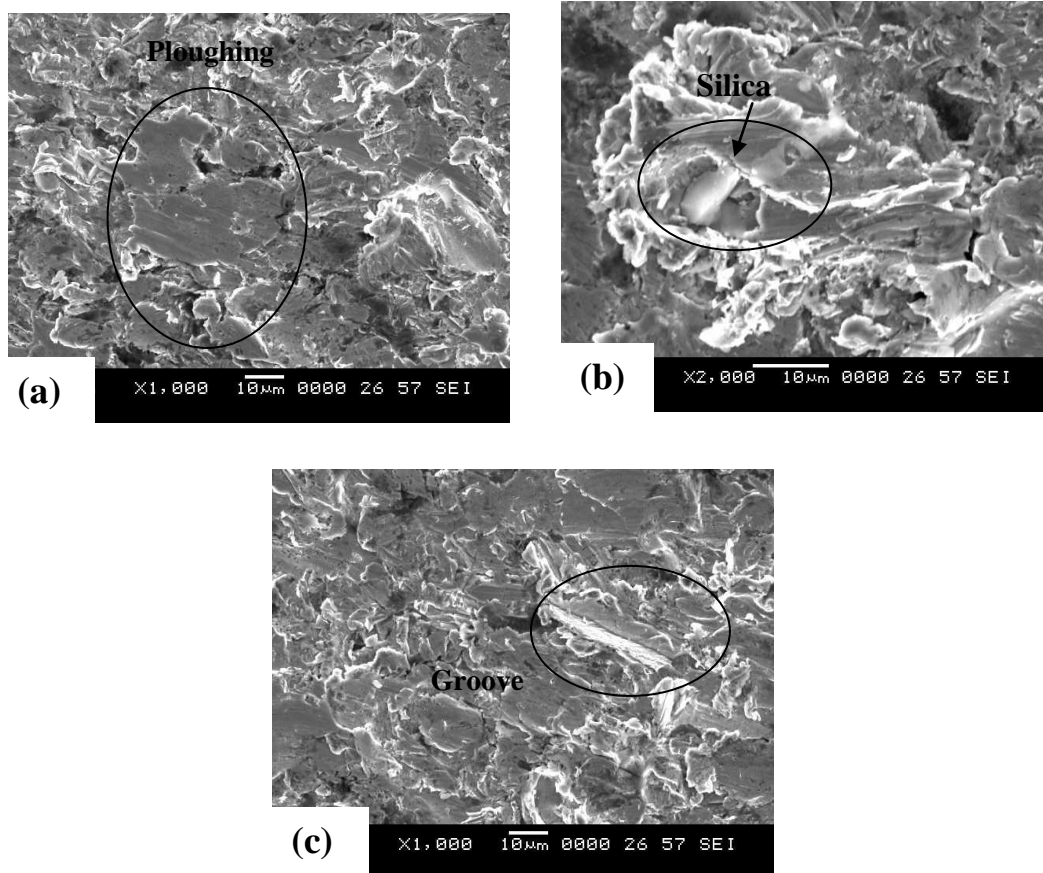


Fig. 7.8 SEM micrographs showing the morphology of eroded surfaces on uncoated Superco-605 with an impact angle of 30°.

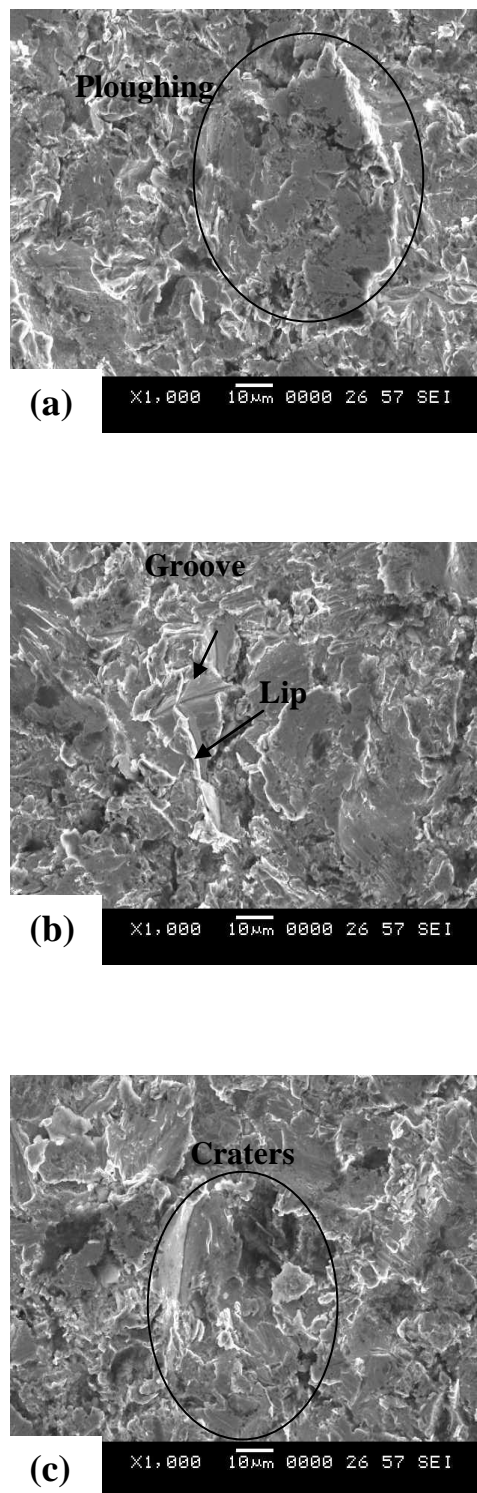
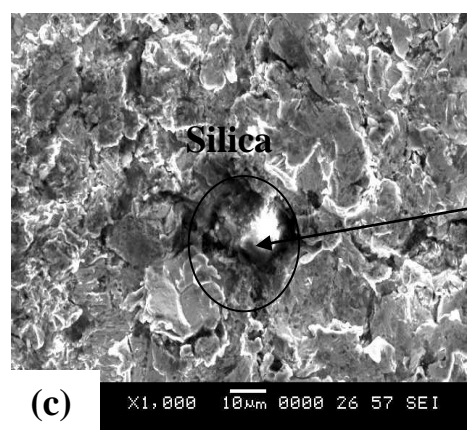
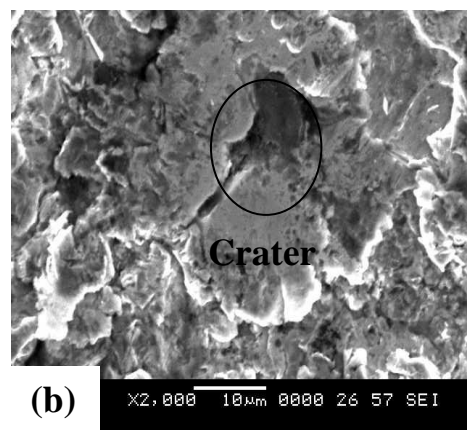
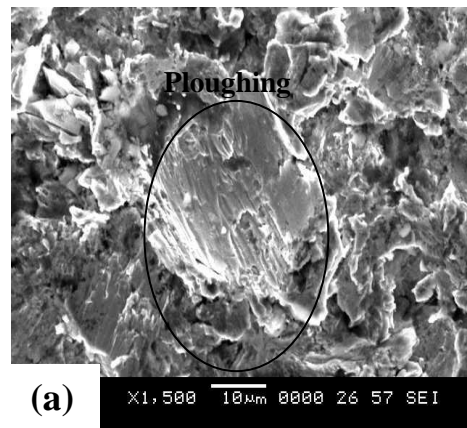


Fig. 7.9 SEM micrographs showing the morphology of eroded surfaces on uncoated Superco-605, with an impact angle of 60°.



67.3% SiO₂
 26.6% FeO
 5.2% CoO
 0.9% NiO

Fig. 7.10 SEM micrographs showing the morphology of eroded surfaces on uncoated Supercor-605 with an impact angle of 90°.

7.1.3 MDN-121

The photographs of the erosion scar produced on the MDN-121 sample, with 30°, 60° and 90° erodent impact angles are shown in Fig. 7.11 a, b, c, respectively. Erosion rate and steady state volume erosion rates are estimated using procedure given in section 7.1.1. It is seen that, the steady state volume erosion rate of the MDN-121 at 30° impingement is higher than that at 60°, 90° (Fig. 7.12b). This is the characteristic behaviour of ductile material under erosion conditions. Similar observations are reported in boiler tube steel by Murthy et al. (2001), Sidhu et al. (2007), Kumar et al. (2008) and Ramesh et al. (2010).

Fig. 7.13 shows the scanning electron micrographs of the eroded scar at 30° impact angle by the impinging erodent particles. There are indications of the sample damage by the silica particles by ploughing (Fig. 7.13a), crater formation (Fig. 7.13b) and the groove formation (Fig. 7.13c). The microstructural features in the scar produced by the erodent particles at 60° impact angle indicates the material damage is due to ploughing, groove formation and entrapment of erodent particles (Fig. 7.14a, b and c). Similarly, the microstructures in the scar produced by the erodent, at 90° impact angle, also indicates that the material damage is due to ploughing and entrapment of silica particles.

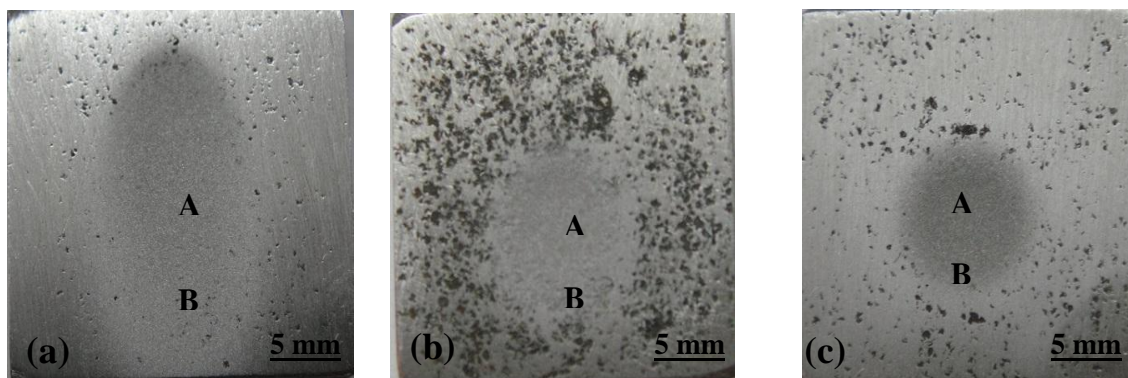


Fig. 7.11 Macrographs of uncoated MDN-121 impacted by silica erodent at different angles. (a) Impact angle of 30° (b) Impact angle of 60° c) Impact angle of 90° .

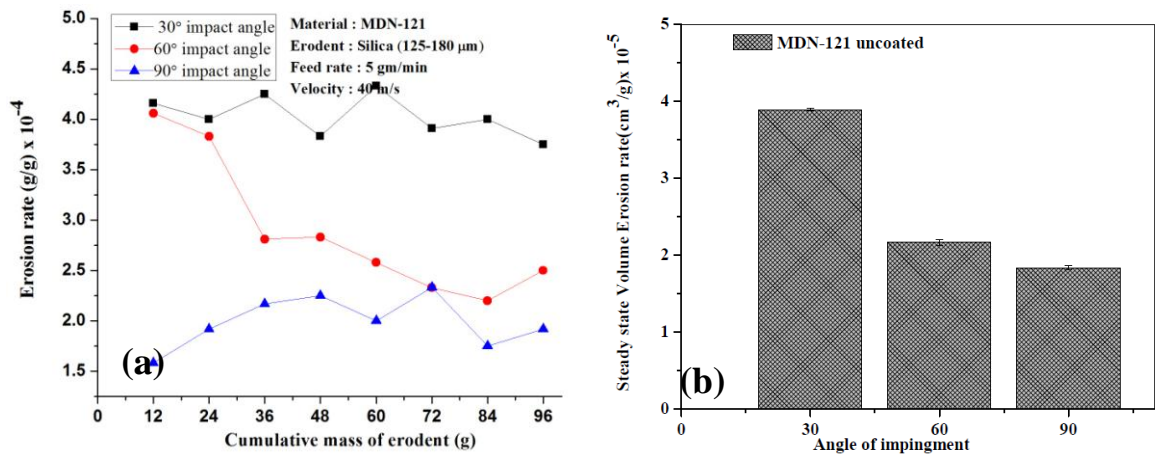


Fig. 7.12 Plot of erosion rate versus cumulative mass of erodent of uncoated MDN-121 steel subjected to erosion at 30°, 60° and 90° impact angle. (a) Variation of the erosion rate (b) Histogram illustrating the steady state volume erosion rate.

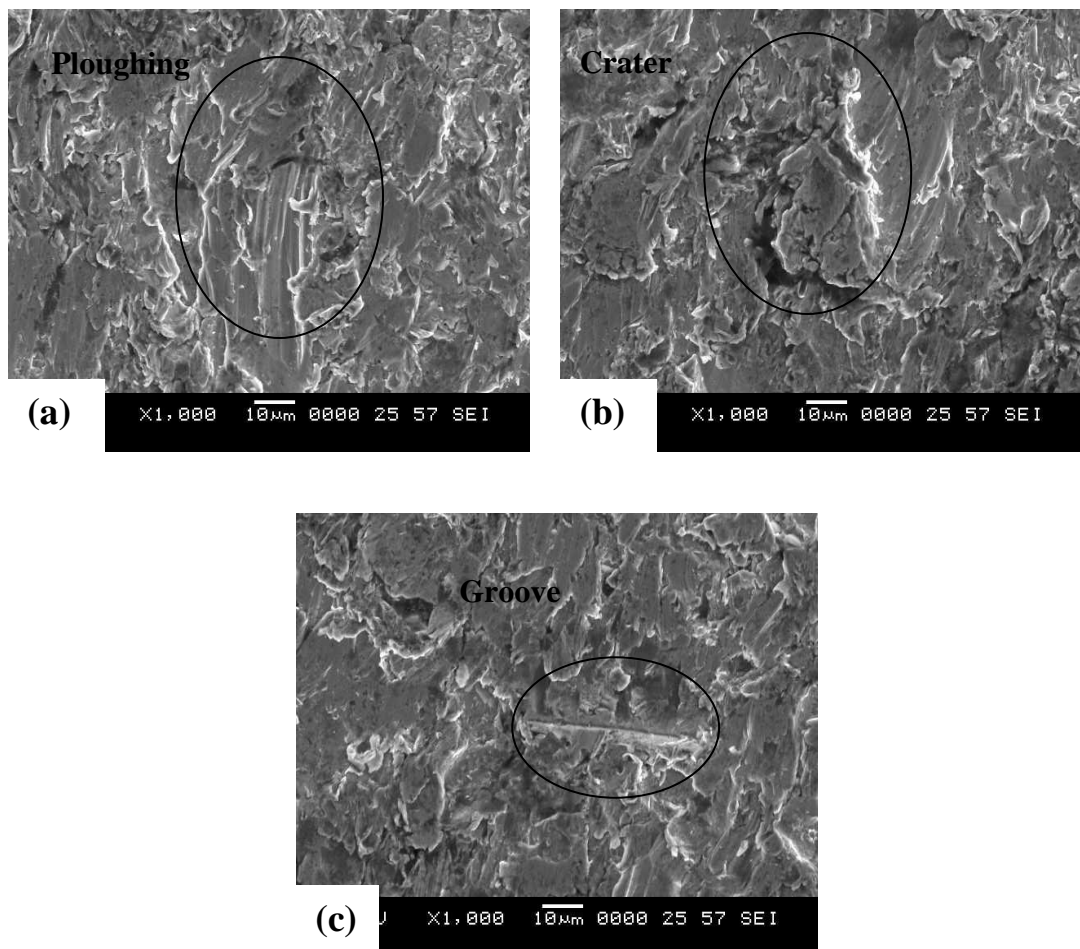


Fig. 7.13 SEM micrographs showing the morphology of eroded surfaces on uncoated MDN-121, with an impact angle of 30°.

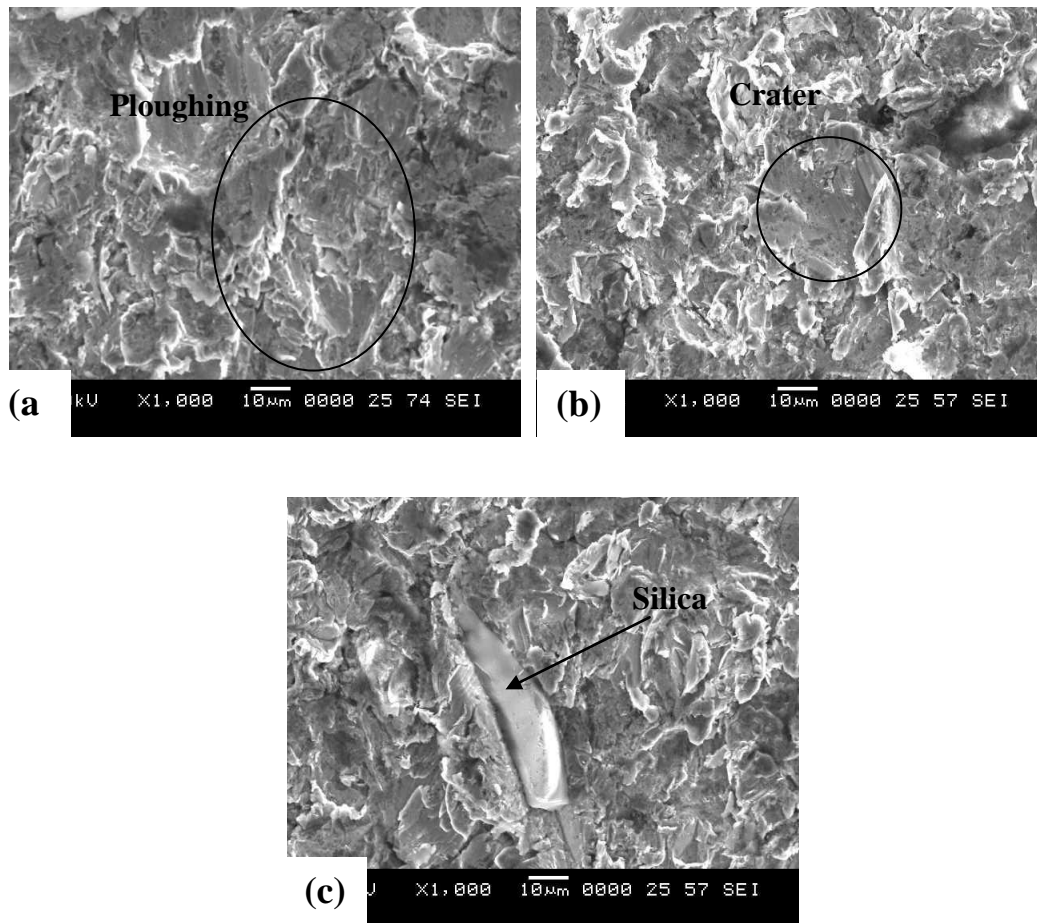


Fig. 7.14 SEM micrographs showing the morphology of eroded surfaces on uncoated MDN-121, with an impact angle of 60°.

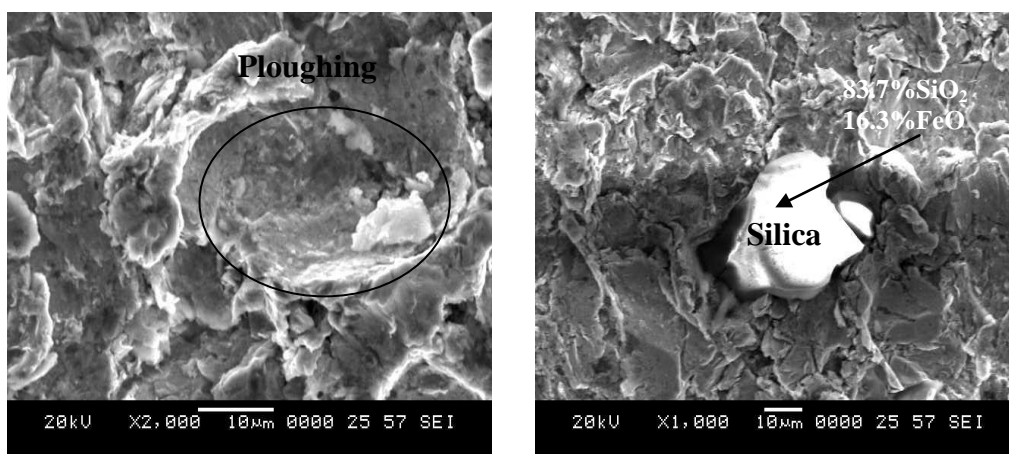


Fig. 7.15 SEM micrographs showing the morphology of eroded surfaces on uncoated MDN-121, with an impact angle of 90°.

7.1.4 Discussion

Plot of erosion rate as a function of the mass of the erodent indicates that for all samples (Ti-31, Superco-605 and MDN-121), the erosion rate is maximum for the case of erosion at 30° angle of impact. The erosion rate is minimum for the case of 90° impact angle. The plots of steady state volume erosion rate vs angle of impact, also indicates that the steady state volume erosion rate is minimum at 90° angle of impact and maximum for 30° angle of impact, for all uncoated samples. Similar behaviour is reported in high temperature materials and explained using relative hardness of erodent particles and the sample being eroded (Lathabai et al. (1998), Hussainova et al. (1999), Shipway and Hutchings (1996), Hearley et al. (1999)). The silica particles used in the present study has an average hardness value of 880Hv (Hp) and, for the Ti-31, Superco-605 and MDN-121, it is 390Hv, 406Hv and 306Hv (Ht), respectively. The ratio of Hp/Ht for Ti-31, Superco-605 and MDN-121 is approximately 2.25, 2.16 and 2.87, respectively. At 90° angle of impact, the harder silica (erodent) particles penetrates into the relatively soft sample surface and acts as a shield against further particles (which are impacting at 90°). This reduces further erosion. When erodent particles impacts at 30°, the hard silica particles, which also have sharp edges and corners, remove the material by ploughing action, continuously. This causes higher value of erosion rate, in the case of 30° impacting angle. All the three substrate materials exhibit ductile erosion behaviour. It is revealed by steady state volume erosion rate vs impact angle plots as presented in Fig. 7.2, Fig. 7.7 and Fig. 7.12 for Ti-31, Superco-605 and MDN-121, respectively. Similar observations are reported by Mishra et al. (2006) and Tabakoff (1995).

The ploughing of the sample surface by the erodent particles is a common method of material removal and SEM micrographs indicate it. Ploughing takes place extensively at 30° impact angle compared to 90° impact angle, for all three uncoated samples. SEM micrographs also indicate severe plastic deformation along with ploughing. The hard silica particles have sheared the material towards sides and in turn produced material lips. Erosion damage with plastic deformation is common in the case of ductile materials. It is reported that ductile materials show more erosion wear at lower impact angles and ploughing is an important mode of wear damage

(Murthy et al. (2001) Hutching (1992), Sidhu et al. (2007) and Kumar et al. (2008)). At impact angles of 60° and 90°, erosive loss is less compared to 30° impact angle. This is due to embedment of silica particles (erodent) in the target material and this is more at a higher impact angle. This acts as a shield against further impacting particles (Mishra et al. (2006), Sidhu et al. (2007), Ramesh et al. (2010)).

In a few situations, the embedded silica particles have fallen off and this has resulted in the formation of cavities. The cavities increase the rate of erosion loss.

7.2 SOLID PARTICLE EROSION STUDIES ON COATED SAMPLES

Solid particle erosion studies were done on 10% Al₂O₃ + CoCrAlTaY, 25% (Cr₃C₂-25(Ni20Cr)) + 75% NiCrAlY and Stellite-6 coated Ti-31 sample. Al-Fadhli et al. (2006) reported that the erosion resistance of HVOF sprayed coating is independent of type of substrate. In this investigation, only Ti-31 is used as substrate for investigation of the erosion behaviour of different coatings.

7.2.1 10% Al₂O₃+CoCrAlTaY coatings

Fig 7.16 shows the macrographs of the erosion scar produced on the 10% Al₂O₃+CoCrAlTaY coated Ti-31, using silica as erodent. The erosion scar produced using impact angles of 30°, 60° and 90° is shown in Fig. 7.16a, 7.16b and 7.16c, respectively. The macrographs show two distinct regions marked by A and B. The centre portion of the eroded scar (A) represents a localized region of material removal and it is surrounded by a region of elastically loaded material (B). The extent of material removal (depth) is severe in A compared to that at B. The area of material damage is more during impact at a lower angle compared to impact at a higher angle.

The plots of erosion rate as a function of cumulative mass of erodent and steady state volume erosion rate as a function of impact angle are presented in Fig. 7.17a and 7.17b, respectively. The plot shows that (Fig. 7.17a), after the initial transient, the erosion rate becomes stabilised to a constant value and the stabilised value is higher for the impact angle of 90° and the lowest for the impact angle of 30°. This is also presented in the plot of steady state volume erosion rate versus impact angle (Fig. 7.17b). The bar chart shown in Fig. 7.17b is similar to the damage of brittle materials under erosion conditions (Sidhu et al. 2007 and Soundararajan 1991).

Generally, brittle materials exhibit more erosive loss at impact an angle of 90° compared to that at 30° .

Fig. 7.18 shows micrographs of the eroded scar produced in 10% Al_2O_3 -CoCrAlTaY coated Ti-31, using an impact angle of 30° . Micrographs clearly indicate the material damage by crater formation (Fig. 7.18a), crack formation (Fig. 7.18b) and attachment of silica erodent (Fig. 7.18c). Though the silica particle is sticking to the coated surface, they are not embedded as observed in the case of uncoated samples (Section 7.1). Fig. 7.19 shows typical microstructures observed in the scar produced with an impact angle of 60° . The following features are observed in the micrographs. Fig. 7.19a shows formation of cracks and lips during the impact with silica particles; Fig. 7.19b shows the attachment of silica particle, Fig. 7.19c shows the Al_2O_3 pull out particles during erosion and Fig. 7.19d shows the crater created due to removal of particle from the surface.

The micrographs of the scar produced during the erosion with an impact angle of 90° are presented in Fig. 7.20. Fig. 7.20a shows the crater and Fig. 7.20b shows the micrograph with indications of crack, Fig. 7.20c shows groove formation due to cutting action of hard silica particles and Fig. 7.20d shows the attachment of erodent particles on the coated surface.

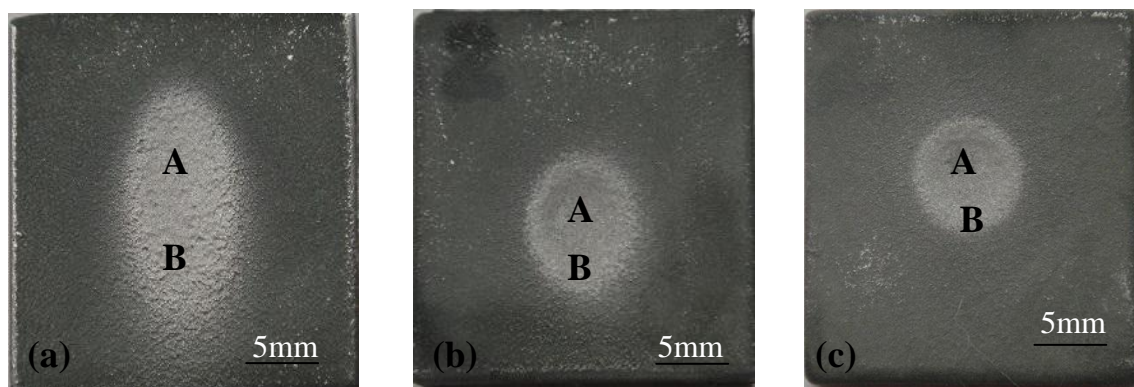


Fig. 7.16 Macrographs of 10% Al_2O_3 +CoCrAlTaY coated Ti-31 impacted by silica erodent at different angles. (a) Impact angle 30° (b) Impact angle 60° (c) Impact angle 90° .

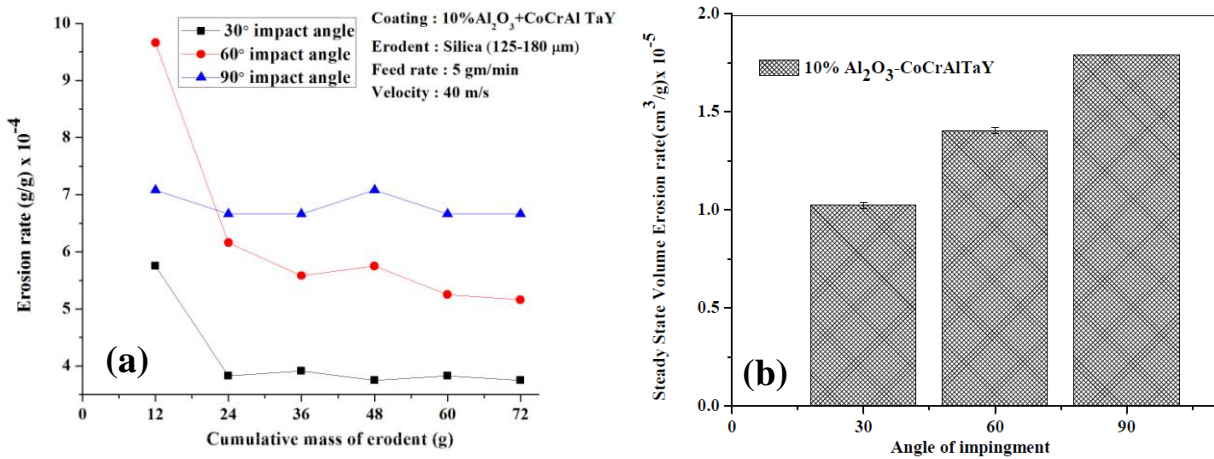


Fig. 7.17 Plot of erosion rate versus cumulative mass of erodent of 10%Al₂O₃-CoCrAlTaY coated Ti-31 subjected to erosion at 30°, 60° and 90° impact angle. (a) Variation of the erosion rate (b) Histogram illustrating the steady state volume erosion rate.

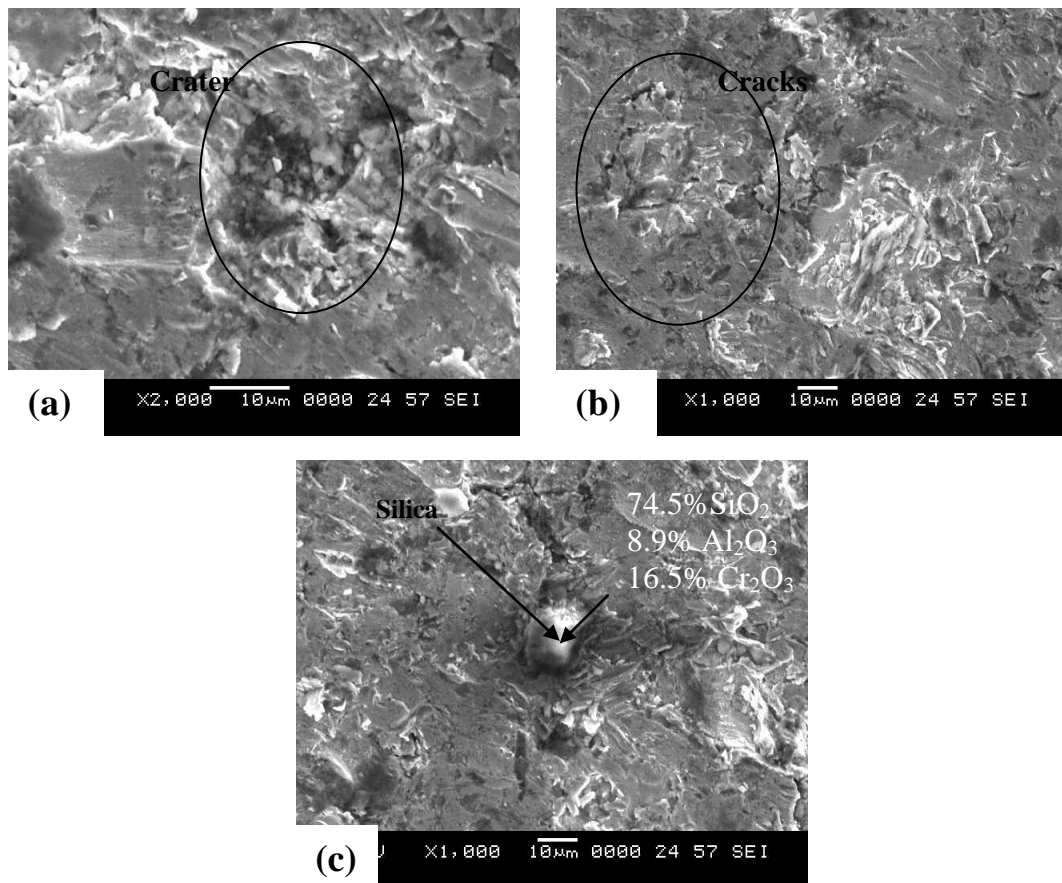


Fig. 7.18 SEM micrographs showing the morphology of eroded surfaces on 10% Al₂O₃+CoCrAlTaY coated Ti-31, with an impact angle of 30°.

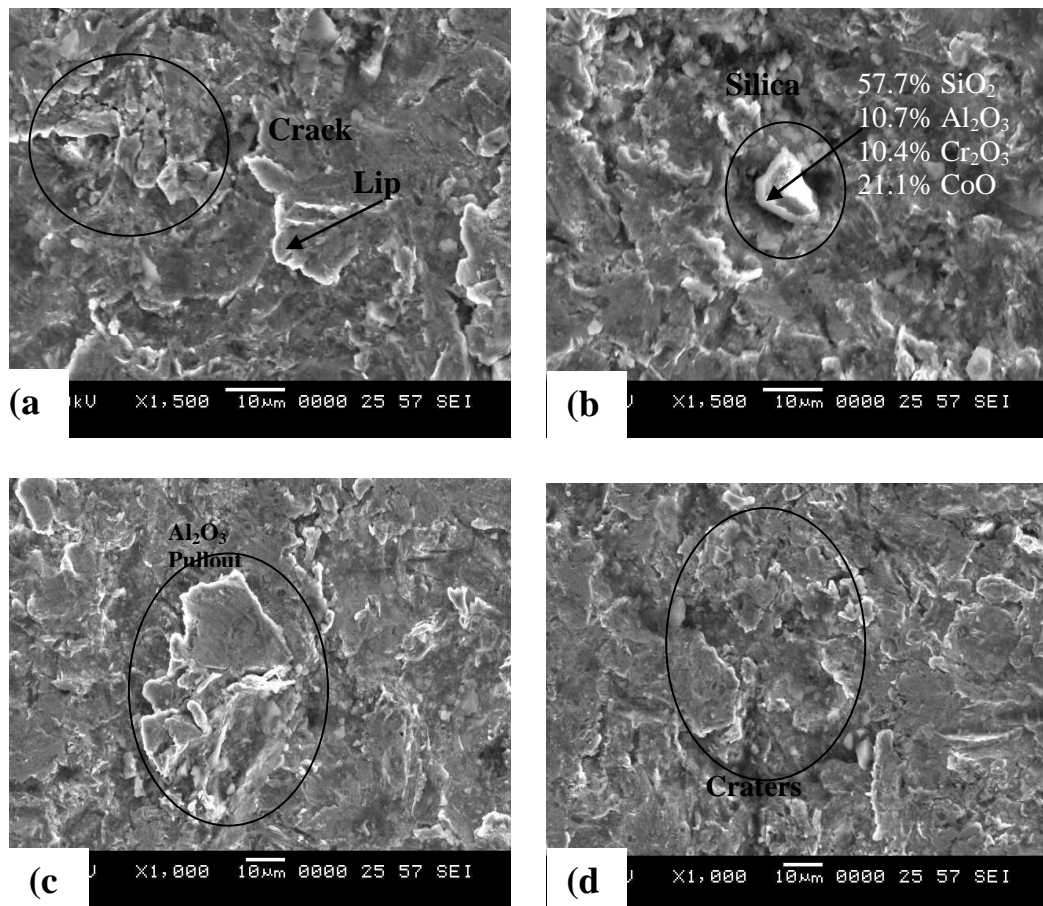


Fig. 7.19 SEM micrographs showing the morphology of eroded surfaces on 10% Al₂O₃+CoCrAlTaY coated Ti-31 with an impact angle of 60°.

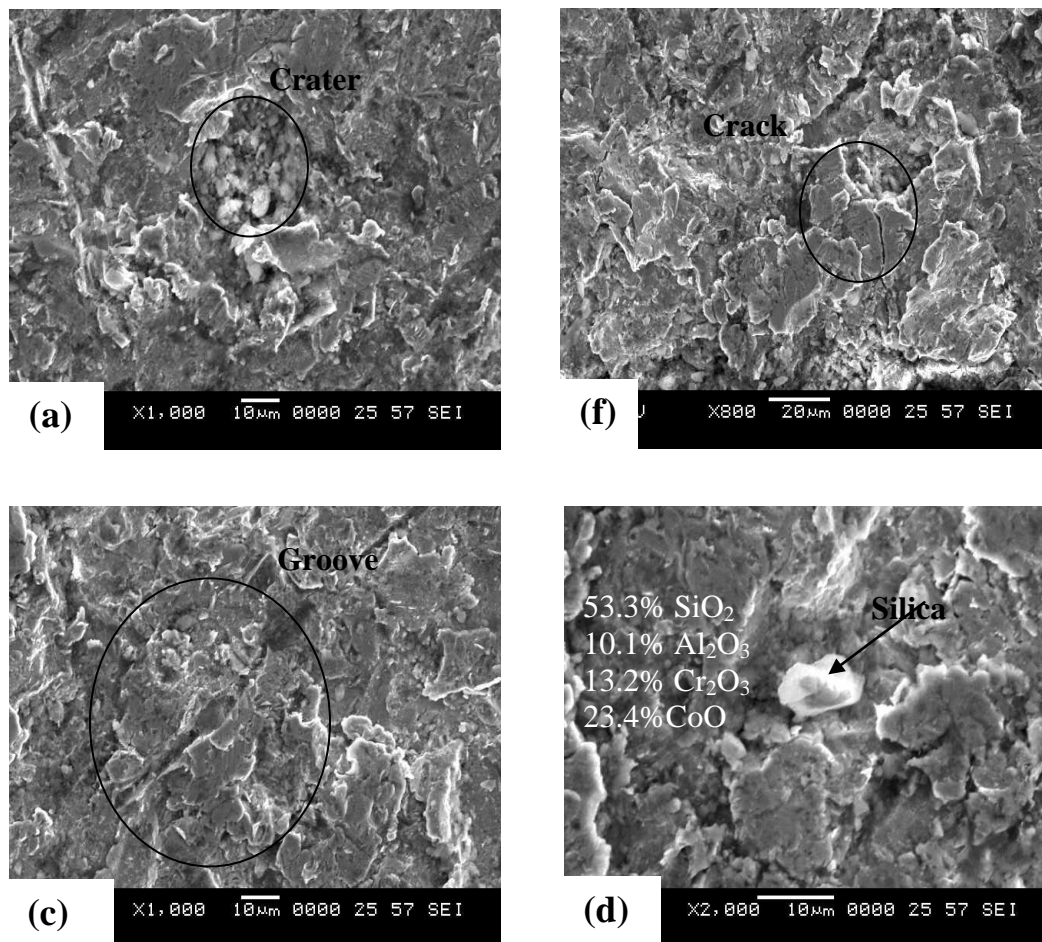


Fig. 7.20 SEM micrographs showing the morphology of eroded surfaces on 10% Al₂O₃+CoCrAlTaY coated Ti-31, with an impact angle of 90°.

7.2.2 25% (Cr₃C₂-25(Ni₂₀Cr)) + 75%NiCrAlY coating

The macrographs of the erosion scar produced on the HVOF sprayed 25% (Cr₃C₂-25(Ni₂₀Cr)) + 75%NiCrAlY coating on Ti-31, eroded with silica particles at impact angles of 30°, 60° and 90° are shown in Fig. 7.21a, b, c, respectively. The macrographs show two distinct regions marked by A and B. The centre portion of the eroded scar (A) represents localized region of material removal and it is surrounded by a region of elastically loaded material (B). Variation of erosion rate as a function of cumulative erodent mass is presented in Fig. 7.22a. Erosion rate is minimum for the impact angle of 90° and maximum for the impact angle of 30°. Similarly, the

steady state volume erosion rate as a function of impact angle is drawn using the concept explained in section 7.1.1 and they are drawn in the form of a bar chart and presented in Fig. 7.22b. The steady state volume erosion rate of the coating at 30° impingement is intermediate and it peaks at a 60° impact angle and it drops to a minimum value at 90°. This behaviour is similar to erosion of materials under mixed mode of erosion as observed by Soundararjan (1991) and Espallargas et al. (2008).

The micrographs of the eroded scar produced at an impact angle of 30° are presented in Fig. 7.23. The indications of ploughing (Fig. 7.23a), craters (Fig. 7.23a) and attachment of silica particles (Fig. 7.23b) are observed. Fig. 7.24 shows the micrographs of the erosion scar produced by the erodent at an impact angle of 60° is shown. The micrographs in Fig. 7.24 show the indications of ploughing (Fig. 7.24a), grooves (Fig. 7.24b), cracks and craters (Fig. 7.24c) and the debris in the form of platelets (Fig. 7.24d). Similarly, Fig. 7.25 indicates the features of eroded scar produced with an impact angle of 90°. It has indications of ploughing (Fig. 7.25a) grooves (Fig. 7.25b) and attachment of debris (Fig. 7.25c). The EDS on the debris indicated that they are chromium rich splats.

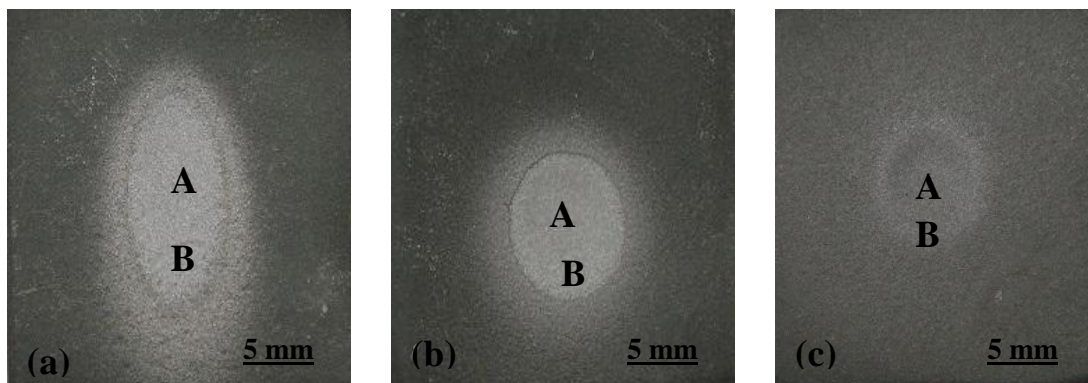


Fig. 7.21 Macrographs of 25% (Cr_3C_2 -25(Ni20Cr)) + 75%NiCrAlY coated Ti-31 impacted by silica erodent at different angles. (a) Impact angle of 30° (b) Impact angle of 60° (c) Impact angle of 90°.

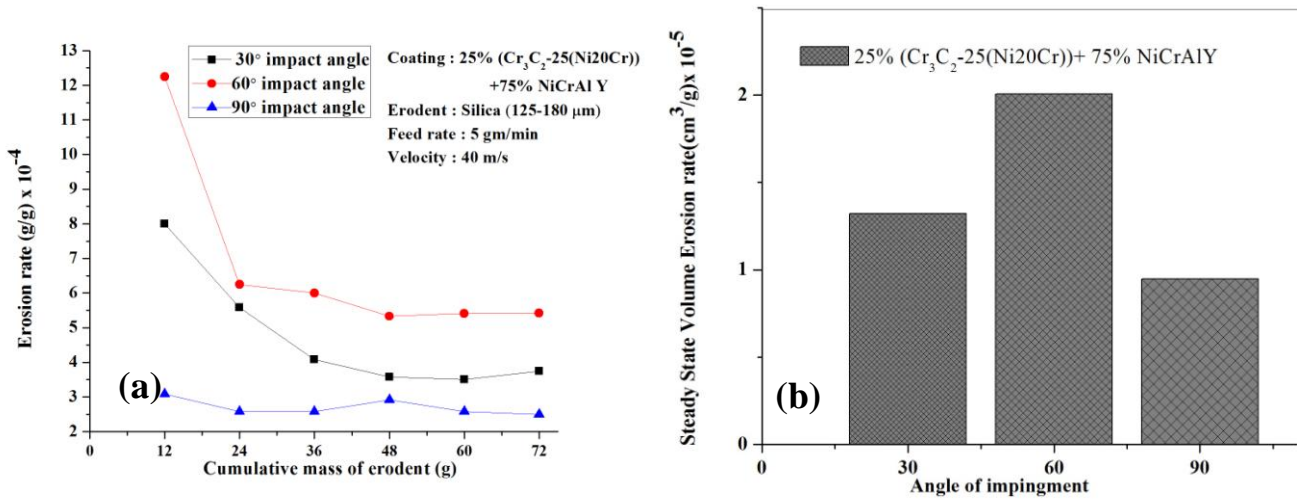


Fig. 7.22 Plot of erosion rate versus cumulative mass of erodent of 25%(Cr_3C_2 -25(Ni20Cr)) + 75% NiCrAlY coated Ti-31 subjected to erosion at 30°, 60° and 90° impact angle. (a) Variation of the erosion rate (b) Histogram illustrating the steady state volume erosion rate.

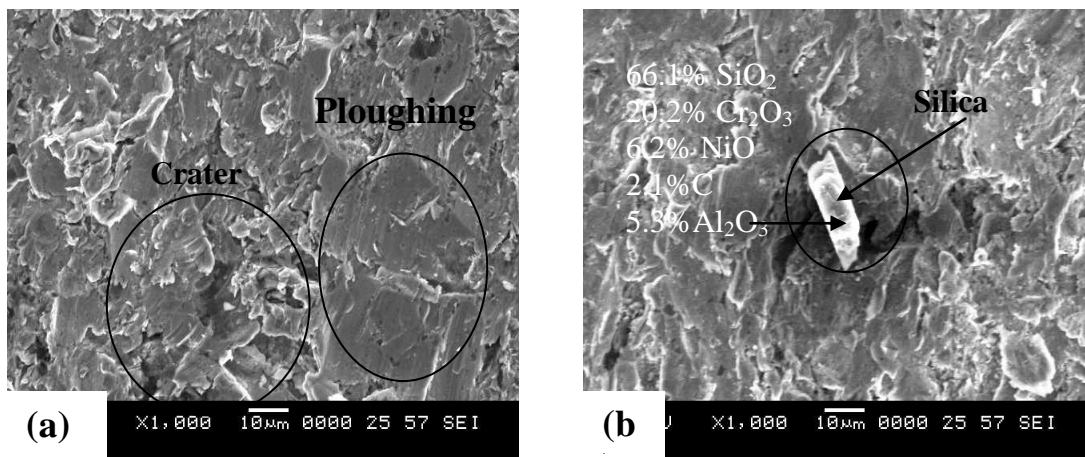


Fig. 7.23 SEM micrographs showing the morphology of eroded surfaces on 25% (Cr_3C_2 -25(Ni20Cr)) + 75% NiCrAlY coated Ti-31, with an impact angle of 30°.

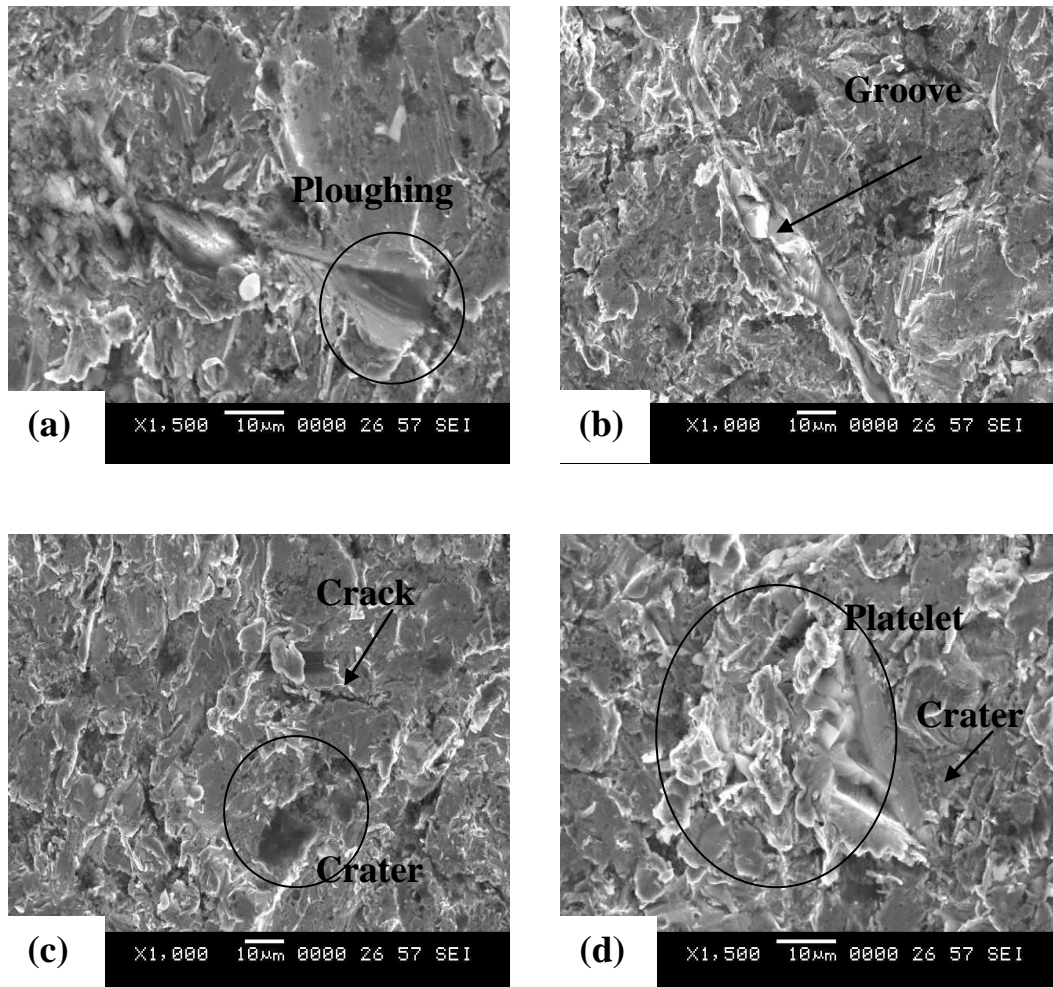


Fig. 7.24 SEM micrographs showing the morphology of eroded surfaces on 25% (Cr_3C_2 -25(Ni20Cr)) + 75%NiCrAlY coated Ti-31 with an impact angle of 60° .

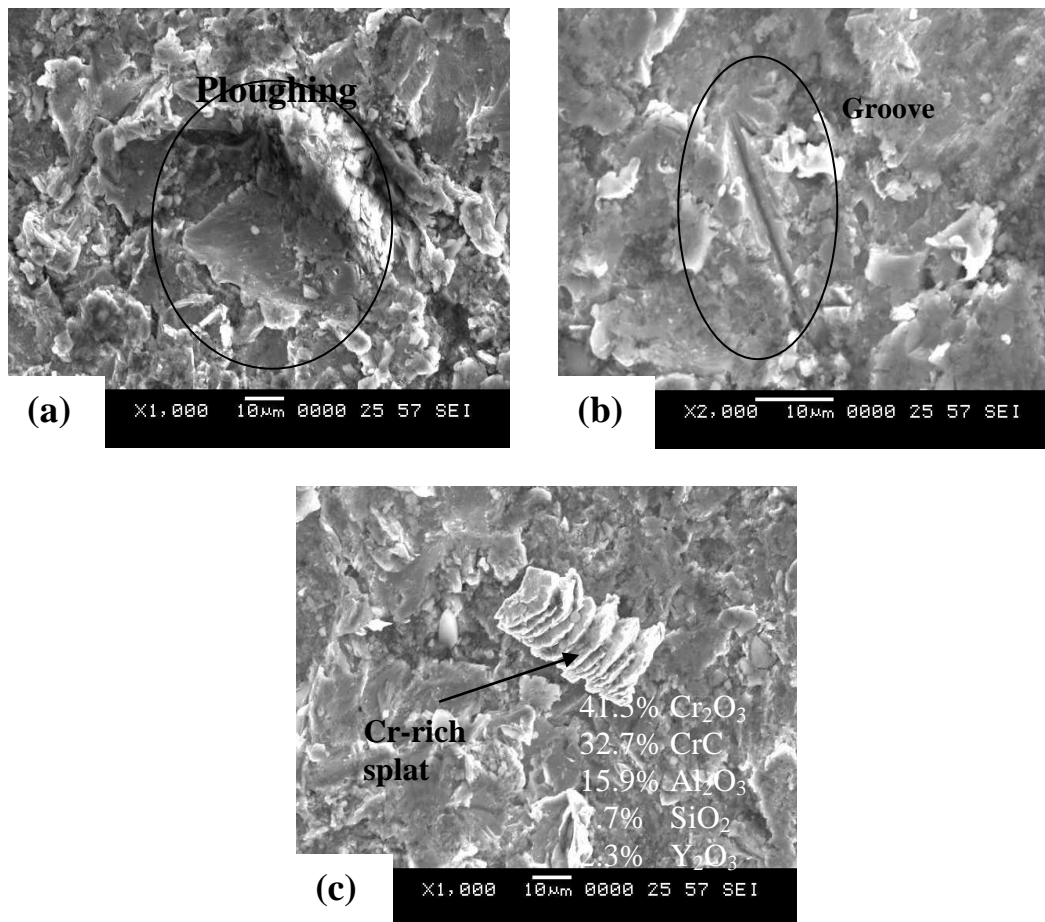


Fig. 7.25 SEM micrographs showing the morphology of eroded surfaces on 25% (Cr₃C₂-25(Ni₂₀Cr)) + 75%NiCrAlY coated Ti-31 with an impact angle of 90°.

7.2.3 Stellite-6 coating

The macrographs of the scar produced on the HVOF sprayed, Stellite-6 coated Ti-31 samples, eroded with silica erodent at impact angles of 30°, 60° and 90° are presented in Fig. 7.26. The macrographs show two distinct regions marked by A and B. The centre portion of the eroded scar (A) represents a localized region of material removal and it is surrounded by a region of elastically loaded material (B). Variation of erosion rate as a function of cumulative erodent mass is presented in Fig. 7.27a. At all impact angles, initially, high erosion rates are observed. After an initial transient period, erosion rate became constant. In Fig. 7.27b, the plots of steady state volume

erosion rate at different impact angles is given and the maximum erosion rate is observed in the case of impact at 90° and minimum with 30° impact angle.

Fig. 7.28 shows micrographs of the scar produced using an impact angle of 30° . The micrographs show the features indicating following types of damaging mechanisms. Fig. 7.28a show clear indications of crater and cracks are visible. Fig. 7.28b show a cobalt rich splat producing out of the eroded surface and Fig. 7.28c show marks of cutting scar due to hard particles eroding on the coating. Fig. 7.29 shows micrographs of the scar produced on the Stellite-6 coated surface using an impact angle of 60° (Fig. 7.29a). Micrographs show the indications of crater formation due to removal of particles, lip formation due to plastic deformation (Fig. 7.29b) and unmelted cobalt rich particle which is exposed due to erosion process (Fig. 7.29c). Micrographs of HVOF sprayed, Stellite-6 coated Ti-31, eroded at an impact angle of 90° is presented in Fig 7.30. Fig. 7.30a show grooves which are sharp and narrow (Fig. 7.30a and Fig. 7.30b) clear indications of crater and cracks are visible.

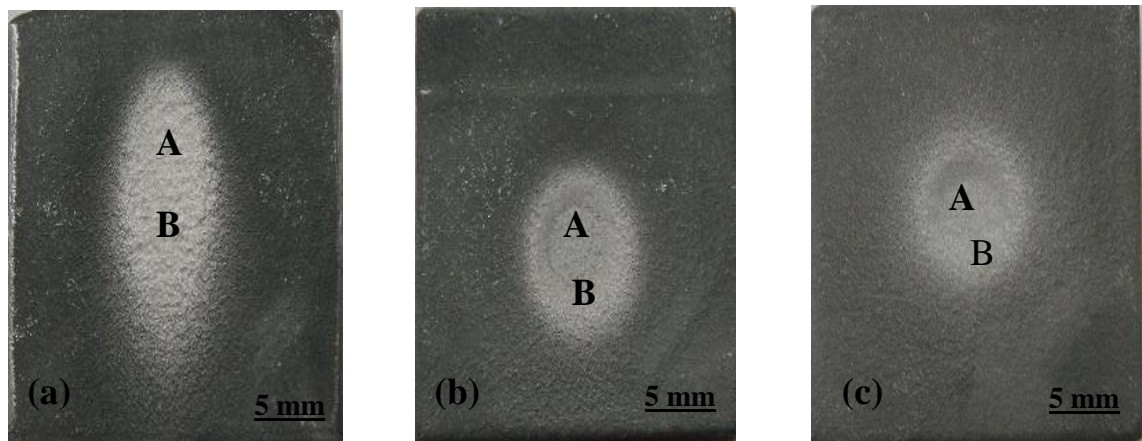


Fig. 7.26 Macrographs of Stellite-6 coated Ti-31 impacted by silica erodent at different angles. (a) Impact angle of 30° (b) Impact angle of 60° (c) Impact angle of 90° .

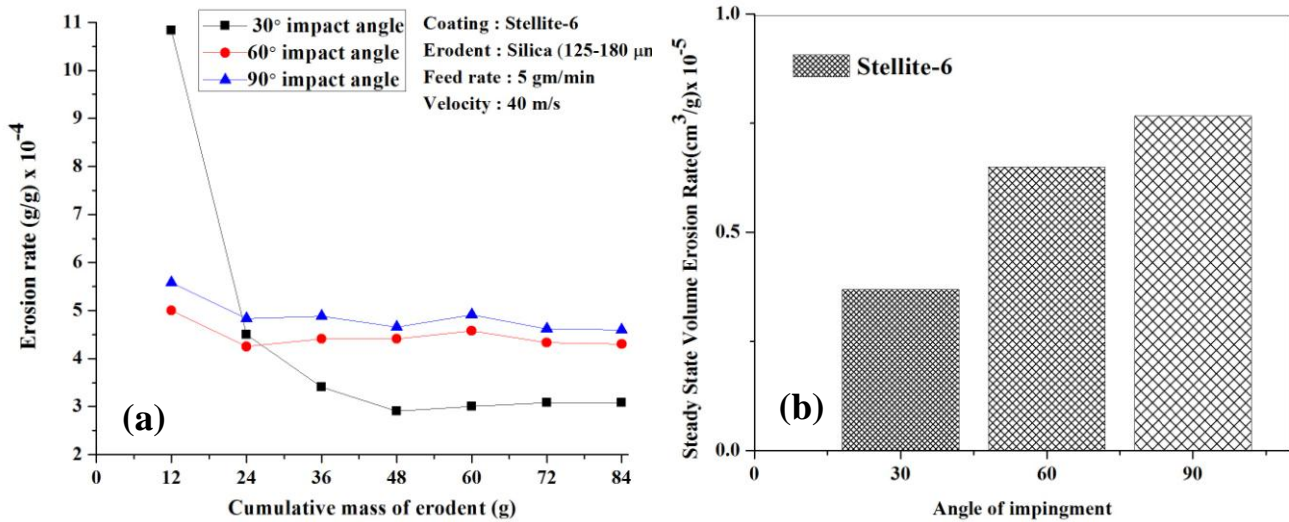


Fig. 7.27 Plot of erosion rate versus cumulative mass of erodent of Stellite-6 coated Ti-31 subjected to erosion at 30°, 60° and 90° impact angle (a) Variation of the erosion rate (b) Histogram illustrating the steady state volume erosion rate.

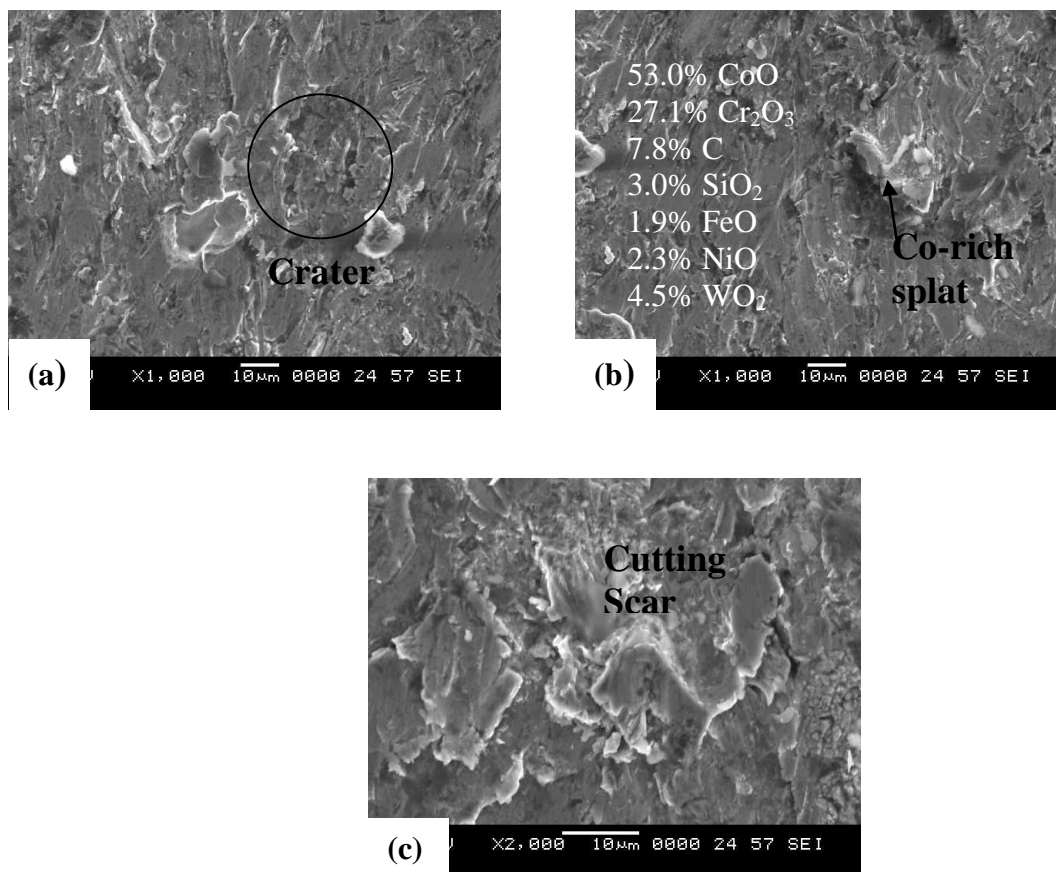


Fig. 7.28 SEM micrographs showing the morphology of eroded surfaces on Stellite-6 coated Ti-31 with an impact angle of 30°.

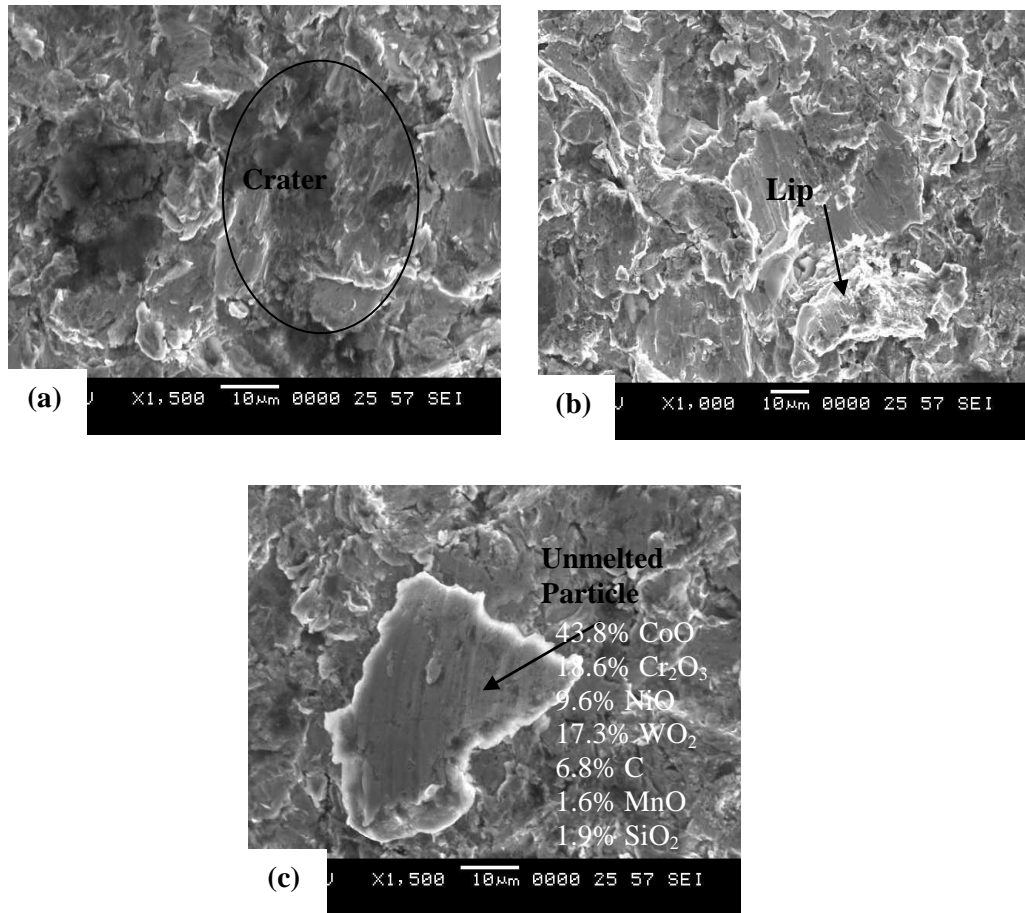


Fig. 7.29 SEM micrographs showing the morphology of eroded surfaces on Stellite-6 coated Ti-31 with an impact angle of 60°.

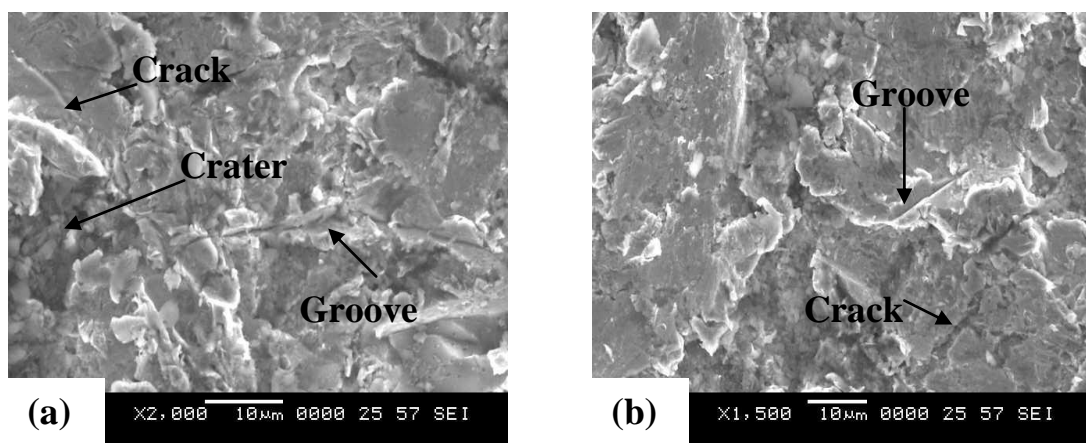


Fig. 7.30 SEM micrographs showing the morphology of eroded surfaces on Stellite-6 coated Ti-31 with an impact angle of 90°.

7.2.4 Discussion

10%Al₂O₃+CoCrAlTaY coating

Fig. 7.17 shows the variation of erosion rate as a function of cumulative mass of erodent for the HVOF sprayed 10%Al₂O₃+CoCrAlTaY coated Ti-31 at various impact angles. The material loss is more at 90° impact angle compared to 30° and 60° impact angles. A dramatic increase in the erosion rate at a higher impact angle (near to 90°) compared to impact angles of 30° or 60° indicates that the material behaviour is brittle under solid particle erosion conditions (Soundararajan 1995). Initially high erosion rates are observed (Fig. 7.17a) as a result of rough outer surface of the as-sprayed coatings (Ra of as sprayed coating-4.1µm, Table 4.4). The globular protuberances on the as-sprayed surface are smoothed out by the impacting particles and the lower steady state erosion condition is reached with the increased cumulative mass of the erodent.

The mechanism of material removal during erosion of brittle materials is explained by Sheldon and Finnie, (1966), and Levy, (1984). It is generally thought that when erodent is sub millimetre scale and angular in shape, erosion occurs by lateral (or conical) cracking. During repeated impacts of hard, erosive particles lateral cracks are formed. Subsequently, they intersect and loosen the chunk of the material which will be removed during next impact (Lawn and Wilshaw, 1975). It is also thought that the similar damage mechanism is active under both normal and oblique impact conditions (Hutchings 1992)

The coating microstructure can be considered as a composite microstructure consisting of a hard phase (consisting of alumina) embedded in a relatively soft matrix made of metallic constituents. In such systems, Hovis et al. (1986) suggested that the relative value of erodent particle size with respect to microstructural scale affects damage mechanism. When erodent particle size is larger compared to microstructural length scale, Hovis et al. (1986) suggested that the damage due to individual impact overlaps the microstructural features and the damage within the feature is constrained by other features. In such cases the damage is mainly due to hard phase cracking of and its dislodgement leading to formation of craters at the surface. The crater formation is also possible if hard, angular particle impacts the soft

matrix at an angle and in turn dislodges the particle from its site. They believe that for this to happen, interfacial strength between soft phase and hard phase must be small.

The SEM micrographs showing the details of microstructural features in scars produced with impact angles of 30°, 60° and 90° shows a multiple modes of damage activity. The cracks are observed in all three impact angles (Fig. 7.18, Fig. 7.19 and Fig. 7.20). Most of the cracks are multiple in nature and limited to local regions. Extending the logic presented by Hovis et al. (1986), we conclude that cracks are generated in Al₂O₃ phase. The propagation of the crack is limited by the presence of soft phase surrounding the hard phase. This limits the damage by the erodent particles.

The SEM micrographs shown in Fig. 7.18, Fig. 7.19 and Fig. 7.20 also indicate that the crater formation is extensive. Coarse, partially molten splats have disintegrated during impact with hard erodent particles and the cracks which are generated during disintegration got connected and separated from the bulk of the coating. Also, in the process they have created small craters. In few locations, complete hard phase have come out. This happens at those locations, where interface is poor due to partial melting of the powders during HVOF spraying. Also, some amount of local oxidation will take place during the flight of semi-molten splat from the HVOF gun towards the sample surface. The oxidation will reduce the strength of the bond between depositing splats. Fig. 7.19d shows a crater formed predominantly in the softer binder region, leading to dislodging of hard particles, whereas the crater formed in Fig. 7.18a and Fig. 7.19a can be thought as due to multiple cracking of hard phase and dislodging of the fragments. Other than that silica particles are embedded in the coated sample (Fig. 7.18c, Fig. 7.19b and Fig. 7.20d). In all images, we notice that the penetration of silica in to the sample is very small. This is a distinct feature compared to penetration of silica in to plain Ti-31 (Fig. 7.4d). Similar interactions between erodent and hard composite coating is reported else where (Soderberg et al. 1981, Sheldon and Finnie 1996, Zambelli and Levy 1991, Levy 1983, Wensink and Elwnpoek 2002, Ramesh et al. 2010, Hussainova et al. 1999).

When hard erodent impacts soft matrix phase present in the composite coating, the matrix phase undergoes plastic deformation. If sharp edge of the angular erodent faces the sample surface, it generates ploughing and groove action. Both generate

flow lips. Ploughing introduces more plastic deformation and strain hardening. Compared Ti-31 alone, the matrix phase in the composite coating is less ductile and the local material (where erodent impacts) becomes brittle. This region is prone to cracking and spalling due to extensive strain hardening.

25% (Cr_3C_2 -25(Ni20Cr)) + 75% NiCrAlY coating

Plot of erosion rate vs cumulative mass of erodent (Fig. 7.22a) show the higher erosion rate at the initial stage and it is attributed to rough surface texture of the as-sprayed coating. The protrusions on the as-sprayed coating are vulnerable to easy erosion by the hard erodent particles. Once the protrusions are levelled off, the continuation of erosion is gradual and relatively slow compared to initial stages. Similar erosion behaviour is reported by Ramesh et al. (2010) in the case of HVOF sprayed WC-Co/NiCrFeSiB composite coating on ASTM-SA210 steel; Sidhu et al. (2006) in the case of HVOF sprayed NiCr coating on ASTM-SA210 steel and Mishra et al. (2008) in the case of HVOF sprayed NiCrAlY coating on nickel based superalloy. The plot of steady state volume erosion rate as a function of impact angle (Fig. 7.22b) shows a peak value at impact angle of 60° , compared to impact angles of 30° and 90° . This indicates that the HVOF sprayed coating exhibits mixed mode of damage (intermediate between pure brittle and pure ductile) under erosion conditions (Hawthorne et al. 1999 and Gang-Chang et al. 2007). The micrographs taken from the scars (Fig. 7.23, Fig. 7.24 and Fig. 7.25) also indicate the mixed mode of erosion. There are microstructural features like ploughing (Fig. 7.23a, Fig. 7.24a and Fig. 7.25a) indicating ductile mode of erosion damage (Ramesh et al. 2010, Murthy et al. 2001, Sidhu et al. 2007). Also there are grooves in the microstructures (Fig. 7.24b and Fig. 7.25b), which is another feature of erosion damage of ductile of materials (Ramesh et al. 2010, Kumar et al. 2008, Hutchings 1992). Microstructures from the same scar also show indications of material damage under brittle mode. Fig. 7.23a, Fig. 7.24c and Fig. 7.24d presents damage in the form of craters. Fig. 7.24c shows damage due to microcracks. Fig. 7.24d also shows platelets formed during the impact. They are indicating that the material undergoes brittle type damage during erosion

(Sheldon and Finnie 1996, Soderberg et al. 1981, Zambelli and levy 1981, Gang-chang et al. 2007 and Hawthorne et al. 1999).

Gang-chang et al. (2007) and Hawthorne et al. (1999) carried out erosion studies on HVOF sprayed Cr_3C_2 -NiCr coating and reported erosion behaviour is in brittle mode. Steady state volume erosion rate is maximum at an impact angle of 90° . Hutchings (1992) and Mishra et al. (2006) reported that the erosion damage in the case of HVOF sprayed NiCrAl alloy is in ductile mode. Steady state volume erosion rate is maximum at an impact angle of 30° . In this investigation, an attempt is made to blend these powders to get a composite coating with improved toughness. Before HVOF spraying, powders are blend in the following ratios- 25wt% (Cr_3C_2 -25(Ni20Cr)) and 75 wt% NiCrAlY. The erosion rate is found to be maximum at 60° impact angle compared to 30° and 90° impact angle (Fig. 7.22b). This suggests that the coating material, behaves neither as purely ductile (Material loss maximum at 15 - 30°) nor purely brittle (Material loss maximum at 90°). It shows a composite behaviour. Similar observations are reported by Murthy et al. (2001). Consequently the morphology of the eroded surface indicates ploughing, grooves and lips in binder matrix and craters, cracks, platelet formation, carbide particle pulled out in the carbide rich region. These mechanisms signify composite ductile and brittle modes of erosion. Similar observations are reported by Ramesh et al. (2010) on HVOF sprayed WC-Co/NiCrFeSiB coating on boiler steel (ASTM-SA210). Composite erosion behaviour depends on the alloying elements and microstructure of the coating (Levy 1988 and Shui et al. 1990).

Stellite-6 coating

Plot of erosion rate vs cumulative mass of erodent (Fig. 7.27a) show initially a transient behaviour and a steady state condition after that. Initial transient is predominant at 30° impact angle. As initial rough surface got evened out during erosion study, the erosion rate became constant. Fig. 7.27b shows steady state erosion rate at different angle. Maximum erosion rate is observed at an impact angle of 90° and minimum erosion rate at an impact angle of 30° . This suggests that the erosion

behaviour of the Stellite-6 coated material is brittle mode. Under this mode maximum erosion loss occurs at an impact angle of 90° (Finnie 1995). The brittle erosion mechanism deals with the material removal due to formation of cracks and craters. When a brittle material is impacted by a hard and sharp particle, the contact area is plastically deformed due to the high compressive and shear stresses and radial cracks are formed (Sidhu et al. 2006 and 2007). During the successive impact of the erodent, plastic deformation increases leading to increase in tensile stresses which finally leads to lateral cracks and material removal. Microstructures (Fig. 7.28a, Fig. 7.29a, Fig. 7.30a and Fig. 7.30b) in the scars indicate extensive formation of craters and cracks indicating that the damage mode is brittle mode indeed. Under brittle mode of erosion formation of cracks and craters is more common at an impact angle of 90° than at 30° and 60° . This is also observed in present set of micrographs. Extensive damage by cracking is observed in Fig. 7.30a and Fig. 7.30b. Similar observations have been reported by Sidhu et al. (2006 and 2007) and Maiti et al. (2007).

7.3 COMPARATIVE DISCUSSION

Fig. 7.31 shows a bar chart indicating volumetric steady state erosion rate for uncoated and HVOF coated Ti-31 alloy at 30° , 60° and 90° impact angle (Soundararajan 1991). From the bar chart it can be inferred that uncoated Ti-31, Superco-605 and MDN-121 alloys exhibit lower steady state volume erosion rate in comparison to all the HVOF coatings under similar test conditions. All the three uncoated alloys exhibit erosion damage under ductile mode and less amount of erosive loss compared to HVOF coated samples. This may be due to the embedment of silica particles into the surface which might bestow some shielding effect against further impacting particles and hence leading to a lower wear loss. Similar observations are reported by Mishra et al. (2006) and Sidhu et al. (2007).

The ratio of the hardness of the erodent particles (H_p) to the hardness of the target (H_t) is an indication of the penetrating ability of the particles in to the target. Experimentally, it is observed that abrasive particles of any shape will cause plastic scratching and penetrate the surface, if $H_p/H_t > 1.2$ (Lathabai et al. 1998, Hussainova et al. 1999, Shipway and Hutchings 1996, Hearley et al. 1999, Hutchings 1992). For

all substrates used in this investigation the ratio is greater than 2 and they indicate that erodent can penetrate into the substrate surface. Many SEM micrographs (Fig. 7.4b, Fig. 7.8b, Fig. 7.10c Fig. 7.14c and others) indicate the presence of silica particles which are penetrated in to the surface. Further, Mishra et al. (2006) reported a higher erosion loss in the thermal sprayed coatings compared to uncoated substrates. They attributed this to presence of porosity in the coatings. Porosities are also observed in the present coatings and they might have contributed to higher erosion loss. Another possibility is strain hardening of surfaces of uncoated substrates. This is similar to strain hardening due to impingement of soft surfaces with shots. Uncoated alloys endure severe plastic deformation in the localized region around the points of impact of each particle. It is believed that all this mechanism are active and they reduce the steady state volume erosion rate of uncoated alloys.

Erosion resistance of the various coatings under study can be arranged in the following sequence:

Stellite-6 > 10% (Al₂O₃)-CoCrAlTaY > 25% (Cr₃C₂-25(Ni20Cr)) + 75% NiCrAlY

Highest erosion resistance of Stellite-6 coating and lowest erosion resistance of chromium carbide coatings can be explained using Hp/Ht ratio. From the reference (Ramesh et al. 2010), we take hardness of the silica as 880 Hv. Using the data reported in Section 4.5, we estimate the Hp/Ht ratio. For the combinations of erodent-Stellite-6 coating and erodent –chromium carbide coating the ratio is 0.9 and 1.5, respectively. From the steady state volume erosion rate plot (Fig. 7.27b) and Hp/Ht ratio we conclude that the erosion loss takes place due to crack generated in the coating due to penetration of the silica erodents. Since the coating is brittle, the cracks easily get interconnected and craters also forms. They contribute for increased erosion loss. The Stellite-6 coating is harder compared to erodent. Still, there can be erosion loss in the Stellite-6 coating. This is explained by Gulden (1978 and 1981) and Shipway and Hutchings (1996). Gulden presented the possibility of lateral microcracking in the target, when it is impacted by an erodent of similar hardness. Lateral microcracking is small in dimension and without interconnection between the cracks. This reduces erosion rate. Shipway and Hutchings (1996) presented an explanation based on the relative hardness of particle and target. He said that when ratio is close to 1, the erosion rate is minimum. The erosion rate of Stellite-6 coating

is lower when compared to both explanations are satisfied in our target-erodent combinations.

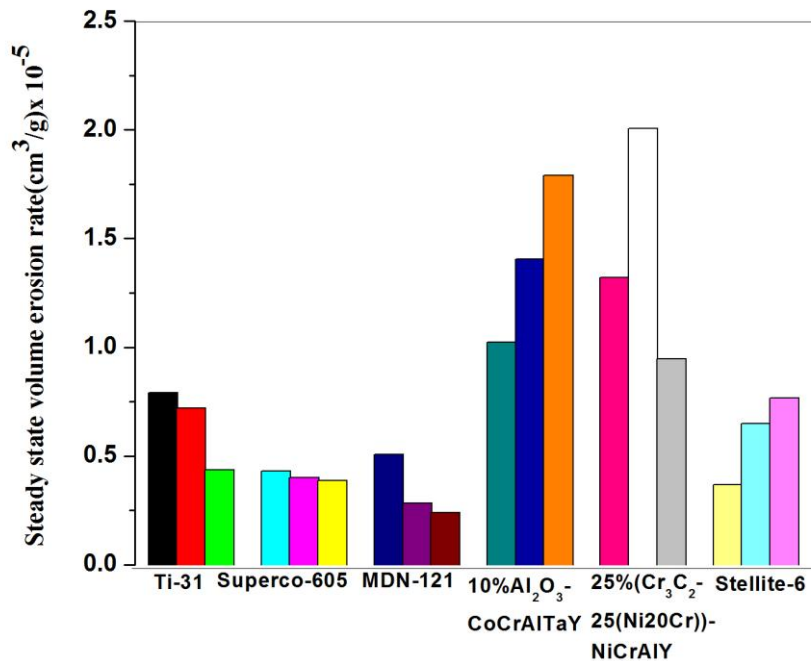


Fig. 7.31 Bar chart indicating volumetric steady state erosion rate for uncoated Ti-31, Superco-605, MDN-121 and HVOF coated Ti-31 alloy at 30°, 60° and 90° impact angle.

CHAPTER 8

**COMPARISON OF CUMULATIVE DAMAGE
DUE TO HOT CORROSION, OXIDATION AND
SOLID PARTICLE EROSION**

This chapter describes the results that have been compiled of hot corrosion, cyclic oxidation and solid particle erosion studies in different sections of the chapter to assess the performance of each coating.

Plot (Fig. 8.1) shows a bar chart of cumulative weight gain of uncoated alloys and HVOF sprayed 10% $\text{Al}_2\text{O}_3\text{-CoCrAlY}$, 25% $\text{Cr}_3\text{C}_2\text{-25(Ni20Cr)}$ + 75% NiCrAlY and Stellite-6 on Ti-31, Superco-605 and MDN-121, during hot corrosion, and cyclic oxidation test conditions. Also, the weight loss of uncoated and HVOF coated Ti-31 alloy during the solid particle erosion studies is presented.

As far as hot corrosion and cyclic oxidation is considered, all three coatings are better compared to uncoated alloys (Superco-605 and MDN-121 were sputtering during the study). Out of the three coatings 25% ($\text{Cr}_3\text{C}_2\text{-25(Ni20Cr)}$) + 75% NiCrAlY coating is beneficial as it offers maximum resistance compared to other coatings. In the case of solid particle erosion, the Stellite-6 coating offers marginally better resistance compared to 25% ($\text{Cr}_3\text{C}_2\text{-25(Ni20Cr)}$) + 75% NiCrAlY coating and significantly better compared to 10% $\text{Al}_2\text{O}_3\text{-CoCrAlY}$ coating. This means that 25% ($\text{Cr}_3\text{C}_2\text{-25(Ni20Cr)}$) + 75% NiCrAlY coating and Stellite-6 coatings are beneficial coatings.

One possible application for the coatings discussed in this investigation is in hot sections of power generations using solid fossil fuels. In these applications, the coatings will be experiencing conditions promoting hot corrosion, oxidation and solid particle erosion, simultaneously. Here we try to estimate cumulative damage, assuming no synergetic interaction between damage mechanisms. We give equal

importance to all three damage mechanisms. We consider damage as positive numbers irrespective of weight gain or weight loss. The substrate considered is Ti-31 and impact angle is 30°.

Cumulative damage (weight gain/loss) = damage due to hot corrosion *0.33 + damage due to cyclic oxidation *0.33 + damage due to erosion *0.33.

The estimated cumulative damage values are tabulated in Table 8.1.

The HVOF sprayed 25% (Cr_3C_2 -25(Ni20Cr)) + 75%NiCrAlY coatings shows superior performance among the coatings used in the present study. It performs well under hot corrosion and cyclic oxidation conditions and fairly good erosion resistance. Excellent oxidation and hot corrosion of this coating is attributed to the formation of Cr_2O_3 and NiO layers at the top of the coating, when it is exposed to harsh environments. It exhibits a composite erosive behaviour (Neither purely ductile nor brittle). Though the chromium carbide is inherently brittle, the coating is tough due to the composite microstructure. The strong carbide particles are held with ductile MCrAlY (M=Ni or Co). The porosity of the 25% (Cr_3C_2 -25(Ni20Cr) + 75% NiCrAlY) coating is very less compared to other two coatings (Ref. Section 4.4). The 10% Al_2O_3 +CoCrAlTaY coating follows after carbide coating and finally Stellite-6 is the least effective coating.

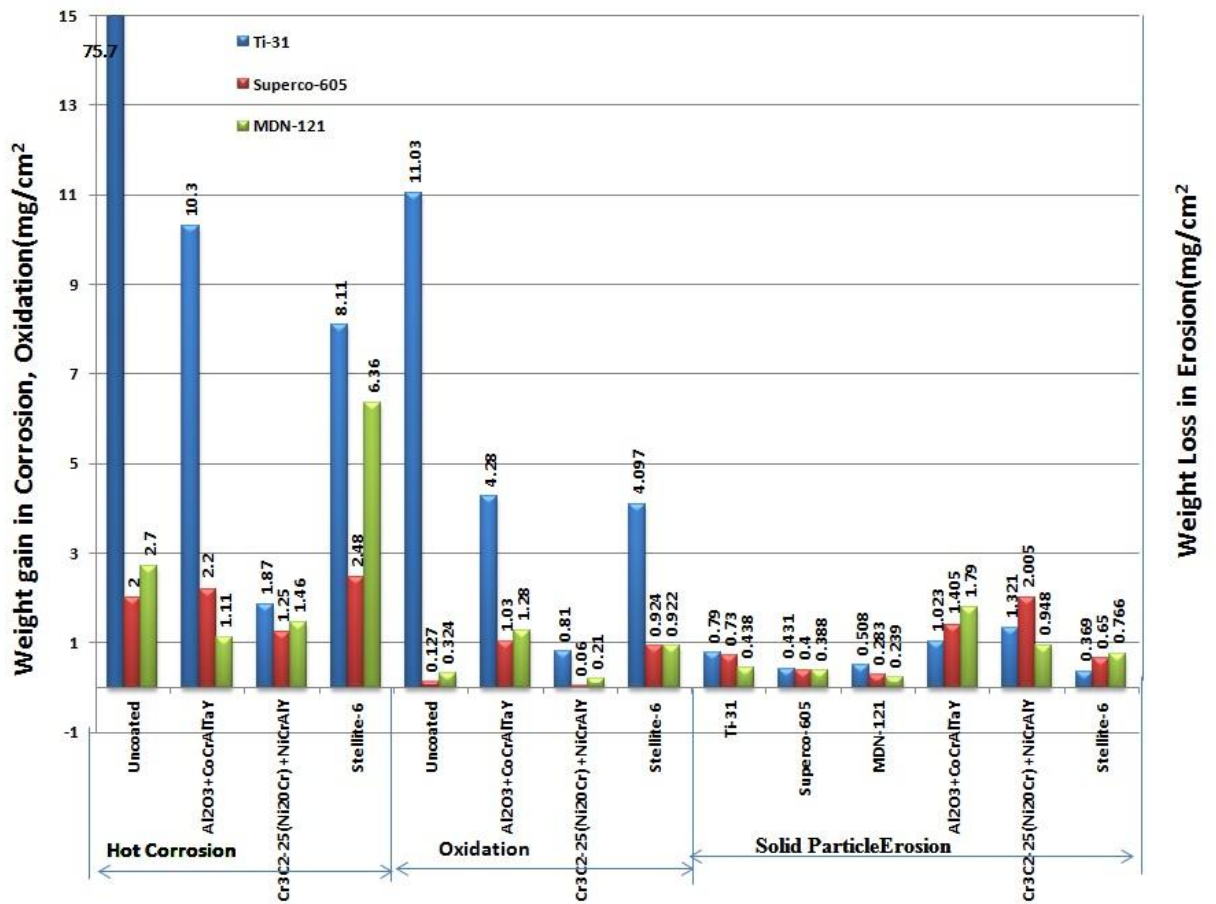


Fig. 8.1 Plot of comparison of cumulative damage due to hot corrosion, oxidation and solid particle erosion.

Table 8.1 Cumulative damage values for HVOF sprayed coatings on Ti-31.

Substrate considered	Coating-1 (10% Al ₂ O ₃ - CoCrAlTaY)	Coating-2 25% (Cr ₃ C ₂ - 25(Ni20Cr)- 75%NiCrAlY)	Coating-3 (Stellite-6)
Ti-31	8.03	3.27	8.12

CHAPTER 9**CONCLUSIONS**

Following are the salient conclusions from the present investigation.

1. HVOF sprayed 10% $\text{Al}_2\text{O}_3+\text{CoCrAlTaY}$, 25% $(\text{Cr}_3\text{C}_2-25(\text{Ni}20\text{Cr})) + 75\%$ NiCrAlY and Stellite-6 coatings are successfully deposited on Ti-31, Superco-605 and MDN-121 substrate materials. Under the given spray parameters, coatings are laminar structured, dense with porosity less than 2%. The thickness is in the range of 260-325 μm .
2. All the coatings have retained the phases observed in starting powder. The 25% $(\text{Cr}_3\text{C}_2-25(\text{Ni}20\text{Cr})) +75\%$ NiCrAlY coating has a nickel rich FCC phase as a principal phase. The 10% $\text{Al}_2\text{O}_3+\text{CoCrAlTaY}$ and Stellite-6 coating shows cobalt rich phase as principal phase. None of the coating materials undergo significant phase transformation during HVOF spraying.

HOT CORROSION STUDIES IN $\text{Na}_2\text{SO}_4-50\%\text{V}_2\text{O}_5$ SALT MIXTURE

3. The spray coating over metallic by HVOF process is proved to be beneficial in resisting the high temperature degradation of the material by hot corrosion. The cumulative weight gain for all three HVOF coated Ti-31, Superco-605 and MDN-121 samples are significantly lower than that of uncoated samples subjected to hot corrosion in $\text{Na}_2\text{SO}_4-50\%\text{V}_2\text{O}_5$ molten salt environment for 50 cycles at 800 °C. Uncoated Ti-31 suffered a higher corrosion rate and intense spalling of oxide scale (TiO_2 ; rutile) is observed. Uncoated Superco-605 and MDN-121 exhibited weight loss during the complete cycles of hot corrosion studies as a result of intense sputtering of the oxide scale formed during hot corrosion. The weight gain of 10% $\text{Al}_2\text{O}_3-\text{CoCrAlTaY}$, 25% $(\text{Cr}_3\text{C}_2-25(\text{Ni}20\text{Cr})) + 75\%$ NiCrAlY and Stellite-6 coated Ti-31, MDN-121 alloys are 1/7, 1/2, 1/55, 1/2, 1/9 and 1/0.4 fraction that of uncoated alloys, respectively.

4. Based on the thermogravimetric data, the relative hot corrosion resistance of the various coating under study can be arranged in the following sequence:

[25% (Cr₃C₂-25(Ni20Cr)) + 75%NiCrAlY] > [10%Al₂O₃+ CoCrAlTaY] > [Stellite-6]

5. All the coated samples exhibit characteristic thick protective oxide scale, composed of oxides and spinel oxides of the active elements of the coating and thereby imparted resistance to the hot corrosion. The superior hot corrosion resistance of 25% (Cr₃C₂-25(Ni20Cr)) + 75% NiCrAlY is attributed to the oxide scale containing a continuous film of Cr₂O₃ which has minimal solubility in highly acidic Na₂SO₄-50% V₂O₅ melt.
6. The study of corrosion kinetics (and parabolic behaviour) during the thermogravimetric studies shows that the rate of corrosion reaction is diffusion limited.
7. The oxide scale on the surface of corroded 10%Al₂O₃+ CoCrAlTaY coatings mainly consisted of α-Al₂O₃ oxides. Because of accelerated oxidation induced by the molten salt, metastable Al₂O₃ has formed in the initial cycles of studies.

CYCLIC OXIDATION STUDIES IN AIR AT 800 °C

8. HVOF coated samples subjected to cyclic oxidation showed considerably lower weight gains than that of uncoated samples. Also, uncoated Ti-31 suffered a higher oxidation rate and spalling of oxide scale. The stress developed due to higher volume of oxide lead to cracks in the scale, in turn resulted in spallation. The scale on the Superco-605 and MDN-121 was exhibiting mild sputtering during the cyclic oxidation study.
9. Based on the thermogravimetric data, the relative oxidation resistance of the various coating under study is arranged in the following sequence:

[25% (Cr₃C₂-25(Ni20Cr)) +75%NiCrAlY] > [Stellite-6] > [10%Al₂O₃+ CoCrAlTaY]

The oxidized coatings appeared to be compact and adherent. The HVOF coated substrate samples are not affected by the oxidizing environment. The oxidation kinetics of all the carbide and Stellite-6 coated Superco-605 and MDN-121 showed nearly parabolic behaviour upto 50 cycles. 10%Al₂O₃+ CoCrAlTaY and Stellite-6 coated Ti-31 alloy showed slight deviation from parabolic behaviour.

- 10.** The superior oxidation resistance of 25% (Cr₃C₂-25(Ni20Cr)) + 75%NiCrAlY is attributed to the thick protective oxide scale developed on the surface during cyclic oxidation. The uppermost layer of the oxide scale mainly consisted of continuous film of Cr₂O₃ which has minimum affinity towards atmospheric oxygen. Added to that the coating was dense and impervious. The weight gain of 10% Al₂O₃-CoCrAlTaY coated Ti-31 is 1/2.5 fraction of the uncoated alloy.
- 11.** Relatively higher oxidation resistance of Stellite-6 coated samples is credited to oxides and spinals of Co, Cr and Si formed on the surface. This protective oxide scale resists oxygen from entering to the coating and reaching the substrate. The refractory SiO₂ helps in maintaining the mechanical properties of the coating. Oxidation of the coating has been observed only at the outermost surface and rest of the coating remains unoxidised, which reflects the protective behaviour of this coating. The weight gain of Stellite-6 coated Ti-31 is 1/13 fraction of the uncoated alloy.
- 12.** Comparatively lower oxidation resistance of 10%Al₂O₃+ CoCrAlTaY coated samples is attributed to some extent to severe internal oxidation along the splat boundary due to higher porosity content. Oxidizing species penetrates in to the coatings through open porosity during the early stage of oxidation, until a continuous and stable protective scale is formed on the surface. The protective oxide scale formed on the outermost surface mainly composed of oxides of cobalt, chromium and aluminium and mixed spinal oxide CoCr₂O₄. The weight gain of 10%Al₂O₃+ CoCrAlTaY coated Ti-31 is 1/2.7 fraction of the uncoated alloy.

SOLID PARTICLE (SILICA) EROSION STUDIES

13. The room temperature erosion resistance of the various coatings on Ti-31 against silica erodent is arranged in the following sequence.

[Stellite-6] > [25% (Cr_3C_2 -25(Ni20Cr)) + 75% NiCrAlY] > [10% Al_2O_3 -CoCrAlTaY]

The superior erosion resistance of Stellite-6 coating is attributed to the high hardness ratio between the coating and the silica erodent. The morphology of the eroded surface shows craters, groove formation in binder matrix and carbide particle pull-out as the prevailing erosion mechanism.

14. The erosion mechanism of 25% (Cr_3C_2 -25(Ni20Cr)) + 75% NiCrAlY is by composite ductile and brittle mode. Unmelted particle bonded by ductile alloy matrix in the coating microstructure facilitates composite ductile-brittle behaviour.

15. The 10% Al_2O_3 -CoCrAlTaY coating exhibits brittle mode of material removal. The surface morphology characterized by deeper craters, and extensive plastic flow signifies brittle mode of erosion.

16. Substrate alloys exhibit lower steady state volume erosion rate in comparison to all the HVOF coatings under similar test conditions. The higher hardness ratio between silica erodent particle and substrate alloys lead to the penetration of silica particles into the surfaces which bestow some shielding effect against impacting particles leading to lower wear loss. Also, the uncoated alloys being ductile in nature, plastic deformation and strain hardening contributes to increased erosion resistance.

REFERENCES

- Ajdelsztajn, L., Picas J.A., Kim, G.E., Bastian, F.L., Schoenung, J. and Provenzano, V. (2002). "Oxidation behaviour of HVOF sprayed nanocrystalline NiCrAlY powder." *Mater. Sci. and Engg.*, 338, 33-43.
- Al-Fadhli, H.Y., Stokes, J., Hashmi, M.S.J. and Yilbas, B.S. (2006). "The erosion-corrosion behavior of high velocity oxy-fuel (HVOF) thermally sprayed Inconel-625 coatings on different metallic surfaces." *Surf. and Coat. Technol.*, 200, 5782-5788.
- Annual Energy Outlook 2003, Energy Information Administration, U.S Department of Energy, 5-6.
- Anuwar, Jayganthan, R., Tewari, V.K. and Arivazhagan, N. (2007). "A study on the hot corrosion of Ti-6Al-4V alloy." *Materials Letters*, 61, 1483-1488.
- Barbooti, M.M., Al-Madfai. and Nassouri. (1988). "Thermochemical studies on hot ash corrosion of stainless steel 304 and inhibition by magnesium sulphate." *Thermochemical Acta*, 126, 43-49.
- Bellman, R. and Levy, A. (1981). "Erosion mechanism in ductile metals." *Wear*, 70, 1-27.
- Bijiwe, J., Logani, C.M. and Tewari U.S. (1989). "On the abrasive wear of some polyimides and their composites." *Proceed. of the Intl. Conf. on Wear of Materials*. Denver, CO, USA, 75-92.
- Bolles, C. (1995). "HVOF thermal spraying an alternative to hard chrome plating." *Weld. J.*, 74(10), 31-35.
- Bornstein, N.S., DeCrescente, M.A. and Roth, H.A. (1975). "Effect of vanadium and sodium on the accelerated oxidation of nickel base alloys." *Int. conf. on Gas Turbine in the Marine* Columbus, U.S.A, 115-148.
- Bunshah, R.F., (1994). "Hand book of deposition technologies for films and coatings."

William Andrew Publishers, 527-532.

Bunshah, R.F., (1994). "Hand book of deposition technologies for films and coatings." William Andrew Publishers, 527-532.

Doychak, J., (1995). "Oxidation behaviour of high-temperature intermetallics." *Intermetallic compounds, principles and practice*, Principles, Eds. Westbrook, J.H. and Fleischer, F.L., Pub. John Wiley & Sons Ltd., England.

Eliasz, Shemesh, G. and Latanision, R.M., (2002). "Hot corrosion in gas turbine components." *Engg. Fail. Anal.*, 9, 31-43.

Espallargas, N., Berget, J., Guilemany, J.M., Benedetti, A.V. and Suegama, P.H. (2008). "Cr₃C₂-NiCr and WC-Ni thermal spray coatings as alternatives to hard chromium for erosion-corrosion resistance." *Surf. and Coat. Technol.*, 202, 1405-1417.

Evans, H.E. and Taylor, M.P., (2001). "Diffusion cells and chemical failure of MCrAlY bond coats in thermal barrier coating systems." *Oxid. Met.*, 55(1-2), 259-265.

Finnie, I., (1958). "The mechanism of erosion of ductile metals." *Proceed. of the Third U.S. National Congress of Applied Mechanics*, 527-532.

Finnie, I., (1960). "Erosion of surfaces by solid particles." *Wear*, 3, 87-103.

Finnie, I., (1972). "Some observations on the erosion of ductile metals." *Wear*, 19, 81-90.

Finnie, I. (1995). "Some reflections on the past and future of erosion." *Wear*, 186-187, 1-10.

Frankel, H.E. and Dapkunas, S.J. (1977). "The necessity of coatings in fossil energy conversion system." *Thin Solid Films*, 45(2), 211-234.

Gang-Chang Ji, Chang-Jiu Li, Yu-Yue Wang. and Wen-Ya Li. (2007). "Erosion

performance of HVOF sprayed Cr₃C₂-NiCr coatings.” *J. of Therm. Spray Technol.*, 16, 557-565.

Geobel, J.A. and Pettit, F.S., (1970). “Na₂SO₄ induced accelerate oxidation (hot corrosion) of nickel.” *Metall. Trans.*, 1, 1943-1954.

Geobel, J.A., Pettit, F.S. and Goward, G.W., (1973). “Mechanisms for the hot corrosion of nickel-base alloys.” *Metall. Trans.*, 1, 261-275.

George, E. Dieter, (1988). “Mechanical metallurgy.” McGraw-Hill book company, Singapore, 11-4, 348-375.

Goyal, G., Singh, H. and Prakash, S. (2008). “Effect of superficially applied ZrO₂ inhibitor on the high temperature corrosion performance of some Fe-, Co- and Ni-based superalloys.” *Appl. Surf. Sci.*, 254, 6653-6661.

Gulden, M.E. (1978).”Solid particle erosion of high technology ceramics (Si₃N₄, glass bonded Al₂O₃ and MgF₂).” W.F.Adler (ed.), *Erosion: Prevention and Useful Applications*, ASTM STP 664, Philadelphia, 101-122.

Gulden, M.E. (1981). “Correlation of experimental data with elastic-plastic impact models.” *J. Amer. Ceram. Soc.*, 64, C59-C60.

Guo, M.H., Wang, Q.M., Gong, J., Sun, C., Huang, R.F. and Wen, L.S. (2006). “Oxidation and hot corrosion behavior of gradient NiCoCrAlYSiB coatings deposited by a combination of arc ion plating and magnetron sputtering techniques.” *Corros. Sci.*, 48, 2750-2764.

Gurrappa, I. (2001). “Identification of hot corrosion resistant MCrAlY based bond coatings for gas turbine engine applications.” *Surf. and Coat. Technol.*, 139 (2-3), 272-283.

Gurrappa, I. (2003). “Influence of alloying elements on hot corrosion of superalloys and coatings: Necessity of smart coatings for gas turbine engines.” *Mater. Sci. and Technol.*, 19, 178-183.

Hawthorne, H.M., Arsenault, B., Immarigeon, J.P., Legoux, J.G. and Parameswaran, V.R. (1999). "Comparison of slurry and dry erosion behavior of some HVOF thermal sprayed coatings." *Wear*, 225-229(2), 825-834.

Hearley, J.A., Little, J.A. and Sturgeon, A.J. (1999). "The Erosion Behavior of NiAl Intermetallic Coatings Produced by High Velocity Oxy-Fuel Thermal Spraying." *Wear*, 233-235, 328-333.

Heath, G.R., Heimgartner, P., Irons, G. and Miller. (1997). "An assessment of thermal spray coating technologies for high temperature corrosion protection." *Material Science Forum*, 251-54, 809-816.

Helai, M. and Hashmi, M.S.J. (1996). "Production of free standing objects by high velocity oxy-fuel (HVOF) thermal spraying process." *J. of Mater. Process. Technol.*, 56(1-4), 431-438.

Hong-yu, Dun-wen Zuo, Yu-li SUN, Fen Xu. and Dan Zhang. (2009). "Microstructure of nanometer Al₂O₃ dispersion strengthened Ni-based high temperature protective coatings by laser cladding." *Trans., of Non-ferrous Metals Society of China*, 19(3), 586-591.

Hovis, S.K., Talia, J.E. and Soatlergood, R.D. (1986). "Erosion in multiphase systems." *Wear*, 108(2), 139-155.

Hui Huang, Chao Liu, Liyong Ni. and Chungen Zhou. (2011). "Evaluation of microstructural evaluation of thermal barrier coatings exposed to Na₂SO₄ using impedance spectroscopy." *Corros. Sci.*, 53, 1369-1374.

Hussainova, I., Kubarsepp, J. and Shcheglov, I. (1999). "Investigation of Impact of Solid Particles against Hard Metal and Cermet Targets." *Tribology, Int.*, 32, 337-344.

Hutchings, I.M. (1992). "*Tribology friction and wear of engineer.*" Edward Arnold Publication, 225, 825-834.

Hutchings, I.M. (1993). "Mechanism of wear in powder technology; A review."

Powder Technol., 76, 3-13.

Hwang, Y. and Rapp, R.A. (1989). "Thermochemistry and solubility's of oxides in sodium sulfate- vanadate solution." *Corrosion*, 45, 933-937.

Kamal, Jayaganthan, R., Prakash. S. and Kumar. (2008). "Hot corrosion behavior of detonation gun sprayed Cr_3C_2 -NiCr coatings on Ni and Fe-based superalloys in Na_2SO_4 -60% V_2O_5 environment at 900 °C." *J. of Alloys and Compounds*, 463, 358-372.

Kamal, Jayaganthan, R., and Prakash. S. (2009). "Evaluation of cyclic hot corrosion behavior of detonation gun sprayed Cr_3C_2 -25%NiCr coatings on Nickel- and Iron-based superalloys." *Surf. and Coat. Technol.*, 203, 1004-1013.

Kamal, Jayaganthan, R., and Prakash, S. (2010). "High temperature cyclic oxidation and hot corrosion behaviors of superalloys at 900 °C." *Bull. Mater. Sci.*, 33(3), 299-306.

Kofstad, P. (1988). "High temperature oxidation of metals." *Elsevier Applied Science*, John Wiley & Sons, London & New York, 465-468.

Kolomytsev, V., Bahanly, M., Sezonenko, A., Ochin, P., Dezellus, P. and Portier, R. (2001). "Thermodynamic properties and thermal stability of the multi component TiNi based alloy ribbons." *Metal Physics and Adv. Technol.*, 23, 111-115.

Kolta, G.A., Hewaidy, L.F. and Felix N.S. (1972). "Reactions between sodium sulphate and vanadium pentoxide." *Thermochem. Acta*, 4, 151-164.

Kosel, T.H. (1992). "Friction, lubrication and wear technology." *ASM Handbook*, 18, 199-205.

Kumar, S., Sarma, and Murthy, B.S. (2008). "A statically analysis on erosive wear behaviour of A356 alloy reinforced with in situ formed TiB_2 particles." *Mater. Sci. Engg.*, 476, 333-340.

Lambert, P., Champagne, B. and Arseneault, B. (1991) "Oxidation and hot corrosion

in Na_2SO_4 -10% V_2O_5 of Ni-17Cr-6Al-0.5Y and Ni-16Cr-5.7Al-0.47Y-5Si, MCrAlY alloys at 700 °C.” *Can. Metall. Quart.*, 30(2), 125-130.

Lathabai, S., Ottmuller, M. and Fernandez, I. (1998). “Solid particle erosion behavior of thermal sprayed ceramic, metallic and polymer coatings.” *Wear*, 221, 93-108.

Lawn, B. and Wilshaw. (1975). “Indentation fracture: principles and applications.” *Mater. Sci. and Engg.*, 10, 1049-1081.

Levy, A. (1983). “Erosion mechanism in ductile and brittle materials.” *Proceedings of 6th Int. conf. on erosion by liquid and solid impact*, Cavendish Laboratory, Cambridge, 75-80.

Levy, A. (1986) “The platelet mechanism of erosion of ductile metals.” *Wear*, 108, 1-21.

Levy, A., Aghazadeh, and Hickey, G. (1984). “The effect of test variables on the platelet mechanism of erosion.” *Rep LBL-17835, Lawrence Berkeley Laboratory*, University of California, Berkeley, CA, USA.

Levy, A.V. (1988). “The erosion- corrosion behaviour of protective coatings.” *Surf. and Coat. Technol.*, 36, 87-406.

Li, H.Q., Wang, Q.M., Jiang, S.M., Gong, J. and Sun, C. (2010). “Ion plated Al- Al_2O_3 films as diffusion barriers between NiCrAlY coating and orthorhombic- $\text{Ti}_2\text{-AlNb}$ alloy.” *Corros. Sci.*, 52, 1668-1674.

Li, L., Zhu, R. and Gesmundo, F., (1996). “Hot corrosion of iron in the presence of salt mixture deposit containing NaCl and V_2O_5 at 600 °C.” *J. Mater. Sci. Technol.*, 12(6), 445-451.

Li-Young NI, Zi-long, W.U. and Chun-gen ZHOU. (2011). “Effect of surface modification on isothermal oxidation behaviour of HVOF-sprayed NiCrAlY coatings.” *Progress in Natural Science; Materials International*, 21, 173-179.

Luer, K.R., DuPont, J.N. and Marder, A.R. (2000). “High temperature sulfidation of

- Fe₃Al thermal spray coatings at 600 °C.” *Corrosion*, 56, 189-198.
- Luthra, and Spacil, H.S. (1982). “Impurity deposits in gas turbines from fuels containing sodium and vanadium.” *J. Electrochemical. Soc.*, 129(3), 649-656.
- Maiti, A.K., Mukhopadhyay, N. and Raman, R. (2007). “Effect of adding WC powder of WC-Co-Cr based HVOF coating and its impact on erosion and abrasion resistance.” *Surf. and Coat. Technol.*, 201, 7781-7788.
- Matthews, A., Areley. and Holiday, P. (1998) “Futures bright for surface engineering.” *Mater. World*, 6, 346-347.
- Meier, G.H., Pettit, F.S. and Briks, N. (1990). “High temperature oxidation and sulphidation processes.” *Proceed. of the International Symposium on High Temperature Oxidation and Sulphidation processes*, Hamilton, Ontario, Canada, 1-15.
- Mingxiang Xie, Shihong Zhang. and Mingxi Li. (2013). “Comparative investigation on HVOF sprayed carbide based coatings.” *Applied Surface Science*, 273, 799-805.
- Mishra, S.B., Prakash.S. and Chandra, K. (2006). ”Studies on erosion behavior of plasma sprayed coatings on a Ni-based superalloy.” *Wear*, 260, 422-432.
- Mobarra, R., Jafari, A.H. and Karaminezhad, M. (2006). “Hot corrosion behavior of MCrAlY coatings on IN738LC”, *Surf. and Coat. Technol.*, 201, 2202-2207.
- Mohanty, M., Smith, R.W., Bonte, M., De Celis and Lugscheider, E. (1996). “Sliding wear behavior of thermally sprayed 75/25 Cr₃C₂/NiCr wear resistance coatings.” *Wear*, 198, 251-266.
- Murthy, K.N., Rao, D.S. and Venkataraman, B. (2001). “Effect of grinding on the erosive behaviour of a WC-Co-Cr coating deposited by HVOF and detonation gun spray process”, *Wear*, 249, 592-600.
- Natesan, K. (1976). “Corrosion-erosion behavior of materials in a coal-gasification environment.” *Corrosion*, 32(9), 364-370.

- Nicholls, J.R. (2000). "Designing oxidation-resistance coatings." *J. of Mater.*, 52, 28-35.
- Nicholls, N. R. and Rickerby, D.S. (2002). "Materials and processes for high temperature surface engineering." *Proceed. Materials Congress 1998 in Cirencester*, in "B278-Materials for high temperature power generation and process plant application", Ed. A. Strang, IOM Communications Ltd., 279-282.
- Niihara, K. (1983). "A fracture-mechanics analysis of indentation-induced palmqvist crack in ceramics." *Mater. Letters*, 2, 221-223.
- Nikitin, V.I. (1987). "The effect of the alloying elements of a CoNiCrAlY system on the corrosion resistance of alloys for protective coatings of gas turbine blades." *Oxidation of Metals*, 53, 241-250.
- Niranatlumpong, P. and Ponton, C.B., Evans, H.E. (2000). "The failure of protecting oxides on plasma sprayed NiCrAlY overlay coatings." *Oxidation of Metals*, 53, 241-250.
- Oskarsson, H. (2007). "Material challenges in industrial gas turbines." *Proc., of Sino-Swedish Structural Materials Symposium*, 11-14.
- Otero, Pardo, Hernaez and Perez. (1990). "The hot corrosion of IN-657 superalloy in Na₂SO₄-V₂O₅ melt eutectic." *Corros. Sci.*, 30, 677-683.
- Perkins, R. A., Chiang, K. T. and Meier, G. H., (1987). "Oxidation characteristics of Ti-25Al-10Nb-3V-1Mo intermetallic alloy." *Scr. Metall.*, 21(11), 1505-1512.
- Pettit, F.S. and Giggins, C.S. (1987). "*Hot corrosion, Ch.12.*" Superalloys II, Sims, C.T., Stollof, and Hagel, (Eds.), Wiley Pub. N.Y., 179-185.
- Pettit, F.S. and Meier, G.H. (1984). "Oxidation and hot corrosion of superalloys." *The Met. Soc. of AIME*, Warrendale, Pennsylvania, 651-687.
- Ramesh, C.S., Seshadri, S.K. and Iyer, K. (1991). "A Survey of aspects of wear of

metal.” *Indian J. of Technol.*, 29, 179-185.

Ramesh, M.R., Satya Prakash, Nath, S.K., PawanKumar Sapra. and Venkataraman, B. (2010). “Solid particle erosion of HVOF sprayed WC-Co/NiCrFeSiB coatings.” *Wear*, 269, 197-205.

Rapp, R. A., Goto, (1981). “The hot corrosion of metals by molten salts.” *Sympos. Fused Salts, Eds.*, 159-160.

Rapp, R. and Zhang, Y.S. (1994). “Hot corrosion of materials: Fundamental Studies.” *J. of Metals*, 46, 47-55.

Rhys-Jones, T.N. and Swindells, N. (1985). “The high temperature of a commercial aluminide coating on IN-738LC and MAR M002 at 700 and 830 °C.” *Corros. Sci.*, 25 (7), 559–576.

Rodríguez, J., Martín, A., Fernández, R. and Fernández. (2003). “An experimental study of the wear performance of NiCrBSi thermal sprays coatings.” *Wear*, 255, 950-955.

Ruff, A.W. and Ives, L.K. (1975) “Measurement of solid particle velocity in erosive wear.” *Wear*, 35, 195-199.

Sheldon, G.L. and Finnie, I. (1966). “The mechanism of material removal in the erosive cutting of brittle materials.” *J. Eng. Ind. Trans.*, ASME, 88, 393-400.

Shigang Xin, Lixin Song, Ronggen Zhao. and Xingfan Hu, (2006). “Influence of cathodic current on composition, structure and properties of Al₂O₃ coatings on aluminium prepared by micro-arc oxidation process.” *Thin Solid Films*, 515, 326-332.

Shipway, P.H. and Hutchings, L.M. (1996). “The role of particle properties in the erosion of brittle materials”, *Wear*, 193, 105-113.

Shrestha, S., Hodgkiess. and Neville. (2005). “Erosion-corrosion behavior of high-velocity oxy-fuel Ni-Cr-Mo-Si-B coatings under high-velocity seawater jet

impingement.” *Wear*, 259, 208-218.

Shui, Z.R., Wang, B.Q. and Levy, A.V. (1990). “Erosion of protective coatings.” *Surf. and Coat. Technol.*, 43/44, 875-882.

Sidhu, H.S., Sidhu and Prakash, S. (2007). “Solid particle erosion of HVOF sprayed NiCr and stellite-6 coatings.” *Surf. and Coat. Technol.*, 202, 232-238.

Sidhu, H.S., Mishra, S.B. and Prakash, S. (2006). “Solid Particle Erosion of HVOF Sprayed NiCr and Stellite-6 Coatings.” *Surf. Coat. and Technol.*, 202, 232-238.

Sidhu, B.S., Puri, D. and Prakash, S. (2005). “Mechanical and metallurgical properties of plasma sprayed and laser remelted Ni-20Cr and satellite-6 coatings.” *Journal of Materials Processing Technology*, 159 (3), 347-355.

Sidhu, T. S., Prakash.S. and Agrawal. (2005). “Studies on the properties of high velocity oxy fuel thermal spray coatings for higher temperature applications.” *Mater. Sci.*, 41, 805-822.

Sidhu, T. S., Prakash. and Agrawal. (2006). “Hot corrosion resistance of high velocity Oxy-fuel sprayed coatings on a nickel-based superalloy in molten salt environment.” *J. Thermal Spray Technol.*, 15 (3), 387-399.

Sidhu, T.S., Malik, A., Prakash, S. and Agarwal, R.D. (2007) ”Oxidation and hot corrosion resistance of HVOF WC-NiCrFeSiB coating on Ni- and Fe- based superalloys at 800 °C.” *J. Thermal Spray Technol.*, 16(5-6), 844-849.

Sidhu, T.S., Prakash,S. and Agrawal, (2006B). “A comparative study of hot corrosion resistance of HVOF sprayed NiCrBSi and Stelite-6 coated Ni-based superalloy at 900 °C.” *Mat. Sci. and Engg.*, 445-446, 210-218.

Simens, E., Browning, G. and Liebhafsky, H. (1955). “*Corrosion.*” 2nd edi., John Willey and Sons, 505-512.

Simons, E.L., Browning, G.V. and Liebhafsky, H.A. (1955). “Sodium sulfate in gas

turbines.” *Corrosion*, 11, 505-514.

Singh, H., (2003). “Studies on the role of coatings in improving resistance to hot corrosion and degradation.” Ph.D. *Thesis Met. & Mat. Eng. Dept.*, Indian Institute of Technology Roorkee, Roorkee.

Singh, H., Puri. D. and Prakash.S. (2005). “Some studies on hot corrosion performance on plasma sprayed coatings on Fe-based superalloy.” *Surf. and Coat. Technol.*, 192, 27-38.

Singh, H., Puri. D. and Prakash.S. (2007). “An overview of Na₂SO₄ and/or V₂O₅ induced hot corrosion of Fe- and Ni- based superalloys.” *Rev. Adv. Mater. Science*, 16, 27-50.

Sobolev, Guilemany. and Nutting, (2004). “High velocity oxy fuel spraying theory, structure-property relationships and applications.” *Maney Publishing*, 12, 564-569.

Soderberg, S., Hogmark, S., Engman, U. and Swahn, H. (1981). “Erosion classification of materials using a centrifugal erosion tester.” *Tribology International*, 14(6), 333-343.

Sreedhar, Masroor Alam, M.D. and Raja, V.S. (2009). “Hot corrosion behaviour of plasma sprayed YSZ/Al₂O₃ dispersed NiCrAlY coatings on Inconel-718 superalloy.” *Surf. Coat. and Technol.*, 204, 291-299.

Stringer John. (1987). “Role of coatings in energy-producing systems: An overview.” *Mater. Sci. and Engg.*, 87, 1-10.

Stringer, J. (1987). “High temperature corrosion of superalloys.” *Mater. Sci. Inc.*, New York, London, Sydney, 1, 1-50.

Sundararajan, G. (1991). “An analysis of the erosion-oxidation interaction mechanisms” *Wear*, 145, 251-282.

Sundararajan, G. and Manish Roy, (1997). “The solid particle erosion behaviour of metallic materials at room and elevated temperatures.” *Tribology International*, 30(5),

339-359.

Tabakoff, W. (1995). "High temperature erosion resistance of coatings for use in turbo machinery." *Wear*, 186-187, 224-229.

Tan, K.S., Wood, R.J.K. and Stokes, K.R. (2003). "The slurry behaviour of high velocity oxy-fuel (HVOF) sprayed aluminium bronze coatings." *Wear*, 255, 195-205.

Tiwari. and Prakash.S. (1997). "Studies on the hot corrosion behaviour of some superalloys in $\text{Na}_2\text{SO}_4\text{-V}_2\text{O}_5$." *Proc. of SOLCEC*, Kalpakkam, India, 22-24th Jan, paper C33, 102-107.

Toma, D., Brandl, W. and Koster, U. (2000). "The characteristics of alumina scales formed on HVOF-sprayed MCrAlY coatings." *Oxidation of Metals*, 53 (1/2), 125-130.

Uusitalo, Vuoristo. And Mantyla. (2004). "High temperature corrosion of coatings and boiler steels below chlorine-containing salt deposits." *Corros. Sci.*, 46(6), 1311-1331.

Wang, B., Gong, J., Sun, C., Huang, R.F. and Wen, L.S. (2003). "The behaviour of MCrAlY coatings on Ni3Al base superalloy." *Mater. Sci. and Engg.*, A357, 39-44.

Wang, Enhou Han. and Wei ki. (2007). "Influence of expandable graphite on fire resistance and water resistance of flame-retardant coatings." *Corros. Sci.*, 49, 2237-2253.

Wasik, (2005). "Effect of fiber volume fraction on fracture mechanics in continuously reinforced fiber composite materials." *M.S.M.E Thesis*, South Florida Univ., Tampa, USA.

Wensink and Elwenspoek, (2002). "A closer look at the ductile-brittle transition in solid particle erosion." *Wear*, 253, 1035-1043.

Wheeler, D.W. and Wood, R.J.K., (2005). "Erosion of hard surface coatings for use in offshore gate valves." *Wear*, 258, 526-536.

Wright, I.G. and Gibbons, T.B. (2007). "Recent developments in gas turbine materials

and technology and their implications for syngas firing.” *Int. Journal of Hydrogen Energy*, 32, 3610-3621.

Yerokhin, A.L., Nie, X., Leyland, A., Mathews, A. and Dwey, S.J. (1999). “Plasma electrolysis for surface engineering.” *Surf. and Coat. Technol.*, 122(2-3), 73-93.

Yuan, F.H., Chen, Z.X., Huang, Z.W., Wang, Z.G. and Zhu, S.J. (2008). “Oxidation behaviour of thermal coatings with HVOF and detonation sprayed NiCrAlY bond coats.” *Corros. Sci.*, 50, 1608-1617.

Zambelli, Levy, (1991). “Particulate erosion of NiO scales.” *Wear*, 68(3), 305-331.

Zhang, Y.S. and Rapp, R.A. (1987). “Solubility’s of CeO₂, HfO₂ and Y₂O₃ in fused Na₂SO₄-30 mol% NaVO₃ and CeO₂ in pure Na₂SO₄ at 900 °C.” *Corrosion*, 43, 348-352.

SCOPE FOR FUTURE WORK

Some of the recommendations for future work are as follows:

1. All the investigated coatings showed promising results in laboratory simulated environment. The electrochemical corrosion behaviour of these coatings should be studied in sulphur and chlorine containing environment.
2. The potential of these coatings should be explored in various salt mixtures relevant to other industrial applications.
3. Elevated temperature erosion behaviour of the coatings may also be investigated.
4. Attempts can be made to estimate the useful life of these coated materials by extrapolation of the laboratory data by mathematical modelling.
5. All these coatings may be exposed to actual service conditions of an industrial turbine to estimate the life of these coatings.
6. Relatively higher porosity content of Stellite-6 coating should be reduced, so as to further enhance the corrosion and oxidation resistance. In this regard effect of post coating treatments such as laser remelting, furnace heat treatment and ion beam treatment should be explored.
7. Hot stage microscopy may be used to understand the development of the scale as well as mechanism of transport of species during the oxidation and hot corrosion runs.

LIST OF PUBLICATIONS

International/National Journals

Jegadeeswaran, N., Udaya Bhat, K., Ramesh, M.R., Prakarthi, S. (2014). “Hot corrosion behaviour of HVOF sprayed Stellite-6 coatings on gas turbine alloys.” *Transactions of Indian Institute of Metals (Springer)*, 67(1), 87-93.

Jegadeeswaran, N., Udaya Bhat, K., Ramesh, M. R. (2013). “Combating corrosion degradation of turbine materials using HVOF sprayed 25% (Cr_3C_2 -25(Ni20Cr)) + NiCrAlY coating.” *Inter. Journal of Corrosion (Hindawi)*, Article ID 824659, 2013, 1-11.

Jegadeeswaran, N., Udaya Bhat, K., Ramesh, M. R. (2013). “Hot corrosion studies on As-received and HVOF sprayed Al_2O_3 +CoCrAlTaY on Ti-31 alloy in salt environment.” *Procedia Engineering. (Elsevier)*, 64, 1013-1019.

Jegadeeswaran, N., Udaya Bhat, K., Ramesh, M. R. (2013). “Oxidation studies on As-received and HVOF sprayed Stellite-6 coating on turbine alloys at 800 °C.” *International Journal of Scientific Engineering Research*, 4(6), 214-220.

Jegadeeswaran, N., Udaya bhat, K., Ramesh, M. R. (2014). “Oxidation resistance HVOF sprayed coating 25% Cr_3C_2 -25(Ni20Cr) + 75%NiCrAlY on Titanium alloy.” *Procedia Materials Science (Elsevier)*, 5(2014), 11-20.

Jegadeeswaran, N., Udaya Bhat, K., Ramesh, M. R. (2012). “Wear studies on wrought and heat treated Nimonic, Titanium and Superco superalloys.” *Int. Journal of Applied Sciences and Engineering Research*, 1(1), 106-117.

International and National Conference Proceedings/presentations

Jegadeeswaran, N., Udaya Bhat, K., Ramesh, M. R., Prakarathi, S. (2012). “Hot corrosion behavior on as-received and HVOF cermets coated Ti-6Al-4V alloy.” *Proceedings of international Symposium for Research Scholars on Metallurgy, Materials Science and Engineering (ISRS 2012)*, IITM, Chennai, 82.

Jegadeeswaran, N., Udaya Bhat, K., Ramesh, M. R. (2013). “Hot corrosion studies on as-received and HVOF sprayed $\text{Al}_2\text{O}_3+\text{CoCrAlTaY}$ on Ti-31 alloy in salt environment.” *Proceedings of Int. Conf. on Design and Manufacturing (ICOND&M 2013)*, IIITDM, Kanchipuram, Chennai on 20/7/2013, MEC 269.

Jegadeeswaran, N., Udaya Bhat, K., Ramesh, M. R. (2011). “Wear behavior on as-received and heat treated turbine blade alloys.” *Proceedings of Joint Inter. Conf on Advanced Materials-2011 (ICAM-2011)*, 19-20 August-2011, BTL Inst. of Tech., Bangalore, 48.

Jegadeeswaran, N., Udaya bhat, K., Ramesh, M. R. (2010). “Adhesive and abrasive wear performance of HVOF sprayed NiCrAl coatings on Ni-based superalloy.” *Proceedings in Int. conf. of Frontiers in Mechanical Engg. (FIME 2010)*, NITK, Surathkal, 1, 70.

Jegadeeswaran, N., Udaya bhat, K., Ramesh, M. R. (2010). “Wear studies on wrought and heat treated Nimonic, Titanium and Superco superalloys.” *Proceedings of NMD-ATM 2010*, IISc, Bangalore, 70.

Jegadeeswaran, N., Udaya bhat, K., Ramesh, M. R. (2014). “Oxidation resistance HVOF sprayed coating $25\%\text{Cr}_3\text{C}_2-25(\text{Ni}20\text{Cr}) + 75\%\text{NiCrAlY}$ on Titanium alloy.” *Int. Conf. on Advances in Manufacturing and Materials Engineering (ICAMME-2014)*, 27-29 March 2014, NITK, Surathkal, MT-03, 1-9.

Jegadeeswaran, N., Udaya bhat, K., Ramesh, M. R. (2014). “Performance of HVOF sprayed $\text{Al}_2\text{O}_3+\text{CoCrAlTaY}$ coating on 12Cr-1Mo steel to combat hot corrosion on turbine alloy.” *Proceedings of Int. Conf. of ICMCTF, USA, ID A1-3-12*, 68.

Bio-Data

Name : JEGADEESWARAN.N
Father's Name : K.NATARAJAN.
Date of Birth : 05-05-1975.
Sex : Male.
Address : 007, Faculty Quarters,
REVA Institute of Technology and Mngt,
Kattigenahalli, Yelahanka, Bangalore-64.
E-Mail Address : jegupavi@yahoo.co.in
Mobile : 9880231308, 0821-2463583.

Educational Qualification

B.E in **MECHANICAL** Passed in 2002 December with First Class (73%) from GCT, Coimbatore – Bharathiyar University.

M.Tech in Industrial Automation and Robotics Passed out in June 2007, First Class with Distinction (85.5%), from Malnad College of Engineering Hassan- VTU, University.

Work Experience

Presently working in REVA University, Bangalore, as a Senior Assistant Professor, Department of Mechanical Engineering, since 1997.

Publications

International Journals Published: 6 and International Conferences Paper Published: 8